# Advanced Battery Management for Novel Zinc-Nickel Single Flow Batteries


Xiang LI (Shawn)

School of Electronic and Electrical Engineering

University of Leeds

A thesis submitted for the degree of

*Doctor of Philosophy*

1st August 2019

# Declaration

The candidate confirms that the work submitted is his own, except where work which has formed part of jointly authored publications has been included. The contribution of the candidate and the other authors to this work has been explicitly indicated below. The candidate confirms that appropriate credit has been given within the thesis where reference has been made to the work of others. Most materials contained in the chapters of this thesis have been previously published in research articles written by the author of this work (Xiang LI (Shawn)), who appears as lead (first) author in all of them.

The research has been supervised and guided by Professor Kang LI, and he appears as a co-author on these articles. All the materials included in this document except for those being cited and referenced are of the author's intellectual ownership.

**A)** Details of the publications which has been used (e.g. titles, journals, dates, names of authors):

**In Chapter 4:**

"A novel rbf neural model for single flow zinc nickel batteries," *Advanced Computational Methods in Energy, Power, Electric Vehicles, and Their Integration. ICSEE 2017, LSMS 2017. Communications in Computer and Information Science, vol 763. Springer, Singapore*, **Published**. Co-author: Kang Li, Zhile, Yang and Chikong Wong. (DOI:*doi.org*/10.1007/978 − 981 − 10 − 6364 − 0_39).

"Teaching-Learning-Feedback-Based Optimization," *Advances in Swarm Intelligence. ICSI 2017. Lecture Notes in Computer Science, vol 10385. Springer, Cham*, **Published**. Co-author: Kang Li and Zhile Yang.
(DOI:*doi.org*/10.1007/978 − 3 − 319 − 61824 − 1_89).

"Joint SoC and SoH Estimation for Zinc-Nickel Single Flow Batteries," *IEEE Transactions on Industrial Electronics (2019).*, **Published**. Co-author: Kang Li, Evan Xiao, and Chi Kong Wong.
(DOI:10.1109/*TIE*.2019.2949534).

"A novel model predictive control scheme based observer for working conditions and reconditioning monitoring of Zinc-Nickel single flow batteries." *Journal of Power Sources 445 (2020): 227282.*, **Published**. Co-author: Kang Li, Evan Xiao, Rui Xiong, Jianhua Zhang, and Peter Fischer.
(DOI:*doi.org*/10.1016/*j.jpowsour*.2019.227282).

**In Chapter 5:**

"Real-time peak power prediction for zinc nickel single flow batteries," *Journal of Power Sources (2019): 227346.*, **Published**. Co-authors: Kang Li, Evan Xiao, Jianhua Zhang, and Min Zheng.
(DOI:*doi.org*/10.1016/*j.jpowsour*.2019.227346).

**In Chapter 6:**

"Joint SoC and SoH Estimation for Zinc-Nickel Single Flow Batteries," *IEEE Transactions on Industrial Electronics (2019).*, **Published**. Co-author: Kang Li, Evan Xiao, and Chi Kong Wong.
(DOI:10.1109/*TIE*.2019.2949534).

"A novel model predictive control scheme based observer for working conditions and reconditioning monitoring of Zinc-Nickel single flow batteries." *Journal of Power Sources 445 (2020): 227282.*, **Published**. Co-author: Kang Li, Evan Xiao, Rui Xiong, Jianhua Zhang, and Peter Fischer.
(DOI:*doi.org*/10.1016/*j.jpowsour*.2019.227282).

**B)** Details of the work contained within these publications which are directly attributable to Xiang LI (Shawn):

With the exceptions detailed in section C, the published work is entirely attributable to Xiang LI (Shawn):
The literature review necessary to construct and originate the ideas behind the published manuscripts, the novel ideas presented in the papers and major editing and processing of the manuscripts.

**C)** Details of the contributions of other authors to the work:

Professor Kang LI, as the primary supervisor, is the co-author for all the publications listed above. These publications have been written under his supervision, benefiting from excellent technical advice, discussions, and editing and proof reading guidance and valuable feedbacks.

Professor Jianhua ZHANG and Professor Rui XIONG have contributed to some technical discussions during visits to their laboratories and performed proofreading to the final drafts of the papers.

The research data has been collected by Mr Shawn LI and Miss YX. LI under the supervision of Dr C.K WONG from the University of Macau, China.

The concepts and the draft manuscripts are also prepared through discussions with Mr Even XIAO.

Dr Peter FISCHER has instructed the battery design and tests.

I am dedicating this thesis to three beloved people who have meant and continue to mean so much to me.

First and foremost, I want to remember my Father Changfa LI whose life was cut short by an accident at the tender age of early thirties. Although he is no longer in this world, his memories continue to regulate my life. May you find peace and happiness in Paradise!

Next, my Mother Yi XIE who raised me up alone and loved me. My Mother with a strong and gentle soul, taught me to believe in the value of hard work.

Last but not least I am dedicating this to my best friend Evan XIAO, who took me to the beauty of Mathematics and Science, and supported me a lot through my toughest period, especially for helping me develop my technology skills. Evan has been my best cheerleader.

# Acknowledgements

Throughout the writing of this thesis, I have received a great deal of support and assistance. Foremost, I would first like to thank my supervisor, Professor Kang LI, whose expertise was invaluable in formulating the research topic and methodology in particular. His continuous support and guidance have helped me to build the foundation of my research and led me through my PhD programme during the last three years. Particularly, a special thank goes to Professor Kang Li to create this research position for me and be patient to inspire me as my life-coach.

To my cheerleader, Dr Peter Fischer: He has been always encouraging and enthusiastic about my progress. And He was always keen to know what I was doing and how I was proceeding, and he has been keeping his fingers crossed for my every research activity. I remember each of his warm hugs whenever a significant milestone was reached. Many Thanks!

I am grateful to following university staff: Dr Benjamin Chong, Dr Petros Aristidou, and Dr Li Zhang for their unfailing support and assistance during the PhD research. I am also grateful to my other colleagues and friends at Queen's University, Belfast and University of Leeds, who have supported me along the way.

A very special gratitude goes out to all down at Queen's University, Belfast, University of Leeds and the Department for Employment and Learning, Northern Ireland for helping and providing the funding for

this work.

With a special mention to Professor Chi Kong WONG and Professor Man Chung WONG at University of Macau. It was fantastic to have the opportunity to work part of my research in their research groups. What a cracking place to work!

I am also grateful to Dr Chang Xiong in Xi'an Jiaotong Liverpool University, Dr Yiming Huang in University of Manchester, Mr Lin Su, whose continuous guidance helped me find my research interests. I also appreciate the research guidance and technical help from Professor Jianhua Zhang for my PhD research.

Last but not least, I would like to thank everyone in the EEN ICaP-Net hub, it was a great sharing laboratory with all of you during the last two years.

Thanks for all your encouragement!

# Abstract

The Zinc-Nickel single flow battery (ZNB) is a new and special type of flow batteries with a number of promising features, such as membrane free and high scalability, and thus has attracted substantial interests in recent years. However, little has been done so far to investigate how to effectively and reliably manage this new type of batteries. Significant developments are required from the engineering prospective: investigation of battery modelling and battery characterization techniques, accurate state estimation, the ability of instantaneous power acceptance and deliverance, the judgement of the battery health, the determination of battery maintenance time, and long-term performance characterization in real applications. This thesis consists of original contributions in the battery modelling and management at system level.

Three battery modelling techniques, namely the artificial neural network (ANN) based battery modelling, electrochemical mathematical battery modelling approaches and the equivalent circuit based battery modelling are examined and compared. Due to the timeliness of the state estimation, the state-of-charge (SoC) estimation needs to be conducted online in the battery management system. In order to improve computing efficiency, an open-circuit-voltage (OCV) observer based on-line joint estimation of both the state-of-charge (SoC) and the state-of-health (SoH) is proposed. At this point, the proposed open-circuit-voltage (OCV) observer can not only enhance the estimation accuracy, but also provide a novel framework where the filter dimension is reduced to one, which offsets the increased complexity

issue when higher order equivalent circuit models (ECMs) are introduced. On the other hand, the performance of battery management system (BMS) is highly dependent on the accuracy of state estimation. By incorporating the merits of model predictive control (MPC) scheme, a novel model predictive control based observer (MPCO) for the working conditions monitoring is then proposed. Two remarkable advantages can be achieved against some current state-of-the-art studies. One benefit comes from the rolling horizon scheme and another is introduced by the imposed constraints on the optimization problem.

Due to the high variability of the intermittent renewable energy sources, load demands, and operating conditions, the state of charge (SoC) is not an ideal indicator to gauge the battery capability to deliver the required services. Alternatively, the peak power is more closely related to the instantaneous power acceptance and deliverance, and its real-time estimation plays a key role in grid-tied energy storage systems. In this thesis, a novel peak power prediction method is developed based on rolling prediction horizon. Four indices are proposed to capture the characteristics of the peak power capability over variable prediction windows. The consequent impact of the electrode material and applied flow rate on peak power deliverability are analysed qualitatively.

From the battery maintenance perspective, longer lifespan can be obtained by the periodic reconditioning. However, there are no indicators to explicitly identify the health status of Zinc-Nickel single flow battery and determine the moment of reconditioning. In this thesis, two health indices in terms of the growth of internal resistance and degradation of the battery capacity are compared. Experimental results confirm that the health status of Zinc-Nickel single flow battery is more sensitive to capacity variations. An indicator according to the capacity changes is thus proposed to judge the timing of reconditioning.

# Abbreviations

| | |
|---|---|
| $3-D$ | three dimension |
| AEKF | adaptive extended karman filter |
| ANN | artificial neural network |
| AUKF | adaptive unscented kalman filter |
| BMS | battery management system |
| CC | coulomb counting method |
| CCCV | constant current and constant voltage method |
| CE | coulombic efficiency |
| CUNY | City University of New York |
| DC | direct current |
| DESS | distributed energy storage system |
| DV | differential voltage |
| DVA | differential voltage analysis |
| ECM | equivalent circuit model |
| EKF | extended karman filter |
| ESS | energy storage system |
| EV | electric vehicle |
| Fraunhofer ICT | Fraunhofer Institute for Chemical Technology |
| FRA | fast recursive algorithm |
| FUDS | federal urban driving schedule |
| GF | gaussian filter |
| HEV | hybrid electric vehicle |
| HPPC | hybrid pulse power characterisation tests |
| IC | incremental capacity |
| ICA | incremental capacity analysis |
| i.i.d. | identically distributed |
| IO | incremental open-circuit-voltage method |
| LSSV | least squares support vector |
| MA | moving average |
| MF | median filter |
| MPC | model predictive control |
| MPCO | model predictive control based observe |
| MPCO | model predictive control scheme based observe |

| | |
|---|---|
| MSE | mean squared error |
| NASA | National Aeronautics and Space Administration |
| OCV | open-circuit-voltage |
| P2D | pseudo two-dimensional model |
| PAs | polyamines |
| PDE | partial differential equation |
| PDF | probability density function |
| PF | particle filter |
| PVAs | polyvinyl alcohols |
| RBF | radial basis function |
| RBFNN | radial basis function neural network |
| RC | resistance and capacity circuit |
| RFBs | Redox flow batteries |
| RLS | recursive least square |
| RMSE | root mean squared error |
| SMO | sliding mode observer |
| SoA | safe operating area |
| SoC | state of charge |
| SoF | state of function |
| SoH | state of health |
| SoP | state of power |
| SP | single particle model |
| TBAB | tetrabutylammonium bromide |
| $T\&D$ | transmission and distribution |
| TLBO | teaching-learning-based optimization |
| TLFBO | teaching-learning-feedback-based optimization |
| VFBs | all-vanadium flow batteries |
| VRLA | valve-regulated lead acid batteries |
| WNN | wavelet-neural-network |
| Zn | Zinc |
| ZNBs | Zinc-Nickel Single Flow Batteries |
| Zn-Air | Zinc-Air Redox Flow Battery |
| Zn-Br | Zinc-Bromine Redox Flow Battery |
| Zn-Ce | Zinc-Cerium Redox Flow Battery |

# CONTENTS

# LIST OF FIGURES

# LIST OF TABLES

# I

# INTRODUCTION

The concept of Redox flow batteries (RFBs) was proposed for almost five decades ago and RFBs are now regarded as one of the most promising and versatile options to store electric energy for both medium sized and large grids as an important category of electrochemical energy storage systems (ESSs). This work targets the management of an innovative RFB type based on the zinc nickel redox couples, namely Zinc-Nickel Single Flow Battery (ZNB), where the originality of this thesis comes from by handling various challenges relating to the management of this new type of batteries. This Chapter begins with a brief introduction of the distinguished advantages and unique battery structure of RFBs. Current progress and facing challenges of ZNBs have been touched in order to detail the contributions and motivations of this work.

## 1.1 Introduction

In recent years, the landscape change in the energy sector has renewed enormous interests in the energy storage systems (ESSs) [8; 9]. This is largely due to the significant renewable generation penetration [10], crucial capital investment on the management of grid peak demands [11] and high cost in grid infrastructure upgrades for reliability and smart grid initiatives [12]. Similar to transmission and distribution (T&D) systems to deliver the electricity over distances to end users, ESS is able to deliver electricity over time when and where the electricity is required [8; 13]. Moreover, the imbalance between the increasing variable renewable generation and the limited capacity of existing assets and the associated challenges can be leveraged through energy storage systems (ESSs). [10]. With improvements in commercial availability, ESS plays a pivotal role in the development of key applications along the entire value chain of the electrical power systems [14; 15]. In particular, the roll-out of ESSs can help facilitate the renewable energy integration, defer capital investment on the generation, transmission and distribution, optimize the power schedule in the peak load shaving, load leveling and shifting, benefit the development of distributed energy storage systems (DESSs) thus enhancing the power quality and the regulation of spinning reserve, and reduce the system cost of emergency backup power instrallations [5; 16; 17; 18].

Form the engineering perspective, the integration of energy storage applications into the power grid promotes high penetration of renewable sources, in particular, the wind and solar power [9; 19; 20]. Long-life rechargeable batteries are not subject to terrain restraints [1], hence can flexibly address the sporadic availability issues of the renewable energy resource, and a number of scaled-up battery systems have been installed alongside renewable generators to improve the power quality and system reliability [21]. In addition, the profit margins of renewable energy suppliers can be increased by introducing the rechargeable batteries in the deregulated market, even providing extra arbitrage over the anticipation [19; 20]. For energy storage in the range of $10kW$ to $10MW$, compared to the existing energy storage systems (ESSs), like the compressed air and hydro-power based

energy storage systems, redox flow batteries (RFBs) are regarded as a promising alternative to lithium batteries and sodium sulphur batteries for next generation grid-tied energy storage devices, due to a number of benefits, such as scalability, safety, depth of discharge, flexibility and rapid response time in millisecond [1; 22].

### 1.1.1 Background of Redox Flow Battery

Redox flow battery (RFB) is one of the most promising grid-tied energy storage technologies in the marketplace. Similar to other electrochemical energy accumulators, RFBs convert the electricity to the chemical energy when they are in the charging modes, and then releasing the stored electrical energy in a controlled fashion once required. Because the redox reactions, i.e., reduction and oxidation take place between two active materials (redox couples) with the assistance of circulating electrolytes to store or release energy, such a kind of battery technique is therefore named as redox flow battery. RFB firstly appeared in a patent [23], and in 1955 Posner [24] revisited this patent. The first flow based secondary cell can be traced back to a Zn-air hybrid RFB framework [25], where the Zn-air hybrid RFB was made with a flowing aqueous solution. It is interesting to note that National Aeronautics and Space Administration (NASA) has promoted the improvement of a modern RFB structure. Motivated by a series ambitious power source plans for the spaceflight [26; 27], NASA pioneered the development of different RFBs such as $Fe-Cr$ battery [28], $Fe-Ti$ battery [29], and $Br^-/Br_3^-$, $V^{2+}/V^{3+}$ and $V^{4+}/V^{5+}$ [27; 29]. Further, NASA defined the electrode configurations [27], and discovered that the energy losses in RFB cycling come from the shunt current [30] and external pumping system [31; 32]. Followed on with new developments in materials, advanced RFBs techniques are introduced, such as $Zn-Cl$ RFB system [33], $Zn-air$ RFB system [34], $Zn-Br$ RFB system [35], $Zn-ferricyanide$ RFB system [36], $H_2-Br_2$ RFB system [37], $all-iron$ RFB system [38], $Br-polysulfide$ RFB system [39] and $all-vanadium$ RFB system in 1985 [40].

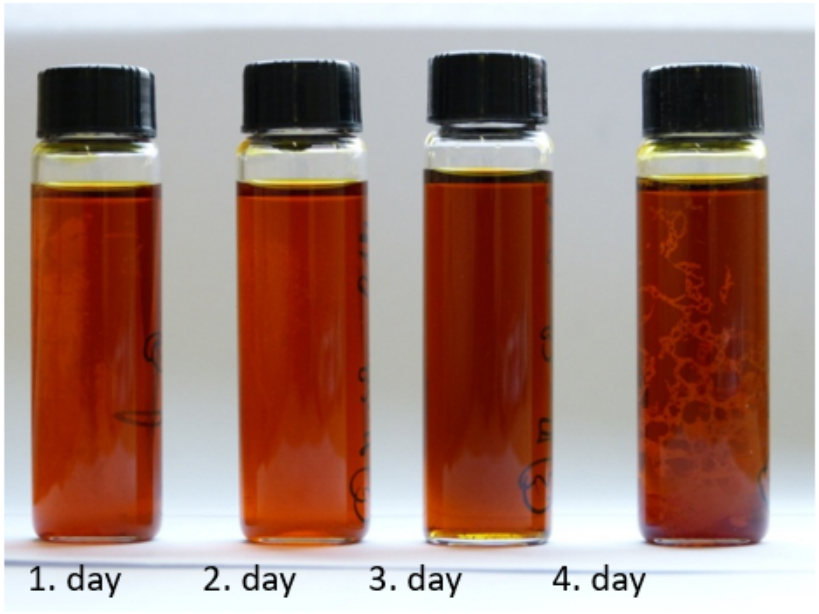


Figure 1.1: The $V_2O_5$ precipitation of electrolyte above $40°C$

Since the introduction of the $all-vanadium$ flow batteries (VFBs), researches are mainly focused on the improvement of electrode structure. As the consequence of commercialization, largely led by the US, the $all-vanadium$ flow batteries (VFBs) pioneered in [40] has become the most popular redox system. Due to vanadium ions used in both tanks to ease the ions cross-contamination problem commonly occurring in other types of RFBs, the lifetime of VFBs is able to be secured hence enhancing its commercial viability. However, the energy density of VFBs is still limited by the intrinsically low solubility of vanadium. Other challenges [1; 21] such as energy wastes, extra costs on membranes, and high system complexities still remain, largely because the fact that the electrolyte is separated into two reservoirs. Further, as shown in Fig.1.1 in our tests, there is a limited temperature window of VFBs due to precipitation of electrolyte above $40°C$. On the other hand, the vanadium prices are skyrocketing due to new regulations introduced in supplying chains like China and some new financial models like leasing are currently under evaluation to offset the increasing costs on raw materials.

In contrast to conventional battery techniques, a typical individual RFB system is relieved from the constraints between storage capacity and the rated power by separating the electrolyte reservoir and the battery stacks [1; 6; 21; 22]. A typical divided RFB framework is illustrated in Fig.1.2, where the applied membrane/separator permits ionic transfer between the electrodes in each half-cell and prevents the cross-contamination of electrolytes stored in the two tanks respectively from being contact with each other [21; 41]. The external pumps drive the recirculation of the electrolytes between the cell stack and the external electrolyte reservoirs. Whereas, the disadvantages of a divided RFB are obvious. Similar to VFBs, the efficiency of such a system is compromised by the structure complexity, energy loss consumed by the pumps, and expensive ionic membranes. Alternatively, an undivided RFBs framework has been proposed, where two redox couples can be dissolved in the same electrolyte. Therefore, only one flowing passenger is left making the system membrane-free. Fig.1.3 gives a comparison between these two frameworks in RFBs. The single flow framework has only one reservoir and one pump to further reduce the energy loss on the pumping system and simplify the structure of the stacks.

Fig.1.4(a) presents a zoom-in view of a typical RFB reactor. Each electrochemical reactor consists of bipolar plates, current collectors embedded in flow flied frames, felt electrodes and membranes/separators. These plates are encased in series with the rigid end-plates/terminals yielding a RFB stack as shown in Fig.1.4(b). The internal reaction rate, stack voltage and induced current are governed by the principles of electrochemical engineering, particularly related with the framework design and materials used [41].

As mentioned above, RFB is favorable due to its unique advantages that battery power design can be independent from the energy/capacity required [41; 42]. In the conventional RFBs techniques, the capacity is only determined by the prescribed electrolyte volume and active species concentration [22; 42]. Stacking more cells in series and enlarging the size of the electrodes can readily increase the desired outputs. Whereas, expanding the volume of the auxiliary tank and

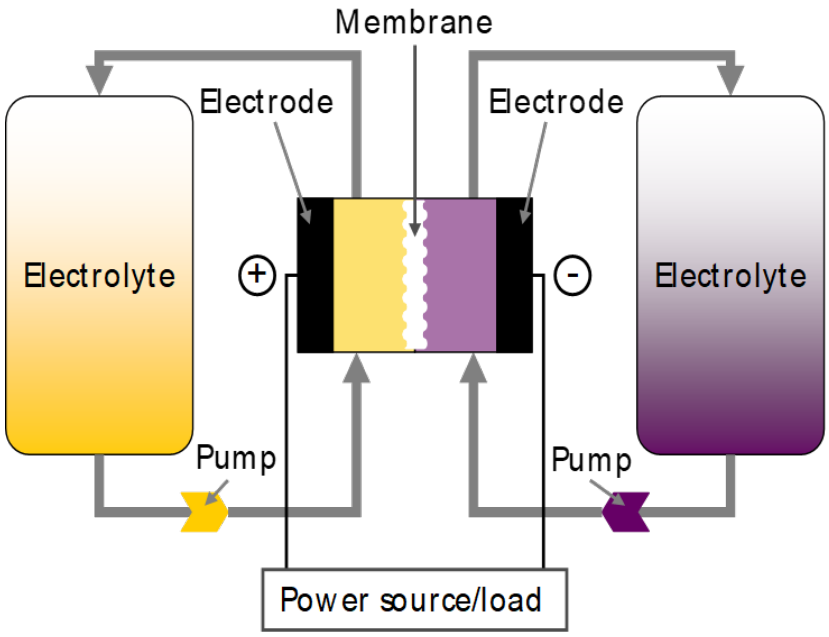


Figure 1.2: A typical divided RFB framework, the electrolyte is recirculating from the tanks to the cell stacks driven by the external pumping control

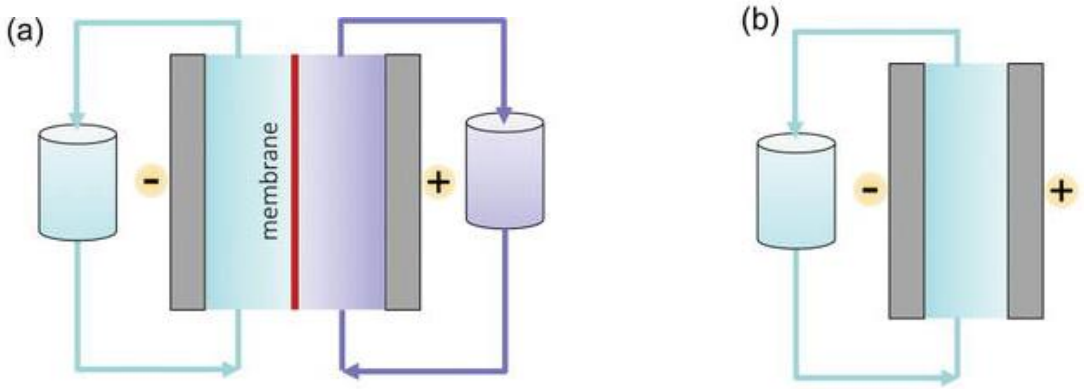


Figure 1.3: The general structure of RFB, (a) a separated framework membranes included and (b) a single flow framework without membranes [1]

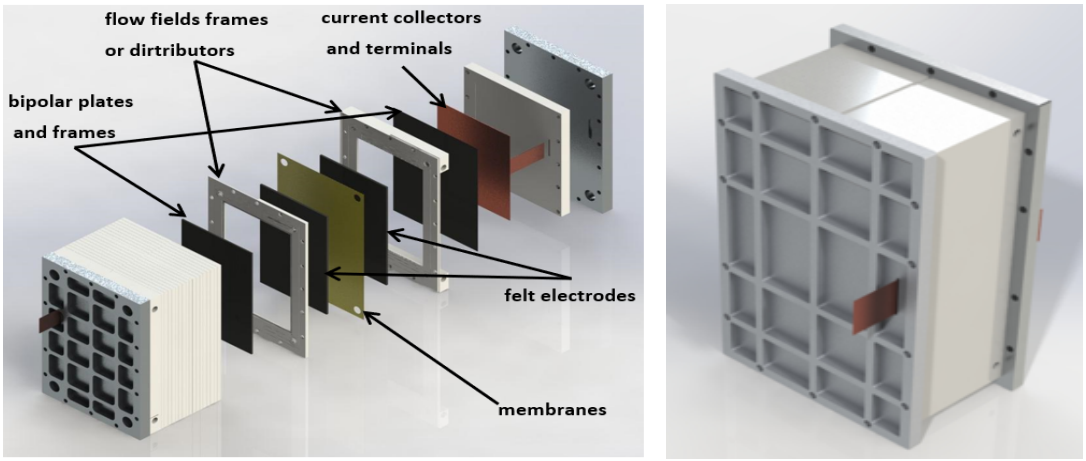


(a) zoom-in view of a typical RFB reactor (b) RFBs stack

Figure 1.4: RFBs stack components a) exploded view of a typical RFB reactor showing its components and b) an assembled stack.

raising the concentration of the electroactive species can increase the battery capacity [1]. This unique characteristic is theoretically capable of optimizing the capacity based on various requirements. Fig.1.5 illustrates the two applications of the FRBs according to different scale requirements. Small size of FRBs in Fig.1.5(a) can be adopted in the utilization of residential energy storage. On the other hand, in Fig.1.5(b), large grid scale VRBs have been used in Fraunhofer ICT, Germany to regulate the wind generators [43]. However, this distinguished factor is not applicable in the case of hybrid RFBs listed in Fig.1.3, which will be detailed in the discussion of Zinc Nickel single flow battery.

Besides, due to the circulating electrolyte, heat generation and dissipation is under control in most cases. Hence the working environment of RFBs is not a restriction. On the other word, RFBs are able to be operated under the normal ambient temperature and pressure environment. Compared with electrolysis-fuel cell plants, the operation of RFBs does not produce pollution emissions leading to offering a safer alternative to other type battery plants such as the fuel cells and lithium cells. Moreover, cell balancing issue when cycling a bulk of lithium batteries does not appear in RFBs operation. For example, in the scenario of widely

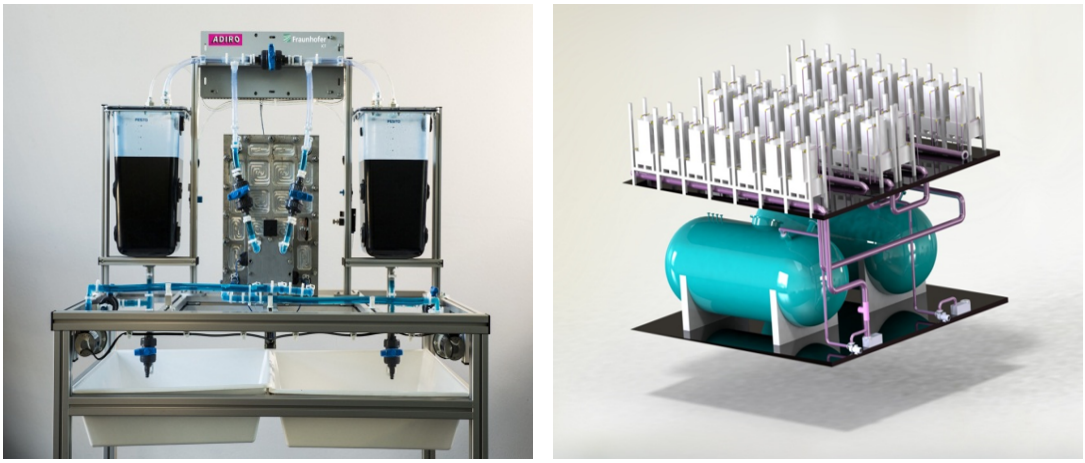

(a) a demonstrator of small scale RFB reactor (b) the schematic diagram of large scale RFBs

Figure 1.5: RFB implementations a) a small scale RFB reactor and b) large scale RFBs.

adopted divided RFBs, the balance issue only needs to be considered between two external electrolytes tanks. Because of the partial re-usability of battery materials [21], the disposal of redox couples is more effective and economical. However, unlike lithium batteries, the aqueous based electrolyte is widely used in RFB, leading to the small solubility of the active species in aqueous electrolyte, which restrains the electrolyte conditions and averages current material density, resulting in relatively low energy density. Considering the combination of the aforementioned factors including the advantages and disadvantages, RFBs have ultimately proved promising in the development of medium- and large-scale energy storage systems [1; 44]. Also, the RBF applications can be deployed alongside the wind, tidal and solar generators. Furthermore, it is interesting to note that if the consumed electrolytes can be substituted promptly leading to a quick recuperation of the used-up RFBs energy, the RFBs is able to be implemented in specialised transportation tools.

### 1.1.2 Development of Zinc Nickel Flow Battery

As alternatives to the lithium batteries and other RFB counterparts, an innovative RFB system based on nickel and zinc redox couples was first proposed

by [45]. The theoretical capacity and energy ratio of Zinc-Nickel single flow batteries (ZNBs) are higher than other RFB counterparts. The intrinsic electromotive force is above $1.72V$ [46], which is much higher than VBFs $1.20V$ [40], leading to an improved specific energy (upper than $85Wh/kg$) [2; 45]. The nominal voltage maintains constant up to $1.60V$ throughout the discharging period [2; 45]. The discharging voltage is relatively constant at broad ranges of current rates. Moreover, the aqueous electrolyte exhibits distinctive stability and non-toxicity under over-charging and over-discharging scenarios [2]. An interesting feature of ZNBs is the membrane-free, which differs from conventional RFB technologies. In this regard, ZNBs employ only a single electrolyte and therefore can operate without a membrane/separator. The expensive membranes are exempted from the system design leading to cost-saving and manufacture-simplifying [45]. The schematic diagram of ZNBs and a $200Ah$ pilot-scale ZNBs application are give in Fig.1.6. Only one pump is required in this system, thus the system efficiency is further improved due to the less power consumed by the pump.

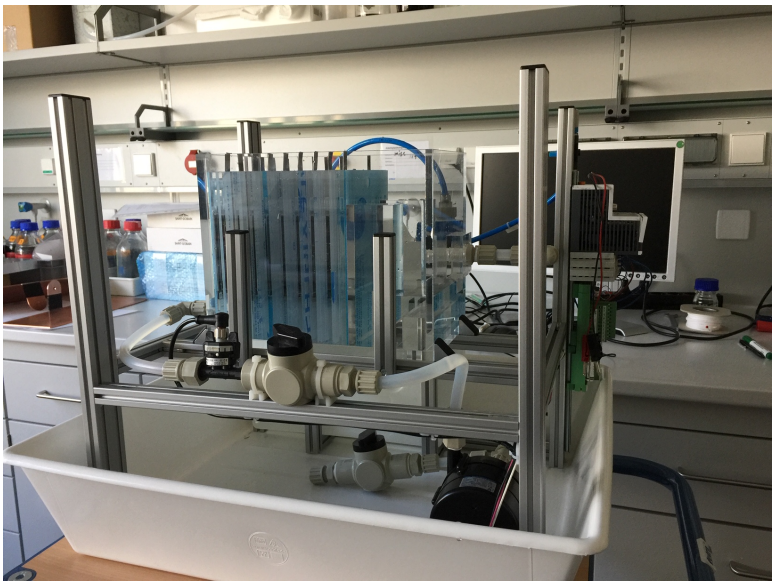

Figure 1.6: A pilot-scale Zinc Nickel flow battery from Fraunhofer ICT, Germany and Leeds, UK

The design of a nickel-zinc flow battery is very similar to an all-lead battery

with a single tank [47]. Zhang et al in 2008 [2] first used copper electrodes for the zinc deposition, which they electroplated with cadmium to avoid gassing. The group later changed the copper electrode to cadmium coated nickel [45]. Other groups also used carbon composite plates. The cathode in a ZNB system is usually made of nickel foam. The nickel hydroxide is coated there in form of a nickel hydroxide paste. Regarding electrolyte, an alkaline zincate solution ($pH > 14$) is applied. The stack design of a nickel zinc flow battery is different from conventional bipolar arrangements in stacks. As illustrated in Fig.1.7, the ZNBs stack usually consists of cell distribution plates, which are holding the electrode and also provide manifolds for the distribution for the zincate electrolyte. The electrodes in such a stack are connected electrically in parallel, which results in a voltage of $1.6V$ OCV of the cell stack. The principal reactions are briefly given as follows.

**Cathode chemical reaction:**

$$2NiOOH + 2H_2O + 2e^- \underset{charging}{\overset{discharging}{\longrightarrow}} 2Ni\,(OH)_2 + 2OH^-$$

**Anode chemical reaction:**

$$Zn + 2OH^- \underset{charging}{\overset{discharging}{\longrightarrow}} Zn\,(OH)_2 + 2e^-$$

**Overall chemical reaction:**

$$Zn + 2H_2O + 2NiOOH \underset{charging}{\overset{discharging}{\longrightarrow}} 2Ni\,(OH)_2 + Zn\,(OH)_2$$

So far the research of ZNBs largely focuses on the bench-scale cells. After a promising magnitude of voltage over $1.6V$ in discharging phase was presented in [45], [48; 49] further examined particular features of the ZNBs. The relationship between applied flowrate and generated zinc morphology has been investigated in [49], and a high rate flow has been reported to maintain the zinc morphology in the good shape during the charging process. More then 1500 cycles have been achieved under a flowrate of $15cm/s$, but the applied current density has to be limited by $20mA/cm^2$. In addition, further research [48] has demonstrated that though gassing occurs in both charging and discharging processes due to the charge efficiency loss, the flowing electrolyte can attenuate the gas evolution

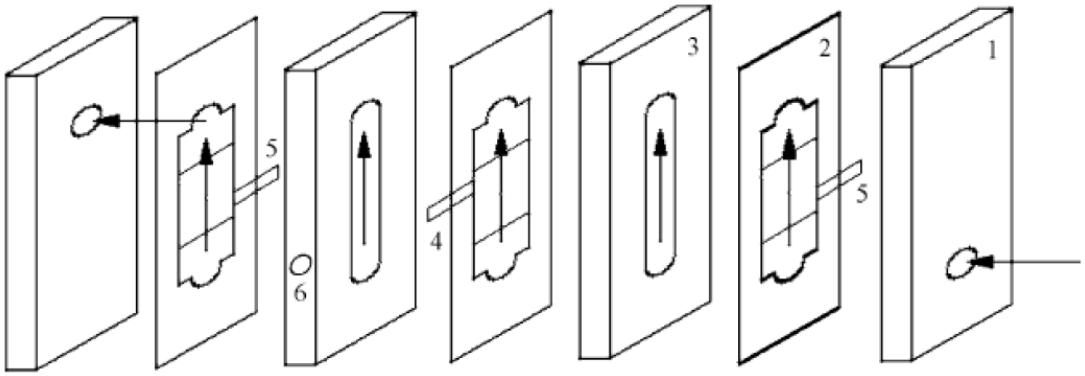


Figure 1.7: A nickel zinc stack design by Chen et al [2], (1) Perspex end plate, (2) rubber gasket, (3) flow passage, (4) work electrode: cadmium-plated nickel plate, (5) counter electrode: sintered nickel electrode and (6) location hole of the reference electrode

process. As a result, the evolved $H_2$ and $O_2$ are less than the gas evolved in a Zinc-air battery, which reduces the safety hazards associated with a mixed $H_2$ and $O_2$ gas releasing. In [50], the influence of additives has been examined. Lead ion and tetrabutylammonium bromide (TBAB) have been tested in their work. The favorable result signifies that these additives can inhibit the growth of spongy zinc, leading to smoother zinc deposition with higher charge efficiency. As shown in Fig.1.8, a commercialization oriented ZNBs project has been carried on in the cellar of energy institute at CUNY for many years [51], in which a $30kWh$ battery string assembled with ZNBs was made at the energy institute. According to their reports, by the end of 2013 summer, the battery string has been operated more than 900 deep cycles retaining the coulombic efficiency over 95%. Followed on under the support of Department of Energy, USA, Con Ed, and NYSERDA, a larger $200kWh$ battery string was constructed by the university spin-off company, Urban Electric Power. These prototypes of ZNBs are designed for a long service life over 10 years, more than $5000 - 10000$ charge cycles. In this regard, this battery string is expected to be able to yield more the $6000 saving per month through the regulation of peak demands in the Steinman Hall. This newly constructed battery string has demonstrated the feasibility of using ZNBs to reduce the peak electrical load in the Steinman Hall resulting in extra

revenue from the decreased electrical utility bill of CUNY. In addition, scaled-up prototypes of ZNBs have been developed as well in CNUY. From $6.5Wh$ research batteries to the $35Wh$ small-scale "workhorse" batteries, the energy institute at CUNY definitely is the pioneer in the commercialization path of ZNBs.

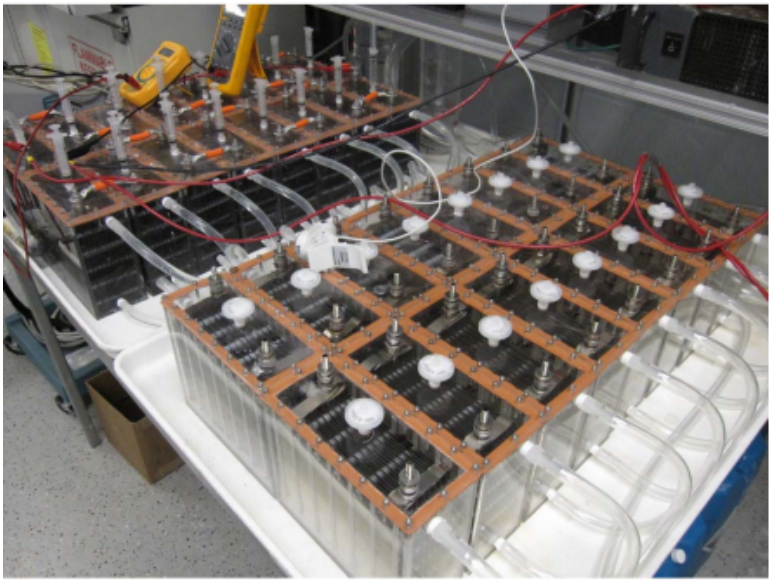

Figure 1.8: A prototype ZNB located in Steinman Hall, CUNY

### 1.1.3 Challenges for Zinc Nickel Flow Battery

Due to the merits of environment friendly, less cost, and alternative to nickel cadmium batteries, ZNBs are expected to replace the lead-acid batteries at the lower cost end of the market in long term. Though ZNBs are innovative and have been announced as a low-cost batteries that are safe, non-toxic, reliable with fast discharge rates and high energy densities, and a promising competitive battery technology to the existing lithium-ion cells, cyclability of this systems is rather poor. In the charging phase, the dendrites are crystalline structures in zinc anode. The growth of zinc dendrites should mainly be responsible for the poor cyclability. In order to scale up ZNBs for commercialization, dendrite build-up has to be addressed in advance. Along with the growth of dendrite, serious side effects may occur when cycling the battery, such as the capacity fluctuations, unstable

terminal voltage signals with voltage jumps, charge efficiency reduction leading to serious gas evolution and manifold blocked due to the loose zinc deposits, etc. For example, in high $pH$ alkaline media ($pH$ greater than 14), this alkaline media encourages the desirable reaction at the sintered nickel form (cathode), and thus the gas formation is limited. However, in this case, as the cell potential drifts higher during the zinc deposition over time, electrode surface conditions are forced to be far away from the favorable environment for $Zn$ formation at the anode and $NiOOH$ oxidation at the cathodes, which is however in favor of gas generation. In Fig.1.9(a), once the discharging process cannot consume all the generated zinc depositions, the flowing electrolyte may take deposition out of the surface of electrodes, then floating with the electrolyte recirculation. At this point, the floating zinc depositions will increase the risk to block the pipe and pump, leading to the halt in pump. Furthermore, after long-term cell cycling, the reactants are consumed leading to the decrease of the charge efficiency, as a consequence the growth of zinc dendrite as shown in Fig.1.9(c) and gas evolution as shown in Fig.1.9(b) become apparent.

Besides, low applied current density is another issue to hinder the viability of ZNBs commercialization [45]. This challenge is also associated with the dendrite build-up. The problem of dendrite formation and zinc morphology variation exists in most Alkaline zinc based cells. Zinc depositions in alkaline media are generated at different $pH$ levels. For example, zinc morphology is the solid zinc hydroxides in low alkalinity. And then, these hydroxides can further alter to zinc oxide, which is highly insoluble. At a higher alkalinity, zinc can dissolve to form zincates, resulting in over-saturated zinc oxide solution. The latter is favourable, because it reduces the anode potential. But in such a high $pH$ alkaline media, it leads to a lower anode potential, resulting in uniform deposition of zinc at the anode. At high current densities, zincate tends to form a sponge-like deposition, which can lead to dendrite formation [52], and than the generated dendrite formation can lead to micro shortages inside of the battery, and thus reducing lifetime tremendously. Thereby, the applied current densities is difficult to reach to an ideal level but maintaining around $20mA/cm^2$ [53].

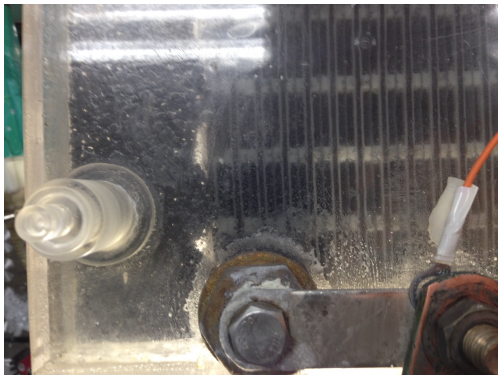

(a) floating undissolved zinc deposition after discharging phase

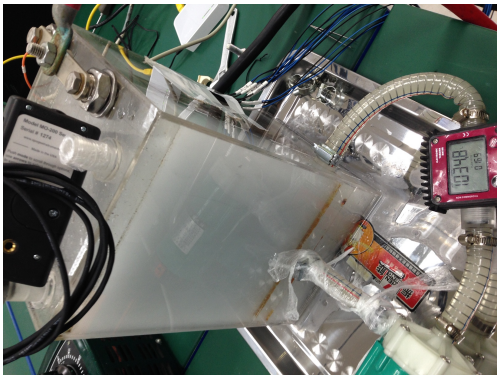

(b) gas evolution over time

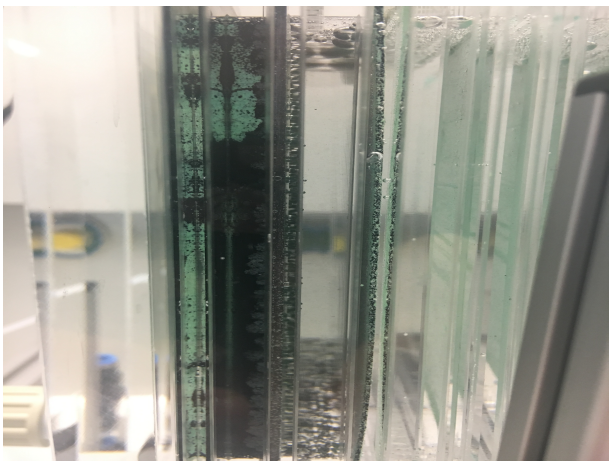

(c) the zinc dendrite build-up after 3.5$h$ charging process

Figure 1.9: Observed issues in our tests, a) the floating undissolved zinc deposition will block the main manifolds and inlet of pump, b) due to loss of charge efficiency, gassing is more apparent, c) the growth of dendrite can be inspected after a long charging protocol

For stationary storage applications, the dendrite growth problem can partially be circumvented by flowing electrolyte like the nickel-zinc single flow battery. Further, for ZNBs, the issues like the sponge-like zinc morphology or zinc dendrite can be partially solved by introducing the "stripping cycles" operation, thus improving the battery lifespan. This procedure was first implemented on ion neutral

*pH* zinc bromine batteries. During these stripping cycles the whole deposited zinc will be stripped from the anode by deep discharging the battery. If all zincs are dissolved, the zinc deposition can be started anew. From the engineering perspective, the stripping method can avoid the battery internal short-out. However, stripping cannot maintain a stable discharging performance as the zinc residual will be accumulated again after per stripping to reduce the active material areas for precipitation, leading to fluctuations in discharging capacity and voltage profiles. As observed in Fig.1.10, voltage jumps take place occasionally, which increases the difficulty in battery management. The fluctuated capacity over time makes the estimation of state of change (SoC) error-prone. The error of SoC estimation can easily lead to overcharge or over-discharge, which will progressively provoke the growth of dendrites associated with non-equilibrium [49]. Besides, the other challenge is to determine the moment of reconditioning/maintenance. Though in [51], reconditioning maintenance has been recommended per 15 cycles, reconditioning time is dependently determined by the materials of electrodes, the structure design, and the applied flow rate. As shown in [54], novel materials can postpone the timing of reconditioning maintenance. Neither over-frequent nor late reconditioning has benefits for the management of ZNBs, resulting in less utility ratio or irreversible capacity degradation respectively.

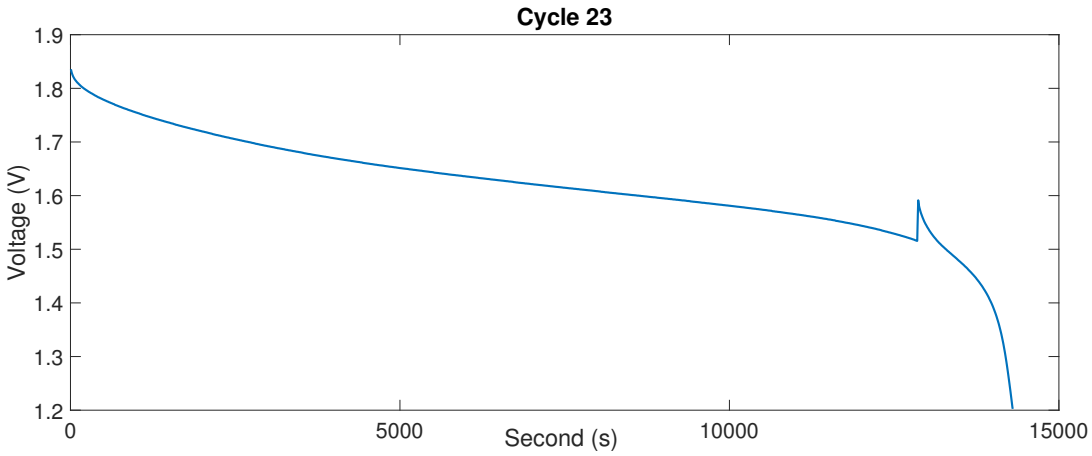


Figure 1.10: An abnormal voltage in discharging process

On the other hand, as mentioned in Section 1.1.1 and shown in Fig.1.3, ZNB framework relies on a low cost, hybrid RFB structure. Hence the expensive membranes have been removed from the battery design, and battery manufacturing has been simplified significantly. However, using the hybrid RFB structure will lose the beauty of RFBs, in which the battery capacity has been restricted by the active areas on the negative electrodes. In other words, the cell capacity cannot be simply increased by either improving reactants concentration or scaling up the tank volume. Additionally, once the applied number of negative electrodes has been confirmed, the battery capacity is thus fixed, losing the flexibility of the RFBs. At this point, this feature impels battery manufacturers and researchers to seek new methods to increase the porosity of anodes. Other side affects have appeared such as the raised manufacturing complexity and cost, so that the viability of a commercial ZNBs is still a pending issue.

## 1.2 Research Motivations and Contributions

ZNBs have been researched from the aspects of material science and chemistry science to improve the cell performance. However none of them fully satisfies the cost and performance requirements. Significant developments and efforts are still required at all levels: investigation of new chemistries, materials engineering, cell design, long-term performance characterization in realistic environments and battery management system design. This work gives a comprehensive coverage of the ZNB management from the engineering perspective, where the characteristics in terms of voltage, power, capacity are investigated. Incorporating with the state-of-the-art battery management system (BMS), this thesis addresses the existing technical issues in ZNB modelling, state estimation and battery maintenance.

The main contributions of this work can be summarized as follows:

1. A new heuristic optimization method, namely, teaching-learning-feedback-based optimization (TLFBO) is proposed based on the existing teaching-learning based optimization (TLBO). The proposed TLFBO is then used to

identify parameters in the artificial neural network (ANN) based nonlinear battery model.

2. Two improved methods are proposed to improve the SoC estimation techniques. One method relies on a newly proposed open-circuit voltage (OCV) observer to address the computing complexity issues when higher order ECMs are used in state estimation but also secure a high estimate precision. On the other hand, inspired by the model predictive control (MPC) paradigm, a model predictive control scheme based observer (MPCO) is developed to further increase the accuracy of SoC estimation. Because the proposed MPCO takes advantages of the mechanism of MPC on rolling horizon framework and solving constraints, the knowledge of the electrochemical process can be incorporated in the state estimation. Substantial experiments and simulations are conducted and the results confirm that the proposed MPCO outperforms some existing approaches in terms of convergence, robustness, effectiveness and generality. In addition, the competitiveness is demonstrated by analytical comparisons against other three state-of-the-art estimators. In this regard, the relationships of the proposed observer with other estimators are summarized briefly.

3. The peak deliverability of ZNBs is elaborated. A novel peak power prediction method is developed based on the rolling prediction horizon algorithms. Four indices are proposed to capture the characteristics of the peak power capability over length-varying prediction windows. The consequent impacts of the electrode material and applied flow rate on peak power deliverability are analysed qualitatively.

4. Two capacity estimation methods are outlined in this work. A couple popular model free methods, i.e., incremental capacity analysis (ICA)/differential voltage analysis (DVA) are used. In particular, due to fluctuations in the battery capacity and voltages, noises and error spikes rejection approaches for processing the raw data are given in details. However, experiments have demonstrated these model free methods are not applicable for capacity estimation of ZNBs. On the other hand, model based capacity estimation

methods are presented alternatively. Along with the proposed OCV observer and MPCO methods, the capacity can be estimated accurately. An indicator according to the capacity changes is thus identified to judge the moment of battery maintenance.

## 1.3 Outline of Thesis

This thesis mainly deals with the development of BMS algorithms for ZNBs, including battery modelling, real-time SoC and SoH estimation, and the judgement of reconditioning moment for battery maintenance.

Fig.1.11 summarizes the interdependence of thesis chapters. The thesis begins with Chapter 1, the background introduction of ZNBs, in which the advantages and unique features of flow batteries are reviewed. Compared with other types of batteries, the main drawbacks of zinc-based flow batteries and the corresponding solutions from the material perspective are discussed in Chapter 2. In order to address the operational issues from the engineering perspective, Chapter 3 presents the details of the design of battery structure and experimental procedures. Then, the research objectives to investigate the advanced battery management to regulate the operation of ZNBs including state estimation, function prediction, and battery maintenance, are introduced. Chapter 4 investigates the online battery modelling and SoC estimation techniques. Incorporating the online SOC estimation technique, Chapter 5 and Chapter 6 details the research on the power deliverability and capacity degradation modes of ZNBs, respectively.

The remainder of the thesis is organized as follows:

- Chapter 2 presents a literature survey on battery management for zinc-based redox flow batteries from the material perspective. A brief introduction to different battery applications encompassing cell performance, challenges, and prospects is given first. Then the existing solutions to the ZNB cycling problems are surveyed from the material perspective.

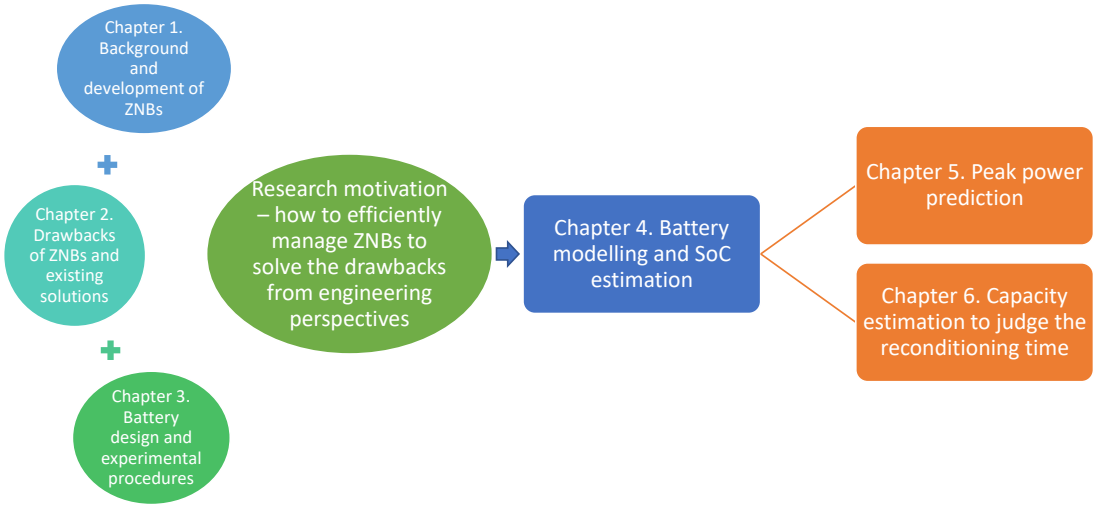


Figure 1.11: The interdependence of thesis chapters

- Δ Chapter 3 focuses on the design of testing regimes and ZNB demonstrator fabrication process. The design procedures of a hand-made ZNB demonstrator is detailed and the testing regimes used in this work are provided as a valuable reference for the peers. In addition, the blueprint for a pilot-scale ZNB is described at the end.

- Δ Chapter 4 studies three popular battery modelling tools, i.e., Artificial Neural Network Model, Electrochemical Mathematical Model, and Equivalent Circuit Model. According to the intrinsic features of ZNBs, the Equivalent Circuit Model (ECM) based battery SoC estimation techniques are elaborated.

- Δ Chapter 5 deals with ZNBs peak power estimation in real-time. Since little work has been done to examine the peak power delivery capability of ZNBs, this Chapter details the procedures of online peak power prediction techniques. In addition, the ability of instantaneous power acceptance and deliverance are examined according to the peak power prediction during the charging and discharging processes. The results confirm the outstanding power deliverability of ZNBs.

- Chapter 6 extends the research work in Chapter 4, the proposed SoC methods are employed in this chapter for State of Health (SoH) estimation. The experimental work has confirmed that the capacity estimate is deemed to be a good indicator for SoH. Other state-of-the-art capacity estimate methods are compared. Based on the observation that the capacity degradation of zinc-nickel flow cell can be correlated with zinc deposition characteristics, a methodology using the capacity estimation as the indicator to determine the reconditioning time for cell maintenance is then proposed.

- Chapter 7 concludes this thesis. The research contributions, as well as some reflections and suggestions for future work, are summarized.

- Chapter 8 itemizes the published work.

# II

# LITERATURE SURVEY

ALKALINE zinc battery cells are regarded as a promising and competitive battery technology to the existing lithium-ion cells. The advantages of alkaline zinc cells are high energy density at low material costs and the usage of non-toxic non-flammable electrolytes. These features make alkaline zinc cells attractive for stationary storage applications. The redox couple of $Zn^{2+}/Zn$ is highly soluble in most aqueous electrolytes, and it generates a more negative standard potential with minimal overpotentials due to the rapid kinetics. Thus, among the redox flow batteries, zinc based flow batteries gradually gain substantial interests and attentions in recent years. However, the performance is greatly affected by the zinc deposition in charging process and zinc corrosion at rest. In addition, in a medium or large scale energy storage system, the behaviours of zinc based flow cells are restrained by the zinc metal deposition. Therefore, researchers have proposed various management methods from the material perspective to remedy the poor cyclability deficiency of different zinc based flow batteries. In the following, two widely adopted cell architectures are compared. This literature survey further reveals that the presented zinc nickel single flow battery (ZNB) has the potential for commercial production. In particular, the existing battery management methods to solve various issues in relation to the zinc-nickel single flow batteries (ZNBs) are reviewed. In addition, comparisons among popular battery applications are given at the end.

## 2.1 Zinc-Bromine Redox Flow Battery

The research of Zinc-Bromine cell can be traced back to 1970$s$ [53], when one of the earliest RBF was presented [1]. After almost four decades of development, Zinc-Bromine Redox Flow Battery (Zn-Br) is now at the commercial stage due to its maturity. There are two major battery developers in the market, i.e., ZBB Corporation in USA, and Redflow Technologies Ltd. in Australia. Zn-Br exhibits some outstanding features compared with other counterparts, as higher energy density ($70Wh/kg$) at lower cost [55; 56].

### 2.1.1 Performance, Challenges and Management

During the charging process, analogous to other zinc-based batteries, metallic zinc is deposited forming into a thin film on the carbon composite negative electrode. In the meantime, bromide ions alter to bromine by oxidization at the positive electrodes, but also commonly reacting with the organic agent, forming a the thick bromine oil that will sink down to the bottom [5; 57]. The reverse reaction occurs during the discharging process, where the zinc oxidizes and elemental bromine reduces, thus generating up to $1.82V$ theoretical cell potential. However, the net efficiency of such a system is not high, around 75% [5]. It is worthy to mention that compared with Zinc-Bromine cell, the reactants and produces in ZNBs are highly soluble, which simplifies the battery cycling procedures significantly, enabling online modeling and state estimation introduced which will be elaborated this thesis.

There are two major hurdles for the Zn-Br commercialization, which needs to be addressed in battery management. The first is the high self-discharging rate. A separator can prevent the migration of bromine ions from traveling across to the zinc electrode compartment [58]. In this regard, the self-discharging rate can be reduced but at an increased cost. On the other hand, the produced bromine has to be stored in one agent [57]. In details, the generated bromine has to be collected by other agents. As a result, the applied organic agents mixed with the bromine ions form an insoluble emulsion [59]. At this point,

the cell operation and battery management are meticulous, and thus a manual battery management has to be carried out. Since the insoluble emulsion contains the produced bromide and has different density from water, the bromide retention can be achieved when circulating the electrolyte to separate emulsion in the bottom of the tank according to the gravity. When the Zinc-Bromine cell is cycling under such a management paradigm, the additional separation procedure adds further efforts to operate the cell. Some commonly used complex agents, such as $N-methyl-N-ethyl-morpholiniumbromide$ and $N-methyl-N-ethyl-prolidiniumbromide$ [1], make the Zn-Br cell very sticky and unclean.

Other commonly noted issues are related to the Zinc electrodes, such as the material corrosion, and dendrite formation over time. At this point, ZNBs are subject to the similar issues when batteries are cycling. In addition, the reaction rate of redox couples $Zn/Zn^{2+}$ is faster than bromide couples, leading to the increasing polarization and ultimate cell failure [59]. This problem can be partially circumscribed by the cell management techniques from the material aspects. From the carbon cathode aspect, special materials should be coated on the surface of the electrodes [60].

### 2.1.2 Cell Prospects

The Zn-Br battery has been researched for over four decades. The first demonstration project in $3kWh$, $10kWh$ and $20kWh$ sub-modules was reported in 1983 [1]. As illustrated in Fig.2.1, $10KWh$ pilot-scale Zn-Br was tested in the Laboratory. A commercial scale of Zn-Br batteries are now available in US and Australia. However, the complex system restrained the development of battery management for Zinc-Bromine cells. More efforts have been made on the material improvements to further increase the cell efficiency as alternative. Up till now, the specific energy of Zn-Br battery reaches up to $440Wh/kg$ with reasonable cycling efficiency around 80%. Due to the high degree of reversibility of the redox couples, the cost of Zn-Br system satisfies commercial requirements.

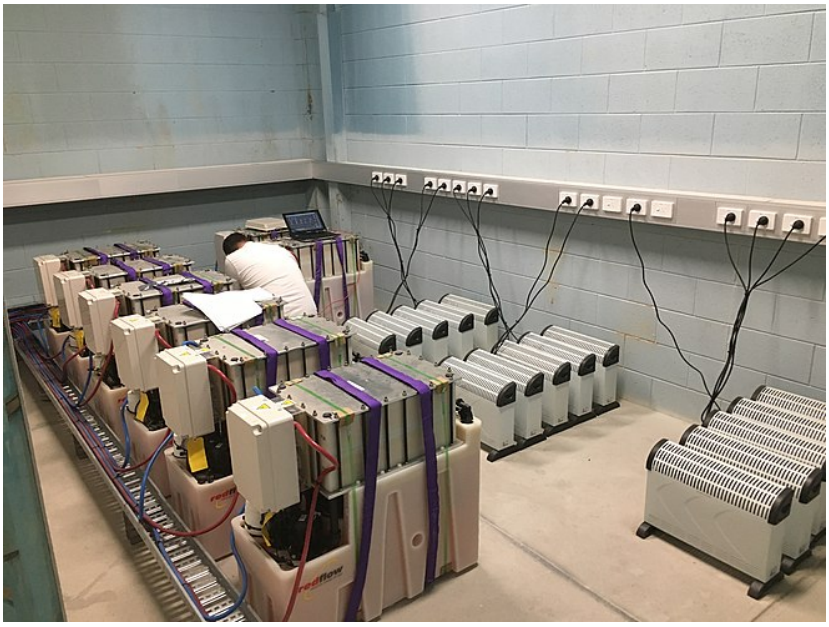

Figure 2.1: RedFlow Zn-Br $10kWh$ flow batteries in a performance testing lab

## 2.2 Zinc-Cerium Redox Flow Battery

The Zinc-Cerium is a newly proposed concept based on a hybrid redox battery framework, and the initiative appeared in two US patents filed in 2004 [61] and 2005 [62]. The research on zinc deposition/stripping and cerium redox half-cell reactions led to the proposal of the Zinc-Cerium redox batteries (Zn-Ce). Though Zn-Ce was introduced not for long, the research on cerium redox couples can be traced back to many decades ago on half-cell investigation of Ce(III) and Ce(IV). The Methanesulfonic acid is commonly employed as the electrolyte due to the ability to dissolve cerium ions [63]. The magnitudes of cell current and voltage are determined by the size of electrodes and the number of cells stacked, respectively. At first, a carefully selected membrane is used in the Zn-Ce cell. However, the mixture of zinc and cerium can yet be observed over time, in practice. In other words, the applied membranes are not strictly effective to proton transport selection. Therefore, the potential for membrane-free battery architecture has been raised, leading to the proposal of a hybrid framework. In this regard, only one electrolyte reservoir is required, in which the zinc and cerium can be

mixed together [64]. Similar to the Zn-Ce, ZNBs take the advantage of this hybrid framework to significantly simplify the complexity of the battery structure and reduce the battery cost. Moreover, the hybrid framework avoid the State of charge (SoC)imbalance between two electrolyte reservoirs. Consequently, the cell SoC may be estimated using the terminal measurements through the proper electrical battery modeling approaches. In addition, the introduced hybrid framework enables the designs of advanced battery management methods from the engineering perspective, which is the main focus in this thesis. As the unique advantage, the cell open-circuit potential of Zn-Ce up to $2.4V$ is relatively high compared with other flow batteries [65], thus a high energy density $25-35\ Wh/L$ was then achieved.

### 2.2.1 Performance, Challenges and Management

In [64] and [66], an undivided Zn-Ce redox flow battery has been examined. Up to $2.1V$ voltage can be achieved in the discharging process when using $20mA/cm^2$ applied current density. The experiments have demonstrated that an averaged energy efficiency above 75% can be guaranteed. The carbon felt electrode has been employed as the positive electrodes. However, the performance is by large affected by the well-known residual zinc deposition issues on the zinc electrodes. At this point, similar to all zinc-based redox flow batteries, how to deposit a uniform, thick zinc layer on the negative electrodes is the main challenge. In the exisiting literature, the majority of management methods to address zinc deposition issues are proposed from the material and chemical perspectives. In particular, for Zn-Ce, a number of studies have been conducted [66; 67; 68; 69; 70]. For example, with the medium of Methanesulfonic acid, it is possible to achieve a dendrite-free zinc deposition with the carbon electrodes [68], incorporating with the proper additives [66]. Whereas, the rate of zinc corrosion when at rest is high, which is deemed to be another problem for the Zn-Ce battery. Without additives [70], the corrosion rate cannot be controlled resulting in significant hydrogen evolution [67]. The corrosion rate tends to increase as the acid concentration and temperature increase. But the corrosion rate will remain at the same level when

the applied current densities vary [67]. Though some additives have been demonstrated to inhibit the gas evolution and dendrite formation effectively, there exists the additives consuming issue, leading to the decrease in effectiveness over time until full depletion. Overall, the used Methanesulfonic acid can help with the formation of a compact zinc layer. The gas evolved and zinc corrosion are the remaining problems to be attenuated. In a word, though current management methods to use chemical additives are able to reduce the corrosion rate and form the compact zinc layers, there is however no effective indicator to assess when the cell begins to fail. As a consequence, battery management methods developed from the engineering perspective are required to further improve the cell operation efficiency.

For the cerium positive electrode, several materials have been discussed in [71]. It has been reported that the carbon felt based positive electrodes can still yield a high potential even at a high applied current density rate up to $50mA/cm^2$, but the cell performance has been compromised by the low stability. As stated in [71], $Pt/Ti$ mesh is the best option for a scaled-up Zn-Ce battery, because the conversion of Ce(III) to Ce(IV) can maintain at over 75% current efficiency. Besides, in order to enhance the kinetics of the Ce(IV)/Ce(III) reaction and increase the stability of Ce(IV) ions, mixed acids solution methods have been proposed [70; 72]. According to [72], an additive with $0.5mol/dm^3$ $H_2SO_4$ can increase the exchange current density in comparison to the usage of Methanesulfonic acid electrolyte only, achieving an energy efficiency of 73%. However, zinc-based flow batteries are commonly operating in the alkaline environment, these management methods solely relying on the acidic additives are thus limited in general. In this thesis, in order to handle the aforementioned issues, a capacity based battery management method is proposed and the proposed method can be broadly used in all kinds of zinc-based cells.

### 2.2.2 Cell Prospects

Currently, there are two types of Zn-Ce redox flow batteries [73] based on the divided Zn-Ce framework. In this regard, the negative electrode may experience the hydrogen emissions, resulting in a progressive acidification of negative electrolytes in the corresponding reservoir. As a result, the acidulated electrolyte speeds up the side reaction to further degrade the cell performance. On the other hand, an undivided Zn-Ce framework has been investigated to avoid the divergence of acid concentration in the two separated half cells. As introduced in Section 1.1.1, the undivided system is a membrane-free framework with the unique advantages to simplify the electrolyte flow circuit, which is also employed in ZNBs. Regarding this novel undivided system, however, most of the available results are still obtained from bench-scale flow cells prototypes in the laboratory environment. The carbon felt based positive electrodes have been thoroughly tested. At low current density $20mA/cm^2$, the charge efficiency can achieve over 80% with energy efficiency above 72%. Though the development of undivided Zn-Ce cell is only partially disclosed, it is noted that this ambitious attempt of the undivided Zn-Ce framework is instructive, which can simplify the cell construction and address the problem of membrane potential drops.

On the other hand, a $2kW$ pilot-scale Zn-Ce battery was evaluated by Plurion Ltd. [65] in Scotland in $2010s$. However, neither the coulombic efficiency nor the energy efficiency was satisfactory. In spite of the early commercial interest and capital investment in the Zn-Ce battery, the previous research has shown that such a system has not yet passed the scale-up tests [73]. Significant advances are therefore required from both the material and engineering perspectives, such as electrode materials selections, optimization of applied current density rate, compound electrolyte compositions tests, cell frame design and advanced battery management system. Further, similar to other zinc-based flow batteries, the capacity loss should be minimised when operating Zn-Ce batteries. Finally, the gas evolution and concentration discrepancy of methanesulfonic acid between the positive and negative half-cells should be attenuated.

## 2.3 Zinc-Nickel RFBs: Challenges and Potential Solutions

The commercialization of nickel zinc battery (ZNB) has been hindered by the well-known dendrite formation and zinc morphology variation over time. Two key problems associated with the NZBs are the swelling of the nickel electrode (cathode) resulted from the uneven current distribution, and the poor cycling characteristics of the zinc electrode (anode) due to the growth of zinc dendrites [74]. Throughout the charging phase, the active materials are redistributed leading to a nonlinear distribution, and the redox reaction is far from the equilibrium status. As a result, a concentrated layer of zincate boundary is grown around the surface of the zinc electrode, resulting in the appearance of dendritic zinc depositions [46; 49]. Once the dendrite is formed, due to the higher current density at the tips, the dendrites growth is more aggressive [75; 76]. These phenomena may eventually lead to battery failures, such as internal short circuits, cell housing damage, capacity deterioration, and unreliable cell performance, etc. As mentioned in Section 1.1, in this work, an advanced battery management system has been proposed from the engineering perspective for ZNBs. Finally, some most recent developments to address various drawbacks of ZNBs are summarized as follows:

1. New chemicals/additives to reduce gassing and dendrite growths during charging phase.

   The electrolyte contains dissolved $ZnO_2$. The formed zincate ions as the active species show inconsistent deposition. Electrolyte additives can help to control the morphology of zinc plating on high alkalinity environment. The integration of additives/dopants into anolyte can potentially reduce the occurrence of undesirable side reactions like sponge-like deposition or dendrite formation. In the industry of alkaline zinc plating, different additives are commonly used.

An important issue is the over potential of the hydrogen evolution. Gassing reaction has been prevented in alkaline batteries with the addition of trace amounts of Mercury, Thallium or Cadmium, as these metals exhibit a very high overpotential against hydrogen evolution reaction [77; 78]. Nevertheless these metals are not favored anymore due to toxic concerns. Today electrolyte additive of Bismuth is often used in alkaline batteries. El-Sayed et al. [79; 80] proposed the addition of trace amounts of nickel salts or $K_3[Fe(CN)_6)]$. Also addition of chromium has been reported to reverse this side reaction. Addition of small amounts of Calcium or Tin can also prevent gassing, because they can stabilize the calcium/Tin zincate formation [78].

Besides, since the negative electrode of ZNBs is analogous to the Zn-Air battery system, the cycling also leads to the dendrite growths. To use bi-functional electrolyte additives for smoothing the zinc deposition and inhibiting the gas evolution is still the most popular strategy, since the effects of electrolyte additives are efficient in not only enabling the complete dissolution of the zinc deposition after per discharge but also depleting zinc ions in the electrolyte to retain the electrode at low potential [78]. Table 2.1 lists the most effective electrolyte additives including the organics, acids, polymers and metal ions. However, it is time-consuming to find a proper additive based on extensive experiments. Alongside the unknown effective volumes of the additives, there is no effective means to determine the moment of additives depletion, making the experiments even more challenging. The effectiveness of additives will be diminished when they are depleted.

2. New surface modification techniques to control the electrode shape

Surface modification techniques have been investigated to improve the long-term cycling performance. Synthesized $ZnO$ was used by [74; 75; 76] to control the shape of anode [76]. There is considerable diversity in the structure of the synthesized $ZnO$, so that substantial experiments are needed before the commercialization.

Table 2.1: Effective electrolyte additives for zinc electrodeposition and dissolution in alkaline bath

| Additives | Electrolyte | Ref |
|---|---|---|
| Calcium hydroxide | Potassium hydroxide | [81] |
| Polyethylenimine | Potassium hydroxide | [82] |
| Thiourea | Potassium hydroxide | [83] |
| Furfuraldehydethiosemicarbazone | Sodium hydroxide | [84] |
| Citric acid | Potassium hydroxide | [85] |
| Tartaric acid | Potassium hydroxide | [85] |
| Succinic acid | Potassium hydroxide | [85] |
| Cellulose | Potassium hydroxide | [86] |
| Polyvinylalcohol | Sodium hydroxide/sodium chloride | [87] |
| Hydroxylamine | Alkaline phosphate/sulfate | [88] |
| Sorbitol | Sodium hydroxide/sodium sulfate | [89] |
| CTAB | Potassium hydroxide | [90] |

3. Current control to suppress the dendrite build-up

   Besides, a compact zinc morphology is achievable through limiting the applied current densities [49]. Nevertheless, the current magnitude is limited at a low level in order to suppress the dendrites growth, which is hardly manageable in real applications. Instead, pulsed current was suggested in [91], where a new method was proposed to generate the compact zinc deposition by altering the charging protocol to high frequency pulse currents. In addition, more effective zinc electrodeposition can be achieved in diluted $KOH$ electrolytes by using the proposed pulsed current charging. In order to implement the pulse charging, to understand the ZNB working conditions is crucial to avoid battery being overcharged, and an accurate state of charge (SoC) estimation is a key. In this regard, the state estimation will be comprehensively researched in this thesis.

4. Flow rate control to suppress the dendrite build-up

In [92] and [93], the relationship between mass transport and flow fluxes has been detailed. The applied flow rate can be expressed as a function of the Reynolds number and current densities, and then a limited current density is introduced as an indicator [94] to further map the flow to the deposition morphology. Particularly, in the laminar regime, dendrite build-up can be suppressed by increasing the flow rates, while compact deposits can be observed in turbulent flow regime. In [94], it has been further reported that longer cycle life can be achieved when applying a flow rate over $15cm/s$. The flow rate is therefore an important factor in zinc dendrite build-up. This method is effective even at high charge rates, where a higher flow rate can encourage the growth of dendrites toward the same direction thus preventing the battery failure from a short circuit. However, circulating electrolytes fast leads to more power consumed and system efficiency reduced.

5. $3-D$ porous electrode design

With the development of materials and manufacturing process, the three-dimensional zinc sponge electrode design has become a focus for producing the next generation RFBs. A three-dimensional zinc sponge electrode has been fabricated in [95]. The proposed $3-D$ electrodes have yielded dendrite free after extensive cycling up to $188mAh/g$ (Zn). Moreover, a Zn/Cu $3-D$ foam electrode has been investigated by [96]. The specific capacity of the $3-D$ Zn/Cu foam electrode can reach up to $620mAh/g$ (Zn) after 9000 cycles tested by their ZNBs prototype, which has exhibited the superior cycling stability. Other research [97] has achieved the similar results that the $3-D$ wired zinc architectures are capable of suppressing dendrite formation innately. However, the design and optimization of a $3-D$ electrode to match the needs of commercialization is still an important topic yet to be fully addressed.

From the application perspective, the concept of periodic reconditioning to prolong the battery service life first appeared in a US patent [73] and further details can be found in [49; 51]. According to the proposed method, after a number of cycles, the reconditioning maintenance operation will be applied to ZNBs, i.e. a slowly trickling discharging cycle will be introduced. In this way, the undissolved zinc depositions can be stripped off from the surface of the electrode. A number of reconditioning experiments have been conducted on bench-top ZNB stacks and grid-tied ZNB applications. The results have demonstrated that the battery life can last for more than 1000 cycles with the introduction of periodic reconditioning [51]. Although the previous research has provided a feasible management method through a periodic reconditioning, the unstable performance of ZNBs has not been fully addressed. Specifically, two challenges are prevailing. One is that the unpredictable zinc dendrites growth and residual uneven zinc morphology lead to the variations in battery capacities after each discharging cycle, resulting in shifting of State of Charge (SoC) estimation. In this regard, unlike other counterparts, the SoC estimation of ZNBs has turned out to be inaccurate and unreliable. The other difficulty is to determine the timing of reconditioning maintenance. The time for reconditioning depends on the used materials of electrodes, the battery architecture, and the applied flow rates. As shown in [54], the introduction of some new materials can postpone the timing of reconditioning. Neither over-frequent nor delayed reconditioning benefits the battery management of ZNBs. On the other hand, the error of SoC estimation can lead to overcharging or over-dischargeing operations, which will aggressively provoke the growth of dendrites associated with non-equilibrium [49]. Therefore, the periodic reconditioning has to be incorporated into a reliable battery management system to effectively operate the ZNBs.

## 2.4 Zinc-Nickel RFBs: Cell Prospects

The challenges with the ZNBs are apparent, and the solutions largely focus on the material aspect. So far, two well-known pilot-scale ZNBs have been developed by

the Zhangjiagang Smart Grid Fanghua Electrical Energy Storage Research Institute Co. Ltd. and the City University of New York. Through the comparison of the published results, ZNBs generally outperform other zinc-based RFBs with less cost, and thus ZNBs have great potential for commercialization.

However, there are still a number of issues yet to be solved, such as the improvement of energy density and electrolyte conductivity, materials selection of the positive electrode, and the control of zinc deposition morphology. Besides, performance improvement and battery management from the engineering prospective have not been well addressed yet and this thesis thus aims to fill in the gaps.

## 2.5 Comparisons: Different Batteries

Table 2.2: Comparison of different battery technologies [1; 4; 5; 6; 7]

| | **Energy density** ($Wh/kg$) | **Power density** ($W/kg$) | **Efficiency** (%) | **Self-discharge** **(rate/day)** | **Life cycle** **(cycles)** | **Capital Cost** ($/$kWh$) |
|---|---|---|---|---|---|---|
| Lead-acid | 30-50 | 75-300 | 85-90 | 0.1%-0.3% | 500-1000 | 200-400 |
| NiCd | 50-75 | 150-300 | 60-70 | 0.2%-0.6% | 2000-2500 | 800-1500 |
| NaS | 150-240 | 150-230 | 75 | ±20% | 2500 | 300-500 |
| Li-ion | 75-200 | 150-315 | 87-92 | 0.1%-0.3% | 1000- | 600-2500 |
| VRB | | | 65-75 | Negligible | 12000+ | 150-1000 |
| ZnBr | 30-50 | | 60-65 | Negligible | 2000+ | 150-1000 |
| Zn-Ni Flow | 20 | | 65-85 | 1%-5% | 10000+ | 300-500/700 |

Table 2.2 compares the the Zn-Ni flow battery with other popular and well-developed battery types. Further discussions are given as follows:

1. **Energy and power density**

   The power density (W/kg or W/L) refers to the ratio between output power and the volume or the gravitational mass of storage devices. Besides, the

energy density is the amount of energy stored in watt-hour per unit volume or weight. As shown in Table 2.2, NaS and Li-ion batteries provide the highest power and energy density. Due to the low active material concentration of the applied aqueous solution, energy densities are lower for flow batteries which restrains the implementations of flow batteries in space limited applications. However, flow batteries naturally release the energy and power anxieties due to the separations of power and energy components as illustrated in Fig.1.2. Combined with the system cost, flow batteries are suitable energy storage systems for power grid to provide large-scale energy demands.

2. **Cycle efficiency**

   The cycle efficiency is used to define the "round-trip" efficiency, which is the ratio of the electricity output to the electricity input. One observation from Table 2.2 is that the cycle efficiency of lithium batteries is the highest, but the capital cost is almost doubled of the cost for Zc-Ni flow batteries. For grid-tied applications, much higher cycle life complemented with low investment makes the Zn-Ni batteries become competitive than lithium batteries.

3. **Life time**

   The life cycle is a crucial index for assessing the cost-efficiency of different batteries technologies. In principle, unlike other types of batteries, there are no solid-to-solid phase transitions in the flow batteries. Therefore, as shown in Table 2.2 flow batteries have longer life time, which is a desirable advantage of flow batteries. It is reasonable to assume that the useful life time of flow batteries can exceed ten years.

# III

# EXPERIMENTAL SETUP AND TESTS

THE design of battery architecture and testing regimes play an important role in the development of Zinc Nickel batteries. Battery leaking, flow channel blocking and aggressive stimulation may lead the premature battery failures in the experiments. In this Chapter, the design procedures of a hand-made ZNBs demonstrator used and tested in this thesis are outlined and the corresponding testing regimes are provided as the benchmarking reference for the subsequent Zinc Nickel batteries tests. In addition, the blueprint for a pilot-scale ZNB is discussed at the end.

## 3.1 Experiment Set-up

The system level investigations of ZNBs is quite limited in the literature, the design of the prototype Zn-Ni flow battery and its testing regimes presented in this thesis would be a valuable reference for future research in this area. A hand-made ZNBs demonstrator has been first fabricated at the University of Macau, which has been tested and investigated in this research. Fig.3.1 illustrates the schematic of the experimental apparatus. The design of this demonstrator was based on the previous studies [2; 45]. Four sintered nickel oxide plates (Jiangsu Highstar Battery Manufacturing) are used as the nickel electrodes (positive/cathodes electrode) and three inert electrodes such as the polished stainless steel sheets are adopted as the zinc electrodes (negative/anodes electrode). All the electrodes are shaped as the $70mm \times 70mm$ squares and are stacked in parallel, while sandwiching the acrylic spacers to prevent the electrolyte leaking from the space between neighbouring electrodes. The designed capacity of this ZNBs demonstrator is $3.70Ah$. The current is collected by two outward $10mm \times 10mm$ rectangular conductors differentiated as positive and negative ends, respectively. In order to reduce the volumetric flow rate of electrolyte and maintain the flow rate evenly, the snakelike design of flow channel is employed to provide longer flow path as depicted in Fig.3.1. The channel pads are $5mm$ thick, and are placed facing to the zinc electrodes. The electrolyte is prepared based on [45], where zinc oxide ($1Mol$) dissolves in the potassium hydroxide solution ($10Mol/L$) and then $20g/L$ Lithium hydroxide is added into the mixture. Additionally, as shown in the zoom-in area of Fig.3.1, gaskets are cut to encircle around the spacer borders to keep the frames sealed. The electrolyte is circulating through the battery stacks and the outside reservoir from bottom to top by a peristaltic pump. The operating flow rate is kept at $19cm/s$ [45]. The battery tester $NEWARECT - 3008W - 15V3A$ generates the testing currents for the ZNBs demonstrator. According to the specification of battery tester, the measurement errors are bounded within 0.1%. Throughout the entire experiments, the room temperature maintains $25 \pm 3°C$, and the output data will be logged by an external host computer. It is notable that the separators are not required in such a single flow system.

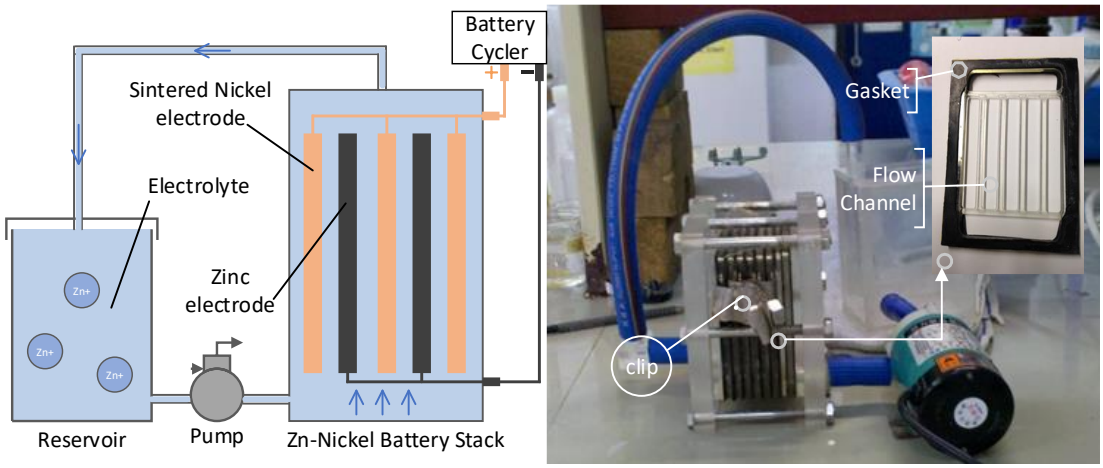


Figure 3.1: Schematic diagram and experimental apparatus

## 3.2 Testing Design

### 3.2.1 Pulse Tests

Three current profiles, $0.5C(1.85A)$, $1C(3.70A)$, and $1.5C(5.55A)$ are fed to the battery stack in pulses. The dis/charging rates are controllable by the variable user-defined width of the pulses, specifically, $15min$ for $0.5C$, $10min$ for $1C$, and $5min$ for $1.5C$ in this work. Differing from the SoC-OCV tests, only pulses are employed to excite the battery over each cycle. The pulsed intervals stabilise the demonstrator while equalising the reaction before the next pulse current is applied. In this work, neither electrode material nor flow channel is well optimised. Therefore, the demonstrator is susceptible to premature degradation due to over-excitation. Given this consideration, the applied pulse tests allow the redox reaction to keep pace with the rate of injected electrical energy to sustain the desirable working condition. For example, $1C$ current rate in pulse is used to excite the batteries in a moderate manner. Consequently, the applied pulse tests protect the unmatured, hand-made ZNBs demonstrator from over-excitations and rapid deterioration. In particular, the battery rests for $15min$ after each pulse to ensure the completeness of the redox reactions. On the other hand, dynamic pulse tests are carried out as well, which reflect the responsive performance of

the battery under the scenario of frequency control [98]. Four pulse patterns in terms of $1C$, $1.5C$, $0.5C$, and $1C$ are consecutively loaded into the battery during charge/discharge processes. The dynamic pulse tests are conducted under an acceptable current stress for short-term testing, aiming to examine the transient behaviours, convergence and tracking performance of the proposed model and observer, while preventing the demonstrator from over-excitation.

### 3.2.2 SoC-OCV Tests

The SoC-OCV table explicitly interprets the monotonous relationships between SoC and OCV, and thus it is widely adopted in the model based real-time SoC estimation. In this paper, the incremental OCV (IO) method is used to obtain the SoC-OCV table. Before the discharging process, the battery demonstrator is fully charged by constant current constant voltage (CCCV) mode. In every charging cycle, $0.5C(1.85A)$ is used to charge the ZNB until the voltage reaches $2.05V$ the upper cut-off voltage, and then the charging cycle will be terminated until the current value drops under the current threshold $0.4A(0.1C)$. According to the Pulse tests, as the ZNB demonstrator is sensitive to the the applied current stress, three moderate current profiles are adopted in the IO method, such as $0.5C(1.85A)$, $1C(3.70A)$, and $1.5C(5.55A)$ to drain off the capacity, when the terminal voltage drops to the lower cut-off value $1.2V$. The length of each constant discharging current pulse is set as 10% SoC drop interval. Afterwards, in order to guarantee the equilibrium of redox reaction, a relaxation period of $30min$ is applied between two discharging intervals. The SoC recorded by CC method is treated as the reference. In addition, the OCV values are logged at the end of each charging/discharging interval to characterise the SoC-OCV curve. OCV values are averaged over the dis/charging phases for calibration purpose. SoC-OCV Table can be then determined as a fifth order polynomial expression [99]:

$$V_{oc} = G(SoC) = \sum_{q=0}^{o} \rho_q SoC^q \tag{3.1}$$

where $o$ is the selected order of least square (LS) polynomial curve fitting method. $\rho_q, \quad q = 1, \cdots, o$ are the polynomial coefficients to fit the nonlinear correlation.

An example of the SoC-OCV function for ZNBs is given below:

$$\begin{aligned} G(x) =& 1.6442 + 0.3471x - 0.7168x^2 \\ &+ 0.98012x^3 - 0.7353x^4 + 0.3300x^5 \end{aligned}$$

### 3.2.3 Capacity Tests

Galvanostatic cycle tests [100] are carried out using the constant charge/discharge rates of $1C$ ($3.70A$). The objective of these tests is to verify the effectiveness of the methods proposed in the thesis to handle the capacity fluctuation issues. In each cycle, the charging phase is terminated once the ZNBs demonstrator has reached its full capacity $3700mAh$. It is notable that the capacity calculation in this paper is based on the ability of nickel electrode. And then, the demonstrator is treated as fully discharged when the terminal voltage $V_t$ drops to the cut-off voltage $1.2V$. However, during the continuous galvanostatic cycling, the residual zinc deposits are accumulated on the zinc electrode. With this effect, the battery capacity is not stable and keeps fluctuating at each discharging cycle. In order to control the ZNBs more accurately, in principle, battery capacity is better to be estimated and updated after each discharge cycle. Therefore, the knowledge of working conditions, i.e. remaining capacity and the tendency of capacity degradation, can be provided by the proposed BMS, which is the key information to determine the timing of reconditioning maintenance and to operate the battery effectively. Besides, similar tests have been conducted on a large-scale $200Ah$ ZNB stacks to further verify the proposed methods in this research.

### 3.2.4 Applicability Tests

To further validate the generality of the proposed observer in more complex current profiles and deal with different electrochemical storage applications, the Federal Urban Driving Schedule (FUDS) test [100] is carried out on a $5Ah$ lithium battery to test the proposed method. The regime of FUDS satisfies the automobile industry standards. In addition, it represents the power requirements in the practical utilization of electric vehicles (EVs). The FUDS test starts with a fully charged state under the CCCV charging mode, and the test is terminated

by consuming all the net capacity.

Throughout each process of above tests, the reference SoC trajectory is obtained by the reliable Colombo Counting (CC) method. All the testing regimens are detailed in Fig.3.2, where the current profiles and voltage responses are depicted in black and red lines respectively.

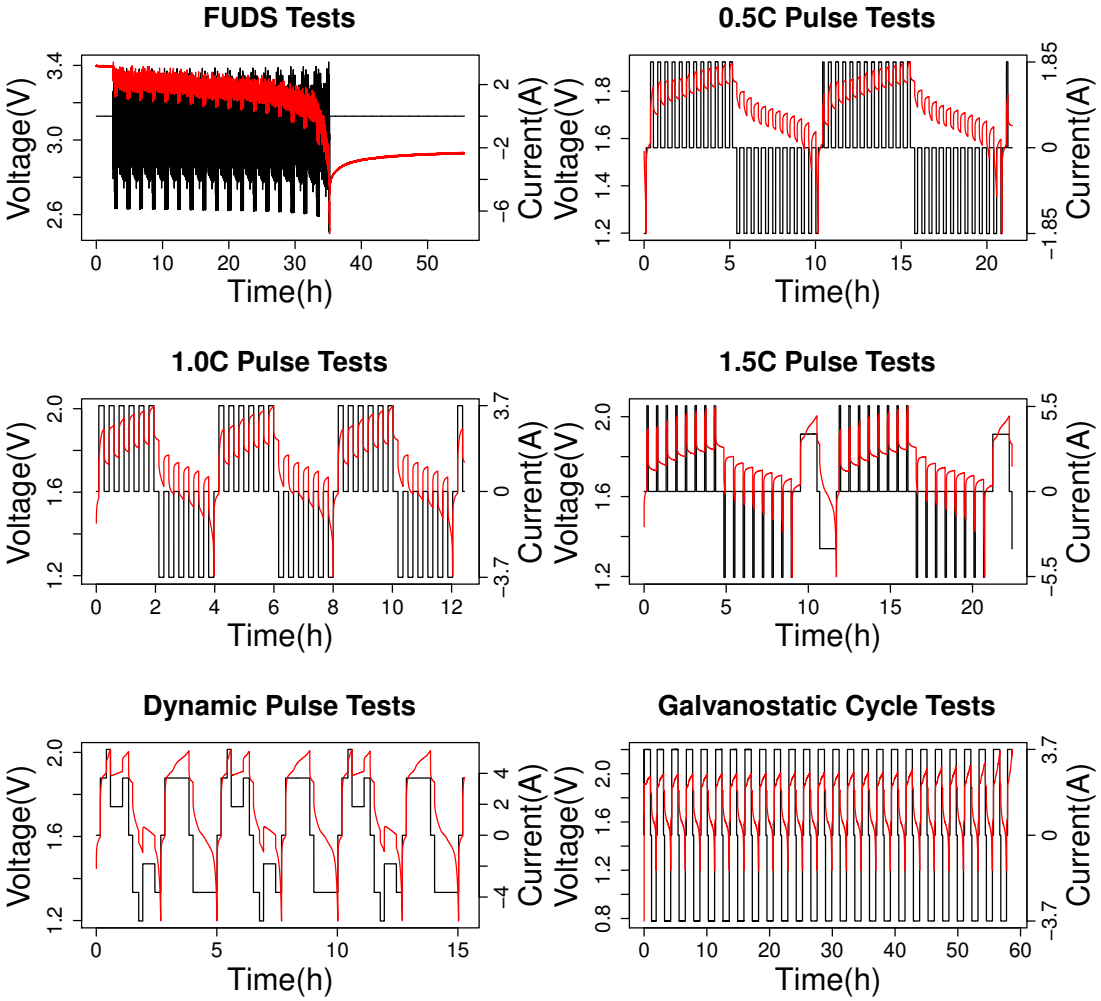


Figure 3.2: Details of the tests, where the red and black lines stand for voltage and current signals respectively

## 3.3 Design Improvements

Based on the experiences gained from the ZNB demonstrator fabricated in Macau, a pilot-scale ZNB has been assembled by our research partner Fraunhofer Institute for Chemical Technology (ICT), led by Dr Peter Fischer. The stack design is different from conventional bipolar arrangements in stacks. The stack consists of cell distribution plates, which are holding the electrode and also provide manifolds for the distribution of the zincate electrolyte. Fig.3.3 illustrates the improved design.

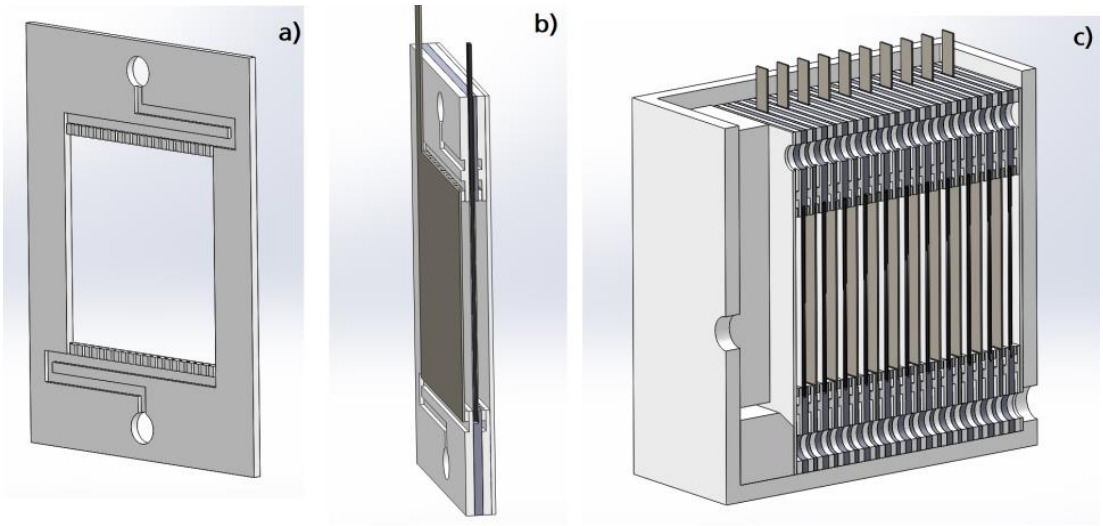


Figure 3.3: a) flow distribution plate of a nickel zinc flow battery: free electrode area $= 100 * 100mm$, b) single cell composed of a zinc electrode (grey), a nickel electrode (black) and two flow distribution plates, c) cut through the center of the nickel zinc flow battery cell made of 11 nickel and 10 zinc electrodes.

The electrodes in such a stack are connected electrically in parallel. This arrangement results in a voltage of 1.6V Open circuit voltage (OCV) of the cell stack. The electrolyte reservoir is made of commodity polymer for the alkaline zinc electrolyte. The volume of the tank is in the range of 1 to 2 litre. A flow cycle consist of the tubing/fluidic connections of the cell with the pumps, where all the apparatuses are made from alkaline resistant materials. A pump is used to

drive the electrolyte circulating from the bottom to the top of the flow distribution plate, resulting uniform flow of electrolyte. A temperature sensor is mounted along with the flow sensors. The transportable housing of alumina profiles with safety containment/tray is used for this demonstrator. The electrodes are made as follows:

A carbon composite plate is used as the anode electrode, and a nickel foam pasted with nickel hydroxide paste acts as the cathode electrode. The electrodes have an active area of $10 * 10cm$ (geometrical area). The electrodes are connected to a terminal. The terminals are collected above the flow distribution plate. In this prototype, there will be 11 nickel hydroxide pasted electrodes (cathode) in parallel connections combined to the plus pole and 10 zinc-deposition electrodes (anodes) in parallel connection combined to the negative pole. The cell connectors are insulated separately.

## 3.4 Conclusion

In this chapter, the cell construction procedures and testing design are briefed. Note that all the tests conducted in this thesis include the pulse tests used for the battery modelling and model verification; the SoC-OCV tests used to build the SoC-OCV relationship; Galvanostatic cycle tests conducted for the capacity estimation; and additional tests on a $5Ah$ lithium battery to verify the generalization of the proposed methods. Finally, the design of a pilot-scale ZNB is introduced.

# IV

# BATTERY MODELLING AND STATE OF CHARGE ESTIMATION

In Battery Management System (BMS), battery modelling is required for monitoring the battery working conditions, estimating the internal states, and diagnosing potential faults. In addition, a comprehensive battery model is able to capture the key characteristics of cell reactions, providing important electrochemical know-how for the manufacturers and academic researchers. Besides, when cycling a cell, the dynamic knowledge of battery states, e.g., State of Charge (SoC), State of Power (SoP), and State of Health (SoH), etc. cannot be measured directly by external sensors and they have to be inferred by the developed battery models. Therefore, the accurate battery modelling and state estimate are essential in BMS. In this chapter, three popular battery modelling tools have been reviewed. According to the intrinsic features of ZNBs, the Equivalent Circuit Model (ECM) based battery State of Charge (SoC) estimate techniques are further elaborated.

## 4.1 Battery Modelling

### 4.1.1 Artificial Neural Network Model

The battery modelling based on Artificial Neural Network (ANN) has been intensively researched in battery management system (BMS) design in early days [101; 102; 103; 104; 105]. It is free of the knowledge of internal electrochemical processes and thus easy to be adopted for different battery systems. In [105], the available capacity of lead-acid batteries is calculated by the ANN. The used model improves the accuracy of the Peukert equation [106; 107]. Then, the wavelet-neural-network (WNN) based battery model is proposed in [102] to reproduce the dynamic electrical characteristics of lithium batteries. For ANN based modelling methods, the terminal signals can be readily fused with the battery shell temperature to build a comprehensive model with improved model accuracy and the resultant models are also adaptable for varying discharge rates. In order to reduce the impact of the measurement noises on the model accuracy, a range of filters are introduced [101; 104]. In some recent studies [103], the OCV (open circuit voltage) is also taken into consideration, leading to a dual neural network battery model, where two ANN models are connected in series. The first model is used to identify the parameters of a electrochemical model. The subsequent ANN model represents the SoC-OCV table. In this regard, the weights of the constructed dual ANN models can represent different physical quantities in the electrochemical process model. However, most of the state-of-the-art ANN models are black-box models and they are error-prone when dealing with unseen data.

In this section, ZNBs are first modelled by on a Radial Basis Function (RBF) neural network. The relationship of the ZNB terminal voltage with other measured variables such as currents is represented by the proposed RBF ANN model. This model can then be used for internal states estimation as long as the proper filters such as EKF or Particle filter (PF) are incorporated. In our proposed RBF model, both the linear and non-linear parameters in the model are tuned through a presently proposed feedback-learning phase assisted Teaching-Learning-Based

Optimization (TLBO) method, namely Teaching-Learning-Feedback-Based Optimization (TLFBO) [108]. Besides, the fast recursive algorithm (FRA) [109] is applied to select the proper inputs and network structure to reduce the modelling error and computational efforts.

### Radial Basis Function Neural Networks

The RBF neural network possesses a simple structure for modelling non-linear systems, which has been intensively researched and used to model other battery types [101]. Herein, a general multiple-input-single-output RBF neural network is considered. The outputs are formulated as follows.

$$y\left(t\right) = \sum_{i=1}^{n} \omega_i \cdot \phi_i(X) \tag{4.1}$$

where $y\left(t\right)$ is the RBF neural model output representing the system outputs in discrete sampling time. $\omega_i$ is the linear parameter and denotes the output weight for the corresponding $i-th$ RBF node. $X$ is the inputs of the ZNB system in terms of the readily measurable terminal voltage and applied current signals. The output of the hidden node is given as follows.

$$\phi_i(X) = exp(-\tfrac{1}{2\sigma_i^2} \left\| X - c_i \right\|),\ i = 1, 2, \cdots, n \tag{4.2}$$

where $\sigma_i$ and $c_i$ are the non-linear parameters in the Gaussian function $\phi_i$ and denote values of width and centre vectors for the corresponding $i-th$ node.

When the RBF network is used to model the ZNBs, three issues, including inputs selection, the number of hidden neurons, and optimization of the linear/non-linear parameters, need to be considered. In this paper, the FRA method is first applied to select both the model structure and identify the significant input terms. The novel TLFBO is proposed to optimize the parameters in the RBF network simultaneously.

### Fast Recursive Algorithm

The Fast Recursive Algorithm (FRA) is a powerful fast forward method to both select the model structure and estimate the model parameters. In this work the battery model is considered as a discrete non-linear dynamic system $f(.)$ including 20 input items and single output outlined as follows:

$$y(t) = f\left(V(t-1), \cdots, V(t-l_{10}), I(t-1), \cdots, I(t-l_{10})\right) \tag{4.3}$$

According to Eq.(4.1), the pre-set 20 input terms as the inputs $X$ for the RBF NN will cause significant computational expenses. Besides, the number of RBF hidden nodes needs to be decided. It is clear that the modelling accuracy and the computational efforts increase as the number of hidden nodes increases. According to [110], the number of RBF hidden nodes can be selected based on a simpler ARX model built from the system input and output data. Thereby, the FRA method is applied to pre-select the RBF neural inputs $X$ and the number of hidden nodes. According to [109], a recursive matrix $\mathbf{M}_k$ and a residual matrix $\mathbf{R}_k$ are defined as the basis for the FRA method.

**Assuming that**

$$\mathbf{\Phi} = \{V(t-1), \cdots, V(t-l_{10}), I(t), \cdots, I(t-l_9)\} \tag{4.4}$$

$$\begin{aligned} \mathbf{M}_k &\triangleq \mathbf{\Phi}_k^T \mathbf{\Phi}_k \quad \mathbf{M}_k \in \Re^{N\times k}, k = 1, \cdots, n \\ \mathbf{R}_k &\triangleq I - \mathbf{\Phi}_k \mathbf{M}_k^{-1} \mathbf{\Phi}_k^T \quad , \mathbf{R}_0 \triangleq I \end{aligned} \tag{4.5}$$

where $V(t-i), i = 1, \cdots, 10$ and $I(t-i), i = 0, \cdots, 9$ are the battery voltage and current at time instant $i$, and these are candidate neural inputs which need to be selected. $\mathbf{\Phi}_k = [\varphi_1, \cdots, \varphi_k]$ , $k = 1, \cdots, p$ represents the selected items from the regression matrix $\mathbf{\Phi}$ and $\varphi_i = [\varphi_i(1), \cdots, \varphi_i(N)]$. Further, the form of recursive matrix is defined as follows.

$$\mathbf{R}_{k+1} = \mathbf{R}_k - \frac{\mathbf{R}_k \varphi_{k+1} \varphi_{k+1}^T \mathbf{R}_k^T}{\varphi_{k+1}^T \mathbf{R}_k \varphi_{k+1}}, \ k = 0, 1, \cdots, n-1 \tag{4.6}$$

Based on [111], $\mathbf{R}$ has the following properties.

$$\mathbf{R}_k^T = \mathbf{R}_k; \quad (\mathbf{R}_k)^2 = \mathbf{R}_k, \quad k = 0, 1, \cdots, n \tag{4.7}$$

$$\mathbf{R}_i \mathbf{R}_j = \mathbf{R}_j \mathbf{R}_i = \mathbf{R}_i, \quad i \geq j; \; i, j = 0, 1, \cdots, n \tag{4.8}$$

$$\mathbf{R}_k \varphi_i = 0, \quad \forall i = 0, 1, \cdots, n \tag{4.9}$$

$E_k$ denotes the modelling error

$$E_k = \mathbf{y}^T \mathbf{R}_k \mathbf{y} \tag{4.10}$$

Applying Eq.(4.6) and Eq.(4.10) and the fundamental properties of recursive matrix from Eq.(4.7) to Eq.(4.9), the net contribution to the cost function by the $(k+1)th$ element can be expressed as.

$$\Delta E_{k+1} = \mathbf{y}^T (\mathbf{R}_k - \mathbf{R}_{k+1}) \mathbf{y} = \frac{\mathbf{y}^T \mathbf{R}_k \varphi_{k+1} \varphi_{k+1}^T \mathbf{R}_k \mathbf{y}}{\varphi_{k+1}^T \mathbf{R}_k \varphi_{k+1}} \tag{4.11}$$

Using the FRA method, the most significant terms with the maximum net contributions are selected to further refine the candidates pools and the number of applied hidden nodes of RBF network. In this work, five important terms with appropriate time lags are chosen, including $V(t-1), V(t-5), V(t-10), I(t), I(t-7)$ and 6 effective hidden nodes are chosen from 20 candidate hidden neurons to predefine the network structure.

### Teaching-Learning-Feedback-Based Optimization

The Teaching-Learning-based-Optimization (TLBO) method mimics the process of knowledge sharing in the class to optimize non-linear dynamic systems. Inspired by the supervised learning, a Feedback learning phase is added to the original TLBO in [108] to increase the converging speed. Followed by the learner phase, the last global optima denoted as the previous teacher collaborates with the newly selected teacher to provide collective feedbacks of the learning results. This new TLBO variant is called TLFBO. In this work, the linear and non-linear parameters of the RBF network are optimized by this novel proposed TLFBO method.

1. **Teacher Phase**
   A teacher is expected to circulate knowledge to improve the mean solution of the whole class. Students learn from the differences between teacher and the mean solution. The updating procedure is formulated below.

$$DM_i = rand_1 * (Teacher_i - T_F * M_i). \tag{4.12}$$

   where $M_i$ is the mean solution, and $Teacher_i$ denotes the teacher who has the best solution. The teaching factor $T_F$ is chosen as 1 or 2.

$$T_F = round(1 + rand_2(0, 1)) \tag{4.13}$$

$$St_i^{new} = St_i^{current} + DM_i \tag{4.14}$$

   where the $St_i^{new}$ is the newly generated population after obtaining the information from the teacher. As aforementioned, the most knowledgeable particle will be the updated teacher for the following populations.

2. **Learner Phase**
   The learner phase is a mutually learning stage where students exchange their knowledge randomly. The optimum solution is achieved through two steps expressed as follows.

$$St_k^{new} = \begin{Bmatrix} St_k^{current} & + & rand_3(St_k - St_j) & if & (St_k < St_j) \\ St_k^{current} & + & rand_3(St_j - St_k) & if & (St_j > St_k) \end{Bmatrix} \tag{4.15}$$

   where according to the fitness function or objective function, the marks of students $St_k$ and $St_j$ are compared randomly.

3. **Feedback Learning Phase**
   Contradictory to the well-known Particle Swarm Optimization (PSO) method [112], though TLBO is a precise exploration, and the convergence speed is slow. Therefore, an extra learning phase is employed to gain feedbacks

from the previous teacher (the previous optima) and current teacher to accelerate the convergence speed as shown in [108]. This procedure can be is formulated as follows.

$$St_i^{new} = St_i^{current} + l_1 * w * D_{last} + l_2 * w * D_{current} \tag{4.16}$$

$$D_{last} = Tr_i^{last} - St_i^{current} \tag{4.17}$$

$$D_{current} = Tr_i^{current} - St_i^{current} \tag{4.18}$$

$$w = (G_{total} - G_{current}/G_{total}) \tag{4.19}$$

where $w$ is the mutation weight to restrain the exploring scope. $l_1, l_2$ range between 0 to 1 and $l_1 + l_2 = 1$, they are used to tune the feedback weights from the selected teachers. $G_{total}$ is the predefined total generations; $G_{current}$ is the current generation index.

The complete TLFBO algorithm is depicted in Fig.4.1 [3].

### TLFBO Based RBF Network Modelling

The Root Mean Squared Error (RMSE) is used as the objective function.

$$RMSE = \sqrt{\frac{1}{N} \cdot \sum_{i=1}^{N} (\hat{y} - y)} \tag{4.20}$$

Based on the Eq.(4.1) and Eq.(4.2), the modelling estimates $\hat{y}$ is calculated. The procedures of building the RBF neural model are given below.

1. **Input Selection**
   As shown in Section 4.1.1, the past battery voltage and current measurements with up to 10 time lags are used as the candidate neural model inputs. Then, an ARX model with 20 terms is constructed, and the contribution of each term is computed. Applying the FRA method, the most 5 significant terms are selected, from which the following 5 significant inputs

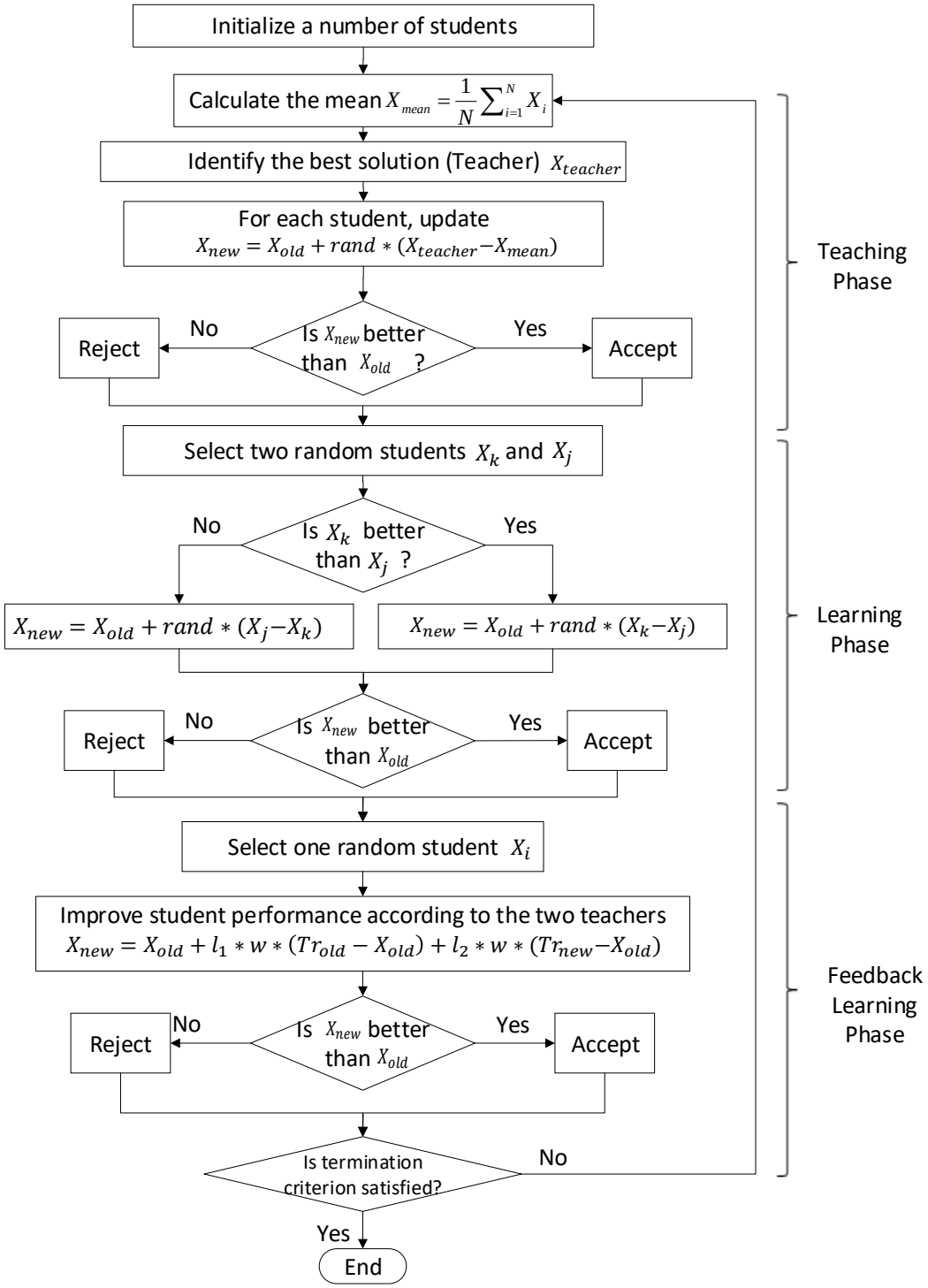


Figure 4.1: Flow chart of the proposed TLFBO algorithm [3]

$V(t-1), V(t-5), V(t-10), I(t), I(t-7)$ are selected to build the RBF neural model.

2. **Network Construction**
   At beginning, the number of hidden neurons was chosen to be 20 by trial and error, where the initial parameters of the RBF neurons are generated randomly. Then, using the FRA method, 6 largest contributors from the original 20 neurons are chosen to build the RBF neural model, and the 6 hidden neurons are further optimized using the TLFBO method as given below.

3. **Network Parameters Optimization**
   The non-linear and linear variables including $\sigma_i$ , $c_i$ and $\omega_i$ in the radial function are optimized simultaneously using the TLFBO given in Section 4.1.1. The optimization procedures are outlined as follows,

   (a) Initialization:

      i. Configure the inputs $X$ and RBF structure in terms of the numbers of neurons $h_n$;

      ii. Pre-set the numbers of generations $G_m = 50$, population size $N_p = 30$ and the upper/lower bounds of each solution as $St_{up} = 5$, $St_{low} = 0$;

      iii. Randomize the first population $St_1$ where the dimension of the parameters is $D = 3 * 6 = 18$, as there are 3 parameters in one neuron to be optimized.

      iv. Check the constraints to adjust the position of all the particles $X_i$ to avoid violating system constraints;

   (b) Teacher Phase:

      i. Compute the objective function $f$ to select the teacher $T_i$;

      ii. Calculate the mean $M_i$ in column-wise;

iii. Apply the different performance between teacher $T_i$ and mean value $M_i$ denoted as $DM_i$ according to Eq.(4.14) to exert the influence of teacher;

iv. Update the generation $St_i^{new}$.

(c) Learner Phase :

i. Compute the objective function $f$ and students mutually exchange the knowledge to improve the solutions described in Eq.(4.15);

ii. Choose most knowledgeable one as the next Teacher;

(d) Feedback Learning Phase:

i. Calculate the differences between students and the previous teacher/current teacher denoted as $D_{last}$, $D_{current}$;

ii. Pre-set the learning weight values as $l_1 = 0.3$, $l_2 = 0.7$ apply the different performance between teacher $T_i$ and mean value $M_i$ denoted as $DM_i$ according to Equ.(4.14) to exert the influence of two teachers;

iii. Update the generation $St_i^{new}$ and choose the most knowledgeable one as the next Teacher.

### Training Error

The training data has been collected from a bench-scale $3.7Ah$ ZNB [93; 113]. For the handmade $3.7Ah$ battery, the charging/discharging current rate is based $1C$ pulse test as depicted in Section 3.2.1. The validation data has been collected from $200Ah$ pilot-scale ZNBs battery using $0.25C$ pulse test for charging and discharging processes. All the details can refer to Section 3.2 and Fig.3.2

The training errors of conventional RBF network and RBF neural model assisted within FRA selection are shown in Fig.4.2 and 4.3. The RMSE modelling errors associated with the two cases are extremely small as $6.77E^{-4}$ and $2.77E^{-5}$ respectively. It is clear that the proposed FRA selection method not only improved the modelling performance, but also reduced the computational efforts significantly.

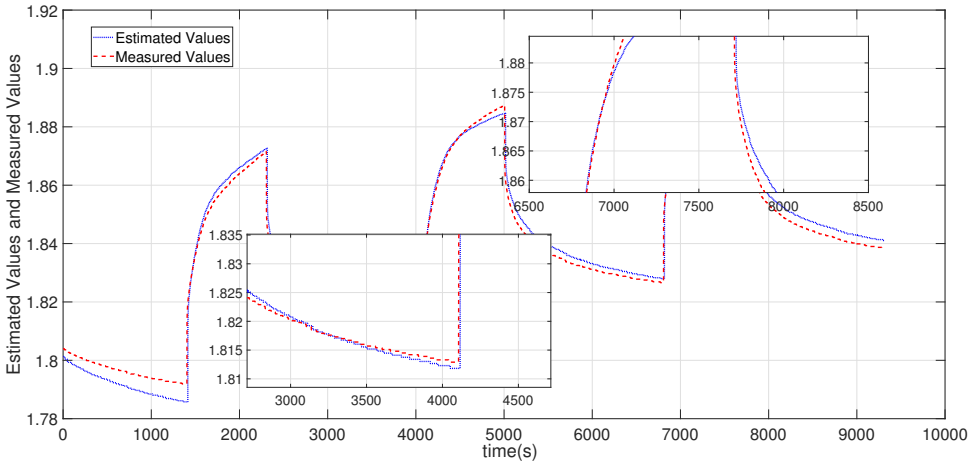


(a) Comparisons between estimated values and measurements

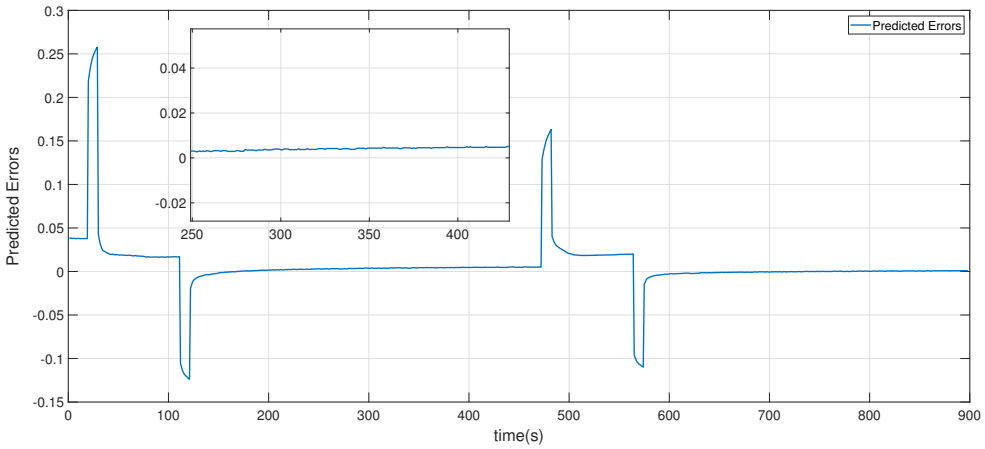


(b) Zoom-in modelling errors

Figure 4.2: TLFBO based RBF modelling without FRA selection

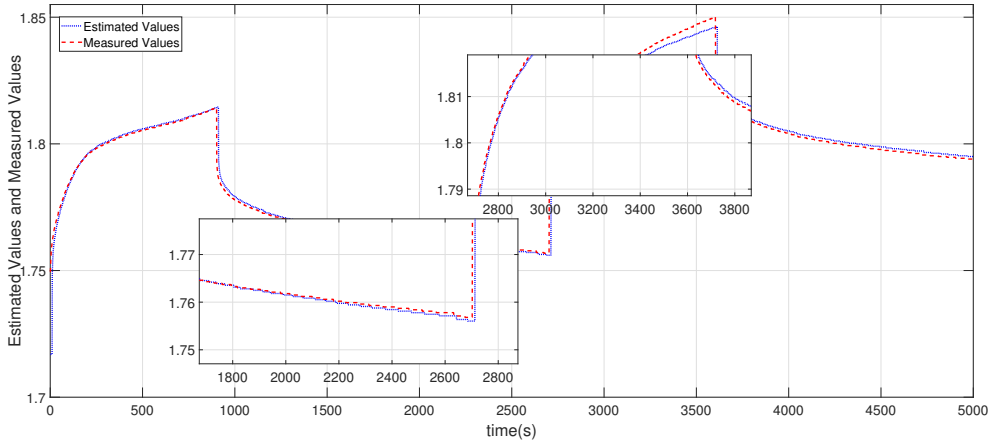


(a) Comparisons between estimated values and measurements

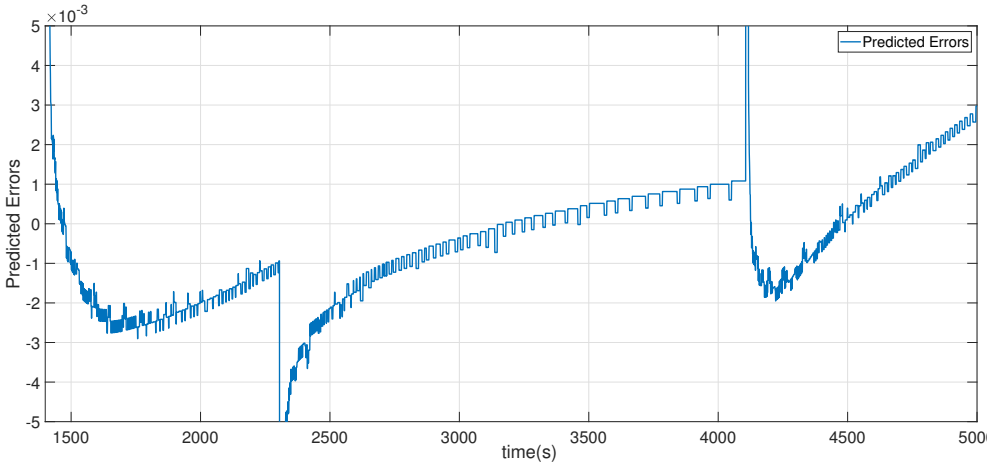


(b) Zoom-in modelling errors

Figure 4.3: TLFBO based RBF modelling with FRA selection

### Validation Error

The validation errors of the two methods are shown in Fig.4.4. The RMSE values are quite similar on these two optimizers as $3.74E^{-2}$ and $2.67E^{-2}$ respectively. However, it can be seen that the proposed TLFBO method outperforms the PSO method in addressing the over-fitting and local optimum issues. The TLFBO is more efficient to optimize the linear and non-linear parameters in the RBF neural model simultaneously. The experimental results show that the developed model can well predict the battery terminal voltage outputs, in terms of both the training accuracy and the generalization capability.

### Discussion

This section presents an example of ANN battery modelling. The proposed BRF based ANN battery model is free of the priori-knowledge of ZNBs, and simple to construct. On the other hand, the accuracy of constructed ANN model satisfies the engineering acceptance. The main novelty of the proposed work is that the usage of FRA method further reduces the computational efforts and simplifies the model structure. Additionally, the nonlinear and linear parameters have been optimized by the proposed TLFBO methods [108]. Such a combination can be applied with appropriate filter design to readily achieve accurate estimates, which will be elaborated in the following Section 4.3. However, as mentioned in Chapter 1 and shown in Fig.1.10, the cycling performance of ZNBs is unstable with unexpected voltage peaks occurred in both charging and discharging processes. This undesirable characteristic of the resultant model will lead to additional training efforts for ANN based battery modelling. The unpredictable voltage peaks will result in large modelling error. One solution to this problem is to adapt the parameters online. However, in order to secure a quick convergence, the number of model parameters have to be limited, which may be not applicable for ANN based battery modelling. Instead of online model identification techniques will be applied to a simple Equivalent Circuit Model (ECM) as detailed in the following Section 4.1.3.

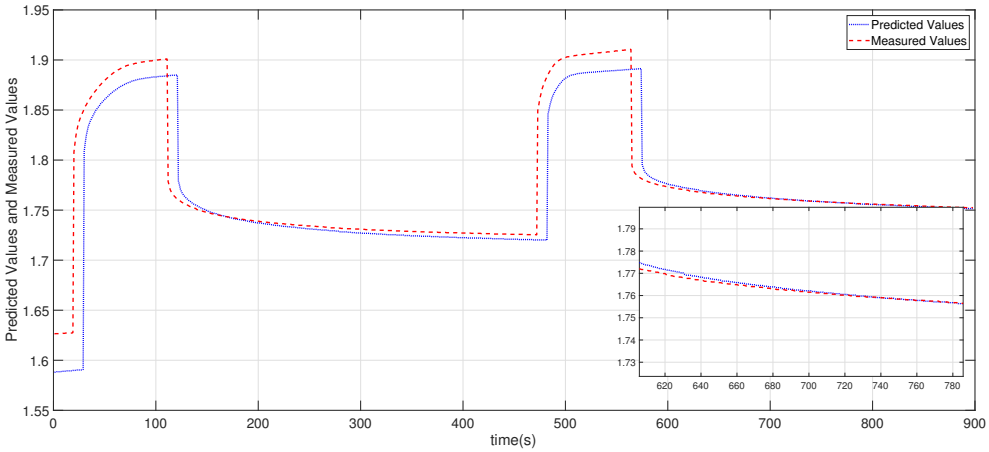


(a) Validation results of TLFBO based RBF modelling

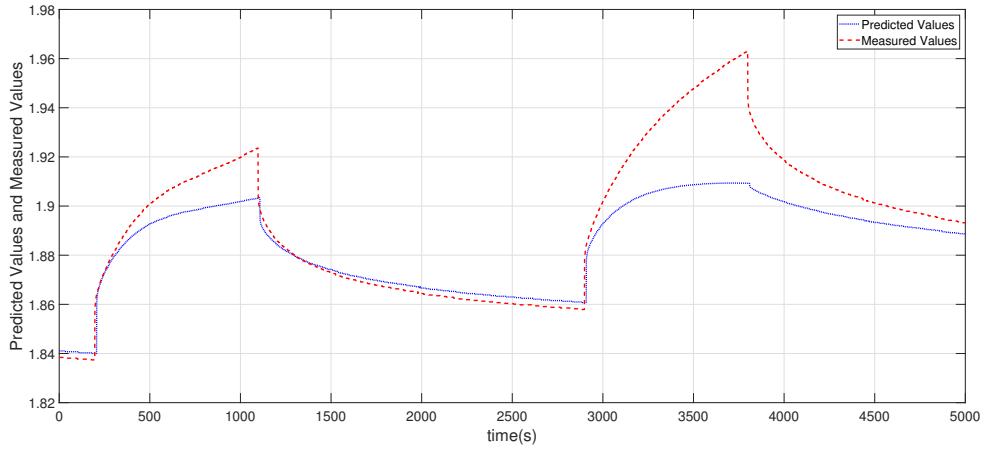


(b) Validation results of PSO based RBF modelling

Figure 4.4: Comparisons of the Validation results

### 4.1.2 Electrochemical Mathematical Model

Electrochemical processes are governed by the conservation laws in charge, mass and momentum. In particular, when the conservation laws are applied to the charges(current) transport in the electrolyte and electrode, the mass transport for each solute species in electrolyte, as well as the momentum in a solution or mixture, a series of partial differential equations (PDEs) can thus be derived to describe the electrochemical process mathematically [114].

For example, the charge conservation obeys the Gauss's law in Eq.(4.21), while the mass transport obeys the Nernst-lanck formula in Eq.(4.22) and the mass continuity in Eq.(4.23).

$$-\nabla \cdot (\varepsilon \nabla \varphi) = \rho \tag{4.21}$$

$$\vec{N_i} = -D_i \nabla c_i - z_i c_i u_i \nabla \phi + \vec{v} c_i \tag{4.22}$$

$$\frac{\partial c_i}{\partial t} + \nabla \cdot \vec{N_i} = R_i \tag{4.23}$$

where $\varepsilon$ is the permittivity constant $(F/m)$, $\varphi$, $\rho$ , and $c_i$ are the potential $(V)$, applied charge density $(C/m^3)$, and concentration of species $i$ $(mol/L)$, respectively. $D_i$ is the diffusion coefficient of species $i$ $(m^2/s)$; $z_i$ is the charge number of species $i$. And $u_i$ and $\vec{v}$ denote the mobility of species $i$ $(m^2/Vs)$ and bulk velocity $(m/s)$, respectively. Finally, $R_i$ stands for the mass source of species $i$ $(1000mol/Ls)$. The above equations together represent the well-known Nernst-Planck-Poisson equitation to describe the charge and mass transport in an infinitely dilute electrolyte in general. The boundary conditions are employed to represent the electrolysis and the penetration process of chemical species at electrodes surfaces and different interfaces. However, due to the high non-linearity of the Nernst-Planck-Poisson equation, much work has to be considered to reduce the computational cost in solving these equations practically.

In general, there are two kinds of methods to simplify the governing equations in different scenarios. The single particle (SP) model [115] and pseudo two-dimensional (P2D) model [115] are commonly used in the literature to reproduce the electrochemical process with high precision. So far, the physical modelling of nickel electrodes in nickel-hydride batteries has been well investigated [116; 117; 118; 119]. However, no physical modelling study of zinc electrodes has been reported in the current literature. In the following section, a the challenges and solutions of ZNB mathematical model briefly reviewed, and the related work can be refer to [120].

### Challenges to solving the PDE models

According to [120], the main functions to be solved are $c_1, c_2, c_H, \phi_S$, and $\phi_l$. Note that $\phi_S$ and $\phi_l$ are the potentials, which have no variability to the position variable $x$ and only depend on time variable $t$. In [120], through the mathematical derivations, two equations involving all five functions but no partial derivative exists can be achieved. Combine these five equations, the system can be easily solved by explicit finite difference scheme, i.e. backward inductions starting from boundary conditions.

However, the stability and convergence will not be guaranteed for solving such a complex system, which increase the uncertainties of the mathematical modelling. On the other hand, the implicit method or Crank-Nicolson method in such a complex system may not be feasible. In other words, specific software or tools are indispensable to solve such a PDE system, which compromises the generality of the mathematical modelling. Additional concern is the value of constants, as they vary for different systems and applied materials. The accuracy of such a system cannot be guaranteed.

### Possible Outcomes

Firstly, the developed mathematical model can be verified by plotting the SOC-voltage curve. For given constant current densities and flow rate, as well as initial conditions for hydroxide ion concentration, zinc ion concentration, and storage

tank volume, by setting up different SOC levels, it is feasible to solve for different voltages. Comparing the simulated curve with experimental curve obtained under the galvanostatic cycling test, validity of this model can be demonstrated. Due to the intrinsic high fidelity of the electrochemical mathematical modeling, terminal voltage changes can be simulated over different SoC when varying the initial conditions such as hydroxide ion concentration, zinc ion concentration, and storage tank volume. For example, one can see the effects of concentration by changing the initial concentration levels for both hydroxide ion and zinc ion, and re-plot the SOC-voltage curve. We should expect to confirm the optimal concentration ranges through the comparison of voltage curve changes according to concentration differences. In this way, ZNBs cell can be optimally designed thus reducing the effort of experimental trials.

In addition, the detailed distribution at one SoC slice can be checked accordingly. At this point, the developed PDE system will be solved when choosing a fixed SoC level. Therefore, different layers of concentrations along the length of the electrodes can be examined by plotting the liquid phase ions and solid phase proton concentration distributions. As a result, various reaction rates occurring at different locations will be observed. The cell structure in particular for the flow channels, can be thus optimised leading to enhanced cycling performance.

Similarly, the distributions of transfer current densities and over-potentials in the porous positive electrode can be further explored, when applying different initial concentration levels. On the other hand, the applied current densities and flow rates can also be changed (one at a time) to see their influences on the cell performance.

The electrochemical mathematical modelling is deemed with high modelling fidelity under the correct settings. Nevertheless, different materials and additives will affect the initial settings and preliminaries, resulting in low the modelling accuracy, and more attempts have to be conducted to prescribe the initial settings. Once such a complex PDE system is developed, it can benefit both manufacturers in cell structure design and the academics in cell material investigation. On the

other hand, to solve the PDE model is time-consuming, which hinders the applicability of electrochemical mathematical modelling for real-time applications.

### 4.1.3 Equivalent Circuit Model

As mentioned above, the cycling behaviours of ZNBs are very sensitive to zinc morphology variation over time, which means the residual zinc deposition will significantly affect the terminal signals. Equivalent Circuit Model (ECM) has been viewed as an effective model in the literature [7]. Substantial researches have confirmed that the ECM based battery modelling techniques and its variants exhibit some distinctive merits such as adaptability, easy implementation and desirable accuracy, and thus it is seen as a promising candidate for the onboard studies [121]. In particular, the combination of ECM and other online model identification algorithms such as recursive least square (RLS) prevails in most battery modelling approaches for the real time applications. In order to solve the modelling error introduced by the large voltage jumps/peaks and adapt to most charging/discharging cycling profiles, in this Section, a commonly used first-order ECM framework is investigated. Specific applications in the following chapters will use a few ECM variants, which will be detailed accordingly.

Generally, the accurate modelling of battery electrical dynamics is the essence of the battery management system (BMS). The higher order ECMs increase the accuracy but will be also compromised by the computational expense and numerical instability. Based on the studies in [122], the first-order ECM is an acceptable trade-off for battery modelling in reproducing the transient and dynamic performances in most cases. Additionally, the first-order ECM is able to simplify the filter design for the state estimation to attenuate the cross-interference in the estimations from the higher dimensions. Fig.4.7 illustrate the basic structure of a first-order ECM, where $R_s$ is the ohmic resistance representing the resistant losses in the electrodes and electrolyte phases. The parallel $RC$ branch mimics the electrochemical behaviours of the ZNBs in terms of the transient responses and relaxation effects. $R_p$ and $C_p$ represent the polarisation resistance and capacitance, respectively. The terminal current and voltage signals are denoted by $I_L$

and $V_t$. When the battery is disconnected from the circuit, the terminal voltage will gradually converge to the equilibrium value denoted as $V_{oc}$.

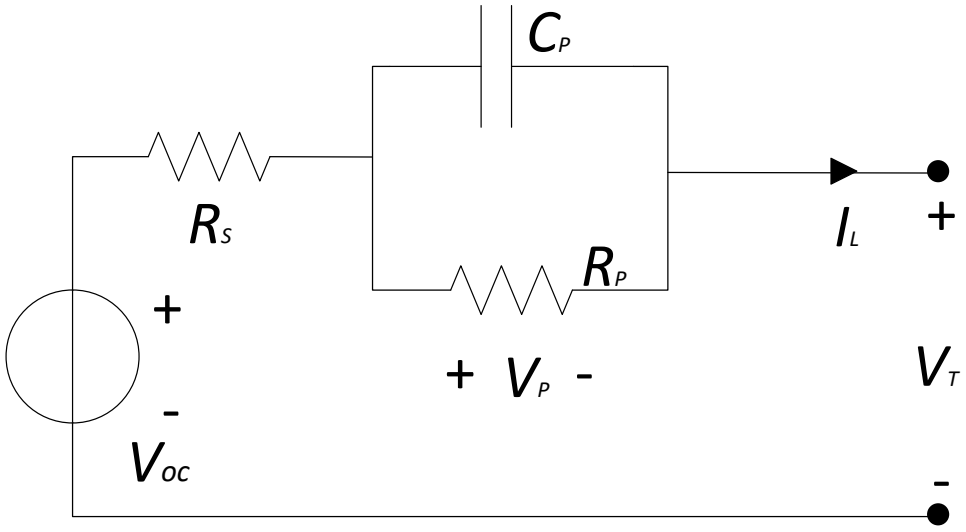


Figure 4.5: Schematic diagram of the first-order ECM

### Online model parameter identification

Herein, the charging current is predefined as the negative sign, and vice versa. In the basis of the $RC$ responses, the first order equivalent electric circuit model can be then expressed as follows:

$$C_p \frac{dV_p}{dt} + \frac{V_p}{R_p} = I_L \tag{4.24}$$

$$V_t = V_{OC} - V_p - I_L R_s \tag{4.25}$$

the discrete-time expression of Eq.(4.33) is of the form:

$$V_p(t) = e^{-\frac{\Delta t_s}{R_p C_p}} V_p(t - \Delta t_s) + \left(1 - e^{-\frac{\Delta t_s}{R_p C_p}}\right) R_p I_L(t - \Delta t_s) \tag{4.26}$$

where the start-up time is 0, and $\Delta t_s$ denotes a fixed time interval. Define $V_p(k) = V_p(k\Delta t_s)$ and the analogous definitions are imposed on $V_{OC}$, $V_t$, and $I_L$. A neat format is given as follows:

$$V_p(k) = e^{-\frac{\Delta t_s}{R_p C_p}} V_p(k-1) + \left(1 - e^{-\frac{\Delta t_s}{R_p C_p}}\right) R_p I_L(k-1) \tag{4.27}$$

According to Eq.(4.32), substituting $V_p = V_{OC} - V_t - I_L R_s$ to Eq.(4.27), the expression of $V_t(k)$ is yielded as:

$$\begin{aligned} V_t(k) = \beta V_t(k-1) - R_s I_L(k) + (\beta \cdot R_s - (1-\beta)R_p) I_L(k-1) \\ + \left(V_{OC}(k) - \beta V_{OC}(k-1)\right), \end{aligned} \tag{4.28}$$

where $\beta = e^{-\frac{\Delta t_s}{R_p C_p}}$. One time step difference is introduced to Eq.(4.37), the differential voltage of $V_t$ is given as:

$$\begin{aligned} \Delta V_t(k) = \beta \Delta V_t(k-1) - R_s \Delta I_L(k) + (\beta \cdot R_s - (1-\beta)R_p) \Delta I_L(k-1) \\ + \left(\Delta V_{OC}(k) - \beta \Delta V_{OC}(k-1)\right) \end{aligned} \tag{4.29}$$

where the last term $(\Delta V_{OC}(k) - \beta \Delta V_{OC}(k-1))$ is treated as the error term, denoted as $e(k)$, due to the slow varying OCV in the ZNBs. In this regard, the regression formula is expressed as:

$$h(k) = \theta^T(k)\phi(k) + e(k), \tag{4.30}$$

where

$$\begin{aligned} &h(k) = \Delta V_t(k), \quad \theta(k) = \boldsymbol{\alpha} = [\alpha_1, \quad \alpha_2, \quad \alpha_3]^T = [\beta, \quad -R_s, \quad (\beta \cdot R_s - (1-\beta)R_p)]^T, \\ &\phi(k) = [\Delta V_t(k-1), \Delta I_L(k), \Delta I_L(k-1)]^T, \quad e(k) = \Delta V_{OC}(k) - \alpha_1 \Delta V_{OC}(k-1). \end{aligned} \tag{4.31}$$

The RLS method [123] is employed to estimate $\theta(k)$ recursively. After obtaining $\hat{\theta}(k)$, the model parameters $[\hat{R}_s, \hat{R}_p, \hat{C}_p]^T$ can be reversely derived by:

$$\begin{aligned} \hat{R}_s &= -\hat{\alpha}_2, \quad \hat{\beta} = \hat{\alpha}_1, \\ \hat{R}_p &= \frac{\hat{\beta} \cdot \hat{R}_s - \hat{\alpha}_3}{1 - \hat{\beta}} = \frac{-\hat{\alpha}_1 \hat{\alpha}_2 - \hat{\alpha}_3}{1 - \hat{\alpha}_1}, \\ \hat{C}_p &= -\frac{\Delta t_s}{\hat{R}_p \log(\hat{\beta})} = \frac{\Delta t_s \cdot (1 - \hat{\alpha}_1)}{(\hat{\alpha}_1 \hat{\alpha}_2 + \hat{\alpha}_3) \log(\hat{\alpha}_1)}. \end{aligned}$$

Assuming independent and identically distributed (i.i.d.) measurement noise, differential treatment further transforms the errors into zero-mean and symmetrically distributed. Hence, constant term explaining the bias is not needed in 4.30. Note that this modelling error may not necessarily be a Gaussian noise sequence globally, but given the differential treatment in formulating the regression equation and utilization of the forgetting factors in RLS, the Direct Current (DC) bias is significantly attenuated, so as for any bias introduced into the model parameter estimation.

In RLS, the forgetting factor $\lambda = 0.98$ is used. Meanwhile, in order to smooth the fluctuations in these variables at different time scales, the multi-timescale RLS algorithm [124] is adopted in the identification process, where the sample rate for $R_s$ is set as $1s$, oppositely, $4s$ are sampling time is used for both $V_p$ and $C_p$. Note that the ZNBs is a slow time-varying system, and different electrical elements have different convergence speeds. In this regard, the multi-time scale RLS with fixed forgetting factors is employed for the online parameter identification in this work.

### Model verification

Since the State of Charge (SoC) can not be accurately measured online by existing sensor techniques, the SoC estimation is fused into the model identification process. Thereby, the accurate battery model not only reproduces the dynamics in the charging and discharging processes and reflects the real-time operating condition but also affirms the fidelity of SoC estimation. Fig.4.6 illustrates the results of EKF based SoC estimation and RLS online model identification. As no prior knowledge is available on the model parameters, the parameters are erroneously initialised as $R_s = R_p = 0.01\Omega$ and $C_p = 1000F$. It is apparent that the model matches the measured terminal voltage in the entire experiments and the error bounds are stabilised less than $0.01V$. The relatively large error spikes can be observed at the start-up point only, due to the intently erroneous initialisation. However, it converges to the reference value quickly within $5s$. The similar pattern is revealed in the SoC estimation. The estimation errors are limited to

1% throughout the tests, which manifests the effectiveness and accuracy of the synthesised RLS based ECM battery modelling approach. Additionally, through the online adaption technique, the influence of the varying ambient environment changes can be easily taken into full consideration. Therefore, the periodic calibration of battery model can be revoked. It is noted that the applied methods relating to SoC estimate will be detailed in the following Section 4.3.

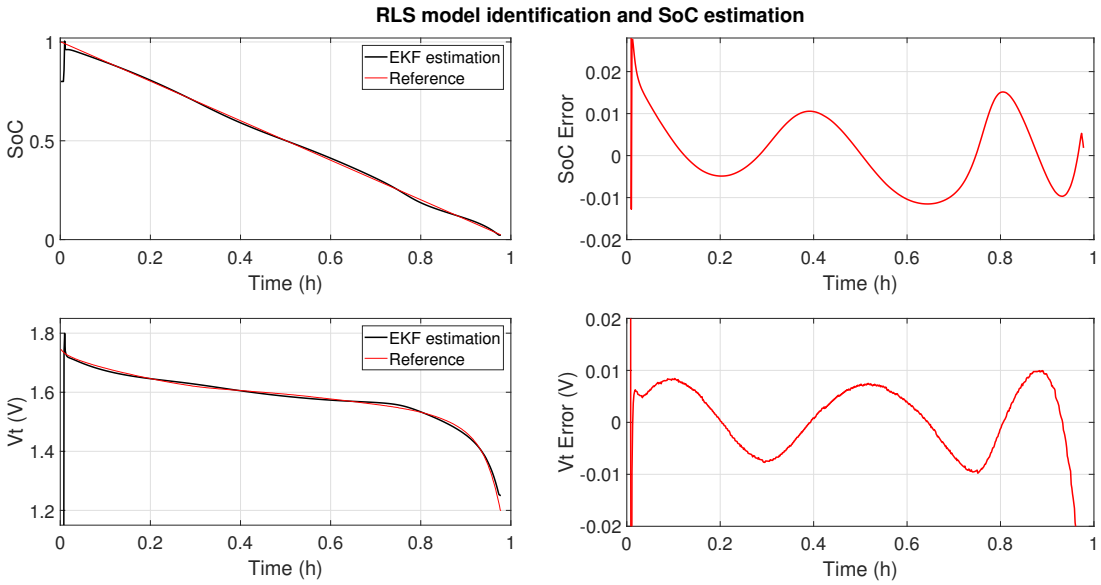


Figure 4.6: Model identification and SoC estimation

## 4.2 State of Charge (SoC) estimate

Battery modelling and state estimation are two primary goals of BMS. According to the real-time estimated battery state information, a well-conditioned battery management system (BMS) can attenuate the concentration polarisation and optimize the applied current densities leading to uniform current distribution. The routine SoC estimation approaches can be divided into four categories. Firstly, the Coulomb counting (CC) is straightforward to implement but suffers from error-prone pitfalls due to SoC initial deviation [125]. The open-loop framework of CC method is also subject to accumulated measurement noise over time.

The second category is comprised of computational intelligence-based approaches which are free of particular battery priori-knowledge [126; 127]. However, as we discussed in Section 4.1.1, their generalization is poor for the unseen data, highly depending on the efforts of cumbersome model training processes, and are intractable for online applications. The look-up open-circuit-voltage (OCV) table method falls into the third category, which relies on the inherent monotonous correlation between SoC and OCV. Nevertheless, to get accurate OCV readings, the battery has to maintain rest in the open circuit state for hours, which makes the pure OCV-SoC method impractical in active duty. Therefore, the equivalent circuit model (ECM) based SoC observer approach within the last category has dominated in most online applications [121; 125; 128; 129; 130]. The model errors and measurement noises can be effectively handled by a close-loop filter design. In other words, ECM is responsible for battery dynamic electrical behaviours modelling, and an appropriate filter can then be designed to observe the internal states of the battery. This combination has been the subject of extensive research, including recursive least squares filter (RLS) [125], canonical Kalman filter counterparts e.g. extended Kalman filter (EKF) [131; 132], adaptive EKF (AEKF) [133], adaptive unscented Kalman Filter (AUKF) [134], as well as other control-oriented based methods e.g. the Luenberger observer [135], sliding mode observer [136], H-infinity filter [137; 138] and particle filter-based data fusion approach [139]. Besides, other effective hybrid SoC estimation methods have also been proposed [140; 141]. Among these implementations, there are two on-going topics surrounding the development of SoC estimation approaches. One is to further enhance the computing efficiency as the scale of BMS chips is getting smaller and more complex. On the other hand, the accurate estimate of SoC is the fundamental step of the subsequent peak power prediction and capacity estimation as indicated in the following Section 5 and Section 6. Though a higher order ECM model guarantees the accuracy [122], it is compromised by the costly matrix calculations [99; 124].

### 4.2.1 Open Circuit Voltage (OCV) Observer based State Estimate

In order to address the aforementioned issue of computing burden in higher order ECM, we develop a novel SoC estimation method based on a proposed Open Circuit Voltage (OCV) observer. It is noted that unlike other parts of this thesis, a second-order ECM is used in this section as an instance to demonstrate the higher computational efficiency of the proposed OCV observer based SOC estimation method using higher order ECM approach. Since the mechanism and applied online parameter identification tool are the same as first-order ECM introduced in Section 4.1.3, corresponding equations and derivation procedures are given as a reference only. Specifically, to compensate for the extra computational effort incurred in using a second order rather than a first order model, which is a critical issue for real-time applications, a new OCV observer is proposed which can not only offset the additional computational cost incurred from using a second order ECM model, but it also helps to reduce the overall computational cost for online SoC estimation.

#### An example of Second-order ECM

Specifically, battery impedance can be illustrated with the second-order ECM given in Fig.4.7. The ohmic resistance $R_s$ stands for the resistant losses of the electrodes and electrolytes. Two parallel resistances and capacitors branches are employed to model the electrochemical behaviours of the ZNBs in the short-term and long-term transient responses and relaxation effects, where $R_1$ is the activation polarisation resistance, $C_1$ is the activation polarisation capacitance, while the concentration polarisation resistance and capacitance are reflected by $R_2$ and $C_2$, respectively. The auxiliary pump system enforces the electrolyte to circle consecutively in the battery stack. Thereby, the relaxation effect will be less significant than lithium-ion batteries, yet it still demands a specific period of time to wait for the terminal voltage, $V_t$, slowly converge to its equilibrium voltage $V_{oc}$. The charging current is predefined as the negative sign and vice versa for the discharging current. The battery transient response can be expressed as follows:

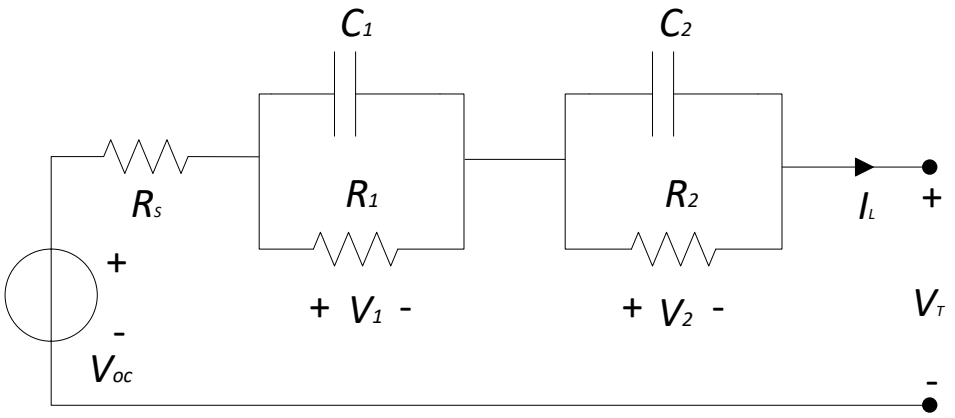


Figure 4.7: Schematic diagram of a second-order ECM

$$V_t = V_{OC} - V_1 - V_2 - I_L R_s \tag{4.32}$$

$$C_l \frac{dV_l}{dt} + \frac{V_l}{R_l} = I_L, \quad l = 1, 2 \tag{4.33}$$

where the terminal current is represented by $I_L$ and the discrete expression of Eq.(4.33) is of the following form [99]:

$$\begin{aligned} V_l(t) =& e^{-\frac{\Delta t_s}{R_l C_l}} V_l(t - \Delta t_s) \\ &+ \left(1 - e^{-\frac{\Delta t_s}{R_l C_l}}\right) R_l I_L(t - \Delta t_s), \quad l = 1, 2 \end{aligned} \tag{4.34}$$

where the time interval $\Delta t_s$ is interpreted as the selected sampling rate. Define $V_1(k) = V_1(k\Delta t_s)$, and the analogous definitions are introduced to $V_2$, $V_{OC}$, $V_t$, $I_L$, therefore, a neat format is given:

$$V_l(k) = e^{-\frac{\Delta t_s}{R_l C_l}} V_l(k-1) + \left(1 - e^{-\frac{\Delta t_s}{R_l C_l}}\right) R_l I_L(k-1), \quad l = 1, 2 \tag{4.35}$$

Rewriting Eq.(4.32) and Eq.(4.35) for time instants $k-1$ and $k$, the expression

of $V_2(k-1)$ can be obtained:

$$\begin{aligned} V_2(k-1) =& \frac{1}{\beta_1-\beta_2}[(\beta_1 V_{OC}(k-1) - V_{OC}(k)) \\ &+ R_s(I_L(k) - \beta_1 I_L(k-1)) \\ &+ (V_t(k) - \beta_1 V_t(k-1)) + \gamma I_L(k-1)] \end{aligned} \tag{4.36}$$

where $\gamma = (1-\beta_1)R_1 + (1-\beta_2)R_2$ and $\beta_l = e^{-\frac{\Delta t_s}{R_l C_l}}$, $l = 1, 2$. For a second order ECM, $R_1C_1 < R_2C_2$, therefore, $\beta_1 < \beta_2$. Shifting $V_2(k)$ and $V_2(k-1)$ in Eq.(4.35), then, the terminal voltage can be concisely formulated as follows:

$$\begin{aligned} V_t(k) =& \alpha_1 V_t(k-1) + \alpha_2 V_t(k-2) + \alpha_3 I_L(k) \\ &+ \alpha_4 I_L(k-1) + \alpha_5 I_L(k-2) + \big(V_{OC}(k) \\ &- \alpha_1 V_{OC}(k-1) - \alpha_2 V_{OC}(k-2)\big) \end{aligned} \tag{4.37}$$

where

$$\begin{aligned} &\alpha_1 = \beta_1 + \beta_2, \quad \alpha_2 = -\beta_1\beta_2, \quad \alpha_3 = -R_s, \\ &\alpha_4 = R_s(\beta_1+\beta_2) - (1-\beta_1)R_1 - (1-\beta_2)R_2, \\ &\alpha_5 = (1-\beta_1)\beta_2 R_1 + (1-\beta_2)\beta_1 R_2 - R_s\beta_1\beta_2. \end{aligned}$$

In order to cancel out the cross-interference between the model identification and state estimation, both $V_1$ and $V_2$ are eliminated from Eq.(4.37). Taking one step time difference into consideration, the differential voltage of $V_t$ is yielded:

$$\begin{aligned} \Delta V_t(k) =& \alpha_1 \Delta V_t(k-1) + \alpha_2 \Delta V_t(k-2) + \alpha_3 \Delta I_L(k) + \\ &\alpha_4 \Delta I_L(k-1) + \alpha_5 \Delta I_L(k-2) + \\ &(\Delta V_{OC}(k) - \alpha_1 \Delta V_{OC}(k-1) - \alpha_2 \Delta V_{OC}(k-2)) \end{aligned} \tag{4.38}$$

where the differential definitions are imposed on the other terms in Eq.(4.38). Based on Eq.(4.37), regression expression is of the form:

$$y(k) = \theta^T(k)\phi(k) + e(k), \tag{4.39}$$

where

$$\begin{aligned} y(k) =& V_t(k) - V_t(k-1), \\ \theta(k) =& \boldsymbol{\alpha} = [\alpha_1, \alpha_2, \alpha_3, \alpha_4, \alpha_5]^T, \\ \phi(k) =& [V_t(k-1) - V_t(k-2), V_t(k-2) - V_t(k-3), \\ & I_L(k) - I_L(k-1), I_L(k-1) - I_L(k-2), \\ & I_L(k-2) - I_L(k-3)]^T. \end{aligned}$$

$e(k)$ is the modelling error consisting of the measurement noise, discretization error, and OCV estimation error, etc. Assuming independent and identically distributed (i.i.d.) modelling error for all variables, differential operation further transforms $e(k)$ into a zero-mean and symmetrically distributed sequence. Hence, constant term explaining the bias is no longer needed in Eq.(4.39). Note that this modelling error may not necessarily be a Gaussian noise sequence globally. But given the differential operation in formulating the regression equation, the bias introduced into the model parameter estimation is significantly attenuated. This is verified in the experimental section.

In order to make the online parameter identification converge, as discussed above the widely adopted RLS method with a predefined forgetting factor $\lambda$ is employed to identify $\theta(k)$ [142]. The forgetting factor is maintained as 0.98. Note that the ZNBs is a slow time-varying system, and different electrical elements, representing different subsystems have different convergence speeds. In this regard, the multi-time scale RLS with fixed forgetting factors is employed for the online parameter identification. According to [142], the errors $e(k)$ will be tuned down to an acceptable level, due to a fixed forgetting factor. Revisiting Eq.(4.39), the slowly time-varying parameters $\theta(k)$ under the different working environments and initial states can be readily calculated. Therefore, the model parameters can be reversely deduced as:

$$\hat{R}_s = -\hat{\alpha}_3, \tag{4.40}$$

$$[\hat{R}_1, \hat{R}_2]^T = \tag{4.41}$$

$$\begin{bmatrix} 1-\hat{\beta}_1 & 1-\hat{\beta}_2 \\ (1-\hat{\beta}_1)\hat{\beta}_2 & (1-\hat{\beta}_2)\hat{\beta}_1 \end{bmatrix}^{-1} \begin{bmatrix} R_s\hat{\alpha}_1 - \hat{\alpha}_4 \\ \hat{\alpha}_5 - \hat{R}_s\hat{\alpha}_2 \end{bmatrix},$$

$$\hat{C}_l = -\frac{\Delta t_s}{\hat{R}_l \log(\hat{\beta}_l)}, \quad l = 1, 2. \tag{4.42}$$

where

$$\Delta = \max{}^{1}\{\hat{\alpha}_1^2 + 4\hat{\alpha}_2,\ 0.000001\}$$

$$\hat{\beta}_1 = \frac{\hat{\alpha}_1 - \sqrt{\Delta}}{2}$$

$$\hat{\beta}_2 = \frac{\hat{\alpha}_1 + \sqrt{\Delta}}{2}$$

### The Proposed OCV Observer

Parameter identification errors and measurement noises are mainly responsible for the inaccuracy of state estimation. The second-order ECM model guarantees a fairly desirable modelling accuracy for most applications, but the overall state estimation accuracy also depends on the filter design. For instance, a fourth order EKF based algorithm has been employed in [128], where the hysteresis effects $V_h$, polarisation voltage $V_1, V_2$, and SoC form the state vector. This scheme simultaneously estimates key states, yet its real-time implementation is computationally expensive. To tackle this issue, this paper presents an OCV observer to simplify the filter design and keep only one dimension of state estimation. Based on Eq.(4.37), the $V_{OC}$ can be estimated using the following equation:

[1] The max operation is to ensure validity of $\sqrt{\Delta}$

$$\begin{aligned}\hat{V}_{OC}(k) =& \hat{\alpha}_1\hat{V}_{OC}(k-1) + \hat{\alpha}_2\hat{V}_{OC}(k-2) + V_t(k) \\ & - \hat{\alpha}_1 V_t(k-1) - \hat{\alpha}_2 V_t(k-2) - \hat{\alpha}_3 I_L(k) \\ & - \hat{\alpha}_4 I_L(k-1) - \hat{\alpha}_5 I_L(k-2) \qquad (4.43)\end{aligned}$$

$$\varepsilon(k) = V_{OC}(k) - \hat{V}_{OC}(k) \qquad (4.44)$$

where $\varepsilon(k)$ is the estimation error of the proposed OCV observer. Due to the operational characteristics of ZNBs, the effects of subtle variations in OCV between two consecutive sampling instants are assumed to be negligible. It is worthwhile to note that $1s$ is set as the sampling rate in this work. According to Eq.(4.43), the OCV observer is stable and consistently produces good performance regardless of the choice of the initial value as long as the identified parameters converge. In this work, the initial $V_{OC}$ is randomly selected between $1.6V$ and $1.85V$, which is ZNBs potential range of OCV in active duty. Since the ZNBs system is slowly time-varying and the charging/discharging regimes are moderate in practice, it can be assumed that the parameter convergence speed is much faster than the system dynamics. Additionally, through a statistical checkout for the recursive expressions, the error is rationally small. Thereby, in the following SoC estimate, the error $\varepsilon(k)$ is regarded as a source of the measurement noise and will be handled by the applied filters. Further, the proposed OCV observer can benefit recent novel methods [137] for the periodic calibration of the OCV-SOC table.

The major novelty of the proposed observer is two-fold. The first is utilisation of differential operation in RLS. When comparing with traditional RLS based method such as in [143], the proposed RLS is more stable to non-stationary data, in which case the traditional method would fail to converge. The second is from the observer-EKF combined system. The traditional method as in [143] directly estimates $V_{OC}$ as one of the states in RLS. However, it would suffer greatly from non-robust data. In the proposed method, the estimate to $V_{OC}$ comes from the comparison of two OCV sources: SoC-OCV table and OCV observer. Integrated into the update step in EKF, the novel observer can thus take the advantage of filters and lead to more robust results.

### Higher order ECM based SoC Estimation Using OCV Observer

The EKF algorithm has been widely used for battery state estimation[99; 124; 125]. The estimation error of proposed OCV observer is complemented by EKF to improve the accuracy. Note however that with the proposed OCV observer, the dimension of the state vector in the EKF is effectively reduced. In particular, the unknown polarisation voltages $V_1, V_2$ are cancelled, resulting in only one SoC state in the EKF. A widely accepted SoC recursion model is given by [131]:

$$SoC(k) = SoC(k-1) - \frac{\eta I_L(k-1)\Delta t_s}{Q} \tag{4.45}$$

where $Q$ denotes battery capacity, and its value keeps constant during a full cycle of charging/discharging but slowly changed through the entire process, which may include multiple cycles. The coulombic efficiency $\eta$ is set as 100% for simplification. Herein, the errors in the proposed OCV observer are viewed as the measurement noise. By combining the OCV observer Eq.(4.43) with the SoC state-space model Eq.(5.5), EKF expression will be re-formulated as:

$$\begin{cases} SoC(k) = F(SoC(k-1)) + w(k) \\ \hat{V}_{oc}(k) = G(SoC(k)) + v(k) \end{cases} \tag{4.46}$$

where $F(SoC(k-1))$ stands for the relationship Eq.(5.5), while $G(SoC(k))$ is the SoC-OCV look-up table obtained from the SoC-OCV test. $w(k)$ and $v(k)$ are the process noise and the measurement noise respectively, which are assumed to be independent, zero-mean, Gaussian noise processes with covariance matrices $\sum_w$ and $\sum_v$, respectively. In this respect, the discrete-time prediction and update equations of EKF are summarized as follows:

### Prediction

$$\hat{SoC}^{-}(k) = F(\hat{SoC}^{+}(k-1))$$
$$\hat{\Sigma}_x^{-}(k) = A_{k-1}\hat{\Sigma}_x^{+}(k-1)A_{k-1}^T + \Sigma_w$$

**Update**

$$\begin{aligned} e(k) &= \hat{V}_{OC}(k) - G(\hat{SoC}^{-}(k)) \\ L_k &= \hat{\Sigma}_x^{-}(k) C_k^T \left[ C_k \hat{\Sigma}_x^{-}(k) C_k^T + \Sigma_v \right]^{-1} \\ \hat{SoC}^{+}(k) &= \hat{SoC}^{-}(k) + L_k \cdot e(k) \\ \hat{\Sigma}_x^{+}(k) &= (I - L_k C_k) \hat{\Sigma}_x^{-}(k) \end{aligned}$$

**Define**

$$\begin{aligned} A_{k-1} &= \frac{\partial F(x)}{\partial x}|_{x=\hat{SoC}^{+}(k-1)} \\ C_k &= \frac{\partial G(x)}{\partial x}|_{x=\hat{SoC}^{-}(k)} \end{aligned} \tag{4.47}$$

where the superscripts $^-$ and $^+$ denote the priori state update and posterior state update phases respectively, where are displayed in Fig.4.16. Then an EKF with reduced dimension can be used for on-line SOC estimation. Further details of EKF can be refereed to [131].

**Computational Cost Analysis**

In this work, the extra computing cost incurred from using the second-order ECM has been offset by the proposed OCV observer, which is another merit of this work. In terms of the computational complexity of using the second-order rather than the first-order ECM with the RLS and EKF, since the proposed method does not require the matrix inverse calculation, they are thus very fast to implement. Furthermore, the increased computational cost is only incurred in the RLS regression, but the developed OCV observer reduces the computational complexity of the EKF which has only one state variable, i.e. SoC.

In general, the theoretical number of operations in a $n-$th order ECM is given below for both traditional RLS-EKF system and the proposed method. The proposed observer and RLS-EKF system are straightforward to be extended to the $n-$th order case. No matter which model is used, the inputs are instant

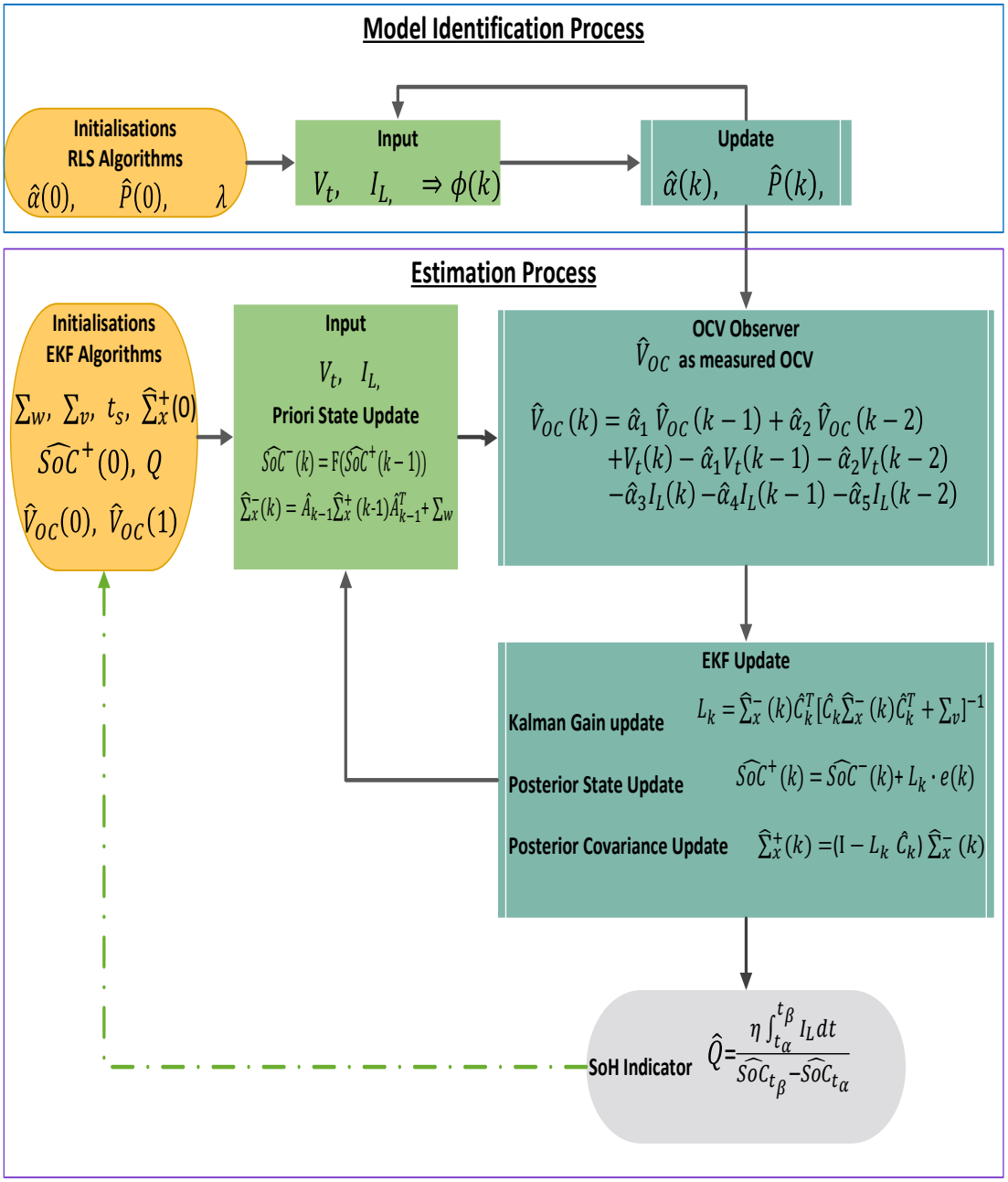


Figure 4.8: Systematic flowchart of the OCV based SoC/Capacity estimation

terminal voltage and current, while the output is instant SoC estimate. The total number of operations in RLS is

$$4(2n+1)^2 + 7(2n+1) + 4 = 16n^2 + 30n + 15$$

The total number of operations in calculating observer is $5n + 2$.
The total number of operations in high dimensional EKF is

$$\text{Predict} : 4n^3 + 13n^2 + 14n + 5$$

$$\text{Update} : 4n^2 + 9n + 7$$

$$\text{Total} : 4n^3 + 17n^2 + 23n + 12$$

If applying the observer in the EKF, the problem becomes one-dimensional. So the number of operations is the above expression with $n = 0$, i.e. 12. Hence, the proposed observer decreases the complexity in EKF from $4n^3 + 17n^2 + 23n + 12$ to $4n^2 + 9n + 19$.

Table. 4.1 lists the computation time for the test-runs on traditional RLS-EKF using the first/second order ECM, as well as on the proposed method. The results include the computational time incurred for running both RLS and EKF (with proposed observer if applicable). This test is based on a complete discharging process which includes 6685 observations. Note that all experiments

Table 4.1: Computational Speed Comparisons

| Method | Traditional EKF | | Proposed Method |
|---|---|---|---|
| | First Order | Second Order | |
| Avg. Time Spent / Step (ms) | 0.06924 | 0.08955 | **0.06218** |

were conducted on a MacBook Air with $1.6GHz$ dual-core Intel Core $i5$ (Turbo Boost up to $2.7GHz$) with $3MB$ shared $L3$ cache. Additionally, the results reveal that the proposed OCV observer based RLS-EKF method is even faster than RLS-EKF using the first-order model and also using the second-order model. It only takes 0.06218 $ms$ for each step including the RLS online regression and EKF based

SoC estimation. In summary, although the use of the second-order ECM has led to the increased computational cost in RLS regression, the introduced OCV observer has reduced the computational cost in the SoC estimation due to the dimension reduction. Overall, a reduced computational complexity is achieved using the proposed method. The proposed framework is thus suitable for on-board applications and has achieved our target to improve the online computing efficiency.

### Algorithm Validation

The proposed approach is first applied to the ZNBs on 4 pulse test data. The testing regimens have been outlined in Section 3.2. The initialisation is prescribed as $R_s = R_1 = R_1 = 0.010\Omega$, $C_1 = C_2 = 1000mF$, $Q = 3.7Ah$ and SoC is erroneously initialised as 80%. The reference OCV values are obtained based on Eq.(3.1) according to reference SoC values, which are acquired using the CC method as mentioned earlier and can refer to Section 3.2.2. Fig.4.10 details the algorithmic performance. The SoC estimation and OCV observer converge to the reference value in less than $5s$, and the error bounds are stabilised within 2%. The subtle discrepancies can be observed during the state shift from the pulse excitation to none. In this situation, the large estimated errors arise from the OCV observer. According to Eq.(4.43), when the demonstrator is disconnected from the circuit, the real OCV value should remain constant until the next current pulse excitation. However, due to the proposed OCV observer, the slow decreasing terminal voltage will be accounted in the OCV observer recursion, leading to a subtle voltage drop in the OCV observations as shown in the Fig.4.12. Whereas, this error is quickly amended by the followed-on SoC estimator. Further, due to the fast convergence of the online RLS identification, the OCV observations will also reach a stable range, and the effects of the terminal voltage drops are attenuated. Fig.4.11 illustrates the convergence of the model parameters in a zoom-in window, wherein all the parameters converge quickly within $8s$. The convergence speed matches well with the assumptions of OCV observer construction and guarantees a faster convergence of the proposed method before changes of the slowly time-varying system becomes significant. In addition, the assumption using in

Eq.4.38 and Eq.4.39 is the term $\Delta V_{OC}(k) - \alpha_1 \Delta V_{OC}(k-1) - \alpha_2 \Delta V_{OC}(k-2)$ sufficiently small and hence can be regarded as the error term $e(k)$ as in Eq.4.39. This hypothesis is further confirmed by the Fig.4.9, which shows that the ratio of the squared error is less than 8% during the first phase ($before$ $216s$) of the simulation. With the RLS method, the modelling errors are attenuated and the parameters converge toward their true trajectories. The ratio of the squared errors is further bounded within 2% after $216s(0.06h)$, which is sufficiently small as the error term $e(k)$. Therefore, Eq.4.38 and Eq.4.39 can be used in this work.

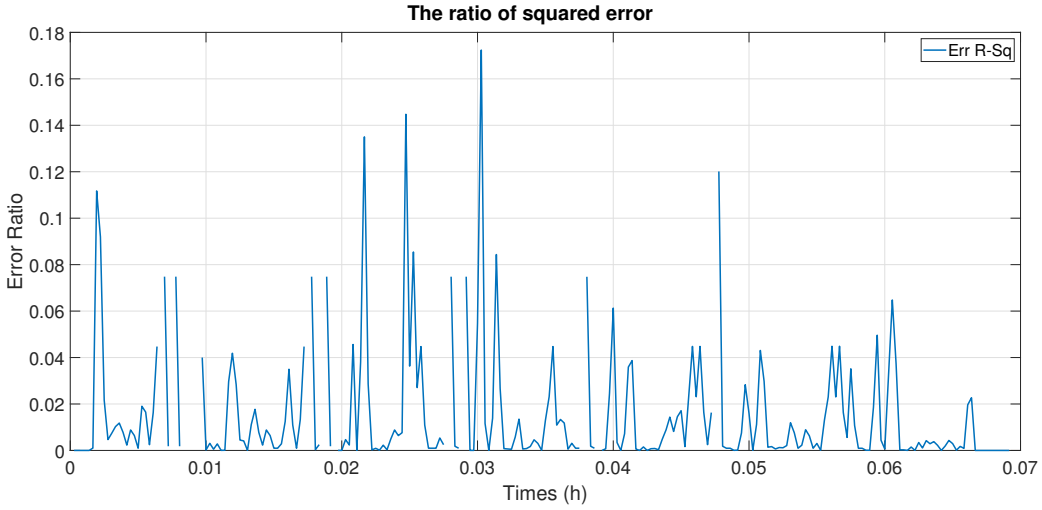


Figure 4.9: The Ratio of Squared Errors

The similar pattern can also be observed in Fig.4.12, where the OCV estimations agree with the reference OCV regularly. The worst case is $0.02V$ voltage divergence. An interesting situation is noticed where once the $1.5C$ current is loaded, the applied current density on the electrode is approaching the material limitation, and this will go against the validity of the SoC-OCV table.

On the other hand, as shown in Fig.4.10, the estimation of internal resistance $R_s$ exhibits a consistent trend. $R_s$ starts with the value of $0.02\Omega$ and maintains

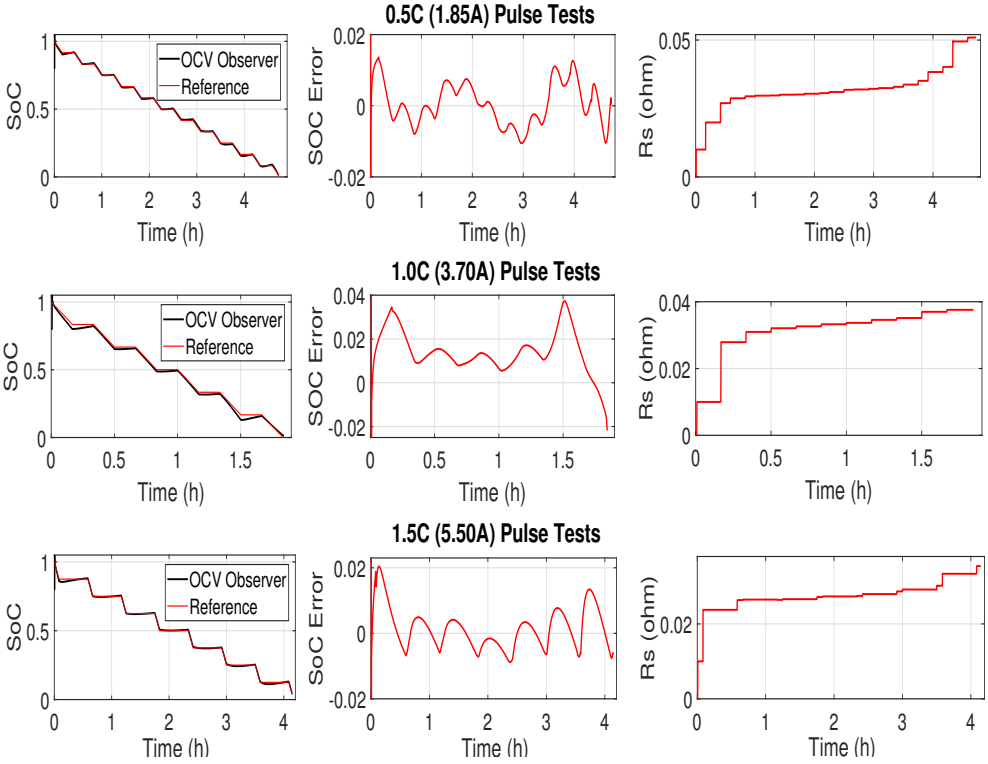


Figure 4.10: SoC and $R_s$ estimation in pulse tests

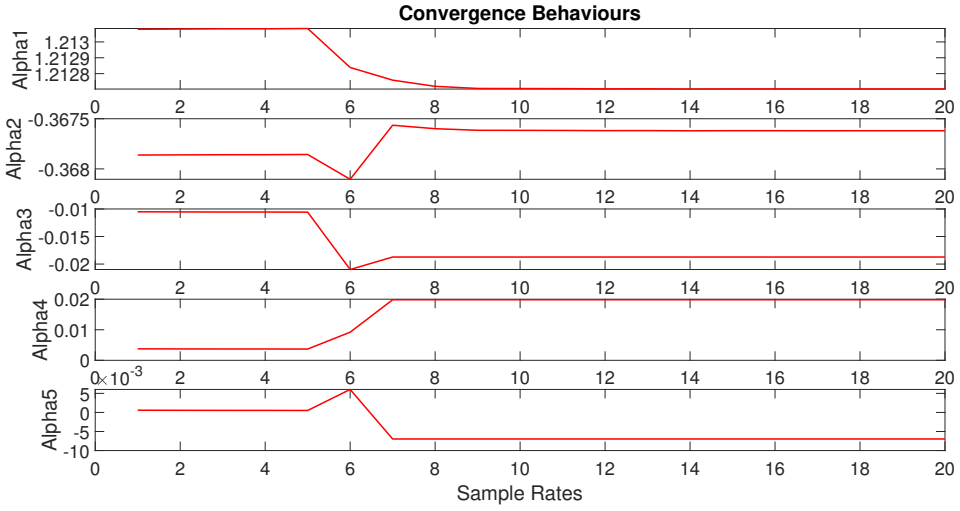


Figure 4.11: Convergence behaviours of the parameters

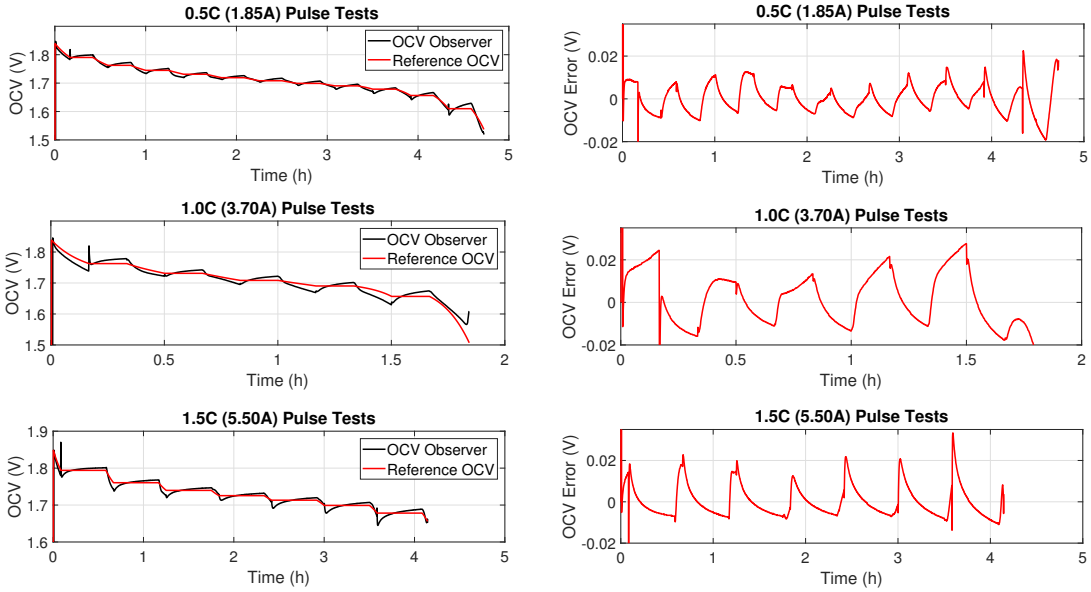


Figure 4.12: Behaviours of OCV observer in pulse tests

around 0.04Ω at the end of discharging. The increased internal resistance is foreseeable, where the reaction product with poor conductance is generated at the end of discharging phase [2]. As depicted in Fig.4.10, higher internal resistance occurs when SoC become lower than 20%. In order to improve the operating efficiency of the ZNBs, the optimal working range should be above 20% SoC.

Additionally, the dynamic pulse tests, listed in Section 3.2.1, are carried out to impose a more complicated current excitations on the demonstrator. Fig.4.13 illustrates the simulation results, which implies that the OCV value can be reliably estimated using the proposed method. In the process of OCV estimation, only a few of error spikes less than $0.03V$ occurred as the feed-in current changes. This is due to the erroneously initial values used in the OCV observer at each new current pulse interval. But the proposed method can reduce the impact of the initial value in a fast manner, almost converging to the reference trajectory within one sample interval. Furthermore, no significant impact on the SoC estimation is observed. Thereby, the proposed OCV observer based SoC estimation has shown a competitive performance at less computational cost. The SoC estimation errors

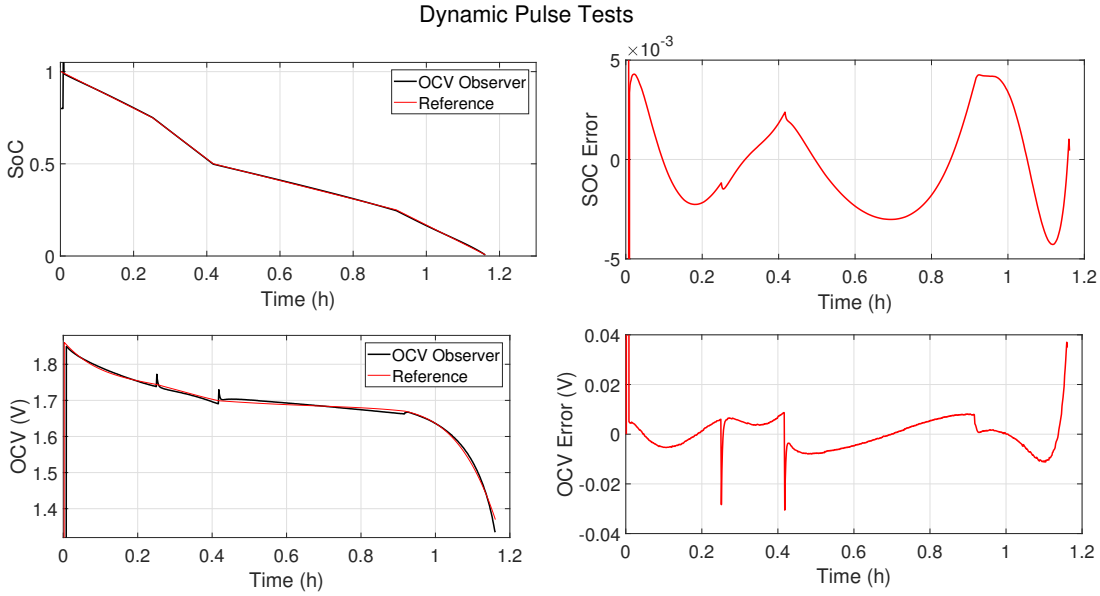


Figure 4.13: Performance in dynamic pulse tests

are bounded within 2%[1]. The effectiveness of the proposed method is further validated by the varying testing regimes introduced in Section 3.2, as shown Table.4.2.

Table 4.2: MSE Values of Different Tests

| | **0.5C** | **1.0C** | **1.5C** | **Dynamic Pulse** |
|---|---|---|---|---|
| SoC | $5.08 \times 10^{-5}$ | $3.29 \times 10^{-4}$ | $4.57 \times 10^{-5}$ | $7.31 \times 10^{-5}$ |
| OCV | $4.55 \times 10^{-5}$ | $2.04 \times 10^{-4}$ | $6.19 \times 10^{-5}$ | $3.82 \times 10^{-5}$ |

### Extendability Analysis

It is notable to mention that the operation dynamics of ZNBs differs from other flow batteries, but is rather similar to the lithium batteries, which are both electrode-dominated. In traditional battery management, only the on-board cur-

[1]Herein, the error bound means the maximum absolute error through whole testing process.

rent $I_L$ and voltage $V_t$ are loaded to excite the model in the absence of any priori-knowledge of specific electrochemistry. In order to manifest the extendability of the proposed method, a $5Ah$ prismatic LiFePO4-Graphite battery made by GWL/Power Company is tested as depicted in Section 3.2.4. The same second-order ECM framework with normal three-dimensional EKF algorithm (polarisation voltage $V_1, V_2$ and SoC) is employed for the fair comparison purpose. Meanwhile, the identification precision is enhanced by a novel multi-timescale RLS method [124]. The identical initial settings for both RLS and EKF are adopted in line with the proposed OCV based method. As illustrated in Fig.4.14, both SoC estimations exhibit larger error bounds than the ZNBs demonstrator. The flaws can be explained by the transitory overshoots occurred on the loaded current profiles. Due to the oversized changes (5C) on the loaded current, the error spikes, derived from the OCV observer, cannot be eliminated and converge as depicted in Fig.4.15. However, the proposed method is shown to be able to attenuate the uncertainties induced by the higher dimensional EKF, achieving an acceptable error bounds less than 8%. With respect to the convergence of SoC estimation, the traditional EKF algorithm converges slowly as well. It is due to the wrong estimates of polarisation voltages $V_1$ and $V_2$. The estimation precision of the traditional EKF method will be deteriorated accordingly as shown in Fig.4.14. Moreover, the apparent modelling flaws can be observed at the end phases in both methods as shown in Fig.4.15, which seem derived from the parameter identification process. In Eq.(4.38), $e(k) = \Delta V_{OC}(k) - \alpha_1 \Delta V_{OC}(k-1) - \alpha_2 \Delta V_{OC}(k-2)$ is regarded as the modelling errors, which is based on the assumption that the magnitude of $e(k)$ is far less than the $\Delta V_t$. Further, this assumption matches the nature of ZNBs. However, the fast falling OCV value in lithium batteries violates the aforementioned assumption, therefore amplifying the modelling errors.

### Discussion

The above work mainly presents how to efficiently control the introduced computational cost with a higher order ECM. A second-order ECM is given as an example to achieve more accurate battery dynamics modelling. Then an improved OCV observer is incorporated with the higher order model to solve the increased

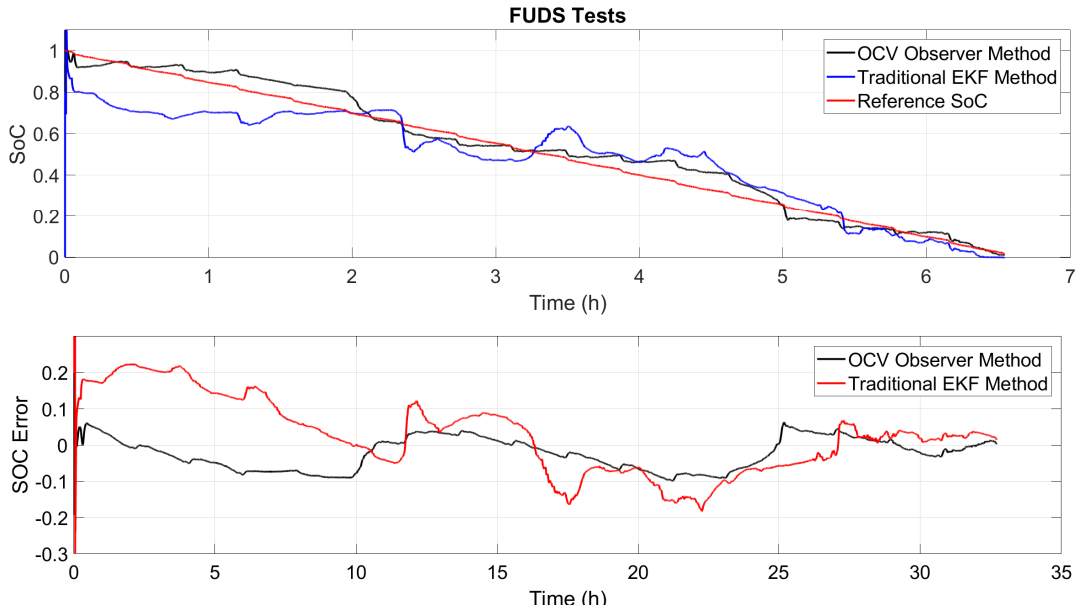


Figure 4.14: SoC estimation in FUDS tests

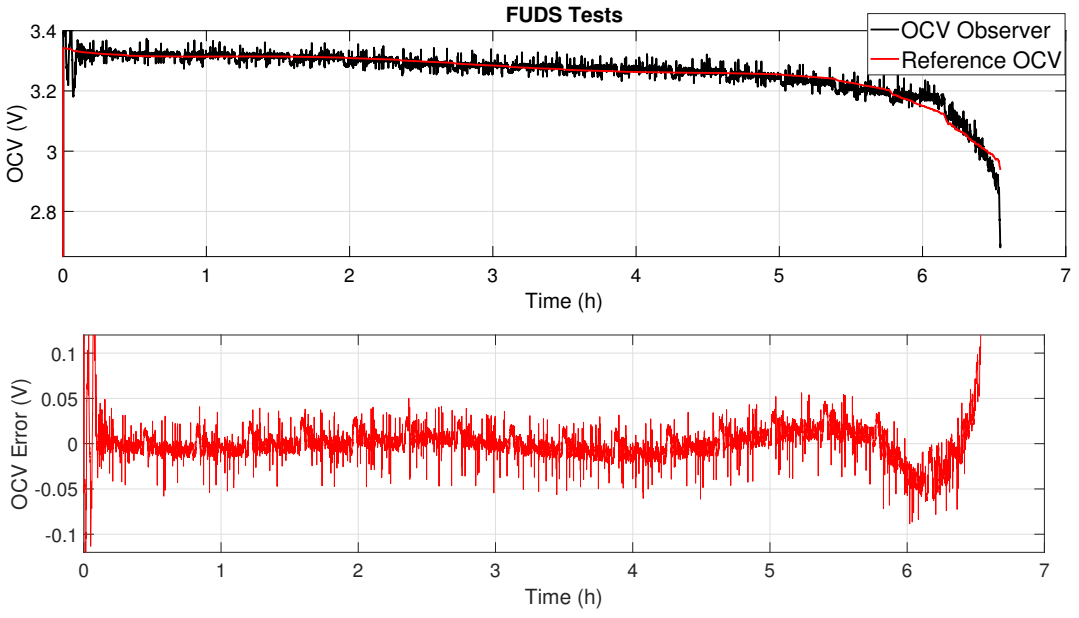


Figure 4.15: Behaviours of OCV observer in FUDS tests

computational complexity issues. In this framework, the model identification process is separated from the state estimation. The proposed OCV observer in recursive format allows a simpler filter design, leading to reduced computational burden and improved performance.

### 4.2.2 Model Predictive Control Scheme Based Observer (MPCO) based State Estimate

The OCV based observer has achieved the reduction of computational cost, especially for the higher order ECM. In this section, a novel Model Predictive Control Scheme Based Observer (MPCO) is introduced to address the measurement noises and intermittent error spikes to enhance the accuracy of the SoC estimation. Model Predictive Control (MPC) is a process control strategy developed in the 1970$s$ [144]. The systematic mathematical model is used to assess the influence of the current control actions on the plant performance in the future [145]. The most remarkable advantage of MPC is multiple constraints handling [146]. Moreover, the optimum solution will be solved at each time step over a finite prediction horizon [147]. Analogous to MPC scheme, in this work, the electrochemical constraints against the state estimates in terms of the polarization voltage and SoC are imposed based on a first-order electrical equivalent model (ECM). On the other hand, the implantation of rolling-horizon (window) technique improves the precision of capacity estimation. Therefore, the influences of capacity fluctuations are attenuated effectively by the proposed method. In addition, the analysis of computational burden and the comparison among other state-of-the-art SoC estimate approaches are provided as well.

#### MPC based Observer Design

Model Predictive Control (MPC) is a powerful scheme taking all the model-based process interactions into consideration, where the best control action at each sampling point will be determined by solving the finite horizon optimization in real time. The MPC scheme has been widely used in the industrial applications. In practice, nearly every application imposes constraints. MPC is a suitable control scheme to advantageously handle the constraints on manipulated variables

and states simultaneously. In this paper, inspired by the control paradigm of MPC [144] and SMO [148], a novel MPC-based SoC observer (MPCO) is introduced in this section. Note in this section, for the sake of simplification, the first-order ECM presented in Section 4.1.3 is used as an example. It is known that the outputs of such a simple ECM are not precise matches to the real measurements. The errors from measurements, discretization process, and parameter identification in RLS have to be compensated by the proposed SoC observer. According to Eq.(4.27), the two-dimensional state equations along with small friction terms are formulated as follows:

$$\begin{cases} SoC(k) = SoC(k-1) - \frac{\eta \Delta t_s}{Q} I_L(k-1) + f_1(k-1) \\ V_p(k) = e^{-\frac{\Delta t_s}{R_p C_p}} V_p(k-1) + \left(1 - e^{-\frac{\Delta t_s}{R_p C_p}}\right) R_p I_L(k-1) + f_2(k-1) \end{cases} \tag{4.48}$$

where $Q$ is the capacity of ZNBs, whilst $f_1$ and $f_2$ stand for the errors not only from measurements, modelling, and discretization, but also from the time-varying parameters identified in RLS. Analogous to other observer/filter designs, the terminal voltage $V_t$ is the main focus of measurement equation:

$$V_t(k) = f(SoC(k)) - V_p(k) - R_s I_L(k) + f_3(k) \tag{4.49}$$

where $f$ is the pre-calibrated SoC-OCV table expressed as $V_{OC} = f(SoC)$. Herein, the $f_1(k)$ and $f_2(k)$ are systematic frictions. In coincidence with the framework of the state equations Eq.(4.48), $f_3(k)$ represents measurement equation friction. Assuming the systematic frictions and measurement friction are independent, and thus are of the expressions as:

$$\begin{bmatrix} f_1(k) \\ f_2(k) \end{bmatrix} \sim N(0, \Sigma), \quad f_3(k) \sim N(0, \sigma^2) \tag{4.50}$$

where $\Sigma$ and $\sigma$ are error covariance matrix and the standard deviation, respectively, which are used to solve control law in the followed-on process. Denotes $\mathbf{x}(k) = [SoC(k), \quad V_p(k)]^T$ and thus the state vector $\mathbf{X}(k)$ and measurement vector $\mathbf{Y}(k)$ for $n$ steps are derived as: ‘

$$\mathbf{X}(k) = \begin{bmatrix} \mathbf{x}(k-n+1) \\ \mathbf{x}(k-n+2) \\ \vdots \\ \mathbf{x}(k) \end{bmatrix}, \quad \mathbf{Y}(k) = \begin{bmatrix} V_t(k-n+1) \\ V_t(k-n+2) \\ \vdots \\ V_t(k) \end{bmatrix} \tag{4.51}$$

where $n$ is the decision window in the MPCO. Therefore, a neat state equation is written as:

$$\mathbf{X}(k+1) = A_k \cdot \mathbf{X}(k) + B_k \cdot \mathbf{u}(k) + \mathbf{f}(k) \tag{4.52}$$

where

$$A_k = \begin{bmatrix} 0 & I_2 & 0 & \cdots & 0 \\ 0 & 0 & I_2 & \cdots & 0 \\ \vdots & \vdots & \vdots & \vdots & \vdots \\ 0 & 0 & 0 & \cdots & I_2 \\ 0 & 0 & 0 & \cdots & A \end{bmatrix}, \quad B_k = \begin{bmatrix} 0 & 0 & 0 & \cdots & 0 \\ 0 & 0 & 0 & \cdots & 0 \\ \vdots & \vdots & \vdots & \vdots & \vdots \\ 0 & 0 & 0 & \cdots & 0 \\ 0 & 0 & 0 & \cdots & B \end{bmatrix},$$

$$\mathbf{u}(k) = \begin{bmatrix} I_L(k-n+1) \\ I_L(k-n+2) \\ \vdots \\ I_L(k-1) \\ I_L(k) \end{bmatrix}$$

$$\mathbf{f}(k) = \begin{bmatrix} 0 \\ 0 \\ \vdots \\ 0 \\ \mathbf{f}(k) \end{bmatrix}, \quad A = \begin{bmatrix} 1 & 0 \\ 0 & e^{-\frac{\Delta t_s}{R_p C_p}} \end{bmatrix},$$

$$B = \begin{bmatrix} -\frac{\eta \Delta t_s}{Q} \\ 1 - e^{-\frac{\Delta t_s}{R_p C_p}} \end{bmatrix}, \quad \mathbf{f}(k) = \begin{bmatrix} f_1(k) \\ f_2(k) \end{bmatrix}$$

Suppose the posteriori-estimate $\hat{\mathbf{X}}(k)$ and the corresponding error covariance matrix $\hat{\mathbf{\Sigma}}_k$ have been obtained after the $k$-th measurement. Thereby, the intermediate priori-estimate $\hat{\mathbf{X}}_-(k+1)$ in the next sample instant can be calculated as follows:

$$\hat{\mathbf{X}}_-(k+1) = A_k \cdot \hat{\mathbf{X}}(k) + B_k \cdot \mathbf{u}(k) \tag{4.53}$$

Afterwards, the posteriori-estimate $\hat{\mathbf{X}}(k+1)$ can be corrected by solving the control law as:

$$\hat{\mathbf{X}}(k+1) = \hat{\mathbf{x}}_-^{(n)}(k+1) + \Delta\mathbf{x}(k+1) = A_k \cdot \hat{\mathbf{X}}(k) + B_k \cdot \mathbf{u}(k) + \Delta\mathbf{x}(k+1) \tag{4.54}$$

where $\Delta\mathbf{x}(k+1)$ is not only the MPC control law obtained from the solution of the quadratic programming as disclosed in the following content, but also the

correction to priori-estimate. The errors of the priori-estimate and posteriori-estimate are expressed as follows, respectively:

$$\begin{aligned} \mathbf{e}_{-}(k+1) &= A_k \cdot \mathbf{e}(k) + \mathbf{f}(k), \\ \mathbf{e}(k+1) &= \mathbf{e}_{-}(k+1) - \Delta\mathbf{x}(k+1) \end{aligned} \tag{4.55}$$

According to the ECM, the posteriori-estimate for $\mathbf{Y}(\hat{k+1})$ can be calculated:

$$\begin{aligned} &\hat{\mathbf{Y}}(k+1) = F(C_1 \cdot \hat{\mathbf{X}}(k+1)) - C_2 \cdot \hat{\mathbf{X}}(k+1) - R_s \cdot \mathbf{u}(k+1) \\ &\approx F(C_1 \cdot \hat{\mathbf{X}}_{-}(k+1)) + \left.\frac{\partial F}{\partial \mathbf{X}}\right|_{\mathbf{x}=C_1\cdot\hat{\mathbf{X}}_{-}(k+1)} \qquad (4.56) \\ &\cdot C_1 \cdot \Delta\mathbf{X}(k+1) - C_2 \cdot \hat{\mathbf{X}}(k+1) - R_s \cdot \mathbf{u}(k+1) \\ &= F(C_1 \cdot \hat{\mathbf{X}}_{-}(k+1)) - C_2 \cdot \hat{\mathbf{X}}_{-}(k+1) - R_s \cdot \mathbf{u}(k+1) \qquad (4.57) \\ &+ \left(\frac{\partial F}{\partial \mathbf{x}} \cdot C_1 - C_2\right) \cdot \Delta\mathbf{x}(k+1) \end{aligned}$$

(4.58)

where due to the nature of recursive properties, a set of $n$ outputs from model can be estimated. A neat form of $\mathbf{Y}(\hat{k+1})$ is thus reformulated as :

$$\hat{\mathbf{Y}}(k+1) = \mathbf{y}_{k+1} + \mathbf{G} \cdot \Delta\mathbf{x}(k+1) \tag{4.59}$$

where

$$C_1 = \text{blkdiag}\{[1 \quad 0], \ldots, [1 \quad 0]\}, \quad C_2 = \text{blkdiag}\{[0 \quad 1], \ldots, [0 \quad 1]\}$$

$$F\left(\begin{bmatrix} x_1 \\ x_2 \\ \vdots \\ x_l \end{bmatrix}\right) = \begin{bmatrix} f(x_1) \\ f(x_2) \\ \vdots \\ f(x_l) \end{bmatrix}, \quad \frac{\partial F}{\partial \mathbf{x}}\left(\begin{bmatrix} x_1 \\ x_2 \\ \vdots \\ x_l \end{bmatrix}\right) = \text{diag}\{f'(x_1), f'(x_2), \ldots, f'(x_l)\}$$

$$\mathbf{y}_{k+1} = F(C_1 \cdot \hat{\mathbf{x}}_{-}(k+1)) - C_2 \cdot \hat{\mathbf{x}}_{-}(k+1) - R_s \cdot \mathbf{u}(k+1), \quad \mathbf{G} = \frac{\partial F}{\partial \mathbf{x}} \cdot C_1 - C_2$$

Analogous to the control paradigm of MPC, the optimal control law i.e. the gain of the proposed MPCO, can be determined by minimizing the following cost function:

$$\begin{aligned} J =& ||\hat{\mathbf{Y}}(k+1) - \mathbf{Y}(k+1)||_Q^2 + ||\mathbf{x}(k+1) - \mathbf{x}_{-}(k+1)||_R^2 \\ =& ||\mathbf{G} \cdot \Delta\mathbf{x}(k+1) + \mathbf{y}_{k+1} - \mathbf{Y}(k+1)||_Q^2 + ||\Delta\mathbf{x}(k+1)||_R^2 \end{aligned} \tag{4.60}$$

where $\hat{\mathbf{Y}}(k+1)$ is the estimated vector of future $V_t$ given the controlled state vector $\Delta\mathbf{x}(k+1)$. On the other hand, $\mathbf{Y}(k+1)$ is the vector of the real voltage measurements, which are considered as references. Herein, the length of the decision horizon is $n$. It is should be noted that differing from the traditional framework of MPC, during each optimization step, the moment $k$ and $n-1$ steps ahead model outputs, which equal to the length of the decision horizon $n$, are compared with the real measurements. By substituting Eq.(4.59) into the Eq.(4.60), a quadratic expression is given:

$$\begin{aligned} J =& \Delta\mathbf{x}(k+1)^T \cdot (\mathbf{G}^T Q\mathbf{G} + R) \cdot \Delta\mathbf{x}(k+1) \\ &+ 2\left(\mathbf{y}_{k+1} - \mathbf{Y}(k+1)\right)^T Q\mathbf{G} \cdot \Delta\mathbf{x}(k+1) + Q_y \end{aligned} \tag{4.61}$$

where $Q_y = \left(\mathbf{y}_{k+1} - \mathbf{y}^{(n)}(k+1)\right)^T \cdot Q \cdot \left(\mathbf{y}_{k+1} - \mathbf{y}^{(n)}(k+1)\right)$. In additional, the positive definite weighting matrices $R$ and $Q$ denote the measurement error covariance and priori-estimate error covariance respectively, which can be derived as follows:

$$Q^{-1} = \mathrm{diag}\{\sigma^2, \sigma^2, \ldots, \sigma^2\}, \quad R^{-1} = A_k \hat{\mathbf{\Sigma}}_k A_k^T + \mathrm{diag}\{0, \ldots, \Sigma\} \tag{4.62}$$

For the unconstrained optimization problem $\min_{\Delta\mathbf{x}(k+1)} J$, an analytical solution could be readily found below:

$$\begin{aligned} \Delta\mathbf{x}^*(k+1) &= (\mathbf{G}^T Q\mathbf{G} + R)^{-1}\mathbf{G}^T Q(\mathbf{Y}(k+1) - \mathbf{y}_{k+1}) \\ &\stackrel{\text{def}}{=} L \cdot (\mathbf{Y}(k+1) - \mathbf{y}_{k+1}) \end{aligned} \tag{4.63}$$

where $L$ is defined to simplify equations:

$$L \stackrel{\text{def}}{=} (\mathbf{G}^T Q\mathbf{G} + R)^{-1}\mathbf{G}^T Q,$$

$$\begin{aligned} I - L\mathbf{G} &= I - (\mathbf{G}^T Q\mathbf{G} + R)^{-1}\mathbf{G}^T Q\mathbf{G} \\ &= (\mathbf{G}^T Q\mathbf{G} + R)^{-1} R \end{aligned} \tag{4.64}$$

According to matrix inverse formula, yielding:

$$(\mathbf{G}^T Q\mathbf{G} + R)^{-1} = R^{-1} - R^{-1}\mathbf{G}^T \left(Q^{-1} + \mathbf{G}R^{-1}\mathbf{G}^T\right)^{-1} \mathbf{G}R^{-1} \tag{4.65}$$

Hence the new covariance matrix will be expressed as:

$$\begin{aligned}\hat{\Sigma}^{+}_{k+1} &= Var[\hat{\mathbf{x}}_{+}(k+1)] = Var[\hat{\mathbf{x}}_{-}(k+1) + \Delta\mathbf{x}(k+1)] \\ &= Var[\hat{\mathbf{x}}_{-}(k+1) - L \cdot \mathbf{y}_{k+1} + L \cdot \mathbf{Y}(k+1)] \\ &= Var[(I - L\mathbf{G})\hat{\mathbf{x}}_{-}(k+1) + L \cdot \mathbf{Y}(k+1)] \\ &= (I - L\mathbf{G})R^{-1}(I - L\mathbf{G})^{T} + LQ^{-1}L^{T} \\ &= (\mathbf{G}^{T}Q\mathbf{G} + R)^{-1}R(\mathbf{G}^{T}Q\mathbf{G} + R)^{-1} + (\mathbf{G}^{T}Q\mathbf{G} + R)^{-1}\mathbf{G}^{T}Q\mathbf{G}(\mathbf{G}^{T}Q\mathbf{G} + R)^{-1} \\ &= (\mathbf{G}^{T}Q\mathbf{G} + R)^{-1} \end{aligned} \tag{4.66}$$

For unconstrained case, calculating $R$ is unnecessary. The only costly calculation might be $(Q^{-1} + \mathbf{G}R^{-1}\mathbf{G}^{T})^{-1}$ in Eq. 4.65, which has $O(n^3)$ time complexity. However, calculating $R$ has 7 times more complexity as the number of rows and columns of $R$ is twice of $\mathbf{G}R^{-1}\mathbf{G}^{T} + Q^{-1}$.

### Constrained formulation on SoC Observer

In order to improve the accuracy of the proposed SoC observer, a couple of constraints can be integrated into the process of the SoC estimation while keeping in line with the MPC paradigm. When incorporating the ZNBs intrinsic electrochemical characteristics into observer formulation, the controlled state variables $\Delta\mathbf{x}(k+1)$ has to be bounded within the feasible regions derived by the potential constraints. Taking polarization voltage $V_p$ as an example, though the enlarged distance among electrodes increases the value of $V_p$, the circulating electrolyte can offset the distance effects to drag $V_p$ back within $\pm 0.06V$. A faster flow rate may even further reduce the polarization voltage. Apart from $V_p$, the varying ranges of SoC also has to be restrained between 0 and 1. Alternatively, the SoC changes can also be limited into other ranges depending on the realistic operating conditions. Therefore, linear constraints e.g. lower and upper thresholds for $SoC$ and $V_p$ are integrated into the control formulation:

$$C_1\Delta\mathbf{X}(k+1) \in \left[\mathbf{s}_l - C_1\hat{\mathbf{X}}_{-}(k+1), \mathbf{s}_u - C_1\hat{\mathbf{X}}_{-}(k+1)\right] \tag{4.67}$$

$$C_2\Delta\mathbf{X}(k+1) \in \left[\mathbf{V}_{p,l} - C_2\hat{\mathbf{X}}_{-}(k+1), \mathbf{V}_{p,u} - C_2\hat{\mathbf{X}}_{-}(k+1)\right] \tag{4.68}$$

where the inequalities Eq.(4.67) and Eq.(4.68) guarantee the states constraints. Then the above problem is transformed to solve a quadratic programming problem under the linear constraints. It is worth noting that in order to comply with the control theory of the MPC, the optimized solutions will be updated at each sampling point, and then only the first control signal with regard to the current instant is loaded to the actuator [149]. Analogously, merely the first line of $\Delta\mathbf{X}$ is employed as the gain value to update the state estimations. Owing to the merits of the imposed constraints, the estimated results will show a perfect match to the theoretical values. And thus the state estimations will converge quickly, providing a more accurate SoC estimation for the followed capacity estimation.

For the $QP$ problem, the solution is solved either in the interior of constrained area, or at the border. Therefore, two cases are discusses as follows. If the solution is in the interior, it is equivalent to the solution without constraints. And if the solution is on the boundaries , it means the solution is actually truncated by constraints. As the true values of the state variables lie in the constraint borders, the solution will have less error variance than no-constraint-solution, leading to less correction effect. However, the state variable is fixed at the constrained values in this case, resulting in 0 variance. In order to cope with filter system, the unconstrained covariance matrix is used to approximate constrained covariance matrix, which is smaller in theory. By doing so, similar to the scheme of $H-$infinity filter, the larger covariance matrix along with a less correction effect brings extra robustness to the estimation.

### Time Complexity Analysis

In this section, only one window is considered. Complexity analysis is more focused on feasibility of online estimation. Multi-window is only considered as a more accurate alternative for capacity updates after each cycle. The general method to solve quadratic programming problem with linear constraints is already sketched in the Section 4.2.3, which is detailed as follows:

1. Suppose the problem is

$$\min_x \frac{1}{2}x^T Qx + f^T x \tag{4.69}$$
$$s.t. \quad C_i x <= g_i, \quad 1 \leq i \leq l \tag{4.70}$$

   where $g_i$ is a number and each $g_i$ represents for a constraint.

2. As the solution will be at the border or within the border for each constraint, consider a combination of the $l$ constraints, and solve the problem with these constraints being equal. For example, if the $i_1$, $i_2$, ..., $i_k-$th constraints are selected, i.e. to solve

$$\min_x \frac{1}{2}x^T Qx + f^T x \tag{4.71}$$
$$s.t. \quad C_i x = g_i, \quad i = i_1, i_2, \ldots i_k \tag{4.72}$$

   The above problem can thus be easily solved using Lagrange multiplier. If the solution satisfies all constraints, it will be kept, otherwise is discarded.

3. Consider all combinations and compare the corresponding results. There will be $2^l$ combinations and less than $2^l$ valid results. Select the one with the minimum cost function value as the global minimum solution.

In this work, the state variable $x$ is two-dimensional. There are four constraints but only 9 possible solutions are attainable, detailed as: one solution without constraints, four with one constraints, and other four with two constraints. The problem with one constraints are thus reduced to a one-dimensional quadratic function minimization problem. Additionally, two constraints directly determine the solution. These are trivial cases to solve. Thereby, little extra time complexity will be added to the problem.

The main computational burden in this work appears in solving the problem without constraints. As stated in the last part of Section of **MPC based Observer Design**, solving this case has similar complexity to $H-$infinity filter, but will be slower than Kalman Filter (EKF), hence also slower than Sliding Mode Observer (SMO). However, they just differ by a small constant scalar. On the

other hand, the experimental time used for each method is summarised in Table 4.3. The elapsed time is tiny as $0.2541ms$ per loop. Although the MPCO proposed in this paper is the slowest among the comparisons, it is yet fast enough for online application.

| Filter Method | SMO | EKF | $H-$finity | MPCO |
|---|---|---|---|---|
| Elapsed Time ($ms$) per Loop | 0.1062 | 0.1364 | 0.1456 | **0.2542** |

Table 4.3: Experimental Time Complexity Comparisons

### The Framework of the Proposed Observer

In this work, the RLS based online identification method is used to parameterize the time-varying system, i.e. the ECM model. Therefore, the effects of aging evolution and varying working conditions have been considered in the process of parameters identification. Afterwards, the identified parameters are applied to the proposed MPCO to obtain a robust SoC estimation. Then the capacity is updated at the end of a full cycle, which will be used as the base capacity in the following cycle to overcome the capacity fluctuation issues. The capacity estimate is regarded as an indicator for the reconditioning and maintenance. The systematic flowchart of the proposed method is given in Fig.4.16. The proposed MPCO ultimately inherits the distinguishing merits of MPC optimal control theory. Two remarkable advantages can be achieved against the current state-of-the-art studies [150]. One benefit comes from rolling horizon theory and the other is introduced by the imposed constraints. Firstly, MPC observer calculates the optimal gain over the multi-window decision horizon rather than using the single window knowledge at instant time. Hence, the proposed observer is capable of handling errors not only from measurements, modelling, and discretization, but also from the time-varying parameters identified in RLS. And MPCO can thus further smooth the disturbance from a sudden measurement fault. Secondly, complemented by the introduced constraints of states in line with electrochemical information, the proposed observer has achieved outperforming accuracy of estimation. Consequently, the built-in constraints on polarization voltage and

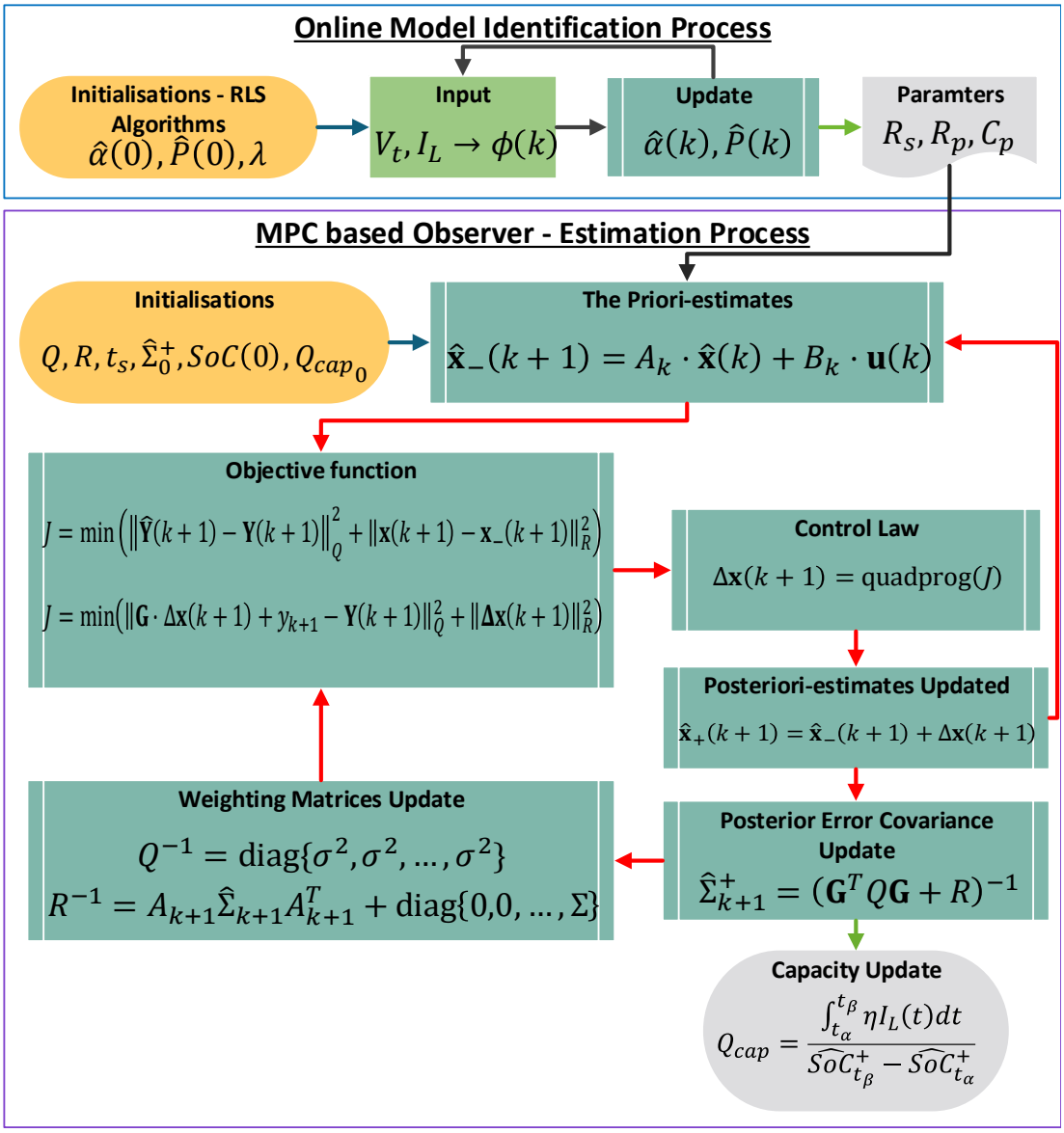


Figure 4.16: Implementation flowchart of the MPCO method

SoC operating range, favourably enhance the stability and convergence of the proposed MPCO. More reliable capacity estimation can be readily achieved in this process to accurately determine the moment of maintenance. The proposed MPCO effectively overcomes the existing deficiency in the management of ZNBs from the application perspective.

### Accuracy of SoC estimates

In this work, the pulse tests listed in Section 3.2.1, as shown in Fig.3.2 are carried out to mimic the practical RFBs working conditions introducing the intermittence of renewable electricity sources. Additionally, for the purpose to compare the performance of state estimates among different algorithms in terms of the SoC tracking performance, transient behaviours, estimation robustness, convergence. etc., a more complex excitation is imposed on the ZNBs, namely dynamic pulse tests as shown in the Fig.3.2. With an intentionally initial SoC error of $-20\%$, the resultant SoC estimation of the proposed MPCO method is compared with the state-of-the-art algorithms such as EKF, $H$-infinity, and SMO. In order to conduct fair comparisons among all SoC estimators, the efforts on the parameters tuning process, e.g. $P$, $\Sigma$, and $\sigma$. etc. are kept in a similar level, besides, it should be noted that the size of the decision window (horizon) is set as one to guarantee the approximate computational burden. The SoC estimation and comparisons are displayed in Fig.4.17.

According to Fig.4.17(a) and Fig.4.17(b), the estimation of MPCO presents a good convergence behaviour to the SoC reference trajectory, resulting from the imposed hard constraints on the polarization voltage estimation $V_p$ revealed in Fig.4.17(c). Specifically, as illustrated in the zoom-in plot of the starting stage, the SoC estimation provided by MPCO converges to the CC reference faster than other counterparts, while SMO shows the slowest convergence performance. The relative poor convergence is foreseeable in SMO, due to its simplest structural design. In this regard, the analytical discussion among different estimators are detailed at the end of this section. Apart from the ending stage, the worst transient behaviours occurs in the first transient pulse, where the current changes from $1C$ to $1.5C$. It can be explained by the effects of the unstable model parameters in the initial stage. As shown in Fig.4.17(b), the estimation performances of EKF, $H$-infinity and SMO, are getting worse in the ending stage. The comparisons of SoC estimate error among these four approaches are detailed in Table.4.4, where the proposed MPCO method provides the best accuracy of the SoC estimation. Additionally, unlike the other counterparts, MPCO exhibits strong robustness,

and the estimation accuracy of MPCO still remains stable yet, with the SoC estimation errors almost bounded within 1.5%. These phenomena are owing to the introduced hard constraints on the polarization voltage $V_p$. As presented in Fig.4.17(c), the proposed MPCO method is capable of not only incorporating the priori-knowledge of the battery intrinsic electrochemical properties into SoC estimation, but also restricting the $SoC$ estimation within reasonable region. Therefore, the SoC estimation is further optimised by the proposed MPCO method. On the other hand, the proposed MPCO inherits the advantages of MPC that are good at handling the non-Gaussian noises according to Eq.(5.1) and Eq.(5.2). In this paper, for the convenience sake, only the Gaussian noises with a standard deviation of $10mV$ is imposed on the voltage measurement for all the SoC estimators. Moreover, the accuracy of capacity estimation will be enhanced by raising the length of the windows, as discussed in the following content Section 6.2.5.

| SoC Error | MPCO | SMO | EKF | H-Infiinty |
|---|---|---|---|---|
| Mean | $-0.0087$ | $-0.0314$ | $-0.0227$ | $-0.0225$ |
| Std. Dev. | 0.0187 | 0.0458 | 0.0229 | 0.0250 |

Table 4.4: Dynamic Charging Profile SoC Estimate Error Summary

### Validation of applicability

In this work, the terminal current and the voltage are used as the excitation signals for the online model identification and state estimation, where the priori-knowledge of ZNBs is incorporated as the constraints into the observer design. In principle, the proposed MPCO method is able to be used for other type of batteries. In order to test the generality of the proposed MPCO, a $5Ah$ prismatic $LiFePO4$-Graphite lithium battery (GWL/Power Company) has been tested. Throughout the entire tests, the same initial settings in the above content and narration are adopted on EKF, $H$-infinity, and SMO approaches as well. The

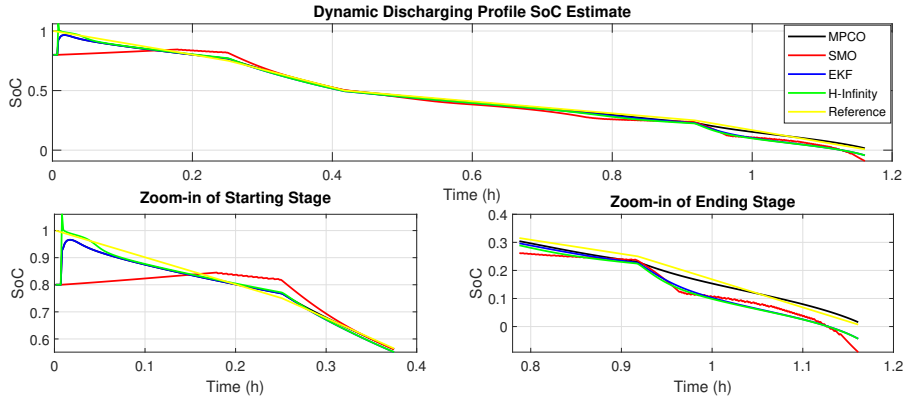


(a) SoC estimations under different filter designs

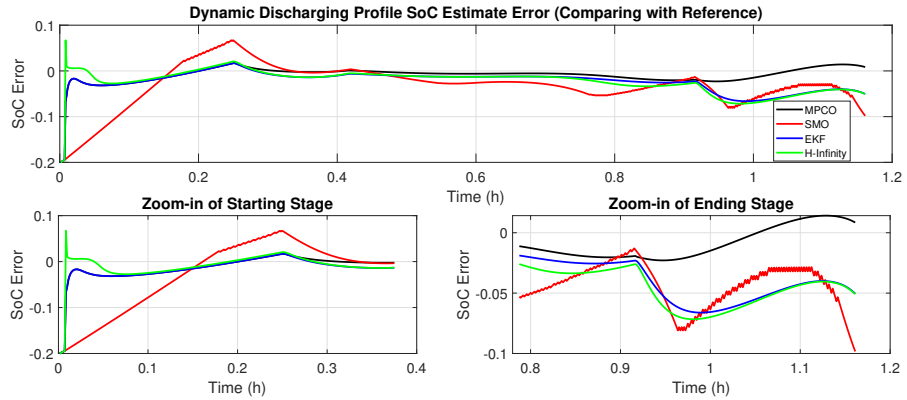


(b) Error of Soc estimation under different filter designs

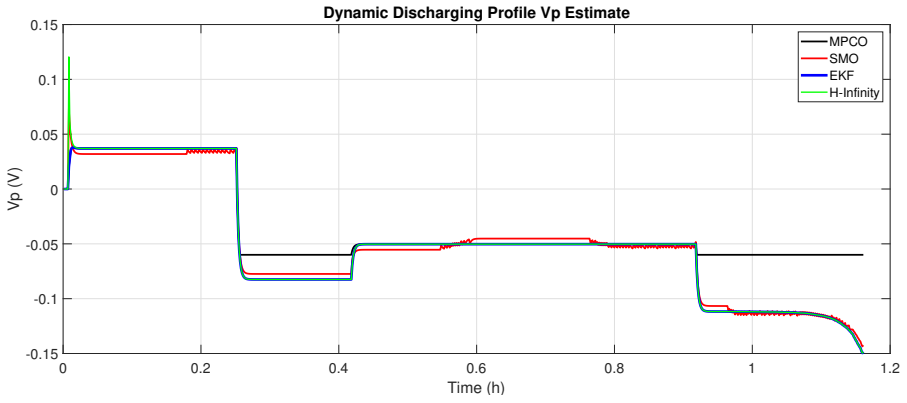


(c) Polarization voltage $V_p$ estimations under different filter designs

Figure 4.17: The state estimation results and comparisons during the dynamic pulse tests

SoC and polarization voltage $V_p$ are restricted within 0 to 1 and $\pm 0.04V$, respectively. The FUDS testing profile, given in the Fig.3.2, is loaded to the lithium battery with the erroneously initial SoC value of $-20\%$. According to the aforementioned, the length of the decision window is set as 1 to provide a short-term comparison of SoC estimation among different SoC estimators. In addition, at the early stage of FUDS tests, an artificial perturbation, $10A$ charging current lasts for $5s$, is intentionally inserted in the input current to evaluate the robustness of the proposed methods.

As shown in Fig.4.18, all the estimators attempt to attenuate the initial errors in a fast manner. As shown in the zoom-ins in Fig.4.18(a), before the artificial perturbation, the SoC estimation converge to the reference value fast. Yet, a slower convergence speed can be observed on SMO, which is in accordance with the ZNBs tests. In other words, EKF, $H-$infinity and the proposed MPCO give similar estimation accuracy and convergence speed. Afterwards, an artificial perturbation in the charging current with a pulse form of $100A$ magnitude is imposed on the input signals at $t = 1000s$. Due to the prescribed constraints on the internal states in the observer design, the proposed MPCO method outperforms among all four approaches, showing up the best performance of disturbance rejecting and robustness. We believe these phenomena are owing to the imposed estimation constraints, which limit the state estimation in a reasonable range and reduce the estimation errors. Additionally, Fig.4.18(b) reveals that SMO provides the worst performance in terms of robustness and convergence at the starting stage, in which the convergence speed can be adjusted by the prescribed value of error covariance. Typically, a large value can converge more quickly, but it will also bring ripples to the SoC estimation, losing the accuracy. However, as depicted in Fig.4.18(b) the error of SoC estimation will remarkably increase when the discharging phase is approaching the end and the terminal voltage is close to the cut-off voltage. It is because of the progressive nonlinearity of SoC-OCV table in the range of lower SoC. In this regard, the utilized first-order ECM is not able to capture the battery dynamics anymore, leading to equally poor performance of MPCO, EKF and H-infinity. However, the primary goal of MPCO to comply with the intrinsic electrochemical properties has still been achieved as

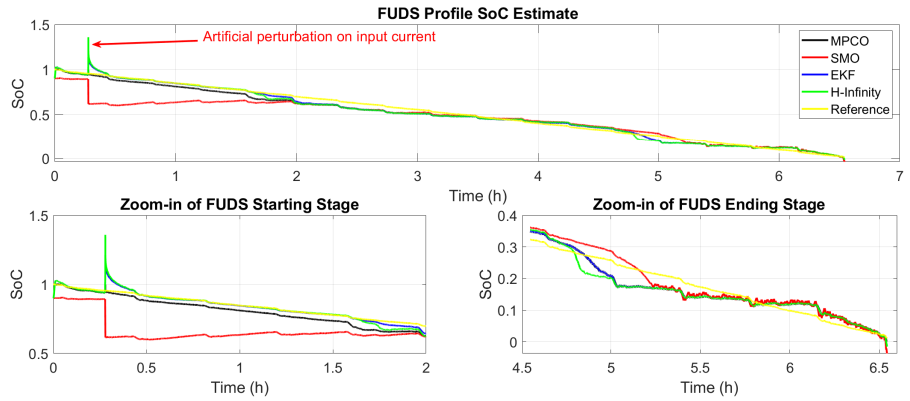


(a) SoC estimations under different filter designs

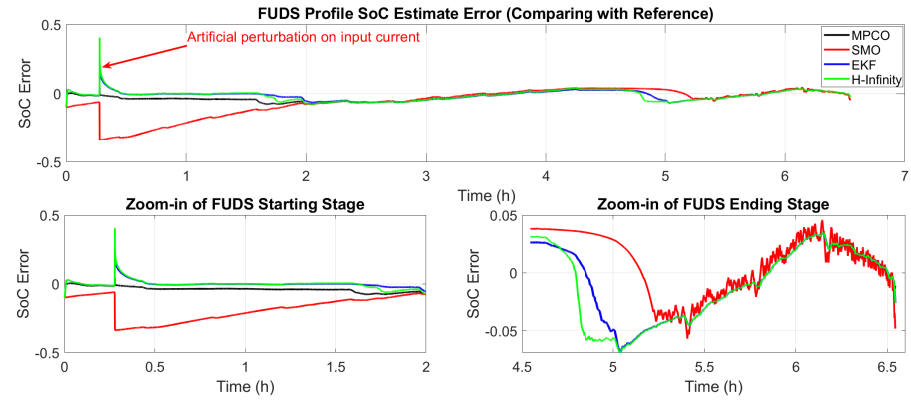


(b) Error of Soc estimation under different filter designs

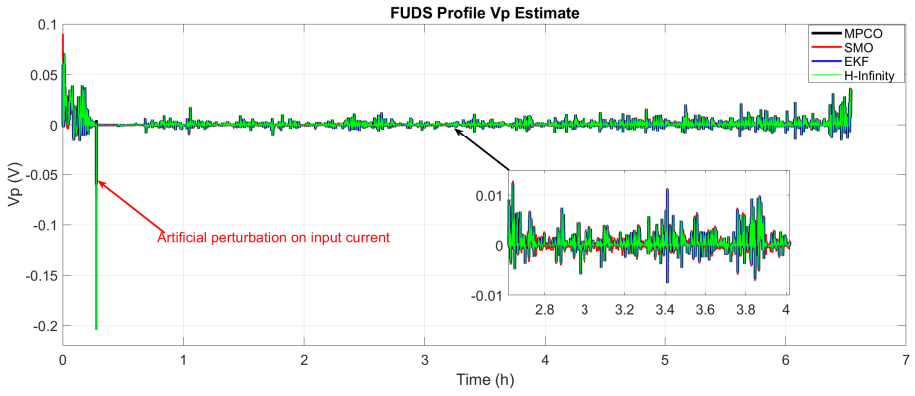


(c) Polarization voltage $V_p$ estimations under different filter designs

Figure 4.18: The state estimation results and comparisons during FUDS tests

depicted in Fig.4.18(c). Based on Eq.(4.67) and Eq.(4.68), the hard constraints are imposed on the polarization voltage and SoC. All the estimated $V_p$ are thus bounded within the empirical value $\pm 0.04V$, which pre-filters out the interference of estimation outliers, leading to more accurate estimation of $V_p$. It is worth noting that the MPCO provides potential ways to leverage the electrochemical knowledge of batteries. If more explicit constraints can be prescribed, in principle, the accuracy of SoC estimation can be increased significantly through the proposed MPCO scheme. The simulation results verify the applicability of the proposed method on other eletrochemical systems. In particular, the proposed MPCO performs competitively on the SoC estimation for lithium batteries, even more effectively in the convergence speed. Additionally, the robustness of the proposed method is stronger than other counterparts.

**Discussion**

This work develops a novel SoC estimation method, namely MPCO, inspired by the MPC mechanism. The RLS method is incorporated with a widely accepted first-order ECM for the parameter identification, which provides a simple implementation of ZNBs modelling not only to ensure the modelling accuracy and adapt to varying working conditions but also to simplify the battery model structure. Moreover, there are two major advantages of the proposed observer. Firstly, based on the inherent electrochemical knowledge, state constraints are incorporated into the estimation process, which brings more robust estimates. Secondly, an attempt in multi-window framework has demonstrated better performance in capacity estimation, which will be elaborated in the Chapter 6. Underpinned by the advantages of the proposed MPCO, this method can provide a robust and reliable SoC estimate , and then MPCO can be readily adopted for ZNBs capacity estimation as well, with a good tracking behaviour to handle the fluctuating capacity issues.

### 4.2.3 Analytical Comparisons among Different Estimators

This section provides a brief analytical comparison among the four different online SOC estimators mentioned in this paper. Firstly, consider the first-order ECM

model given in Eq.(4.73):

$$\begin{aligned} x(k) &= A_k \cdot x(k-1) + B_k \cdot u(k) + \omega_k \\ y(k) &= f(x(k), u(k)) + \nu_k \end{aligned} \tag{4.73}$$

where $x_k$ is the state variables vector, which represents $[SoC(k), V_p(k)]^T$ in previous sections, and $y_k$ is the measurement variable, which is the measured $V_t$ in the modelling process. $\omega_k$ and $\nu_k$ denote the updating error and measurement error respectively. Starting with the simplest and fastest method, namely Sliding Mode Observer (SMO), this observer updates the state vector estimate according to measurement equation by:

$$x^+(k) = x^-(k) + \begin{cases} g_1, & f(x^-(k), u(k)) > y(k) \\ g_2, & f(x^-(k), u(k)) < y(k) \end{cases}$$

where $g_1$ and $g_2$ satisfy

$$\begin{cases} g_1^T \frac{\partial f}{\partial x} < 0, & f(x, u(k)) > y(k) \\ g_2^T \frac{\partial f}{\partial x} > 0, & f(x, u(k)) < y(k) \end{cases}$$

Due to the simple structure of SMO, the advantages of SMO are obvious. It is straightforward to be utilised, and thus has the smallest computational burden. Furthermore, the updating step vector $g_1$ and $g_2$ are easy to find. On the other hand, the disadvantages of SMO are apparent as well. The most unbearable one is that the arbitrary selection for $g_1$ and $g_2$ might result in poor convergence, which has been reflected in the aforementioned simulation.

To overcome the drawbacks of SMO, the Kalman Filter/Extended Kalman Filter (EKF) acts as an advanced method which maintains the basic logic on sliding of SMO, but further introduces the covariance matrix of the state vector. The Kalman gain has secured the sliding requirements on $g_1$ and $g_2$ in SMO:

$$\begin{aligned} K_k &= P_{k|k-1} C_k^T (C_k P_{k|k-1} C_k^T + \Sigma_\nu)^{-1} \\ x^+(k) &= x^-(k) + K_k e_k = x^-(k) + g_k \\ e_k^T C_k g_k &= e_k^T C_k K_k e_k = e_k^T C_k P_{k|k-1} C_k^T (C_k P_{k|k-1} C_k^T + \Sigma_\nu)^{-1} e_k \\ &= e_k^T C_k P_{k|k-1} C_k^T e_k (C_k P_{k|k-1} C_k^T + \Sigma_\nu)^{-1} > 0 \end{aligned}$$

For one-dimensional measurement variable $y(k)$, it is easy to affirm that the above value is positive. In other words, the Kalman Filter (KF) can be viewed as choosing customized $g_k$ ($g_1$ and $g_2$ in SMO) at each time instant. The KF estimation aims at acquiring state estimate with the smallest covariance matrix, i.e. any linear combination of state variables with the smallest variance. In this way, KF, therefore, should exhibit the strongest convergence.

However, Kalman Filter also shows its limitations. The most widely argued point is the assumption that errors follow normal distributions. This priori knowledge is not applicable to most cases in the real world. In order to solve this issue, the $H-$infinity filter has been proposed, in which the problem is formulated within the engineer-nature gaming system. Comparing with Kalman Filter, the $H-$infinity filter has the following gain value and covariance matrix update:

$$\begin{aligned}
\hat{S}_k &= L_k^T S_k L_k \\
P_{k|k} &= P_{k|k-1}\left(I - \theta \hat{S}_k P_{k|k-1} + C_k^T \Sigma_\nu^{-1} C_k P_{k|k-1}\right)^{-1} \\
K_k &= P_{k|k} C_k^T \Sigma_\nu^{-1}
\end{aligned}$$

As mentioned above, KF aims to minimize the variance in the form of any linear combination of state variables. The $H-$infinity is only interested in the user-defined linear combination of state variables, i.e. $L_k x(k)$. Another difference is in user-defined parameter $\theta$. This positive value will make the covariance matrix and gain value slightly larger than in Kalman Filter, intentionally leading to a more robust result at the expense of larger covariances. In addition, it can be verified with simple algebra that when $L_k = I$ and $\theta = 0$, $H-$infinity is equivalent to Kalman Filter.

Nevertheless, all three methods discussed above cannot cope with constraints issues. The method proposed in this paper is based on MPC framework to induce constrained estimates. It can also be shown that without constraints, the performance of MPCO is equivalent to the Kalman Filter, which has further guaranteed the correctness of the rationale behind the proposed MPCO method. Besides,

MPCO is easy to understand and readily implementable.

Finally, a brief discussion on time complexity is provided. It is clear that SMO has the least computational burden, because of the simplest structure designed. The Kalman Filter is the second fastest approach. The computational complexity of $H-$infinity is slightly higher than Kalman Filter, and the method proposed in this paper is equivalent to $H-$infinity. It is noteworthy that all these four methods have linear time complexity ($O(n)$), which means they only differ by a constant scalar. This analysis has been further confirmed by Table.4.3

## 4.3 Conclusion

In this chapter, three popular battery modelling tools including the ANN battery model, Electrochemical battery model and ECM have been revisited. Among them, the ANN is straightforward for implementation and free of specific electrochemical knowledge but it is intractable for adaption to varying working conditions once the main framework has been affirmed. Therefore, due to the interference of occurred intermittent voltage peaks/jumps when cycling ZNBs, ANN-based battery modelling loses its accuracy in the cases of abnormal voltage profiles. The Electrochemical battery model uses the Partial Differential Equation (PDE) to represent the main electrochmical process taking place in the electrolyte and the surface of electrodes, which can serve as an analytic tool for the battery manufacturers and academic in electrochemical research. Though Electrochemical battery model is a white-box model which can be used for battery design, it is difficult to be used for real-time battery management. And the parameters in such a model are always identified according to the engineering experience, which weakens the accuracy and practicability of electrochemical battery modelling. Besides, the solutions of PDE are time-consuming and require the help of special solvers. ECM is commonly used in online battery modelling and the subsequent state estimations. Due to the intermittent and unpredictable voltage spikes/jumps over ZNB cycling, the online ECM identification is suitable for real time battery management. Less computing cost and more accurate SoC

estimation with desirable robustness, are the two targets achieved in this chapter. An OCV observer based SoC estimate method is proposed to reduce the computational cost due to the introduction of higher order ECMs. On the other hand, the developed MPCO can provide more accurate SoC estimate against other counterparts. The competitiveness of MPCO is demonstrated by analytical comparisons against other three the state-of-the-art SoC estimators. In this regard, the relationships of the proposed MPCO with other SoC estimators are summarized briefly. The proposed SoC estimation methods will be used for the subsequent work on peak power prediction and remaining capacity estimation to be presented in the following chapters.

# V

# PEAK POWER PREDICTION

Zinc Nickel single flow batteries (ZNBs) can be used as large scale stationary energy storage devices, connected to the renewable energy sources to improve the power quality. Due to the high variability of the intermittent renewable energy sources, load demands, and the operating conditions, the state of charge (SoC) is not an ideal indicator to gauge the potential cycling abilities of Zinc Nickel single flow batteries (ZNBs). The peak power, so-called "State of Power (SoP)" is more closely related to the instantaneous power acceptance and deliverance, and its real-time estimation plays a key role in grid-based energy storage systems. Little work has been done so far to examine the peak power delivery capability of Zinc Nickel single flow batteries (ZNBs). To bridge this gap, this chapter details the corresponding procedures of online peak power prediction techniques. In addition, the instantaneous power acceptance and deliverance of ZNBs have been discussed according to the resultant peak power predictions during the charging and discharging processes.

## 5.1 Peak Power

Underpinned by the on-line battery modelling and real-time SoC estimation methods presented in previous chapters, another objective of this thesis is to investigate the instantaneous power deliverability of ZNBs. The peak power capability is an instantaneous state relating to the loading capacity in battery applications [151; 152; 153]. It can be interpreted by the maximum remaining abilities of a battery to meet the subsequent power demands [121; 154]. Battery SoC only represents the ratio of the residual charges in a specific operating point to the capacity. Relying only on such knowledge, it is still not possible to know exactly how much power can be drawn from the battery in a specific demanding time window. When ZNBs are used as the grid-tied energy storage system, it is imperative to know its absorbing and delivering limitations at time-varying working conditions. For instance, in the renewable energy market [155], the state information of peak power will assist the system operator to regulate the amount of battery absorption/delivery power in response to the instantaneous changes in supply and demand, and to abnormal operation conditions. For instance, the information of peak power is critical to protect the battery stack when the instantly excessive generation from renewable power by wind turbines and solar panels is greater than the its accepting potential of energy storage systems. Thereby, an accurate prediction of the peak power capability is pivotal for safely and reliably operating the grid-based ZNBs energy storage systems.

The essence of peak power prediction is to render the value of the maximum power in a short-term without violating the safe operating area (SoA) [153]. Over the past decades, the hybrid pulse power characterisation tests (HPPC) are broadly adopted in the lithium batteries online tests [100]. HPPC tests at once were also considered for other electrical accumulators like all-vanadium redox flow batteries (VRBs). The research of [156] reports the temperature dependency in the peak power prediction. However, the HPPC method restrains the magnitudes of terminal voltages. The HPPC based peak power prediction is thus flawed due to the absence of constraints imposed on the SoC estimation, leading to the overoptimistic prediction at higher and lower SoC segments. In addition, the

HPPC prediction fails to consider the effects of increasing resistance at the low SoC segments. Overpredictions will be problematic for the battery operation as it may result in overcharging/discharging peoblems [157]. In contrast, the model based peak power prediction is more reliable and effective [152; 158]. With the merits of the real time model identification, the uncertainties arising from the varying conditions will be addressed easily. Hence a suitable battery model is indispensable in accurate peak power predictions.

For real time applications, the ECM models are among the most popular ones [7]. In [154] and [123], a first order ECM model is adopted to achieve accurate peak power predication in short-term prediction horizons. While, [159] and [151] improved the model by integrating the thermal model with the ECM to ensure the model fidelity and investigating the current dependency of the internal resistance, respectively. Analogously, Zhang [160] proposed an ECM model taking into account of the ion diffusion process. However, the offline model training is highly dependent on the experimental dataset and is not online adaptable. The performance can be significantly deteriorated for given unseen data. Recently, Wei et al [123] investigated the peak power prediction of VRBs. The peak power predictions are made over different prediction horizons, which is regarded as the benchmarks for RFBs. However, a common drawback of the state-of-the-art methods is that the terminal current signal applied across the predictive horizon is assumed to be a constant value. Thereby, the correlation between terminal signals in terms of current and voltage is assumed to be rigorously monotonous. The peak power prediction is thus converted to a problem of how to ascertain the peak current while the peak current is solved from a set of equality constraints. However, in reality, the terminal signals (current/voltage) are time-varying and highly dynamic.

To overcome the aforementioned drawbacks, in this chapter, the first-order ECM based state space model and the broadly accepted recursive least square (RLS) method are adopted as well to capture the battery dynamics and update the model parameters in real time. Then the SoC is estimated online by the Extended Kalman filter (EKF). With these preliminaries, the peak power predic-

tion of ZNBs is achieved online using the prediction horizon concept where the prediction of peak power is calculated in the range from $1s$ to $20s$ [161] with the assistance of the linear programming technique. In addition to the peak power, three additional indices, namely the the peak current, peak terminal voltage, and peak SoC, are designed to render the user-end comprehensive insights into the information of peak power against various prediction horizons. Finally, the additional current bounds due to the influences of material and flow rates are discussed as a supplementary discussion.

## 5.2 Online Peak Power Prediction

Motivated by the receding horizon concept in model predictive control that has been widely adopted in process industry [146; 162], a moving horizon scheme for peak power prediction is proposed in this section. This method handles the dynamics of the current and voltage within the prediction window, where the discharging and charging currents are not assumed to be constant. Similar to the MPC [162] strategy, the constraints could be explicitly formulated in the peak power prediction equations, and constraints on the terminal voltage, SoC, flow effects, and electrode material limitation can all be included. This approach can thus easily search the optimum by solving linear programming problems, whilst taking all the constraints into the optimisation process. If one variable reaches to its constraint, the discharging and charging current in the prediction horizon will be fixed. In this regard, it enables the safe operations.

### 5.2.1 SoC Online Estimation based on EKF Algorithm

Since SoC represents the ratio of the remaining charge to the nominal capacity value at a specific operating time instant, the first step to predict peak power after a specific moment is to estimate the SoC value of current time instant. The CC method is readily implementable and reliable, but it is subject to the unknown perturbations and initial deviations [124]. Additionally, the SoC-OCV look-up table is an open-loop method, in which the SoC can be read straightforward from

the inherent monotonous SoC-OCV table. Nevertheless, the pre-trained SoC-OCV table has to be calibrated periodically, due to the effects of the battery degradation. Additionally, the measurement noises and uncertainties introduced into the model are still not dealt with appropriately. In our case, as the ZNBs cycling behaviours fluctuate with the zinc deposition growth, the efficiency of the above methods may be affected by the fluctuations. As a widely accepted method, the extended Kalman filter (EKF) estimates the SoC values in a closed-loop manner and dynamically filter out the measurement noises and uncertainties introduced into the SOC estimation compared with the open-loop method. Thus in this work, the EKF is employed to estimate the SoC firstly. Based on Eq.(4.27), a two-dimensional state equation can be derived as:

$$\begin{cases} SoC(k) = SoC(k-1) - \frac{\eta \Delta t_s}{Q} I_L(k-1) \\ V_p(k) = e^{-\frac{\Delta t_s}{R_p C_p}} V_p(k-1) + \left(1 - e^{-\frac{\Delta t_s}{R_p C_p}}\right) R_p I_L(k-1) \end{cases} \tag{5.1}$$

The terminal voltage signal $V_t$ is formulated as the measurement equation:

$$V_t(k) = f(SoC(k)) - V_p(k) - R_s I_L(k) \tag{5.2}$$

where $V_{OC} = f(SoC)$, thereby, $f$ is formulated through the OCV tests [137] which correlates OCV with SoC. A standard expression of EKF is then formulated as follows:

$$\begin{cases} \mathbf{s}(k) = \mathbf{A}_k \cdot \mathbf{s}(k-1) + \boldsymbol{b}_k \cdot I_L(k-1) + \mathrm{w}(k) \\ V_t(k) = F(\mathbf{s}(k), I_L(k)) + \mathrm{v}(k) \end{cases} \tag{5.3}$$

where

$$\mathbf{s}(k) = [SoC(k) \quad V_p(k)]^T, \quad \mathbf{A}_k = \begin{bmatrix} 1 & 0 \\ 0 & e^{-\frac{\Delta t_s}{R_p C_p}} \end{bmatrix},$$

$$\boldsymbol{b}_k = \left[ -\frac{\eta \Delta t_s}{Q} \quad (1 - e^{-\frac{\Delta t_s}{R_p C_p}}) R_p \right]^T,$$

$$F(\mathbf{s}, I) = f(s_1) - s_2 - R_s I, \quad \frac{\partial F}{\partial \mathbf{s}} = [f'(s_1) \quad -1].$$

$\mathrm{w}(k)$ and $\mathrm{v}(k)$ are the process noise and the measurement noise respectively, which are assumed to be independent, zero-mean, Gaussian noise processes with covariance matrices $\sum_w$ and $\sum_v$. In this respect, the discrete-time prediction

and update equations of EKF are summarized as follows:
Prediction

$$\hat{\mathbf{s}}^{-}(k) = \mathbf{A}_k \cdot \hat{\mathbf{s}}^{+}(k-1) + \boldsymbol{b}_k \cdot I_L(k-1)$$
$$\hat{\Sigma}_{\mathbf{s}}^{-}(k) = \mathbf{A}_k \hat{\Sigma}_{\mathbf{s}}^{+}(k-1)\mathbf{A}_k^T + \Sigma_w$$

Update

$$e(k) = V_t(k) - F(\hat{\mathbf{s}}^{-}(k), I_L(k))$$
$$\mathbf{L}_k = \hat{\Sigma}_{\mathbf{s}}^{-}(k)\mathbf{H}_k^T \left[\mathbf{H}_k \hat{\Sigma}_{\mathbf{s}}^{-}(k)\mathbf{H}_k^T + \Sigma_v\right]^{-1}$$
$$\hat{\mathbf{s}}^{+}(k) = \hat{\mathbf{s}}^{-}(k) + \mathbf{L}_k \cdot e(k)$$
$$\hat{\Sigma}_{\mathbf{s}}^{+}(k) = (\mathbf{I} - \mathbf{L}_k \cdot \mathbf{H}_k)\hat{\Sigma}_{\mathbf{s}}^{-}(k)$$

Define

$$\begin{aligned} \mathbf{A}_k &= \begin{bmatrix} 1 & 0 \\ 0 & \hat{\beta} \end{bmatrix}, \\ \mathbf{H}_k &= \frac{\partial F(\mathbf{s}, I_L(k))}{\partial \mathbf{s}}|_{\mathbf{s}=\hat{\mathbf{s}}^{-}(k)} = [f'(\hat{SoC}^{-}(k)) \quad -1] \end{aligned} \tag{5.4}$$

where $\hat{\beta}$ is the identified parameter in Eq.(4.30) and Eq.(4.31), and the superscripts $^{-}$ and $^{+}$ denote the priori state update and posterior state update phases respectively. For the details of the EKF based SoC estimation adopted in this work, please refer to [131].

### 5.2.2 Battery State Space Model for Peak Power Prediction

It should be noted that in this work, the combination of first-order ECM and RLS is used to model battery dynamics and identify the model parameters in real-time. In this regard, refer to Section 4.1.3, the induced computational cost is under control but also the accuracy is a good match to ZNBs online modelling request. Due to the implicit relationship between SoC and current $I_L$, the CC method can be expressed as:

$$SoC_k = SoC_{k-1} - \frac{\eta I_L(k-1)\Delta t_s}{Q} \tag{5.5}$$

where $Q$ denotes the slowly changing battery capacity. It should be noted that the value of $Q$ is assumed to be constant within the first half of discharging and charging cycle. The coulombic efficiency $\eta$ is set as 100% for simplification. By applying the Taylor approximation to the equation of $V_{OC} = f(SoC)$, a recursive formula for $V_{OC}$ is yielded accordingly:

$$\begin{aligned} V_{OC}(k+i|k) &= f(SoC(k+i|k)) \approx V_{OC}(k) + f'(SoC(k))\,[SoC(k+i|k) - SoC(k)] \\ &= V_{OC}(k) - f'(SoC(k))\frac{\eta \Delta t_s}{Q}\sum_{j=0}^{i-1} I_L(k+j) \end{aligned} \tag{5.6}$$

Since the change of SoC depends on the slowly accumulating current effect, during the period of two consecutive sample instants, the values of $SoC(k+i|k)$ and $SoC(k)$ are very close. The above equation could then be reformulated as:

$$V_{OC}(k+i|k) = V_{OC}(k+i-1|k) - f'(SoC(k))\frac{\eta \Delta t_s}{Q} I_L(k+i-1) \tag{5.7}$$

Combined with Eq.(5.1) and Eq.(5.2), the battery model can be expressed in the state space form. Therefore, a three-dimensional predictive state equation system is formulated as follows:

$$\begin{cases} \mathbf{x}(k+i|k) = \mathbf{P}_k \cdot \mathbf{x}(k+i-1|k) + \boldsymbol{q}_k \cdot u(k+i-1) \\ y(k+i|k) = \mathbf{C}_k \cdot \mathbf{x}(k+i|k) + d_k \cdot u(k+i) \end{cases} \tag{5.8}$$

where

$$\mathbf{x}(k+i|k) = [SoC(k+i|k) \quad V_p(k+i|k) \quad V_{OC}(k+i|k)]^T,$$

$$\mathbf{P}_k = \begin{bmatrix} 1 & 0 & 0 \\ 0 & e^{-\frac{\Delta t_s}{R_p C_p}} & 0 \\ 0 & 0 & 1 \end{bmatrix}, \quad \boldsymbol{q}_k = [-\frac{\eta \Delta t_s}{Q} \quad (1 - e^{-\frac{\Delta t_s}{R_p C_p}})R_p \quad - f'(SoC(k))\frac{\eta \Delta t_s}{Q}]^T,$$

$$y(k+i|k) = V_t(k+i|k), \quad \mathbf{C}_k = [0 \quad -1 \quad 1]^T, \quad d_k = -R_s, \quad u(k+i) = I_L(k),$$

According to the rolling horizon scheme, the prediction of the state vector and input variable ($I_L$) are further denoted by $\mathbf{x}(k+i|k)$, and $u(k+i)$, respectively. Therefore, the neat expression of $\mathbf{x}(k+i|k)$ can be then derived as follows:

$$\mathbf{x}(k+i|k) = \mathbf{P}_k^i \cdot \mathbf{x}(k) + \sum_{j=0}^{i-1} \mathbf{P}_k^{i-1-j} \boldsymbol{q}_k \cdot u(k+j) \tag{5.9}$$

Impose the vector notation on the prediction state $\mathbf{x}(k+i|k)$, and Eq.(5.9) can be then expanded over a prediction window of $n$ steps:

$$\vec{\mathbf{x}}^{(n)}(k) = \begin{bmatrix} \mathbf{x}(k+1|k) \\ \mathbf{x}(k+2|k) \\ \vdots \\ \mathbf{x}(k+n|k) \end{bmatrix} = \mathbf{P}_k^{(n)} \cdot \mathbf{x}(k) + \mathbf{P}_{q,k}^{(n)} \cdot \begin{bmatrix} u(k) \\ u(k+1) \\ \vdots \\ u(k+n-1) \end{bmatrix} \tag{5.10}$$

$$= \mathbf{A}_{x,k}^{(n)} \cdot \vec{\boldsymbol{u}}^{(n)}(k) + \boldsymbol{b}_{x,k}^{(n)} \tag{5.11}$$

where

$$\mathbf{P}_k^{(n)} = \begin{bmatrix} \mathbf{P}_k \\ \mathbf{P}_k^2 \\ \vdots \\ \mathbf{P}_k^n \end{bmatrix}, \quad \mathbf{P}_{q,k}^{(n)} = \begin{bmatrix} \boldsymbol{q}_k & \mathbf{0} & \cdots & \mathbf{0} \\ \mathbf{P}_k \cdot \boldsymbol{q}_k & \boldsymbol{q}_k & \cdots & \mathbf{0} \\ \vdots & \vdots & \vdots & \vdots \\ \mathbf{P}_k^{n-1} \cdot \boldsymbol{q}_k & \mathbf{P}_k^{m-2} \cdot \boldsymbol{q}_k & \cdots & \boldsymbol{q}_k \end{bmatrix},$$

$$\vec{\boldsymbol{u}}^{(n)}(k) = \begin{bmatrix} u(k+1) \\ u(k+2) \\ \vdots \\ u(k+n) \end{bmatrix},$$

$$\mathbf{A}_{x,k}^{(n)} = \mathbf{P}_{q,k}^{(n)} \cdot \begin{bmatrix} \mathbf{0} & \mathbf{0} \\ \boldsymbol{I}_{n-1} & \mathbf{0} \end{bmatrix}, \quad \boldsymbol{b}_{x,k}^{(n)} = \mathbf{P}_k^{(n)} \cdot \mathbf{x}(k) + \mathbf{P}_{q,k}^{(n)} \cdot \begin{bmatrix} u(k) \\ 0 \\ \vdots \\ 0 \end{bmatrix}$$

Similarly, a set of $n$ ahead predictions $y(k+i|k)$ can be accordingly deduced as follows:

$$\vec{\boldsymbol{y}}^{(n)}(k) = \begin{bmatrix} y(k+1|k) \\ y(k+2|k) \\ \vdots \\ y(k+n|k) \end{bmatrix} = \begin{bmatrix} \mathbf{C}_k & \mathbf{0} & \cdots & \mathbf{0} \\ \mathbf{0} & \mathbf{C}_k & \cdots & \mathbf{0} \\ \vdots & \vdots & \vdots & \vdots \\ \mathbf{0} & \mathbf{0} & \cdots & \mathbf{C}_k \end{bmatrix} \tag{5.12}$$

$$\cdot \vec{\mathbf{x}}^{(n)}(k) + \begin{bmatrix} d_k & 0 & \cdots & 0 \\ 0 & d_k & \cdots & 0 \\ \vdots & \vdots & \vdots & \vdots \\ 0 & 0 & \cdots & d_k \end{bmatrix} \cdot \vec{\boldsymbol{u}}^{(n)}(k)$$

$$= \mathbf{A}_{y,k}^{(n)} \cdot \vec{\boldsymbol{u}}^{(n)}(k) + \boldsymbol{b}_{y,k}^{(n)} \tag{5.13}$$

where

$$\mathbf{A}_{y,k}^{(n)} = \mathrm{diag}(\mathbf{C}_k, \mathbf{C}_k, \cdots, \mathbf{C}_k) \cdot \mathbf{A}_{x,k}^{(n)} + \mathrm{diag}(d_k, d_k, \cdots, d_k),$$
$$\boldsymbol{b}_{y,k}^{(n)} = \mathrm{diag}(\mathbf{C}_k, \mathbf{C}_k, \cdots, \mathbf{C}_k) \cdot \boldsymbol{b}_{x,k}^{(n)}$$

Note that the peak power prediction horizon is often set within short-term view (in the range from $1s$ to $20s$). At an operating point, the RLS based model identification will be executed first to update the parameters. The model dynamics will be fully taken into the following prediction steps. Herein, the prediction window (prediction horizon) $n$ begins from $1s$ and ends at $20s$. The imposed constraints on the voltage, SoC and current are strictly guaranteed at each prediction step.

### 5.2.3 Moving Horizon Scheme based Optimisation

Due to the similar equation derivation and optimisation procedure for both the charging and discharging phases, only the discharging phase is selected for presentation in this section. In this regard, the average power in the prediction window is to be maximized. In the meantime, the $SoC$ and $V_t$ are confined within their particularly allowable ranges. Hence, the objective function can be further interpreted as:

$$\begin{aligned} P_{peak}^{dis} &= \max_{\vec{\boldsymbol{u}}^{(n)}(k)} \frac{1}{n} \sum_{i=1}^{n} u(k+i) y(k+i|k) = \max_{\vec{\boldsymbol{u}}^{(n)}(k)} \frac{1}{n} \vec{\boldsymbol{u}}^{(n)}(k)^T \cdot \vec{\boldsymbol{y}}^{(n)}(k) \\ &= \max_{\vec{\boldsymbol{u}}^{(n)}(k)} \vec{\boldsymbol{u}}^{(n)}(k)^T \cdot \mathbf{A}_{y,k}^{(n)} \cdot \vec{\boldsymbol{u}}^{(n)}(k) + \boldsymbol{b}_{y,k}^{(n)^T} \cdot \vec{\boldsymbol{u}}^{(n)}(k) \end{aligned} \tag{5.14}$$

Combined with constraints on the voltage, current, and SoC, the optimization problem can be stated as follows:

$$\max_{\vec{\boldsymbol{u}}^{(n)}(k)} \frac{1}{2}\vec{\boldsymbol{u}}^{(n)}(k)^T \cdot \left(\mathbf{A}_{y,k}^{(n)} + \mathbf{A}_{y,k}^{(n)^T}\right) \cdot \vec{\boldsymbol{u}}^{(n)}(k) + \boldsymbol{b}_{y,k}^{(n)^T} \cdot \vec{\boldsymbol{u}}^{(n)}(k) \tag{5.15}$$

$$s.t. \quad \begin{bmatrix} V_{t,min} \\ V_{t,min} \\ \vdots \\ V_{t,min} \end{bmatrix} \leq \vec{\boldsymbol{y}}^{(n)}(k) = \mathbf{A}_{y,k}^{(n)} \cdot \vec{\boldsymbol{u}}^{(n)}(k) + \boldsymbol{b}_{y,k}^{(n)} \leq \begin{bmatrix} V_{t,max} \\ V_{t,max} \\ \vdots \\ V_{t,max} \end{bmatrix},$$

$$\begin{bmatrix} SoC_{min} \\ SoC_{min} \\ \vdots \\ SoC_{min} \end{bmatrix} \leq \mathrm{diag}(\boldsymbol{e}_1, \boldsymbol{e}_1, \cdots, \boldsymbol{e}_1) \cdot (\mathbf{A}_{x,k}^{(n)} \cdot \vec{\boldsymbol{u}}^{(n)}(k) + \boldsymbol{b}_{x,k}^{(n)}) \leq \begin{bmatrix} SoC_{max} \\ SoC_{max} \\ \vdots \\ SoC_{max} \end{bmatrix},$$

$$\begin{bmatrix} I_{L,min} \\ I_{L,min} \\ \vdots \\ I_{L,min} \end{bmatrix} \leq \vec{\boldsymbol{u}}^{(n)}(k) \leq \begin{bmatrix} I_{L,max} \\ I_{L,max} \\ \vdots \\ I_{L,max} \end{bmatrix}$$

where $\boldsymbol{e}_1 = [1 \quad 0 \quad 0]$ is a unit vector. The above problem is a convex optimization problem, as matrix $-\left(\mathbf{A}_{y,k}^{(n)} + \mathbf{A}_{y,k}^{(n)^T}\right)$ is positive definite. Consequently, it can be solved using the quadratic programming. Once the optimal solution $\vec{\boldsymbol{u}}_{opt}^{(n)}(k)$ is obtained, the peak average power can be predicted as:

$$P_{peak}^{(n)}(k) = \frac{1}{n}\sum_{i=1}^{n} V_t(k+i|k)|_{\vec{\boldsymbol{u}}_{opt}^{(n)}(k)} \cdot u_{opt}(k+i) \tag{5.16}$$

In addition to the peak power, three plus indices encompassing the peak current, peak terminal voltage, and peak SoC are used jointly over a varying prediction horizon:

$$I_{L,peak}^{(n)}(k) = \frac{1}{n}\sum_{i=1}^{n} u_{opt}(k+i), \tag{5.17}$$

$$V_{t,peak}^{(n)}(k) = \frac{1}{n}\sum_{i=1}^{n} V_t(k+i|k)|_{\vec{\boldsymbol{u}}_{opt}^{(n)}(k)}, \tag{5.18}$$

$$SoC_{peak}^{(n)} = \frac{1}{n}\sum_{i=1}^{n} SoC(k+i|k)|_{\vec{\boldsymbol{u}}_{opt}^{(n)}(k)} \tag{5.19}$$

This above elaborated approach makes full use of the dynamic correlations between battery terminal current and voltage, while the amplitude of the future current does not have to be a constant, an assumption imposed by the existing approaches. Further, the over-optimistic and over-pessimistic predictions are avoided, rendering reliable and safe operations in the future. Compared with the existing methods, the predictions of the peak power at each instant SoC state are solved simply by the linear programming. The average peak power prediction presents the power limit in the corresponding prediction horizon, and all other peak power predictions over the relative prediction horizon can then be discounted. The computational cost of the proposed method is also competitive for online applications, in comparison with the existing methods.

## 5.3 Experimental Results and Peak Power Prediction

Based on the previous research [2; 45], a hand-made 3.7$Ah$ ZNB prototype has been tested in this study as introduced in Section 3.1. As described in Section 3.2.3 and Fig.3.2, ZNBs are cycling with the Galvanostatic regime, which is commonly adopted in the flow battery test. The testing data will be used for the RLS based model identification in real time. For the sake of comparison, the SoC trajectory is recorded by the coulomb counting method. Furthermore, the proposed methods provide the instantaneous prediction purely relying on the correlation between terminal signals e.g. current and voltage, it promises the abilities to be generalised for other batteries counterparts.

### 5.3.1 Peak Power Prediction Considering both Voltage and SoC Constraints

The loaded current and applied flow rate play an important role in shaping the behaviours of ZNBs. However, they are not only limited by the microscopic reactions on the electrodes such as the mass transfer and ion immigration but also by the selected materials due to side reactions and zinc deposition formation. For

the sake of simplification, the effects of flow rate will be decoupled from the cut-off voltage and operating SoC constraints, and it has been discussed separately in Section 5.3.2.

The ZNBs are favourable energy storage systems, which have a very high energy and power densities explained by a desirably practical range of operating voltage and SoC. In the literature [2; 45], ZNB is able to tolerate the broad scope of operating SoC (from 0 to 100%) and voltage (from $0.8V$ to $2.05V$). Imposing the voltage and SoC restraints on the ZNBs, the predicted peak power value over different prediction windows is shown in Fig.5.1. And Fig.5.2 illustrates the thorough predictions at three selected SoC states. Since the almost identical mechanism and constraints are employed for charging and discharging, in this section, only the prediction results at the discharging phase are detailed.

Four different indices in terms of the peak current, peak SoC, peak voltage and peak power are introduced to give a comprehensive assessment of the predictions over different prediction windows. Furthermore, these four indices as a whole depict the maximum power supplying capability at the different SoC states.

### Discharging Phase

Fig. 5.1 and Fig.5.2 show the dynamics of constraint variables along discharging process over different prediction windows. There are four main observations which can be inferred from these subplots:

1. **The proposed ZNBs system possesses highly desirable peak power deliverability over the entire discharging process.** As illustrated in the second subplot of Fig.5.1, for the majority of the operating time, the peak power prediction will stay at $38W$ for this small ZNB prototype ($3.7Ah$). Specifically, in the lower SoC ranges (0.17) as shown in the second subplot of Fig.5.2, the peak power deliverability still maintains over $20W$, where this observation also reveals that ZNBs are very promising energy storage systems amongst a range of defined RFBs.

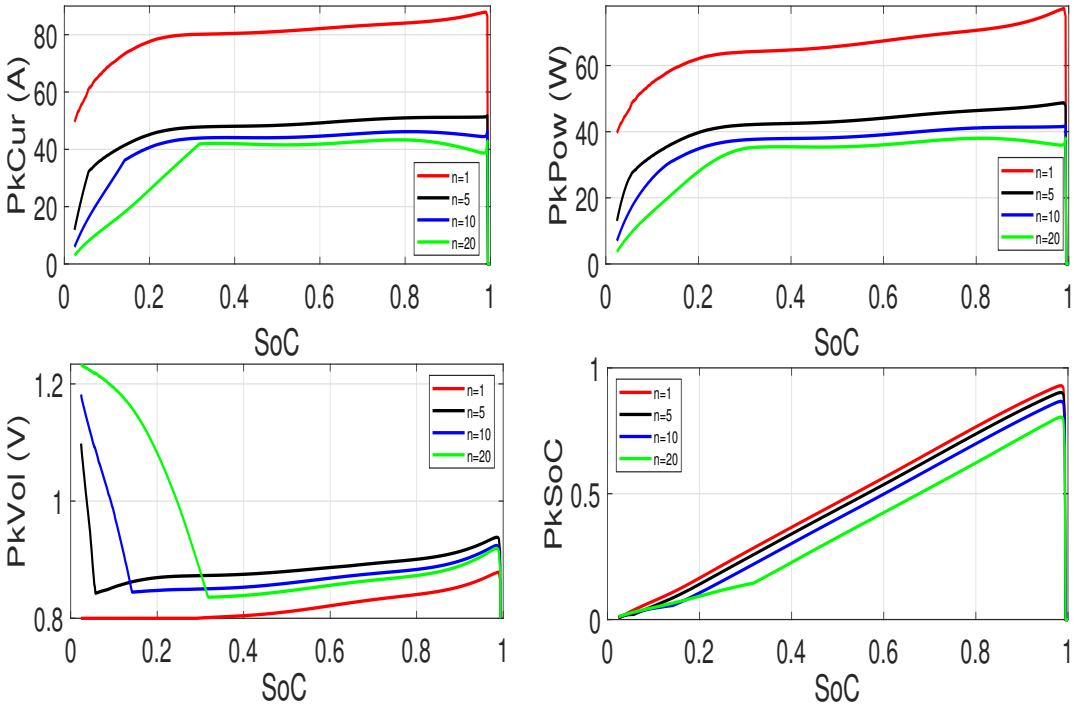


Figure 5.1: Peak power prediction along the discharging process

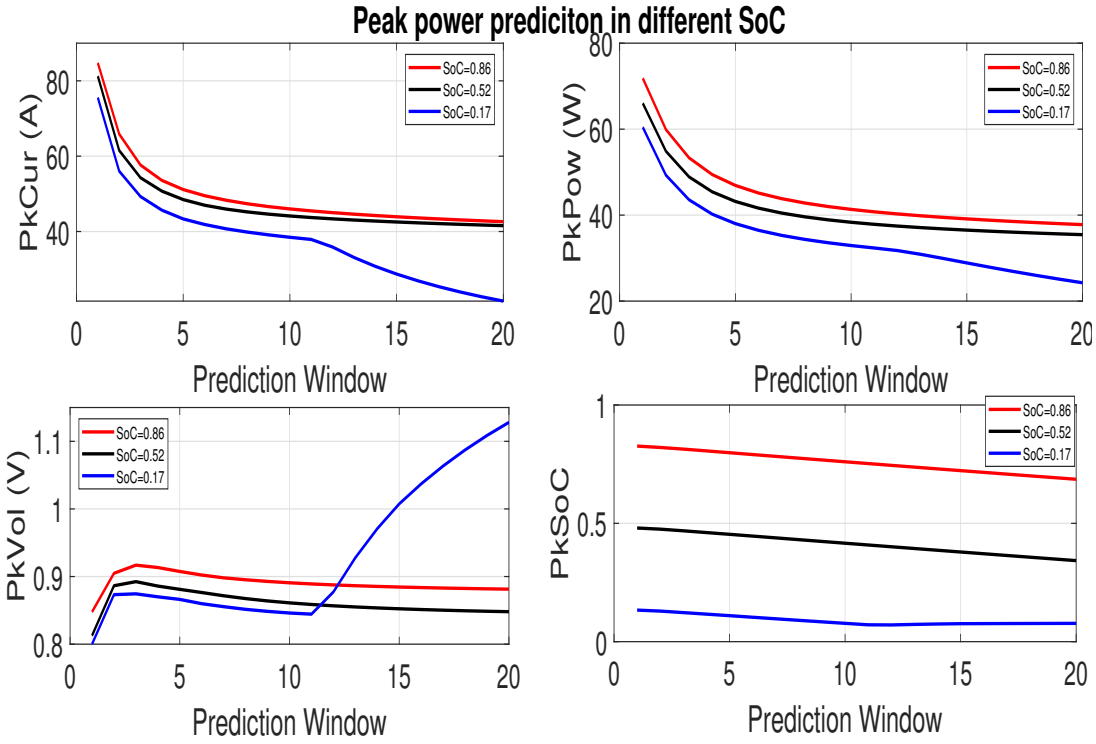


Figure 5.2: Peak power prediction against different SoC states in the discharging process

2. **The constraints on peak voltage and SoC are complementary, which alternatively affect the peak power predictions.** By inspections from the third and fourth subplots of Fig.5.1, the turn points represent the timing when the control modes are switched from cut-off voltage control to SoC control. However, it has to be noted that the cut-off voltage constraint is only applicable, when the prediction window comes to $n = 1$, because in this case the SoC constraint only considers one time step, resulting in the extremely high discharging current (depicted in the first subplot of Fig.5.1).

3. **The prediction results of the longer prediction window $n$ are very sensitive to the SoC and cut-off voltage constraints.** As shown in Fig.5.1 and Fig.5.2, the proposed four indices are sketched to illustrate the changes in prediction windows, where the predicted peak values are reduced as the length of the prediction horizon increases. The instantaneous power is greater over short prediction horizons i.e. $n \leq 5$ as illustrated in the second subplot of Fig.5.2. However, as the gradual prediction window increasing, the maximal power delivered is reduced distinctively. In addition, as shown in the first and second subplots of Fig. 5.2, except for the prediction horizon $n = 1$, similar patterns are evident for both the peak current and peak power predictions, where the cut-off voltage is the main constraint cross the whole discharging phase. The third subplot of Fig.5.2 reveals that if the length of the prediction window is short, the cut-off voltage as the major applicable constraint, will dominate the predictions cross the entire discharging process. While the fourth subplot of Fig.5.2 further details the SoC constraint is only applicable when the battery is operating at a relatively lower SoC range (17%) and that the prediction window is longer than $n = 10$.

4. **For optimal operation, ZNBs are not recommended to operate at a lower SoC range.**

The above observations show that the four indices can provide a reliable and comprehensive characterisation of the predicted power delivery capability. In addition, the proposed maximal power prediction scheme can assist with optimal

battery discharging operations. To further elaborate the adequacy of the four indices to characterise the power delivery capability at different SoC states, additional Fig. 5.3 is given to illustrate the prediction results over different prediction windows. Again, the prediction results confirm the previous observations.

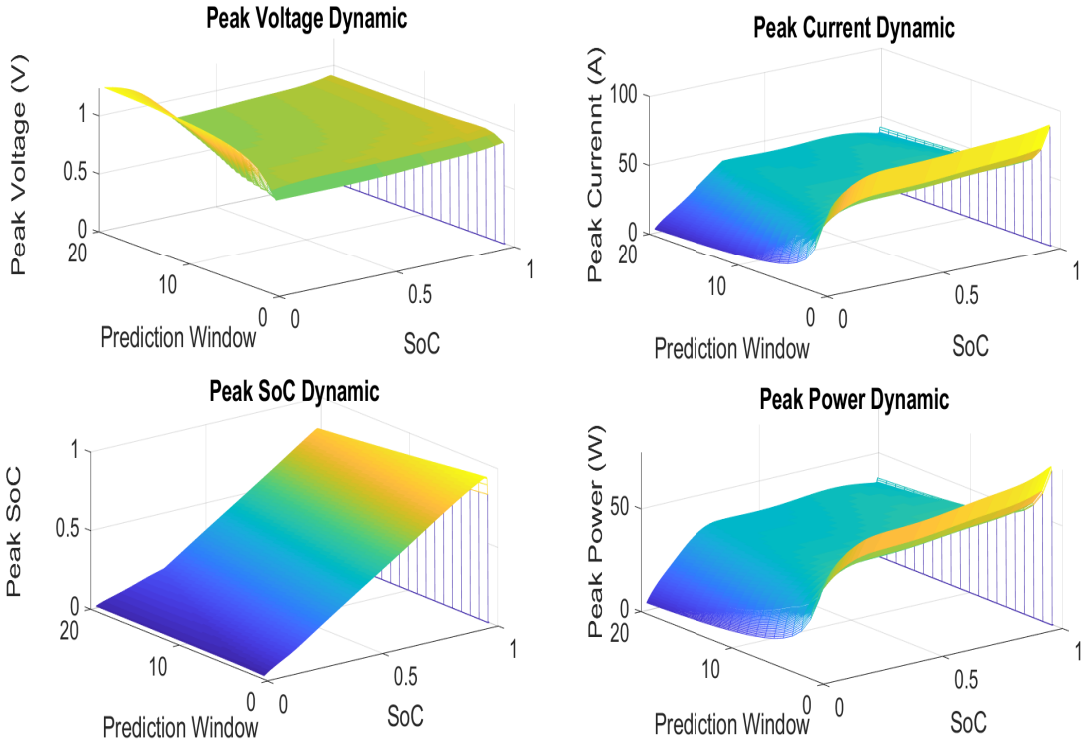


Figure 5.3: Peak power prediction dynamics in 3D view

For short prediction windows, in order to provide the maximum power delivery, the predicted peak values are subject to the discharging cut-off voltage control. As the prediction window increases, the voltage control will give way to the SoC control, and the SoC threshold starts to dominate the predictions. As a consequence, the predicted peak power is reduced and the operation moves to the voltage and SoC control modes. These observations can be interpreted by the fact that the remaining charges in the battery are gradually drawn out by the peak discharging current over a long prediction horizon. It is further revealed that the peak current drops to the normal value for the 20$s$ prediction window.

Therefore, it is meaningless to adopt longer prediction horizons ($> 20s$). On the other hand, the discharging potential decreases significantly as the SoC drops, which implies that meticulous attention should be paid to the lower SoC range for the operation safety.

Fig.5.4 presents a zoom-in view at one predicted time instant over the $20s$ prediction horizon. By using the proposed moving windows scheme, at each time instant, 20 predicted discharging current values ($I_L$) will be produced, among which the average predicted value is regarded as the peak value in the discharging process. Unlike existing approaches, the battery dynamics are taken into account in the proposed scheme in predicting the peak power capacity within an operation window. Another remarkable feature of this method is that constraints imposed on the state variables are satisfied to maintain safe battery operation. An interesting observation is drawn from the results is that most of the predicted values of discharge currents are identical as shown in first subplot which agrees with the results obtained by other approaches presented in the literature. For different SoC states (0.86 and 0.17), it is seen inspected that a larger SoC renders a broader operating potential as revealed by the higher peak values of the four indices. While for a lower SoC state, the SoC constraint easily affects the battery operating potentials as shown in the fourth subplot and that all the four indices are reduced significantly.

### Charging Phase

The proposed approach is also applied to the charging process, and the prediction results are briefly illustrated in Fig.5.5 and 5.6. Similarly, the cut-off voltage prevails in most cases, except for a longer prediction window and larger SoC states. When the prediction window >= 5, it is apparent that the value of predicted peak current decreases, resulting in drops in the predicted power. However, as the prediction horizon further increases, the predicted values are almost similar. At the beginning of the charging phase, due to lower SoC values, similar to the discharging phase discussion, the voltage constraints prevail as reflected in all the predicted values. As the charging proceeds, the effective constraints have

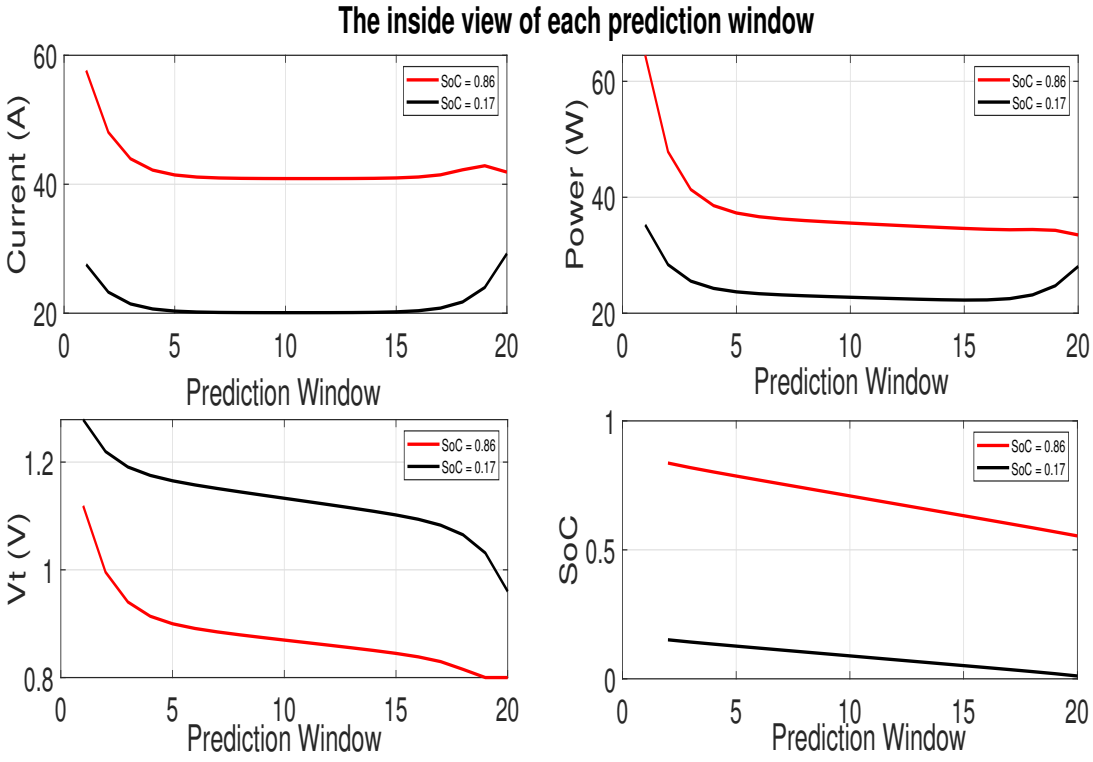


Figure 5.4: The inside view of each prediction window

been shifted from the voltage control to both the voltage and SoC controls. On the other hand, for long prediction windows, the instantaneous charging abilities are weakened. At the end of charging phase, the SoC control completely replace the voltage control, as shown in the fourth subplot of Fig.5.6. Therefore, it is essential to avoid overcharging at the end of the charging phase.

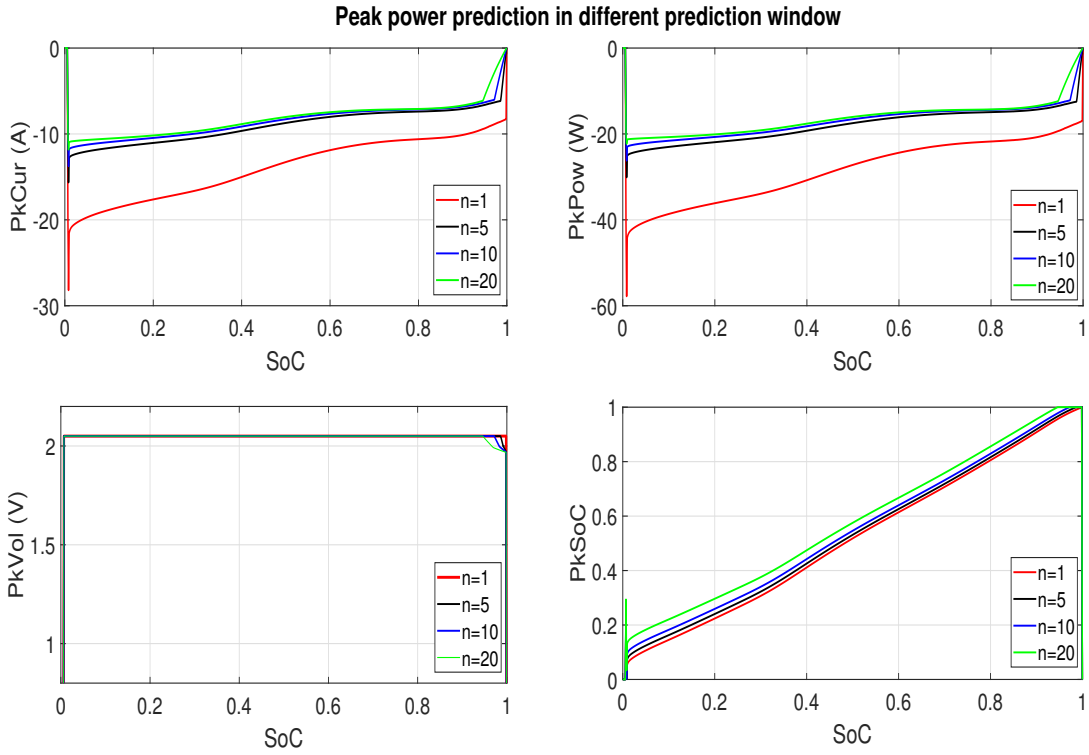


Figure 5.5: Peak power prediction along the charging process

### 5.3.2 Discussions on the Current and Flow Rate Constraints

#### Current Constraint

The used materials and the structure of ZNBs are two major limiting factors for applied current density on the surface of electrodes, thus the magnitude limit of the imposed current of the battery stack. Existing work reveals that the battery

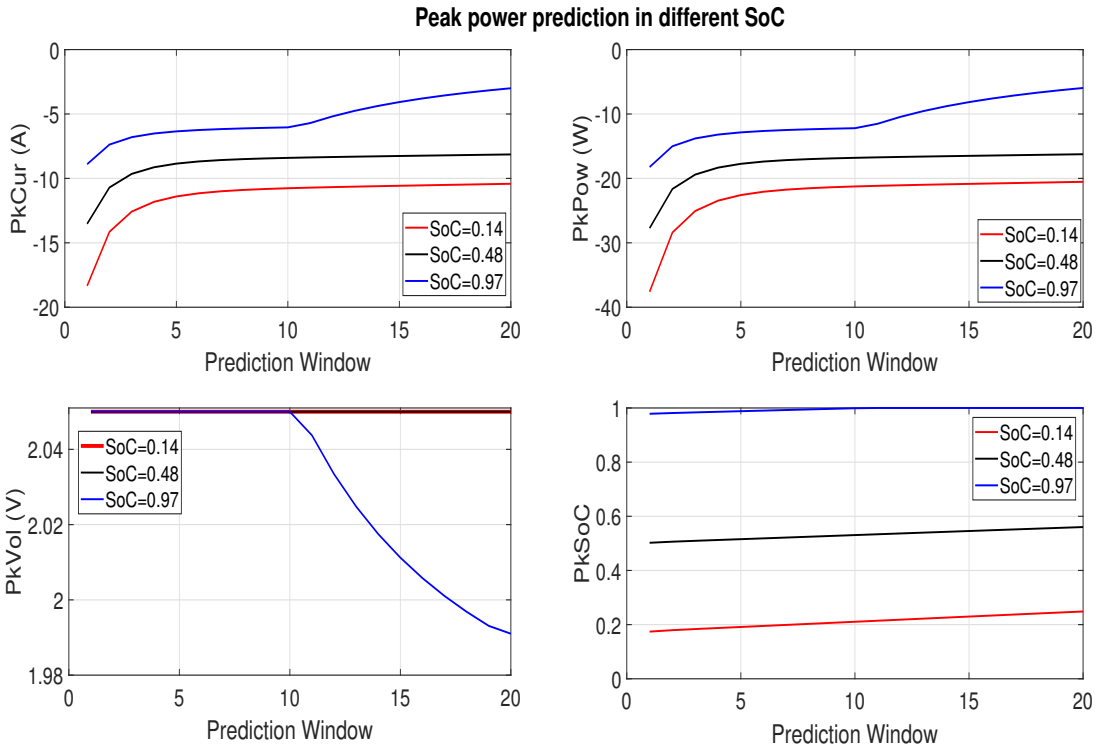


Figure 5.6: Peak power prediction in different SoC states in the charging process

performance is bounded by the nonuniform zinc deposition and the oxygen evolution [49]. These side effects become more serious under higher applied current densities. Therefore, ZNBs have to be operated at low current densities (below $20mA/cm^2$ ) [45] in the past, which is not acceptable in the real applications. Much of the work that has been done so far in the literature mainly focuses on the development of new materials for the battery, and a continuous charge-discharge cycle test at $80mA/cm^2$ operating current density on a new material design shows that the average coulombic efficiency (CE) stays at 96% [163]. Similar promising results are also reported in other published work. The latest $Ni-3D\ Zn$ configuration [54; 97] has demonstrated fourfold increase in the applied current density, and the cost can be significantly reduced. Note that popular materials in RBFs used in existing batteries, including the one used in this study, are still not optimally designed. Given these considerations, only approximated current constraints are imposed in this study, for a bench-marking reference. Once the accurate constraints are confirmed, it can be readily integrated into Eq.(5.15) according to the proposed algorithms. The detailed analysis is presented below for the ZNBs.

In this work, the $N_iOOH$ sheets (positive electrode) and the stainless steels sheets (negative electrode) are stacked in parallel. Then, all the electrodes are machined into $7cm*7cm$ size. If the applied current density is set up as $80mA/cm^2$, the loaded current thresholds is then calculated as $80mA/cm^2*7cm*7cm*7 = 27.440A$, in which 7 individual cells are stacked in parallel. As illustrated in the second subplot of Fig.5.7, the predicted peak current is irrelevant to the current constraints in the charging phase, implying that in the charging phase, other constraints prevail over the acceptable bounds for the charging current.

On the other hand, in the discharging phase, the first subplot reveals that the situation is reversed. With the exception for small SoC ranges (between 0 to 0.2) over longer prediction horizons, other predicted peak current will be constrained by the material-determined current threshold $27.440A$. This implies that the state-of-the-art electrode materials are though far from the optimum, which is the main challenge of ZNBs. Nevertheless, even with this limitation,

when compared with other RFBs, ZNBs still exhibit the highest instantaneous discharging peak power due to the relatively lower cut-off voltage (0.8V). As new materials are introduced, the material-determined current threshold 27.440 can be further relaxed.

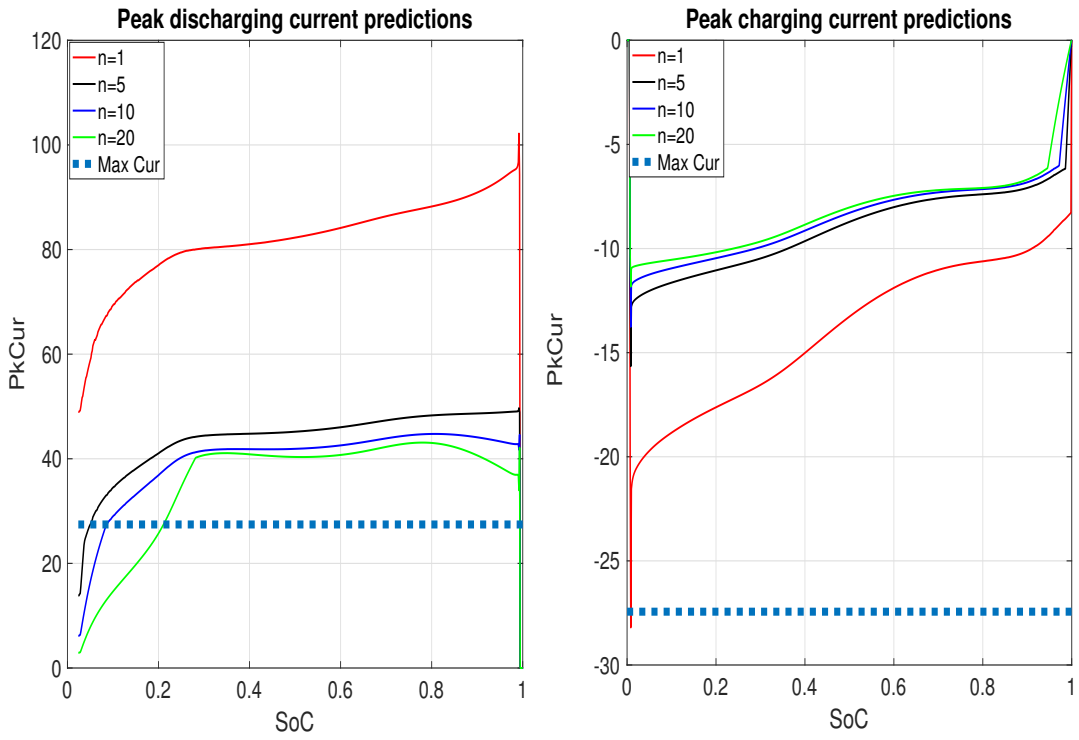


Figure 5.7: Predicted peak current considering material limits

### Flow Rate Constraint

The electrolyte in ZNBs will take away the generated heat and moderate the thermal influence on the battery operations. The introduction of the flowing assisted system also helps to attenuate the dendrite formation [2; 45; 164]. As a consequence, the entire lifespan of ZNBs can meet the acceptable industry requirement. Therefore, the flow rate has a significant impact on the ZNB operation efficiency.

To achieve compact zinc deposition, the flowing velocity on the surface of electrodes should be sufficiently big to achieve steady convection control for the immigration reaction. The forced convection of the electrolyte close to the working electrodes will generate a constant thickness of the diffusion layer $\delta_N$. Two widely accepted assumptions are taken into the consideration [93]:

* **Flow direction.** The flow direction is ideally in parallel to the electrode plates and perpendicular to the diffusion direction of the reactive ion.

* **Laminated distribution.** The laminar flow of the electrolyte is assumed. As the presentation of friction, the flow velocity near the electrodes is zero. While the velocity maintains at the steady velocity $u_0$ far from the electrodes ($> \delta_{Pr}$).

Given the above assumptions, for the steady convection control of the reaction, the thickness of the diffusion layer $\delta_N$ can be formulated as [93]:

$$\delta_N \approx D^{1/3}\nu^{1/6}y^{1/2}u_0^{-1/2} \tag{5.20}$$

where $D$, $y$ and $\nu$ are the diffusion constant, length of the plate, and viscosity coefficient of the supporting electrolyte ($10Mol \quad KOH + 1Mol \quad ZnO$), respectively. Therefore, the maximal tolerant current densities $I_{lim}$ at a certain flowing velocity $u_0$ can be derived reversely:

$$I_{lim} = nFD\frac{c_0}{\delta_N} \approx nFD^{2/3}\nu^{-1/6}y^{-1/2}u_0^{-1/2}c_0 \tag{5.21}$$

where $n$ is relative to the redox reaction for a given amount number of participated electrons. $c_0$ stands for the time-varying bulk concentration of zinc. $F$ and $\delta_{Pr}$ represent the Faraday equation, namely the Faraday's constant and the thickness of Prandt's boundary layer, respectively. In a normal charging/discharging cycling, the concentration of zinc will be replenished or consumed with the progress of the redox reactions. As a consequent, the bulk concentration of zinc is SoC dependent variable and can be represented on the form:

$$c_0 = c_i - \frac{SOC(\%) \times C_{bat}(Ah) \times 3600}{nF \times V} \tag{5.22}$$

where $V$ is the total volume of the electrolyte, and $C_{bat}$ is the rated capacity of the battery. While $c_i$ represents the initial zinc concentration.

Theoretically, the applied current densities are bounded by the flow rate and other inherent aspects as interpreted by Eq.(5.21). In this work, the flow rate is large enough to eliminate the side influences. Note that in real applications, due to superbly high concentration of electrolytes applied, the subtle fluctuations of the concentration caused by the redox reaction is negligible. Throughout the entire discharging and charging phases, the zinc concentration is varied slightly, rather stable. Thereby, the magnitude of the limited current densities $I_{lim}$ is relative stable during the reactions. Due to Eq.(5.21) and Eq.(5.22), the similar assumptions have also been applied to the analysis of other RBFs, and in this work, the current constraints incurred by the flow rate can be ignored in ZNBs.

## 5.4 Conclusion

This chapter solves an engineering issue through presenting a novel peak power prediction approach for the Zinc Nickel single flow batteries. The proposed differential calculations in Chapter 4 are used for RLS based real-time model identification to acquire an accurate battery model, thus the uncertainties incurred by different operating conditions can be addressed in real time. Then an EKF based SoC estimator is employed to acquire precise estimation which is verified in the experiments. With these preliminaries, a window-based peak power prediction framework is proposed which guarantees that the dynamics of current and voltage across the entire prediction windows are fully taken into the considerations. The proposed framework is capable of incorporating all the constraints on the current, voltage, and SoC. Experimental results confirm the effectiveness of the proposed scheme. Further, four indices are derived to assess the power delivery/absorption capabilities of ZNBs while operation constraints are guaranteed. The influences of the used material and flow rate on the peak power predictions are analysed qualitatively, providing a bench-marking paradigm in the RFBs research.

# VI

# BATTERY HEALTH AND MAINTENANCE

So far, grid-scale Zinc Nickel flow batteries have been tested at both Energy Institute of the City College of New York and some Chinese companies such as Zhangjiagang Smart Grid Fanghua Electrical Energy Storage Research Institute Co. limited. They have claimed either the current efficiency or the energy efficiency is desirable. Nevertheless, the cyclability of this system is rather poor, which is hindered by the zinc dendrite build-up and zinc morphology variation over time. In order to handle the poor cyclability issue, the monitoring and evaluation of battery health are indispensable. A periodic maintenance to recondition the cell can strip off the whole deposited zinc from the anode by deep discharging the battery, and then the cell can be operated afresh. In this chapter, following Chapter 4, the state-of-the-art capacity estimation methods along with a novel model predictive control scheme based SoC observer are presented to obtain more accurate capacity estimation online. On the other hand, the induced computing complexity when applying higher order ECMs has been offset by another introduced OCV observer, thus achieving faster capacity estimation. We have found that the capacity degradation of zinc-nickel flow cell can be correlated with zinc deposition characteristics. From this perspective, we first attempt to determine the reconditioning moment for cell maintenance of ZNBs.

## 6.1 Battery Health

The cell health so-called the State of Health (SoH) is an indicator to represent the life condition. In general, SoH describes the remaining deliverability of the specified performance against to a fresh cell. SoH is a long-term, composite index rather than an absolute measurement that considers many battery factors such as the remaining acceptance of charges, the growth of internal resistance, the releasable capacity, terminal voltage distortion, etc. Through the SoH measurement, users can have the basic insights into the left lifetime of the cell. At this point, SoH can also serve as an indicator to conduct the cells maintenance and replacement. During the use-time of a battery, its health is getting deteriorated inevitably due to the changes in internal physics and chemistry. Different kinds of batteries are thus sensitive to different features. In other words, SoH is a subjective measurement varied in different battery applications and it cannot be measured directly like SoC. For example, the cyclability and deliverability play important roles when it comes to EV. Thereby, the remaining capacity always appears to come to the limitation firstly. The SoH is thus derived from the comparison between current capacity and the rated capacity. On the other hand, for the heavy load hybrid electric vehicle (HEV), in order to deliver the as largest as possible specified power, the current flow is much high. Hence even a small increase of the direct current (DC) resistance will lead to a significant heat generation, which may lead to disastrous outcomes. The SoH in this scenario needs to consider the battery resistance growth. In most cases, SoH is calculated from as ratio between current DC resistance and its initial value.

As mentioned earlier, the upscale of ZNBs has been hindered by the well-known zinc deposition problem [2; 165; 166]. It is difficult to judge the SoH of a flow based ZNB, because the morphological variations of zinc depositions lead to the fluctuations in capacity and drops in life cycle. The reactions happen in zinc anode should mainly be responsible for the poor cyclability [49; 165]. Zinc depositions in alkaline media can happen at different $pH$ levels [68]. In low alkalinity zinc reacts with the electrolyte to form solid zinc hydroxides. These hydroxides can further alter to zinc oxide, which is highly insoluble. At a higher $pH$ value,

zinc can dissolve to form zincates, resulting in a form of over-saturated zinc oxide solution. The latter is favourable, because it reduces the anode potential [2; 68]. But in such a high $pH$ solution, nonuniform deposition of zinc at the anode limits the cyclability of zinc-nickel battery. Specifically, at high current densities, zincate tends to form a sponge-like deposition, which can lead to dendrite formation. If the cell is cycling with such a poor condition, micro shortages will occur inside of the battery, resulting in lifetime drops tremendously [49; 167; 168]. The problems of dendrite build-up can partially be circumvented by forcing the flows of electrolyte. The first communication [2; 45] has demonstrated the flowing electrolyte is able to achieve significant improvements of the life cycles [51], while suppressing both dendrite formation and morphological variation. That is the main reason why such a kind of flow based ZNB has gained more and more attentions. However, the capacity of flow based ZNBs have not yet ever stable during the cycling process. It is interesting to note that the zinc nickel redox flow cell has the advantage, that in case of sponge-like or dendritic zinc deposition, the battery can be reconditioned by the so-called "stripping cycles" [169]. After the strip cycle, the entire deposited zinc will be stripped from the anode by deep discharging. If all zinc is dissolved, the zinc deposition can be started anew. In this way, favorable service life is achievable. However, the stripping cycles have renew the cell capacity. In other words, the SoH may be refreshed to the initial again [49]. The above processes lead to a difficulty in SoH estimation of ZNBs. According to the previous research on the zinc reaction, the capacity estimation can be assumed that is the key element in the health evaluation of ZNBs. On the other hand, since performing the battery maintenance in time can recondition the cell health, it is important to determine the reconditioning time to secure the cell in a good healthy status.

Besides, the battery internal resistance is a crucial feature to the SoH evaluation. In general, the gradually increased resistance reflects the degree of the ageing state and the growth of zinc dendrite. However, as given in Fig.6.1, the estimation of internal resistance $R_s$ exhibits a consistent trend. $R_s$ starts with the value of $0.02\Omega$ and maintains around $0.04\Omega$ at the end of discharging. The increased internal resistance is foreseeable, where the reaction product with poor

conductance is generated at the end of discharging phase [2]. Whereas, as less as 0.02Ω changes in resistance can be observed during one cycle, this phenomenon signifies the fact that the health of ZNBs is resistance insensitive. Higher internal resistance occurs when SoC become lower than 20%, which implies the optimal working range should be above 20% SoC, in order to improve the operating efficiency of the ZNBs. As ZNBs are connected in bulk to supply as much as possible electricity for the grid-based utilization, working ranges of ZNBs are routinely limited within its optimum. Therefore, the growth of internal resistance is illegible. In other words, the capacity should be regarded as an important feature to evaluate the battery health. Hence in the following sections, the capacity has been selected as the measurement of ZNBs healthy status.

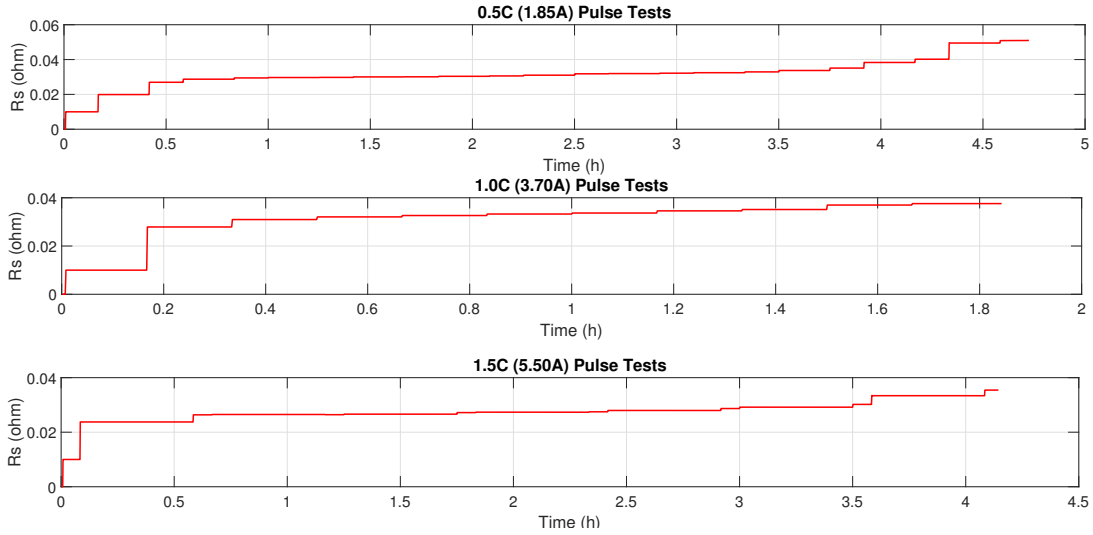


Figure 6.1: DC Internal resistance ($R_s$) estimation in pulse tests

## 6.2 Capacity Estimation

The accurate diagnosis of capacity degradation is indispensable to safety and efficiently manage ZNBs. As stated above, capacity is a reliable index to describe the SoH of ZNBs rather than others. There are many studies and discussion on how to evaluate the health status of batteries based on the capacity estimate [124; 133;

170; 171; 172; 173; 174; 175; 176; 177; 178; 179; 180; 181; 182; 183], which can be roughly categorised as three groups. Model-based methods dominate most of the corresponding research [124; 133; 170; 171; 172], in which the ECM is employed to first estimate the SoC and then the capacity can be derived as the inverse of Colombo counting methods. In this regard, the related preliminaries and detail work have been described in Section 6.2.4. On the other hand, learning based approaches have been used to estimate the capacity by features extraction from the current and voltage profiles [173; 174; 175; 176; 177; 178; 179; 180; 181; 182; 183]. These methods are able to represent the nonlinear relationship between the extracted features and capacities. For example, in [178], realistic profiles including the driving schedule, internal resistance, polarization resistance, terminal signals and voltage variation have been trained by least squares support vector (LSSV) to gain the capacity estimation. Nevertheless, in order to obtain measurements in bulk, thousands of cycles are conducted in lithium-ion batteries, which is impractical for ZNBs operation. Additionally, the growth of dendrite does not possess the empirically statistical characteristics, which means the terminal signals may be influenced by the residual zinc depositions to exhibit weak characteristics in statistics. It is foreseeable that the learning based approaches are unsuitable for the capacity estimate of ZNBs. The third group is regarded as a fast capacity estimation method based on the incremental capacity analysis (ICA) / differential voltage analysis (DVA). This group has been used to sort the voltage data and split the SoC into pieces of narrow intervals firstly. And then, different regression models according to the sorted SoC narrow intervals will give the capacity estimation in a fast action [179; 180]. The related work has been investigated in Section 6.2.1, Section 6.2.2, and Section 6.2.3.

In this Chapter, two popular methods have been used for ZNBs capacity estimation. One method depends the calculations from the differential voltage and differential capacity, namely incremental capacity analysis (ICA) and differential voltage analysis (DVA). The other is on the basis of the real-time battery modelling and SoC estimation techniques. Followed-on, a novel model predictive control scheme based observer (MPCO) and a newly developed OCV observer are used to evaluate and update the cell capacity in real-time.

### 6.2.1 Incremental Capacity Analysis (ICA)

The ICA method can be used in both battery degradation identification and the SoH estimation with less computational cost. In principle, ICA is an ideal tool to accommodate in different types of batteries by just reading terminal voltages and capacity [184]. In this regard, the measurements are used directly without the requirement of a battery model. ICA approach is easy to understand and thus readily to be implemented in the real-time applications. Incremental Capacity (IC) value can be calculated by differentiating the subtle changes in battery capacity to the corresponding terminal voltage changes as follows [185]:

$$\frac{dQ}{dV} = \frac{\Delta Q}{\Delta V} = \frac{Q_t - Q_{t-1}}{V_t - V_{t-1}} \tag{6.1}$$

where $Q_t$ and $V_t$ stand for the capacity value and terminal voltage at $t$ instant. ICA is able to be employed in either charging phase or discharging phase. When applying ICA, different voltage patterns on the voltage curve will be translated as the electrochemical information [186]. In particular, the existing voltage flat plateau will be transformed into a couple of identifiable peak/valley points and illustrated in the newly calculated IC plot [187]. During the cell internal redox reactions, the flat potential plateau means local coordination of transition metal ions remains unchanged. Once there is a phase transition or change in oxidation state, potential changes abruptly. For lithium ion batteries, the potential plateau appears at the point where charging or discharging leads to formation of a new phase on one of the electrodes. The potential will remain the same as long as both initial and final phase exist on the electrode. If charging goes through formation of the non-stoichiometric compound and gradual change of its composition, the voltage will also gradually change with SoC. Therefore, the degradation modes and different reaction stages can be easily identified by the plotted IC curve. In addition, the peak/valley points on the IC curve signify the on-going ion transportation along with the reaction time scale (SoC), which means each peak/valley represents a unique electrochemical process taking place inside the cell [188]. Thereby, the variations of peaks/valleys position and intensity imply the corresponding electrochemical processes occur in advance or are

postponed, which is closely related to the battery capacity fading and can be used to identify the degrees of discharging and charging processes [186; 187]. Normally, after plotting the IC curve, a simple regression model [189] can be established by the peaks/valleys distribution to fast estimate the capacity at specific SoC stages.

According to the previous research [179; 182; 190; 191] on the differential analysis, ICA has been demonstrated as an effective tool to fast evaluate the capacity online. Two stages related capacity fading modes have been found in [190; 191] though the analysis of IC curve, in which the loss of anode and cathode materials are the main culprits. In [179], ICA has been used incorporating with the support vector regression to estimate the battery capacity on-broad through a partial charging data. The results have revealed the intensity of peaks/valleys in IC curve can be correlated with the capacity loss. Though ICA is promising, two main drawbacks of ICA obstruct its implementation. One is that the requirement of static charging and discharging voltage-capacity profiles [181]. In order to track of the corresponding electrochemical processes, the loaded current stress not only should be limited but also the current is always constant, which is problematic and unrealistic in the most EV/HEV based applications. The other problem is that the differential analysis is very sensitive to the measurement noise and trembling [189]. To transfer the voltage-capacity information into IC curve, the method is intuitive as is applies numerical derivation on the raw data directly. In this regard, the IC curve will be definitely polluted by noises so that the peak and valley points may be overwhelmed in the noise spikes.

On the other hand, when operating ZNB, additional trouble has been raised. As mentioned in Section 1.1.3, the residual zinc depositions on the negative electrodes will lead to capacity fluctuation and unpredictable sudden voltage jumps as depicted in Fig.6.3(a). Since ZNBs are routinely installed with the renewable energy sources as the stationary energy storage, the cycling regime is moderate to satisfy the static charging and discharging requirements. The challenges relating to noise pollution and voltage jumps remain as the targets of this work. In the following sections, we thus mainly focus on addressing the smoothing problem

and eliminating the voltage jumps.

Fig.6.2 and Fig.6.3 take two discharging patterns into discussion, where the raw voltage-capacity data were collected from normal discharging cycle 16 without voltage jump issue and abnormal discharging cycle 23 with a sudden voltage jump, respectively. In order to smooth the IC curve, the moving average (MA) [192] is used to remove measurement noises from the numerical derivative on the raw data but preserve the useful information. In this work, the sliding horizon is denoted as $k$, where the cases of $k = 20, 40, 60, 80$ and 100 are compared. It should be noted that the applied MA is a simple filtering technique and thus the unweighted mean of the both sides of central data is used to filter out the noises. This function guarantees that variations in the mean are in line with the variations in the data rather than being shifted. Afterwards, the median filter (MF) is expected to offset the intermittent voltage jump influences [193]. Fig.6.2(a) gives an example of the IC curve achieved directly by the numerical derivative method, where the time interval $\Delta = 5s$. The results are foreseeable, the IC curve has been polluted by the noises largely. It seems only one voltage valley can be observed, but it is impossible to identify its position due to the noises pollution. Fig.6.2(b) and Fig.6.3(b) present the smoothed results in different horizons after individually applying MA and MF. As the length of horizon is increased, the pattern of IC curve is getting clear. However, the improved smoothing effect may lead to a deformation of obtained IC curve and thus resulting in false interpretation of features on the IC curve. As given in Fig.6.2(b), when the $k > 80$, the noises have been limited into acceptable levels. After applying $k = 100$, a smoother IC curve is achieved without information loss. Considering the computational cost, when applying MA filter, $k = 100$ is appropriate for smoothing IC curve in our case. On the other hand, in the comparison between Fig.6.2(b) and Fig.6.2(c), MF is able to attenuate the influence of the low frequency impulse noises on the IC curve.

Whereas, when it comes to the abnormal cycle with a sudden voltage jump, as illustrated in Fig.6.3, using the horizon $k = 100$, MA is efficient to handle most high frequency noises as previous one. In Fig.6.3(c), MF is then introduced on the sets of pre-filtered data by MA, to yield enhanced smoothing effect. In such

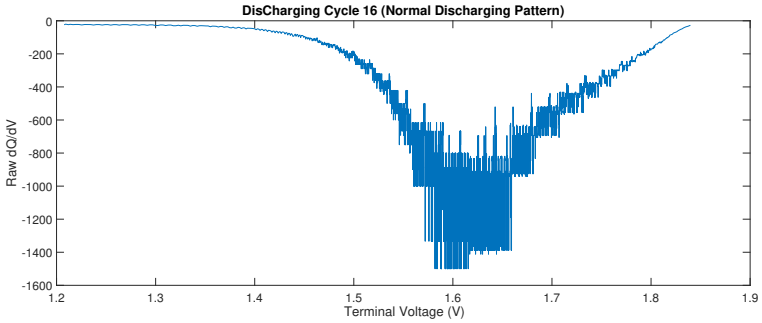


(a) without applying Moving Average

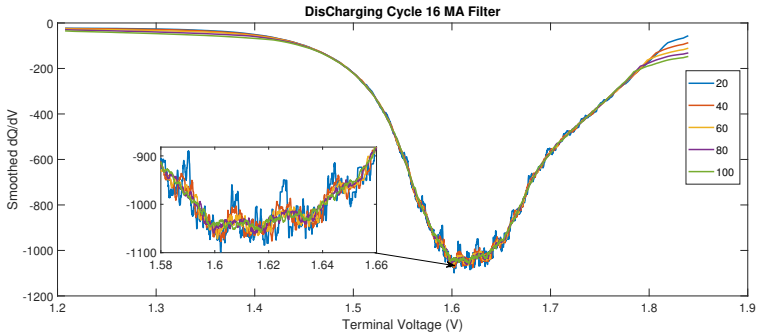


(b) after applying Moving Average (MA) Smoother

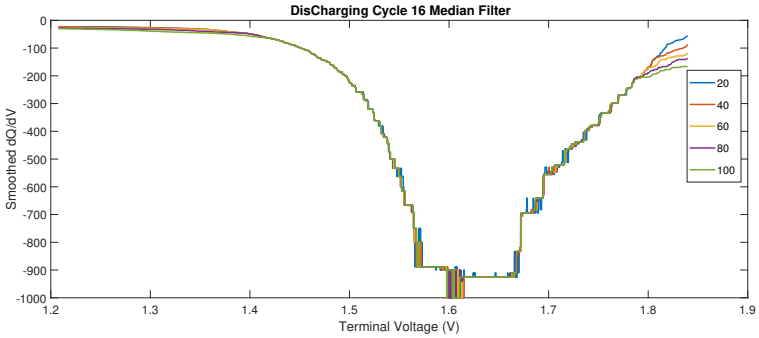


(c) after applying Median Filter (MF)

Figure 6.2: An example of normal discharging pattern: IC discharging curve(s) of 200Ah pilot-scale ZNBs under current rate of $0.25C$ with sampling rate of $1s$ (a) without applying Moving Average (MA) Smoother (b) after applying average smoothing methods with different horizons of 20, 40, 60, 80, and 100 (c) after applying Median Filter (MF) to cancel the influences on measurement error spikes.

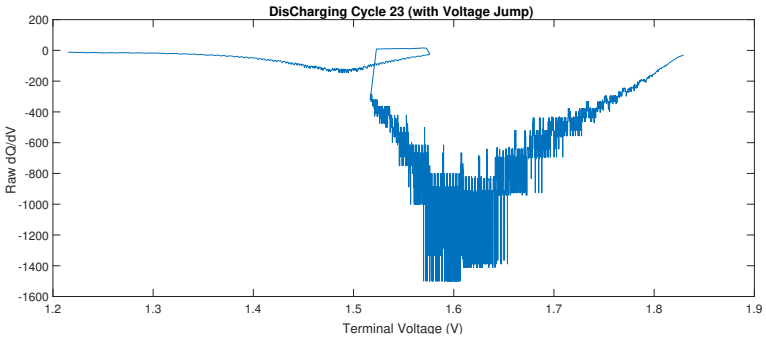


(a) without applying Moving Average

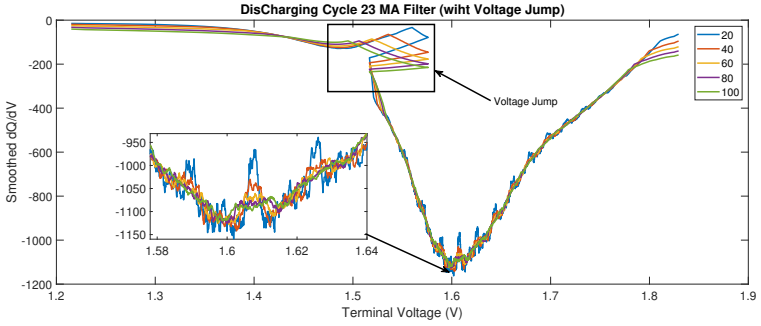


(b) after applying Moving Average (MA) Smoother

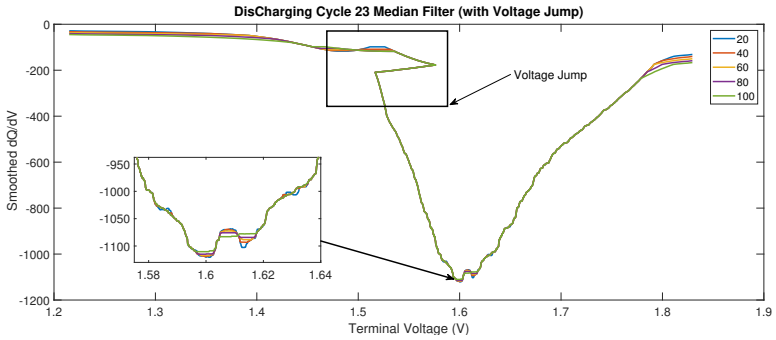


(c) after applying Moving Average (MA) and Median Filter (MF)

Figure 6.3: An example of unstable discharging pattern (voltage jump inclusive): IC discharging curve(s) of 200Ah pilot-scale ZNBs under current rate of $0.25C$ with sampling rate of $1s$ (a) without applying Moving Average (MA) Smoother (b) after applying average smoothing methods with different horizons of 20, 40, 60, 80, and 100 (c) Median Filter (MF) introduced on the sets of pre-filtered data with MA to offset measurement error spikes.

a combination, MF successfully filters out the low frequency intermittent spikes, generating satisfactory reductions of high frequency noises and low frequency spikes. Even in the case of $k = 20$, the combination of MA and MF is able to improve the curve smoothing effect significantly while preserving all the significant features of IC curve. Nevertheless, as shown in Fig.6.3(b) and Fig.6.3(c), the voltage jumps make the IC curve deformed, where it does not signify the on-going electrochemical reaction. What's worse, this flaw cannot be remedied from the IC curve after applying the combination of MA and MF. In other word, incorrect characteristics of electrochemical processes may be extracted from the plotted IC curves, leading to failures in the subsequent capacity estimation. Hence, further attempts are required to deal with the low frequency intermittent voltage jumps.

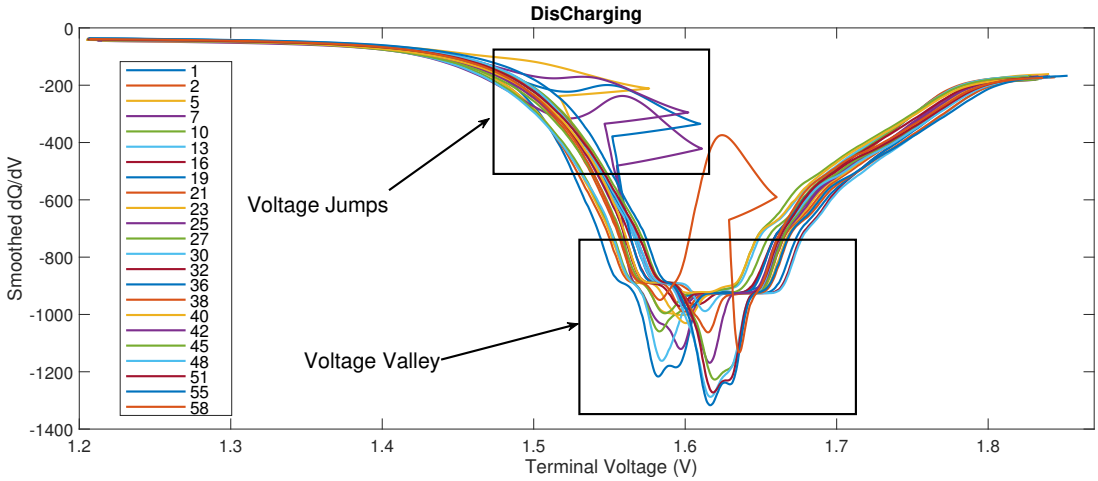


Figure 6.4: Variation of valley positions and intensity under different cycles, where the numbers are the labels of tested cycles

Fig.6.4 presents the variation of valley positions and intensity according to the plotted IC curves under different cycles, in the case of $k = 80$. It is worth to note that in order to achieve the static cycling patterns, the Galvanostatic cycle tests are conducted on a pilot-scale $210Ah$ ZNBs to log the raw voltage-capacity dataset. During the Galvanostatic cycling, reconditioning is performed per 30 cycles [194]. After the reconditioning, the battery health is regarded anew. It

can be seen from Fig.6.4, this set of IC curves is polluted seriously by the voltage jumps occur in abnormal cycles. Thereby, the valley positions are not identifiable from the IC curves. On the other hand, it seems the depth of valleys are getting shallow as the number of cycles increases. But the evolution of valley position changes is hard to be recognised. As a result, the used combination of MA and MF fails to address the voltage jump issues. The experimental results signify that the random white noise can be reduced, however, the voltage jump is sustained.

As shown in Fig.6.3(c), the applying MF solely cannot offset the voltage jumps in the unstable discharging cycles, leading to irregularity in presentation. Hence the corresponding feature points of voltage valley are difficult to be extracted. Similar to the functionality of MF, Gaussian Filter (GF) was introduced in [195] to eliminate the low frequency noises as well. As mentioned before, the discharging behaviour of ZNBs is not stable resulting in the appearance of voltage jumps occasionally. Due to the appearance of low frequency voltage jumps, GF has been used in this work to separate the low frequency variations from the higher frequency noises. In this way, the smoothing effects are further enhanced to eliminate the influences of the low frequency voltage jumps on IC curves.

Denote the length of moving horizon is $k$. A GF employs the Gaussian distribution expressed with the following wight functions [195]:

$$G(x) = \frac{1}{\sigma\sqrt{2\pi}} exp(\frac{1(x-\mu)^2}{2\sigma^2}) \tag{6.2}$$

where $\mu$ is the mean value and $\sigma$ is the standard deviation controls the filter horizon, which have set as 0 and the $k/2$, respectively. In principle, $\mu$ adjusts how effective each data in the horizon is. Normally, the value of $\mu$ is set to be 0 to serve as the biggest effect on the smoothed updates. $\sigma$ is a user-defined parameter to determine smoothing degree. Specifically, a big value of $\sigma$ will lead to smoother effect but it may lose features exist in the raw dataset. Also, we present the cases of $k$ = 20, 40, 60, 80 and 100. Unlike the MA averaging the neighbours to smooth each data point and playing equal weights in the entire horizon, GF replaces the data points by a weighted average of neighbours. Hence, the nearest

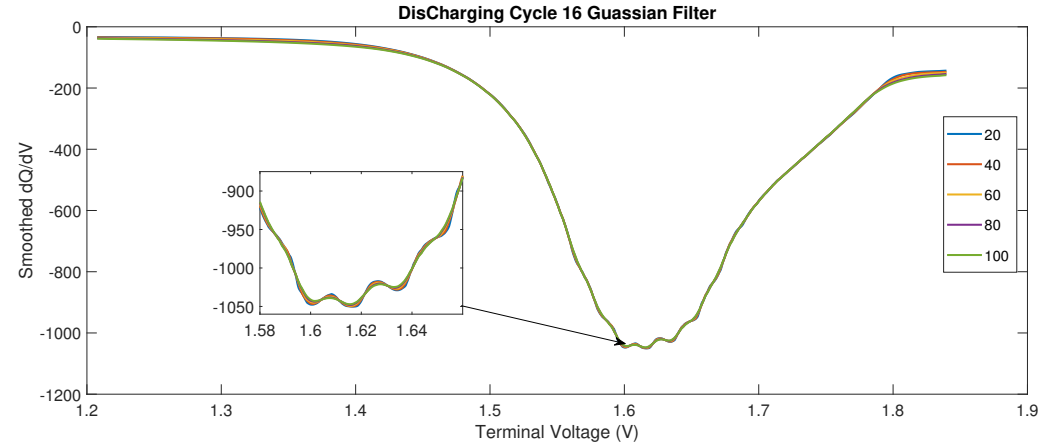


(a) after applying Gaussian filter (GF)

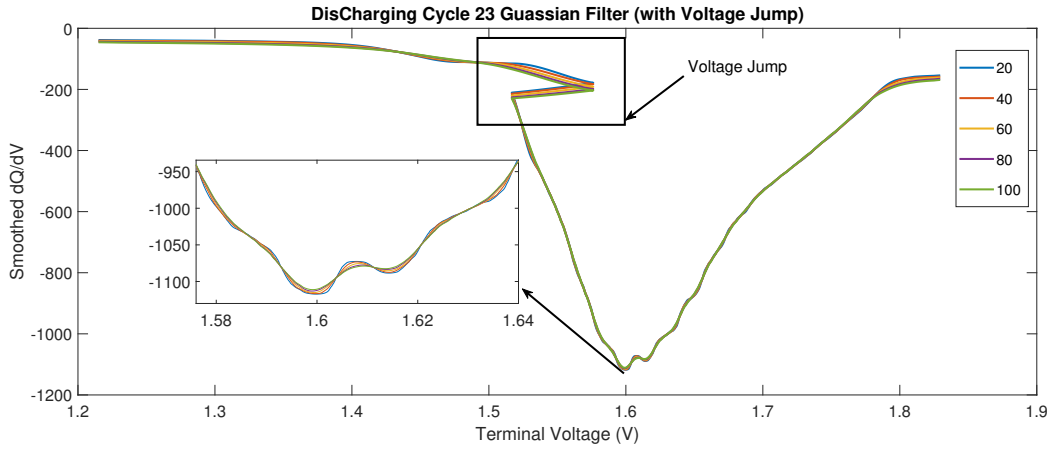


(b) after applying Gaussian filter (GF) (abnormal)

Figure 6.5: An example of unstable discharging pattern (voltage jump inclusive): IC discharging curve(s) of 200Ah pilot-scale ZNBs under current rate of $0.25C$ with sampling rate of $1s$ (a) (b) after applying Gaussian filter (GF) with different horizons of 20, 40, 60, 80, and 100 on ab/normal discharging cycles, respectively

data plays a more important role on the average while the distant data does less.

Similar to the implementation of MF, GF is introduced on the sets of pre-filtered data by MA to provide satisfactory reductions of the variability. However, as given in Fig.6.5, the results still cannot eliminate the influence of voltage jumps. In the comparison between Fig.6.3(c) and Fig.6.5(b), the combination of MA and GF is able to offer enhanced smoothing effect against the combination of MA and MF. There is no significant improvement of smoothing effect can be observed when applying longer horizons. Even in the case of $k = 20$, the noises can be effectively removed and the features can be well preserved on IC curves. However, further investigation is required to offset the interference of intermittent voltage jumps.

### 6.2.2 Differential Voltage Analysis (DVA)

Though Section 6.2.1 discusses the experimental results of ICA method and demonstrates the effectiveness of MA, MF and GF, one intractable issue remains in reducing the influence of low frequency voltage jumps on IC curves. As defined in Eq.6.1, differential voltage analysis (DVA) approach is derived from the inverse calculation of ICA, which can be expressed as follows:

$$\frac{dV}{dQ} = \frac{\Delta V}{\Delta Q} = \frac{V_t - V_{t-1}}{Q_t - Q_{t-1}} \tag{6.3}$$

In the comparison of ICA, DV curve refers to the battery capacity rather than refers to the terminal voltage. In this regard, DVA might be able to overcome the flaws of voltage profiles such as the intermittently occurred voltage jumps, thus handling the voltage jumps problem. In [196], the DVA has been employed to analyse the mechanism of battery capacity fading. The DV curve has successfully implied that the side reaction taking place on the negative electrodes leads to the main degradation of battery capacity. Furthermore, the research of [193] has indicated that, despite cell degradation, the shape of DV curves near the first peak has been relatively stable, and the position and intensity have been almost constant. In this work, the procedures of DVA are aligned with ICA method. Firstly, the raw DV curve is obtained through the numerical derivatives.

Afterwards, the combination MA and GF method is used to smooth the DV curves. Herein, the length of horizon is set as 20 to moderate the computational burden.

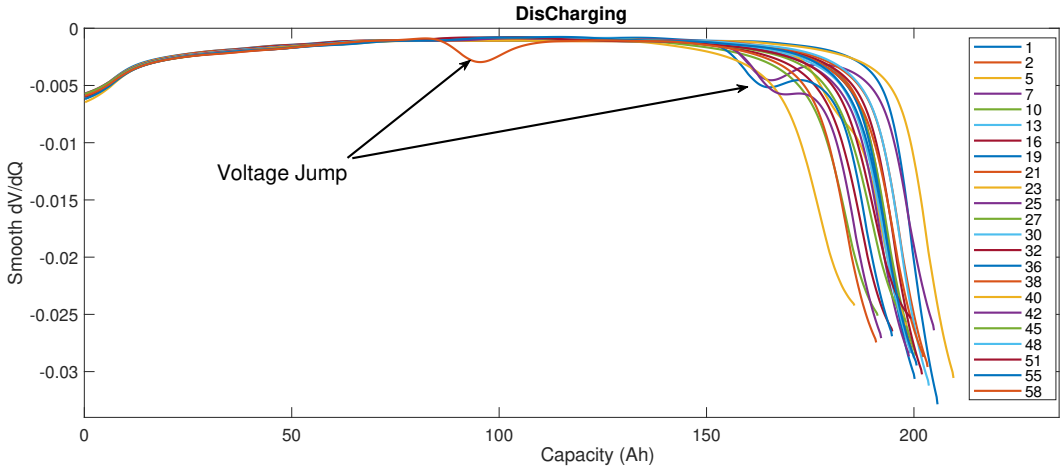


Figure 6.6: Differential voltage curves (dV/dQ) of 200Ah pilot-scale ZNBs under current rate of $0.25C$ with sampling rate of $1s$

As shown in Fig.6.6, the plotted DV curves are in alignment with the hypothesis. The most of the intermittently occurred voltage jumps have been filtered. Though the patterns of DV curves maintain almost constant until the three quarters of the entire discharging process, no obvious peaks/valleys can be observed from the obtained DV curves. Since the applied horizon is selected as short as 20, this phenomenon cannot be referred to a over-smoothing problem. Hence, we believe the DVA method is inapplicable to ZNBs.

### 6.2.3 Probability Density Function (PDF) method

According to the previous discussion in Section 6.2.1 and Section 6.2.2, neither CIA nor DVA can fully circumvent the voltage issues. In order to offset the effects of the unpredictable upward voltage jumps, the Probability density function (PDF) based dis/charging data analysis has been introduced in this work. The PDF method was fist discussed in [197] to evaluate SoH of EV batteries. In essence, the rationales behind PDF method is equivalent to DVA. Herein, denote

$\delta V$ as the voltage interval to discretize probability density function. For instance, $0.01V$ is the applied discretization interval as given in Figure 6.7. In each interval, the number of observations is then to be counted, and converted to density by dividing by the total number of observations and interval size.

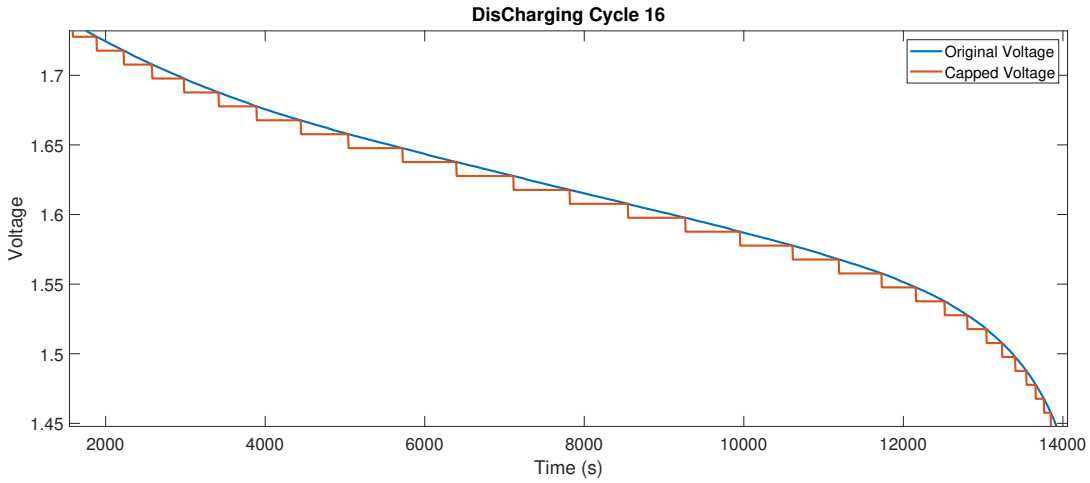


Figure 6.7: Demonstration on PDF Method

Then the discretized density function is obtained as illustrated in Figure 6.8. Through smoothing over the density according to some kernel function, the resultant density can be easily plotted.

In the normal voltage profile, the voltage curve is supposed to be monotonic. Therefore, in the discretized density calculation, $[V, V + \Delta V)$ is considered as the voltage interval. Assume there are $m$ observations in this interval as follows:

$$(V_1, Q_1), \ldots, (V_m, Q_m)$$

Because the Galvanostatic cycle test, the discharging and charging current are both constant, a neat expression is given as:

$$Q_2 - Q_1 = Q_3 - Q_2 = \cdots = Q_m - Q_{m-1} = \delta Q, \quad Q_m - Q_1 = (m-1) \cdot \delta Q$$

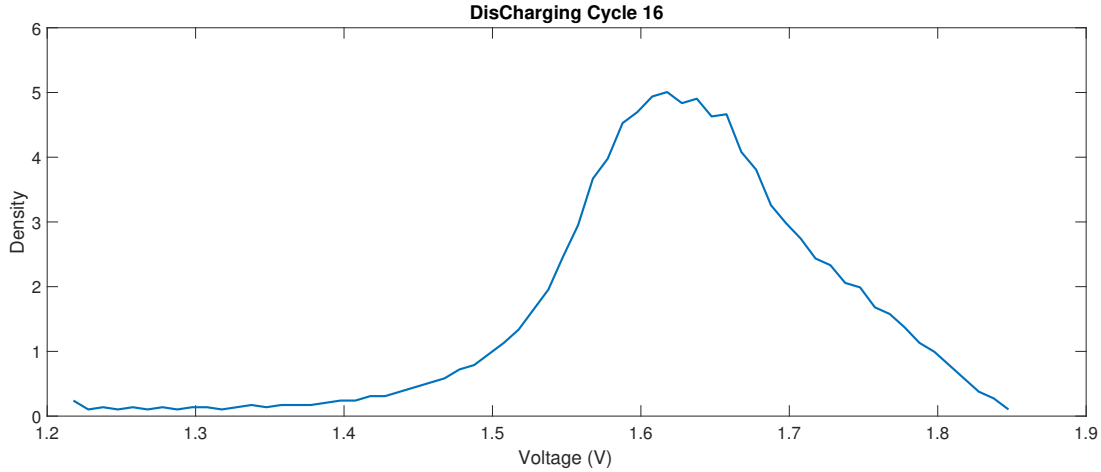


Figure 6.8: Discretized Density

Denote $(V_0, Q_0)$ to be the observation just before the observation $(V_1, Q_1)$. In the discharge process, the voltage relationship can be of the following form:

$$V_0 \geq V + \Delta V > V_1$$
$$Q_0 = Q_1 - \delta Q$$

Hence, the discretized density will be calculated as:

$$f_{DD}(V + \Delta V) = \frac{m}{N \cdot \Delta V} \tag{6.4}$$

where $N$ is the total number of observations. As for DVA, the voltage curve is denoted as function $V_i = g(Q_i), \forall i = 0, 1, \ldots, m$. Assume $Q' = g^{-1}(V + \Delta V)$ and $Q'' = g^{-1}(V)$ such that $Q_0 \leq Q' < Q_1$ and $Q_m \leq Q''$. Then the DVA calculates the derivative at $V + \Delta V$ as:

$$f_{DV}(V + \Delta V) = \frac{Q'' - Q'}{\Delta V}$$

If the derivative curve is normalized such that $\int f_{DV}(V)dV = 1$, the following expressions can be achieved accordingly:

$$f_{DV}^{n}(V+\Delta V)=\frac{Q''-Q'}{(Q_{max}-Q_{min})\Delta V}=\frac{Q''-Q'}{N\cdot\delta Q\cdot\Delta V}$$

Recall the constant current in battery cycling, there thus exists $(m-1)\cdot\delta Q < Q''-Q' < (m+1)\cdot\delta Q$. Hence the normalized derivative can be formulated as follows:

$$\frac{m-1}{N\cdot\Delta V} < f_{DV}^{n}(V+\Delta V) < \frac{m+1}{N\cdot\Delta V} \tag{6.5}$$

Compare the above equation with 6.4, and derive that:

$$||f_{DD}-f_{DV}^{n}||_{\infty} < \frac{1}{N\cdot\Delta V}$$

where $||\cdot||_{\infty}$ represents the infinity norm. The above analysis discusses the similarity between PDF method and DVA method.

It was believed that the PDF method can handle the upward voltage jump while DVA can not. In either CIA or DVA, the voltage curve has to be monotonic voltage curve. Whereas in the abnormal tests, the discharging voltage is not stable and the upward voltage jump in the discharge curve means non-monotonic voltage curve, which messed up the DVA definition. As there might be two different $dQ/dV$ values at the same $V$, where one is ahead of the jump, and the other is after the jump. When using the PDF method, we take the advantage of distribution calculation, which focuses on the distribution of voltage. In other words, applying the PDF method on jump data is the same as sorting data to eliminate jumps and then applying the PDF method. The distribution of voltage guarantees the same value for both jump data and sorted data. Hence, the discharging voltage profiles with voltage jump data are not problematic for PDF method.

In this work, the PDF method is introduced on the sets of pre-filtered data by MA, to reduce the influence on voltage jumps. It can be seen from Fig.6.9(c),

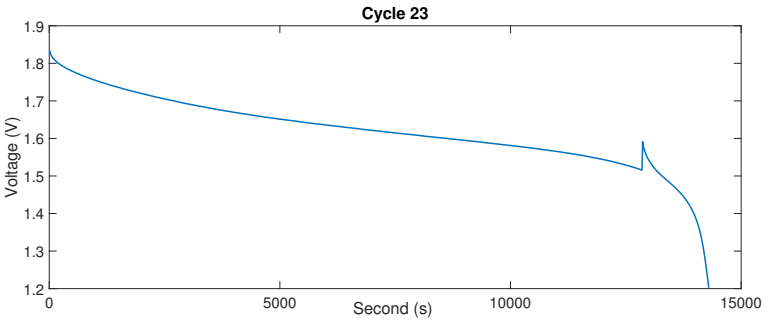


(a) abnormal voltage jump

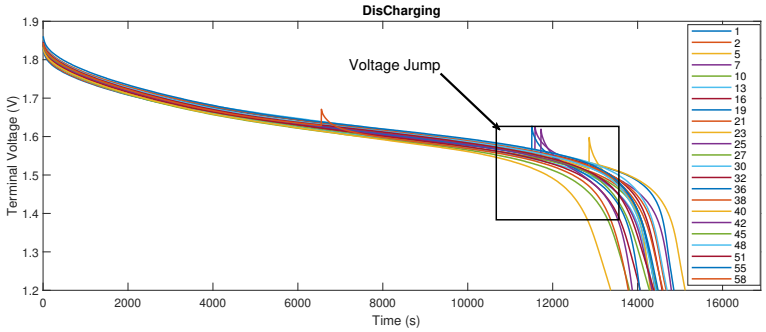


(b) discharging voltage profiles

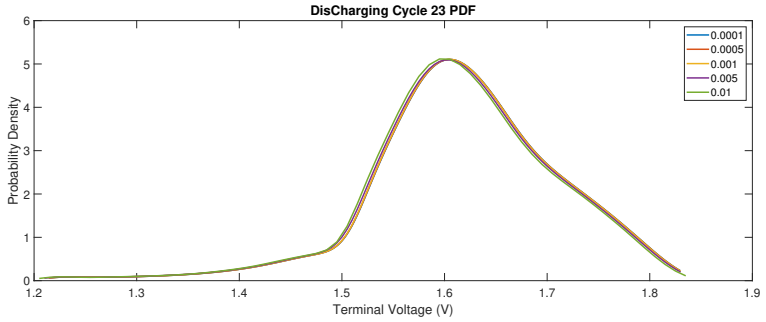


(c) after applying the Probability density function (PDF) method

Figure 6.9: An example of unstable discharging pattern (voltage jump inclusive): IC discharging curve(s) of 200Ah pilot-scale ZNBs under current rate of $0.25C$ with sampling rate of $1s$ (a) (b) a specific cycle with abnormal voltage jump occurred and discharging voltage profiles (e) Probability density function (PDF) method with different intervals applied to offset voltage jump.

the results conform to our anticipation, where all the voltage jumps have been filtered out. The obtained PDF curves are smooth enough among different lengths of voltage intervals. In addition, as given in Fig.6.10(a), only one peak can be identified form the bunch of PDF curves, and the peak positions are relatively fixed corresponding to the early stage of discharging process. More specifically, the height of peak is getting small with the battery cycling. Once the reconditioning performed, the height of peak (cycle 30) returns back to the initial cycle (cycle 1) again. But another problem has been raised, when extracting the peak points from Fig.6.9(c). As shown in Fig.6.10(b), due to such a broad range of peak positions as long as one quarter of discharging process, the built regression model cannot well match the extracted peak points. In other words, the each peak point randomly occurs during the one quarter of discharging process, so that its distribution might be stochastic bringing difficulty to model. This phenomenon might be interpreted by intrinsic reaction of flow based ZNBs. As aforementioned before, the peak/valley points are related to the flat voltage plateau. However, there may be no significant voltage plateau when cycling the ZNBs. One hypothesis provided by us could be responsible for the above Fig.6.9(c). As the kinetics of the electrochemical processes are changed due to the applied flowing electrolytes, which speeds up the reactions for electroplating/electrolytic processes. Therefore, the suppression factors in the mass transportation have been attenuated. In other words, despite the voltage jumps, the charging and discharging voltage profiles are shaped flatness and smoothness in the entire cycling process, as depicted in Fig.6.9(a) and Fig.6.9(b). The upward/downward voltage steps are unidentifiable, leading to the failures of both CIA and DVA in the capacity estimation of ZNBs.

### 6.2.4 OCV Observer for Capacity Estimation

The estimation of SoH has been reviewed as another functionality of BMS to evaluate the battery performance online. As discussed above, the capacity estimation can be regarded as a key index to judge the health state of flow based ZNB. Compared with the model free methods, i.e. CIA and DVA, the model based capacity estimate methods have come out much earlier. In this regard, the

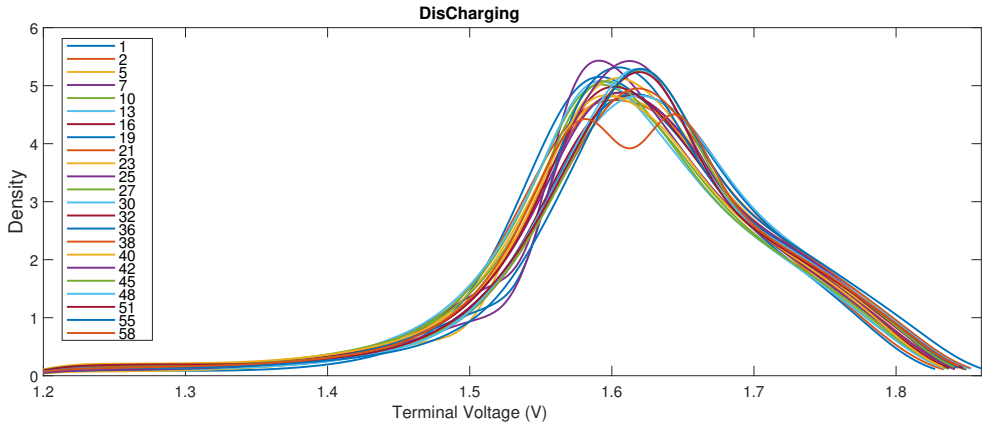


(a) Variation of peak positions and intensity

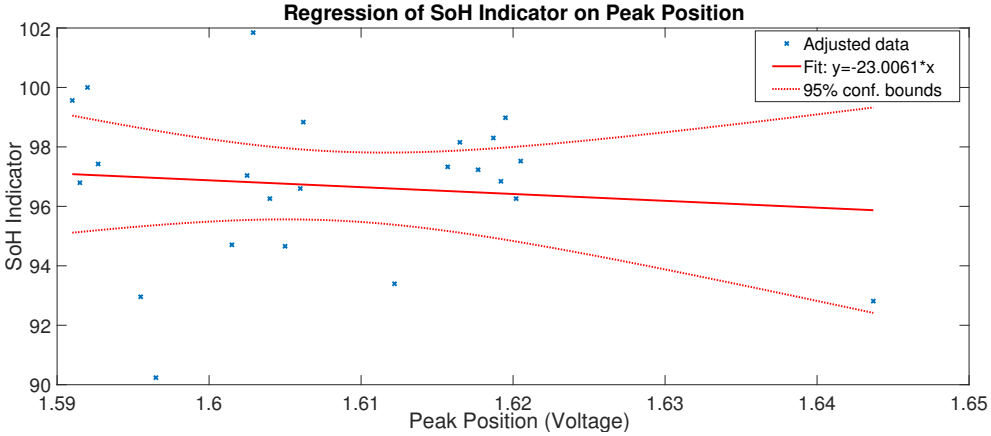


(b) Peak points distribution

Figure 6.10: PDF discharging profiles of 200Ah pilot-scale ZNBs under current rate of $0.25C$ with sampling rate of $1s$. Herein, the SoH is defined as the ratio of releasable capacity to the rated capacity. (a) Variation of peak positions and intensities under different cycles (b) the battery SoH as function of the position of peaks.

capacity estimation can be derived from the accurate estimate of SoC. For example, in [198], an online method is proposed for SoH estimation of valve-regulated lead acid (VRLA) batteries. It combines the SoC estimation using the EKF and a neural-network battery model with the correlation analysis between SoC and OCV using fuzzy logic and RLS method. In [121], a co-estimation scheme of SoC, SoH, and state of function (SoF) is proposed for lithium-ion batteries, where SoC estimation is achieved using EKF, while battery parameters related to the SoH and SoF are identified online through RLS method. Besides, coulomb counting method [199; 200] has been adapted widely to calculate the released charges for capacity estimation. However, unlike the model based SoC estimator using a close loop to update its outputs, the calculated capacity relays on an open loop framework, which is highly conditional on SoC accuracy. Though overwhelming studies have been conducted on the capacity estimation based on different battery types, two issues still remain. One is the accuracy of capacity estimate. Since the capacity estimation is derived from SoC values, many aspects during the calculation and measurement processes may affect the estimate precision. A basic architecture of capacity estimation can be summarised as: ($S1$) model identification; ($S2$) SoC estimation; ($S3$) capacity estimation. Therefore, errors can result from many areas. In order to yield accurate capacity estimation, the errors from measurements, discretization process, and parameters identification.etc. have to be compensated by the SoC estimator. On the other hand, simplification of capacity estimate architecture results in reducing computing burden to save the memories of BMS chips is another topic in research. Additionally, few progresses has been achieved in the literature to estimate the ZNBs capacity. The zinc dendrites build-up make the design of capacity estimator complex, which requires the implemented SoC estimator exhibiting a good robustness to reject the intermittent error spikes and disturbances. Meantime, the computing complexity is of the subject to the limitation of online implementations.

In this section, as an extension of Section 4.2.1, the proposed OCV observer based SoC estimate method can serve for the followed-on capacity estimation. Particularly, when in the cases of accuracy demanding, higher order ECM are used to model the ZNBs electric dynamics. At this point, the proposed OCV

observer can further attenuate the computational burden and limit the computing time cost. Revisiting Eq.(5.5), the capacity can be interpreted by the ratio of the accumulated coulomb count to the SoC change within a certain period of time:

$$\hat{Q} = \frac{\eta \int_{t_\alpha}^{t_\beta} I_L dt}{\hat{SoC}_{t_\beta} - \hat{SoC}_{t_\alpha}} \tag{6.6}$$

where $t_\alpha$ and $t_\beta$ are the two pre-defined time instants, and the coulombic efficiency $\eta$ is set as 100% for simplification. Note that the robustness of SoC estimations $\hat{SoC}_{t_\alpha}$ and $\hat{SoC}_{t_\beta}$, is the prerequisite to accurate capacity estimate. A longer time interval may efficiently make SoC estimate converge and filter out short-term temporal influences from other factors such as measurement noises, ambient temperature fluctuations, SoC estimation flaws, etc. $\hat{SoC}_{t_\alpha}$ and $\hat{SoC}_{t_\beta}$ are obtained by the EKF algorithm, for which the system is specified in Eq.(4.46).

### Analysis of Capacity Estimation

When applying the OCV observer based SoC estimation method under galvanostatic cycle testing regime as outlined in Section 3.2.3 and illustrated in Fig.3.2, the capacity can be thus obtained from Eq.(6.6). It should be noted that in order to achieve accurate capacity estimation, herein, the second-order ECM has been employed to repreduce the ZNBs electrical characteristics. Fig.6.12 presents the a representative result of galvanostatic cycle tests. The discharging capacity is not constant but rather resides around the nominal value. Slight increases of the discharging capacity are observed since the active materials have been fully activated. However, after 20 cycles, the accumulated zinc depositions incur an apparent capacity drops, and 10% capacity degeneration can be detected suddenly. Simultaneously, the discharging curves as shown in Fig.3.2 are becoming steep dramatically. This is followed by the observations that the ZNB will lose its discharging capacity in the forthcoming circles quickly. This phenomenon is also reported in [49], which implies that the reconditioning operation is preferred. In Fig.6.12, the estimated capacities match the reference values very well, which demonstrates that the proposed approach is suitable for the SoH monitoring, capacity correction, and the indicator for the reconditioning maintenance. According to Eq.(5.5), a poorly estimated capacity value will lead to a serious

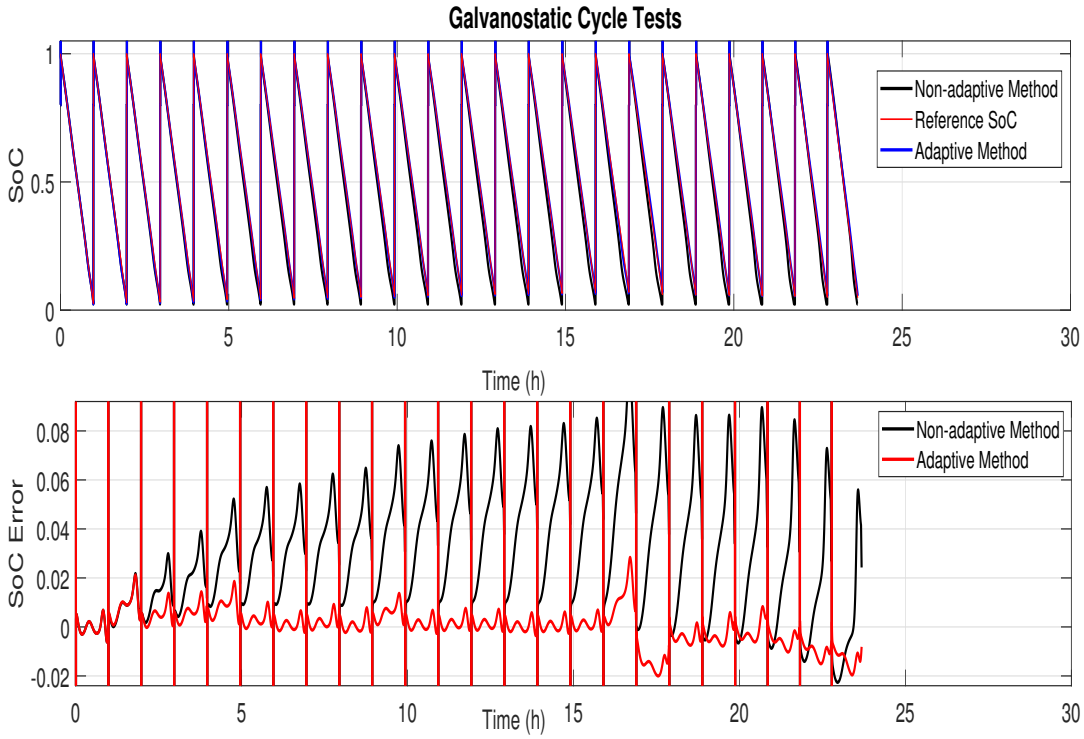


Figure 6.11: SoC estimation in galvanostatic cycle tests

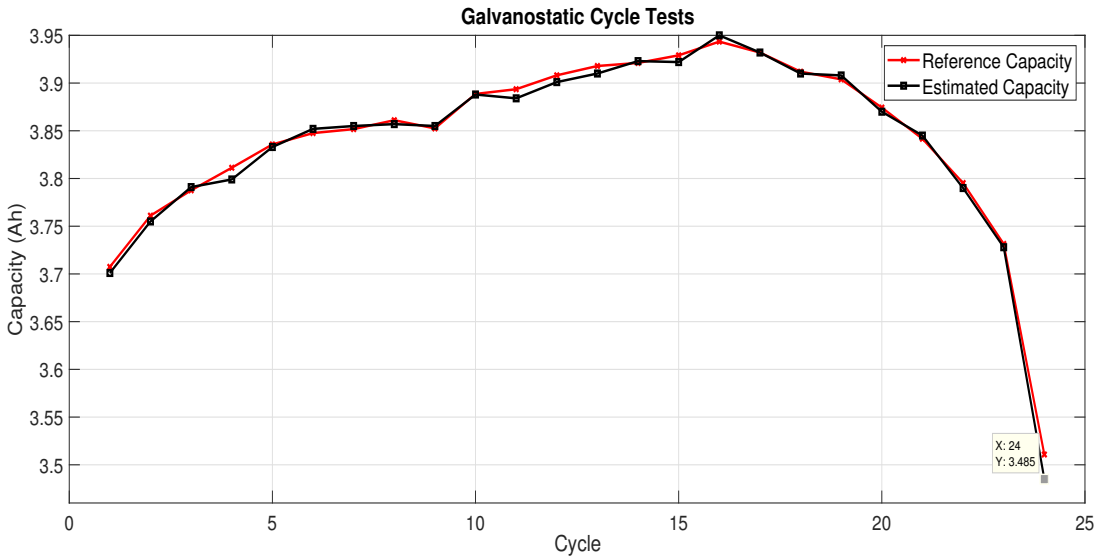


Figure 6.12: Capacity change in galvanostatic cycle tests

deviation of the SoC estimation. In this regard, the capacity is better to be evaluated and updated after each cycle to ensure the accurate SoC estimate, namely adaptive capacity estimation. In this work, the adaptive capacity estimation by the proposed approach is compared with a non-adaptive method as displayed in Fig. 6.11. The non-adaptive method exhibits error-prone SOC estimations resulting from the interference of incorrect capacity estimations. Oppositely, the capacity updates are incorporated into the SoC estimation process, resulting in the SOC estimation error bounds being within 2% range. The results thus confirm the effectiveness and efficacy of the proposed method. On the other hand, in terms of the computing cost in time, Table 4.3 lists the entire computation time for the test-runs on traditional RLS-EKF using the first/second order ECM, as well as on the proposed method using OCV observer based second-order ECM. Although the use of the second-order ECM has raised the computational cost in RLS regression, the introduced OCV observer has reduced the computational cost in the SoC estimation due to the dimension reduction. According to the comparisons in Table 4.3, when applying the proposed methods, the entire time cost relating to SoC and capacity estimation, is even less than solely using the first order ECM. However, due to the implementation of higher order ECM, the accuracy of capacity estimation has been secured as the comparisons in Fig.6.12 without any compromised resulting from the dimension reduction. The proposed OCV observer based capacity estimation approach is thus readily achievable on board.

### 6.2.5 MPC Observer for Capacity Estimation

According to Eq.6.6, the developed MPCO approach in Section 4.2.2, provides another framework using the multi-windows method to improve the accuracy of the SoC estimation. Followed-on, the capacity estimate has been thus benefited by the improved SoC estimation. Similar to the above discussion, the time intervals should be set sufficiently large to make SoC estimate converge. In this attempt, $t_\alpha$ and $t_\beta$ are prescribed as the 100 sample points after the start-up and 100 sample points ahead of the end-point, respectively.

### Capacity estimation and effects of windows sizes

A major objective of the proposed MPCO is to estimate capacity dynamically. The proposed MPCO is used for the SoC estimation over the galvanostatic tests as depicted in Fig.3.2. In this work, in order to obtain a robust estimation of capacity, different horizon window of the state variable are tested. Furthermore, the effects of window size are discussed.

Fig.6.13(a) concludes the resultant SoC estimates over 15 discharging cycles. Large error spikes only occur at the starting stage of each discharging cycle, due to the intentional $-20\%$ SoC initialization error. However, all the applied methods attenuate the initial errors and converge quickly. Through comparison with EKF in Fig.6.13, MPCO has remarkably outperformed in the SoC estimation. In this regard, as the number of cycling increases, the SoC estimations provided by EKF are going far from the CC references, where larger discrepancies can be observed after 10 cycles. These phenomena can be explained from two aspects. Firstly, even single window MPCO outperforms EKF due to the constraints in SoC estimation. At the start of each cycle, an intentional SoC initialization error is considered. The SoC constraints help in faster convergence and prevent underestimation (below 0) at the end of each cycle. While EKF is tend to underestimate SoC when approaching later cycles (from 11 to 15) due to weak traceability of battery capacities. The underestimation of SoC then results in poorer capacity estimates as detailed in Fig.6.13(b). With the constraints in the proposed MPCO, this cross-interference can be more manageable. Secondly, as illustrated in Fig.6.13(b), longer window outperforms in the convergence speed of the capacity estimation. For instance, when the window length increases to 6, the capacity estimate converges to the reference value quickly, bringing the estimation error down to tiny values, merely after 1 cycle. As interpreted by Eq.(4.60), in the process of solving objective function, more previous measurements are involved in the optimization when longer windows are used. Consequently, the past SoC estimates are updated as well, becoming closer to the SoC-OCV table. Except for the faster convergence speed, the performance of these counterparts (window lengths from 1 to 6) is comparable and outperforms traditional EKF, which is

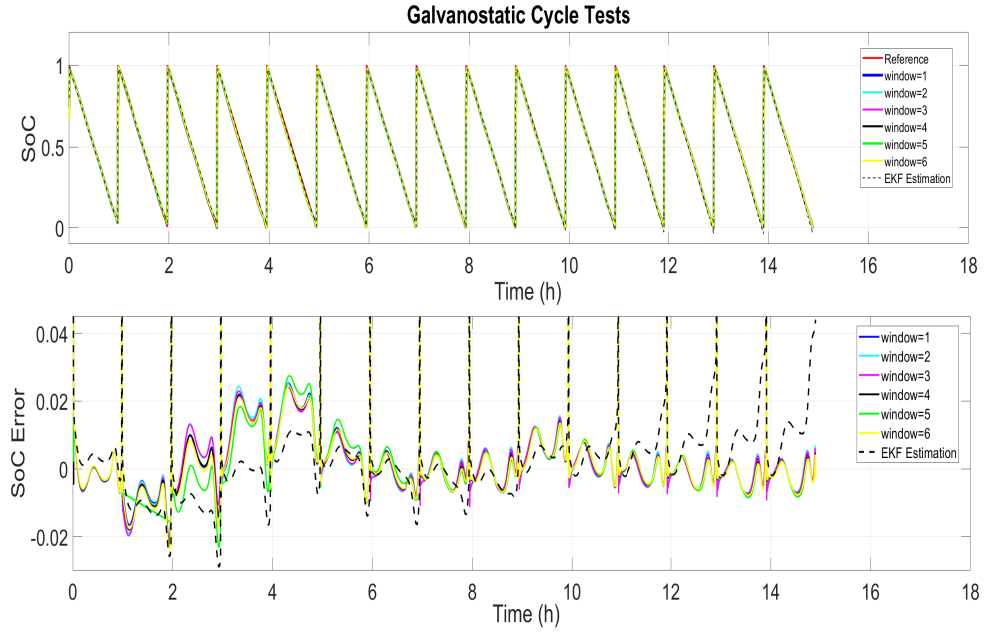


(a) SoC estimation under different windows

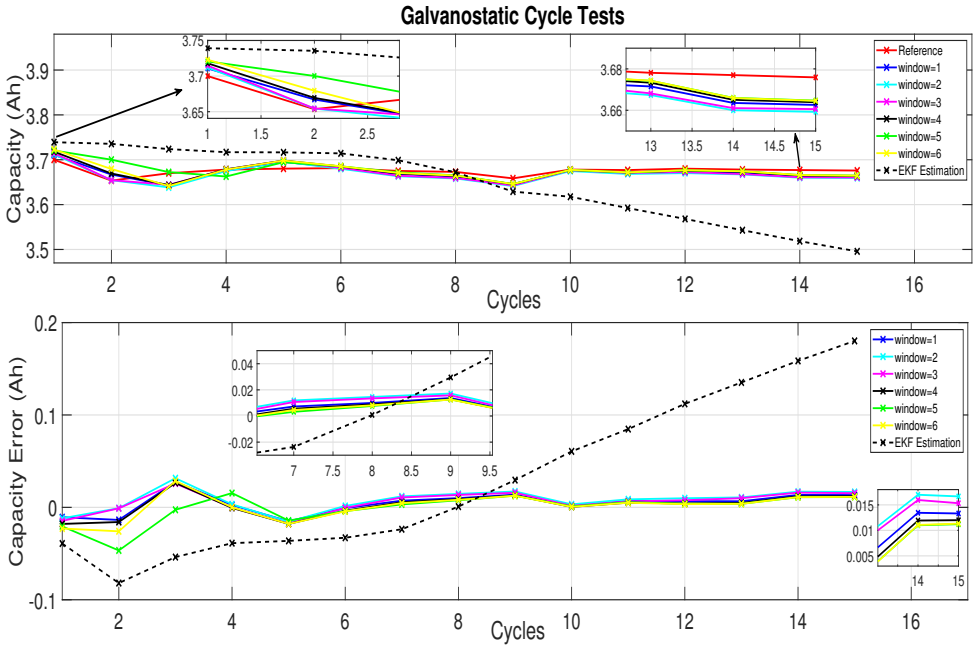


(b) Capacity estimation under different windows

Figure 6.13: Capacity estimation and effects of windows sizes during the galvanostatic cycling tests

foreseeable as explained in previous context. Throughout the entire 15 discharging cycles, the estimation errors of the capacity are subtle, only within ±2%. According to Eq.(6.6), the accurate estimation of SoC thus reinforces the precision of capacity estimates accordingly. The simulation results further verify the effectiveness of the proposed MPCO method as given in Fig.6.13. Therefore, the proposed MPCO is able to reflect the dynamics of the practical capacity, with an outperforming performance compared with traditional EKF model based estimation no matter the length of the window used.

## 6.3 Battery Maintenance

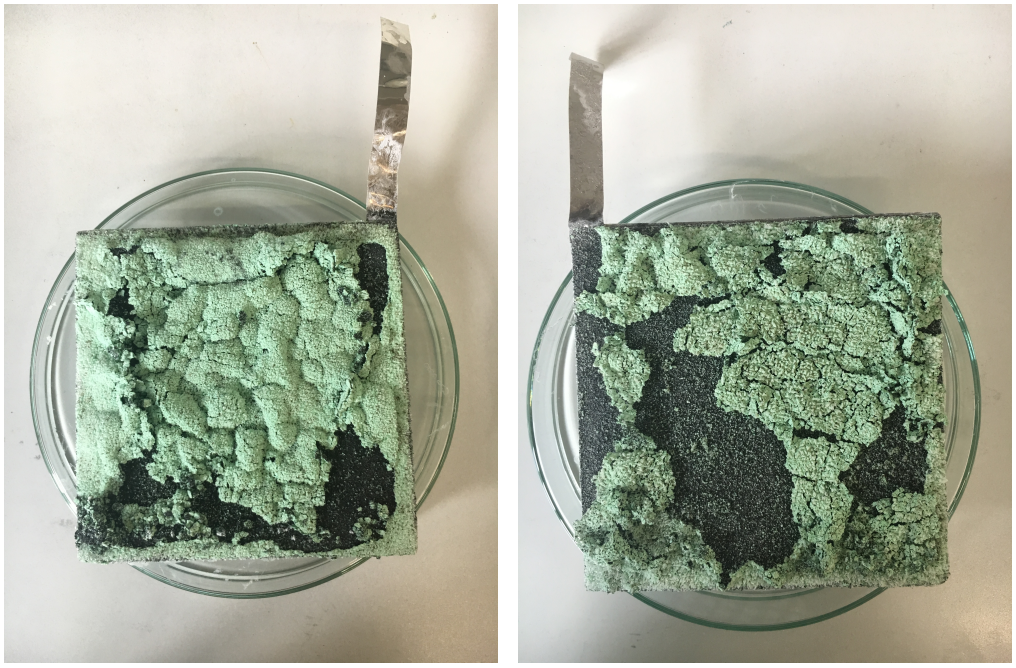

(a) First test sample (b) Second test sample

Figure 6.14: Zinc electrode degradation and deformation after several cycles

A significant challenge of the viability of commercial flow based ZNBs is the well-known phenomena of dendrite formation and zinc morphology variation over time. In specific, the morphologies of the build-up zinc depositions on the zinc

electrodes will conspicuously affect the cell capacity when cycling ZNBs. Undissolved zinc depositions are the culprits to the capacity degradation and poor cyclability. Researches have suggested that the implementation of varying flow rates and periodic inversion of the electrolyte could extend the service life. Though applying electrolyte flow to traditional ZNBs can significantly prolong the lifetime by reducing both dendrite formation and morphological variation, a periodic battery maintenance has to be conducted to strip all the residual zinc depositions off from the electrodes then making the battery anew. As discussed above, the periodic reconditioning operation is the most effective approach to prevent the ZNBs from the internal short-circuit and capacity degradation [45; 49]. Substantial investigations on bench-scale and grid-scale ZNBs, have indicated that a periodic reconditioning operation (every 15/20 cycles) [49], i.e. discharging the ZNBs in a trickle current profile, would effectively reactivate the battery. By doing so, even after 3000+ cycles, ZNBs are still performing well [51]. However, little contribution has been made on identifying the reconditioning moment in the literature. In practice, frequent or premature recondition maintenance will lead to a waste of energy in the storage system, because the process of trickle discharging can last for more than a day. Additionally, if ZNBs are cycling under the poor conditions, the chain reactions to damage the cell housing and electrodes catastrophically will be progressively provoked. As shown in the Fig.6.14(a) and Fig.6.14(b), the preliminary studies signify that in poor operating conditions, ZNBs are of the subject to two main issues, which are anodes self-corrosion and cathodes transformation. The latter one specifically refers to active materials stripping and swelling. As a result, the effective reaction areas of electrode are not stable leading to the variations in capacity, and it will then deteriorate the accuracy of SoC estimate.

In this work, the estimated capacity has been employed as an indicator to determine the time for the battery maintenance. The capacity gauging is executed followed by the SoC estimation, while the current capacity information will be calibrated online. If the estimated capacity suddenly drops to 90% of the nominal capacity, the stripping circle will be executed to recondition the ZNBs. In this regard, two advanced ECM model-based online capacity estimation and

updates methods i.e. OCV observer and MPCO, have been well-introduced in the above Section 6.2.5 and Section 6.2.4. The moment for reconditioning operation is readily reflected by the accurate capacity estimation, which will de-risk the over-cycling issue of ZNBs and extend the lifespan to the full extent in a real application. Fig.6.13, Fig.6.11 and Fig.6.12 further confirm the efficacy of the proposed assumptions. Due to the high accuracy of the estimation, the estimated capacity is an appropriate indicator to determine the time of reconditioning.

## 6.4 Conclusion

Zinc-nickel single flow batteries (ZNBs) have been demonstrated as a promising alternative to lithium batteries for next generation grid-tied energy storage. However, due to the dendritic growth, the working behaviours of ZNBs are not stable, particular in capacity fluctuations and voltage jumps, when cycling the cells. Therefore, the accurate capacity estimation is important but intractable. In this chapter, two electrical features including the growth of cell DC resistance and cell capacity degradation, which both affect the health status of ZNBs, are compared. Because ZNBs cycling performance is more sensitive to the capacity variations over time, the estimated capacity value has been chosen as the health index to judge the SoH of flow cell. ICA and DVA methods are reviewed comprehensively in this work. As the highly promising tools in battery capacity estimation, both ICA and DVA approaches are model free and straightforward to be implemented. Whereas, due to the ZNBs intrinsic electrochemical process taking place over the redox reactions, neither ICA nor DVA is capable of yielding an accurate capacity estimation under the static cycling scenario. On the other hand, although longer lifespan can be obtained by the periodic reconditioning maintenance according to the existing research, there is no mature method to identify the moment of reconditioning. In order to overcome the voltage excursions occurred during cell abnormal cycling, underpinned by the already proposed battery modelling and state estimation techniques presented in Chapter 4, the ECM model-based online battery identification technique has been employed in this work. Two methods are discussed: OCV based observer secures the efficient computing cost when

using higher order ECM, in which the higher order ECM guarantees the accuracy of battery modelling and SoC estimation. In addition, MPC is a popular optimization paradigm in the process control. By incorporating with the merits of MPC, a novel MPCO has been developed for the working conditions monitoring and capacity estimation. Strong evidence from substantial experiments and simulations manifests the convergence, robustness, effectiveness and generality of the proposed MPCO methods. The competitiveness is demonstrated by the analytical comparisons against transitional model based EKF estimator. At last, the capacity estimation is regarded as an indicator to judge the moment of reconditioning. If the estimated capacity loss drops more than 10% of the rated capacity, ZNBs should stop from the current cycling to conduct the battery maintenance.

# VII
# CONCLUSION AND FUTURE WORK

The Zinc Nickel Single Flow Battery (ZNB) distinguishes itself from other Redox Flow Batteries (RFBs) for its outperforming performance, competitively low cost and environmental impact, and simplicity in structure design. Substantive researches have been conducted from the electrochemical and material aspects, which has manifested a brilliant prospect of Zinc Nickel single flow batteries. However, related research from the engineering aspects has not been touched in particular for battery modelling, state estimations, power deliverability and battery health management. This thesis presents the original work on Zinc Nickel flow battery modelling and management.

## 7.1 Summaries and Main Contributions

This thesis have studied the battery management system for zinc nickel single flow batteries (ZNBs), encompassing the state-of-the-art techniques in ZNBs battery modelling, state of charge estimation, battery health judgement, remaining capacity estimation, peak power prediction and battery maintenance management. On the other hand, valuable guidance to the peers in terms of the cell construction and testing design has been provided. The contributions of this thesis are summarized as follows:

- **A new heuristic optimization method (TLFBO) has been proposed.**

  In order to identify the nonlinear parameters in the ANN-based RBF battery model, the teaching-learning feedback based optimization (TLFBO) method has been proposed to improve the performance of traditional teaching-learning based optimization (TLBO) method. A new learning phase, namely feedback learning is employed to guarantee the convergence. In this regard, the computing cost is reduced while maintaining high modelling accuracy.

- **The differential operations have been introduced into the ECM based online battery modelling.**

  According to the experimental observations, ZNB is a time-varying slow system. Therefore, the subtle variations of open-circuit voltage are negligible. In this thesis, the differential operation is applied to the terminal voltage equations to eliminate the unknown OCV terms. In this way, the ECM can be reformulated in a regression equation, where the model inputs are instantaneous currents and terminal voltages, and the model outputs are the identified parameters. These parameters are directly used in the subsequent OCV observer construction and state estimation.

- **An new OCV observer is developed.**

The novelty of the proposed observer is two-fold. The first is utilisation of differential operation in RLS. When comparing with other method, the proposed differential operation is more stable for non-stationary data, in which case the traditional method would fail to converge. The second is from the observer-EKF combined system. The traditional SoC estimators directly estimate VOC as one of the states in RLS. However, it may suffer greatly due to inconsistent data. In the proposed method, the estimate to VOC comes from the comparison of two OCV sources: SoC-OCV table and OCV observer. Integrated into the update step in EKF, the novel observer can thus take the advantage of filters and lead to more robust results. For an instance, in this work, a second-order ECM is applied to achieve more accurate modelling of the battery dynamics. Then an improved OCV observer is incorporated with the higher order ECM to solve the arisen complexity issues. Further, the model identification process is separated from the state estimation. The proposed OCV observer in a recursive format allows a simpler filter design, leading to reduced computational burden and improved performance.

- **A novel framework of the SoC observer is introduced by the inspiration of model predictive control (MPC), namely, model predictive control scheme based observer (MPCO).**

  There are two major advantages of the proposed SoC observer. Firstly, based on the inherent electrochemical knowledge, state constraints are incorporated into the estimation process, which brings more robust estimates. Secondly, an attempt in multi-window framework has demonstrated better performance in capacity estimation. In this way, the developed MPCO is able to provide more accurate SoC and capacity estimate. The resultant experiments and simulations have verified the convergence, effectiveness, and the generality of the proposed MPCO approach. Additionally, the relationships among the state-of-the-art SoC estimators have been discussed briefly in this work.

- **A novel peak power prediction method is developed based on rolling prediction horizon scheme.**

  In this thesis, a novel framework for ZNBs peak power prediction has been described. The RLS based real-time model identification process is first introduced to acquire an accurate battery model, thus the uncertainties incurred by different operating conditions can be addressed in real time. Then an EKF based SoC estimator is employed to acquire precise estimations which is confirmed in the experiments. With these preliminaries, a window-based peak power prediction framework is proposed which guarantees that the dynamics of current and voltage across the entire prediction windows are taken into the considerations. The proposed framework is capable of incorporating all the constraints on the current, voltage, and SoC. In addition, four indices are proposed to capture the characteristics of the peak power capability over length-varying prediction windows. Finally, the consequent impact of the electrode material and applied flow rate on peak power deliverability are analysed qualitatively.

- **A comprehensive discussion in terms of SoH monitoring, capacity estimations, battery maintenance has been provided.**

  In this thesis, two health factors of ZNBs including the growth of cell DC resistance and cell capacity degradation are compared. Because ZNBs cycling characteristics is more sensitive to the capacity variations over time, the estimated capacity value has been chosen as the health index to judge the SoH of ZNBs flow battery.

  Followed on, two effective capacity estimation tools, i.e., ICA and DVA, are then reviewed comprehensively, which are favourable with advantages in model-free and straightforward to be implemented. Whereas, due to the ZNBs intrinsic electrochemical process taking place over the redox reaction, neither ICA nor DVA is capable of providing an accurate capacity estimation under the scenario of ZNBs cycling. The corresponding rationales

behind the failures of ICA/DVA are given resorting to a related discussion and resultant experiments.

On the other hand, although longer lifespan can be obtained by the periodic reconditioning maintenance according to the existing research, there is no mature method to identify the moment of reconditioning. In order to overcome the voltage jumps occur in the cell cycling, underpinned by the proposed battery modelling and state estimation approaches in this thesis, the ECM based online battery identification technique has been employed in this work to provide capacity estimation and keep capacity updated. The two main contributions are: (1) OCV based observer offset the extra computational cost incurred by introducing a higher order ECM, in which the higher order ECM employed guarantees the modelling accuracy. (2) The novel MPCO has been used to yield more accurate capacity estimation. MPCO calculates the optimal gain over the multi-window decision horizon rather than using the single window knowledge at instant time. Hence, the proposed MPCO is capable of handling errors not only from measurements, modelling, and discretization, but also from the time-varying parameters identified in RLS. In addition, MPCO can further smooth the disturbance from a sudden measurement fault. Thereby, the proposed MPCO has significantly increased the accuracy of the capacity estimation.

At the end, a comparative study on both adaptive and non-adaptive SoC/SoH estimation has been conducted, and the experimental results have confirmed the superiority of the adaptive method. Underpinned by the accurate estimation of the capacity degradation, this thesis employs a capacity-based indicator to determine the time of reconditioning maintenance. The proposed method can thus determine the moment for battery maintenance. At this point, the cell utilization should be increased significantly. Moreover, the proposed method may effectively extend the service life of ZNBs due to the accurate identification of the reconditioning time, while presenting a highly promising solution for the real applications.

## 7.2 Further Work

In this thesis, key elements in building an advanced battery management systems for ZNBs have been discussed. For ZNBs, the electrolyte is continuously circulated by the external pumping system. Since the pumps and relative piping systems have been installed routinely nearby the cell stacks, in principle, it will not introduce any significant logistical problems. However, according to the previous investigation, a flowing electrolyte is able to suppress the dendrite build-up and force the dendrite growths toward one direction, thus prolonging the service life of ZNBs. It is thus reasonable to infer that the benefits of flowing electrolyte likely reside primarily during the charging process. Therefore, the discharging process may require a new protocol. Whereby flow is only needed during the charging process, but then eliminated in the following discharging process. At this point, the pump and the corresponding flow apparatuses can be released from the entire procedure.

As a result, an interesting and portable ZNBs system may be proposed then, thus allowing for a broad array of potential applications in the future. In other words, the new ZNBs will only be connected to the pump for electrolyte circulation when charging it. And then, this system can be discharged pump-free in any environment and condition to provide electrical power. According to this assumption, more efforts need to be conducted such as the focuses to investigate the effects of flow-free discharging protocols on the cell cycling characteristics, to set up the new discharging protocols to protect the cell when discharging under a flow-free mode, and to determine the new battery maintenance regimens. An extension to this interesting hypothesis, such a simplified system can be used for a specified transportation system to lower the capital cost ultimately. In this regard, a more comprehensive battery management system is indispensable, in order to achieve safe operation.

# VIII

# PUBLICATION LIST

## 8.1 Conference Papers

1. **Xiang, Li**, C. K. Wong, and Z. L. Yang. **"A novel flowrate control method for single flow zinc/nickel battery."** 2016 International Conference for Students on Applied Engineering (ICSAE). IEEE, 2016.

2. **Xiang, Li**, Kang, Li, and Zhile Yang. **"Teaching-learning-feedback-based optimization."** International Conference on Swarm Intelligence. Springer, Cham, 2017.

3. Li, Zhang, Kang Li, Dajun Du, Minrui Fei, and **Xiang Li**. **"State-of-Charge Estimation of Lithium Batteries Using Compact RBF Networks and AUKF."** In Advanced Computational Methods in Energy, Power, Electric Vehicles, and Their Integration, pp. 396-405. Springer, Singapore, 2017.

4. **Xiang, Li**, Kang Li, Zhile Yang, and Chikong Wong. **"A novel rbf neural model for single flow zinc nickel batteries."** In Advanced Computational Methods in Energy, Power, Electric Vehicles, and Their Integration, pp. 386-395. Springer, Singapore, 2017.

5. Xuan, Liu, Kang Li, and **Xiang Li**. **"The Electrochemical Performance and Applications of Several Popular Lithium-ion Batteries**

**for Electric Vehicles-A Review."** In Advances in Green Energy Systems and Smart Grid, pp. 201-213. Springer, Singapore, 2018.

6. Yihuan, Li, Kang Li, **Shawn Li**, and Yanxue Li. **"FRA and EKF Based State of Charge Estimation of Zinc-Nickel Single Flow Batteries."** In Advances in Green Energy Systems and Smart Grid, pp. 183-191. Springer, Singapore, 2018.

7. Li, Zhang, Kang Li, Zhile Yang, **Xiang Li**, Yuanjun Guo, Dajun Du, and Chikong Wong. **"Compact Neural Modeling of Single Flow Zinc-Nickel Batteries Based on Jaya Optimization."** In Proceedings of CEC 2018, pp. 851-856. IEEE, 2018.

8. Miodrag, Vidakovic, Bruno Rente, Matthias Fabian, **Xiang Li**, Peter Fisher, Kang Li, Tong Sun, and Kenneth TV Grattan. **"Flow measurement inside a zinc-nickel flow cell battery using FBG based sensor system."** In Seventh European Workshop on Optical Fibre Sensors, vol. 11199, p. 1119915. International Society for Optics and Photonics, 2019.

## 8.2 Journal Papers

1. **Shawn, Li**, Kang Li, Evan Xiao, and Chi Kong Wong. **"Joint SoC and SoH Estimation for Zinc-Nickel Single Flow Batteries."** IEEE Transactions on Industrial Electronics (2019). (Impact Factor 7.503)

2. **Shawn, Li**, Kang Li, Evan Xiao, Jianhua Zhang, and Min Zheng. **"Real-time peak power prediction for zinc nickel single flow batteries."** Journal of Power Sources (2019): 227346. (Impact Factor 7.467)

3. **Shawn, Li**, Kang Li, Evan Xiao, Rui Xiong, Jianhua Zhang, and Peter Fischer. **"A novel model predictive control scheme based observer for working conditions and reconditioning monitoring of Zinc-Nickel single flow batteries."** Journal of Power Sources 445 (2020): 227282. (Impact Factor 7.467)

# REFERENCES


[1] P. Leung, X. Li, C. P. De León, L. Berlouis, C. J. Low, and F. C. Walsh, "Progress in redox flow batteries, remaining challenges and their applications in energy storage," *Rsc Advances*, vol. 2, no. 27, pp. 10125–10156, 2012. 18, 22, 2, 3, 4, 5, 6, 7, 8, 23, 33

[2] L. Zhang, J. Cheng, Y.-s. Yang, Y.-h. Wen, X.-d. Wang, and G.-p. Cao, "Study of zinc electrodes for single flow zinc/nickel battery application," *Journal of Power Sources*, vol. 179, no. 1, pp. 381–387, 2008. 18, 9, 10, 11, 36, 79, 113, 114, 124, 128, 129, 130

[3] X. Li, K. Li, and Z. Yang, "Teaching-learning-feedback-based optimization," in *International Conference on Swarm Intelligence*, pp. 71–79, Springer, 2017. 19, 49, 50

[4] D. Rastler, *Electricity energy storage technology options: a white paper primer on applications, costs and benefits*. Electric Power Research Institute, 2010. 22, 33

[5] H. Chen, T. N. Cong, W. Yang, C. Tan, Y. Li, and Y. Ding, "Progress in electrical energy storage system: A critical review," *Progress in natural science*, vol. 19, no. 3, pp. 291–312, 2009. 22, 2, 33

[6] B. Li and J. Liu, "Progress and directions in low-cost redox-flow batteries for large-scale energy storage," *National Science Review*, vol. 4, no. 1, pp. 91–105, 2017. 22, 5, 33

[7] J. Meng, G. Luo, M. Ricco, M. Swierczynski, D.-I. Stroe, and R. Teodorescu, "Overview of lithium-ion battery modeling methods for state-of-charge estimation in electrical vehicles," *Applied Sciences*, vol. 8, no. 5, p. 659, 2018. 22, 33, 60, 105

[8] X. Luo, J. Wang, M. Dooner, and J. Clarke, "Overview of current development in electrical energy storage technologies and the application potential in power system operation," *Applied energy*, vol. 137, pp. 511–536, 2015. 2

[9] K. Divya and J. Østergaard, "Battery energy storage technology for power systemsâan overview," *Electric Power Systems Research*, vol. 79, no. 4, pp. 511–520, 2009. 2

[10] A. Evans, V. Strezov, and T. J. Evans, "Assessment of utility energy storage options for increased renewable energy penetration," *Renewable and Sustainable Energy Reviews*, vol. 16, no. 6, pp. 4141–4147, 2012. 2

[11] D. Akinyele and R. Rayudu, "Review of energy storage technologies for sustainable power networks," *Sustainable Energy Technologies and Assessments*, vol. 8, pp. 74–91, 2014. 2

[12] Y. Liangzhong, Y. Bo, C. Hongfen, J. Zhuang, Y. Jilei, and X. Jinhua, "Challenges and progresses of energy storage technology and its application in power systems," *Journal of Modern Power Systems and Clean Energy*, vol. 4, no. 4, pp. 519–528, 2016. 2

[13] A. Nottrott, J. Kleissl, and B. Washom, "Energy dispatch schedule optimization and cost benefit analysis for grid-connected, photovoltaic-battery storage systems," *Renewable Energy*, vol. 55, pp. 230–240, 2013. 2

[14] B. Dunn, H. Kamath, and J.-M. Tarascon, "Electrical energy storage for the grid: a battery of choices," *Science*, vol. 334, no. 6058, pp. 928–935, 2011. 2

[15] W.-l. ZHANG, M. Qiu, and X.-k. LAI, "Application of energy storage technologies in power grids," *Power System Technology*, vol. 7, pp. 3–9, 2008. 2

[16] J. M. Eyer and S. M. Schoenung, "Benefit/cost framework for evaluating modular energy storage: a study for the doe energy storage systems program.," tech. rep., Sandia National Laboratories, 2008. 2

[17] P. F. Ribeiro, B. K. Johnson, M. L. Crow, A. Arsoy, and Y. Liu, "Energy storage systems for advanced power applications," *Proceedings of the IEEE*, vol. 89, no. 12, pp. 1744–1756, 2001. 2

[18] S. Van der Linden, "Bulk energy storage potential in the usa, current developments and future prospects," *Energy*, vol. 31, no. 15, pp. 3446–3457, 2006. 2

[19] P. J. Hall and E. J. Bain, "Energy-storage technologies and electricity generation," *Energy policy*, vol. 36, no. 12, pp. 4352–4355, 2008. 2

[20] S. Vazquez, S. M. Lukic, E. Galvan, L. G. Franquelo, and J. M. Carrasco, "Energy storage systems for transport and grid applications," *IEEE Transactions on Industrial Electronics*, vol. 57, no. 12, pp. 3881–3895, 2010. 2

[21] A. Z. Weber, M. M. Mench, J. P. Meyers, P. N. Ross, J. T. Gostick, and Q. Liu, "Redox flow batteries: a review," *Journal of Applied Electrochemistry*, vol. 41, no. 10, p. 1137, 2011. 2, 4, 5, 8

[22] C. P. De Leon, A. Frías-Ferrer, J. González-García, D. Szánto, and F. C. Walsh, "Redox flow cells for energy conversion," *Journal of Power Sources*, vol. 160, no. 1, pp. 716–732, 2006. 3, 5

[23] W. Kangro, "Verfahren zur speicherung von elektrischer energie," *German patent DE*, vol. 914, p. 264, 1949. 3

[24] A. Posner, "Redox fuel cell," *Fuel*, vol. 34, pp. 330–338, 1955. 3

[25] M. Vertes, E. Katsoulis, J. Oxley, and K. Alfredson, "Zinc/air high energy density rechargeable energy storage system.," tech. rep., LEESONA MOOS LABS DIV LEESONA CORP GREAT NECK NY, 1966. 3

[26] L. H. Thaller, "Electrically rechargeable redox flow cells," in *9th Intersociety Energy Conversion Engineering Conference*, pp. 924–928, 1974. 3

[27] L. Thaller, "Redox flow cell development and demonstration project, calendar year 1977 [r]," *Cleveland: National Aeronautics and Space Administration*, 1977. 3

[28] M. A. Reid and R. F. Gahn, "Factors affecting the open-circuit voltage and electrode kinetics of some iron/titanium redox flow cells," 1977. 3

[29] J. Giner, L. Swette, and K. Cahill, "Screening of redox couples and electrode materials," 1976. 3

[30] P. R. Prokopius, "Model for calculating electrolytic shunt path losses in large electrochemical energy conversion systems," 1976. 3

[31] N. Hagedorn, M. Hoberecht, and L. Thaller, "Nasa redox cell stack shunt current, pumping power, and cell performance tradeoffs," 1982. 3

[32] K. Michaels and G. Hall, "Cost projections for redox energy storage systems," 1980. 3

[33] P. Carr, P. C. Symons, and D. J. Aller, "Operational zinc chlorine battery based on a water store," Mar. 27 1979. US Patent 4,146,680. 3

[34] A. Appleby, J. Jacquelin, and J. Pompon, "Charge-discharge behavior of the cge circulating zinc-air vehicle battery," tech. rep., SAE Technical Paper, 1977. 3

[35] H. Lim, A. Lackner, and R. Knechtli, "Zinc-bromine secondary battery," *Journal of the Electrochemical Society*, vol. 124, no. 8, pp. 1154–1157, 1977. 3

[36] G. B. Adams, "Electrically rechargeable battery," Dec. 25 1979. US Patent 4,180,623. 3

[37] R. Yeo and D.-T. Chin, "A hydrogen-bromine cell for energy storage applications," *Journal of The Electrochemical Society*, vol. 127, no. 3, pp. 549–555, 1980. 3

[38] L. Hruska and R. Savinell, "Investigation of factors affecting performance of the iron-redox battery," *Journal of the Electrochemical Society*, vol. 128, no. 1, pp. 18–25, 1981. 3

[39] R. J. Remick and P. G. Ang, "Electrically rechargeable anionically active reduction-oxidation electrical storage-supply system," Nov. 27 1984. US Patent 4,485,154. 3

[40] M. Skyllas-Kazacos, M. Rychcik, R. G. Robins, A. Fane, and M. Green, "New all-vanadium redox flow cell," *Journal of the Electrochemical Society*, vol. 133, p. 1057, 1986. 3, 4, 9

[41] L. Arenas, C. P. De León, and F. Walsh, "Engineering aspects of the design, construction and performance of modular redox flow batteries for energy storage," *Journal of Energy Storage*, vol. 11, pp. 119–153, 2017. 5

[42] L. F. Arenas, C. P. de León, and F. C. Walsh, "Redox flow batteries for energy storage: their promise, achievements and challenges," *Current Opinion in Electrochemistry*, 2019. 5

[43] T. Gerber, P. Fischer, K. Pinkwart, and J. Tübke, "Segmented printed circuit board electrode for locally-resolved current density measurements in all-vanadium redox flow batteries," *Batteries*, vol. 5, no. 2, p. 38, 2019. 7

[44] W. Wang, Q. Luo, B. Li, X. Wei, L. Li, and Z. Yang, "Recent progress in redox flow battery research and development," *Advanced Functional Materials*, vol. 23, no. 8, pp. 970–986, 2013. 8

[45] J. Cheng, L. Zhang, Y.-S. Yang, Y.-H. Wen, G.-P. Cao, and X.-D. Wang, "Preliminary study of single flow zinc–nickel battery," *Electrochemistry Communications*, vol. 9, no. 11, pp. 2639–2642, 2007. 9, 10, 13, 36, 113, 114, 123, 124, 129, 155

[46] B. S. Kwak, D. Y. Kim, S. S. Park, B. S. Kim, and M. Kang, "Implementation of stable electrochemical performance using a fe0. 01zno anodic material in alkaline ni–zn redox battery," *Chemical Engineering Journal*, vol. 281, pp. 368–378, 2015. 9, 28

[47] A. Hazza, D. Pletcher, and R. Wills, "A novel flow battery: A lead acid battery based on an electrolyte with soluble lead (ii) part i. preliminary studies," *Physical Chemistry Chemical Physics*, vol. 6, no. 8, pp. 1773–1778, 2004. 10

[48] Y. Ito, M. Nyce, R. Plivelich, M. Klein, and S. Banerjee, "Gas evolution in a flow-assisted zinc–nickel oxide battery," *Journal of Power Sources*, vol. 196, no. 15, pp. 6583–6587, 2011. 10

[49] Y. Ito, M. Nyce, R. Plivelich, M. Klein, D. Steingart, and S. Banerjee, "Zinc morphology in zinc–nickel flow assisted batteries and impact on performance," *Journal of Power Sources*, vol. 196, no. 4, pp. 2340–2345, 2011. 10, 15, 28, 30, 32, 123, 128, 129, 149, 155

[50] Y. Wen, T. Wang, J. Cheng, J. Pan, G. Cao, and Y. Yang, "Lead ion and tetrabutylammonium bromide as inhibitors of the growth of spongy zinc in single flow zinc/nickel batteries," *Electrochimica Acta*, vol. 59, pp. 64–68, 2012. 11

[51] D. E. Turney, M. Shmukler, K. Galloway, M. Klein, Y. Ito, T. Sholklapper, J. W. Gallaway, M. Nyce, and S. Banerjee, "Development and testing of an economic grid-scale flow-assisted zinc/nickel-hydroxide alkaline battery," *Journal of Power Sources*, vol. 264, pp. 49–58, 2014. 11, 15, 32, 129, 155

[52] J. Diggle, A. Despic, and J. Bockris, "The mechanism of the dendritic electrocrystallization of zinc," *Journal of The Electrochemical Society*, vol. 116, no. 11, pp. 1503–1514, 1969. 13

[53] X. Li, C. P. de León, F. Walsh, R. G. Wills, and D. Pletcher, "Zinc-based flow batteries for medium-and large-scale energy storage," in *Advances in Batteries for Medium and Large-Scale Energy Storage*, pp. 293–315, Elsevier, 2015. 13, 22

[54] Y. Cheng, H. Zhang, Q. Lai, X. Li, D. Shi, and L. Zhang, "A high power density single flow zinc–nickel battery with three-dimensional porous negative electrode," *Journal of Power Sources*, vol. 241, pp. 196–202, 2013. 15, 32, 123

[55] L. Zhang, H. Zhang, Q. Lai, X. Li, and Y. Cheng, "Development of carbon coated membrane for zinc/bromine flow battery with high power density," *Journal of power sources*, vol. 227, pp. 41–47, 2013. 22

[56] Q. Lai, H. Zhang, X. Li, L. Zhang, and Y. Cheng, "A novel single flow zinc–bromine battery with improved energy density," *Journal of Power Sources*, vol. 235, pp. 1–4, 2013. 22

[57] J. H. Yang, H. S. Yang, H. W. Ra, J. Shim, and J.-D. Jeon, "Effect of a surface active agent on performance of zinc/bromine redox flow batteries: Improvement in current efficiency and system stability," *Journal of Power Sources*, vol. 275, pp. 294–297, 2015. 22

[58] J.-D. Jeon, H. S. Yang, J. Shim, H. S. Kim, and J. H. Yang, "Dual function of quaternary ammonium in zn/br redox flow battery: capturing the bromine and lowering the charge transfer resistance," *Electrochimica Acta*, vol. 127, pp. 397–402, 2014. 22

[59] Y. Munaiah, S. Dheenadayalan, P. Ragupathy, and V. K. Pillai, "High performance carbon nanotube based electrodes for zinc bromine redox flow batteries," *ECS Journal of Solid State Science and Technology*, vol. 2, no. 10, pp. M3182–M3186, 2013. 22, 23

[60] Y. Munaiah, S. Suresh, S. Dheenadayalan, V. K. Pillai, and P. Ragupathy, "Comparative electrocatalytic performance of single-walled and multiwalled carbon nanotubes for zinc bromine redox flow batteries," *The Journal of Physical Chemistry C*, vol. 118, no. 27, pp. 14795–14804, 2014. 23

[61] R. Clarke, B. Dougherty, S. Harrison, P. Millington, and S. Mohanta, "Us patent 2004/0202925 a1," *Cerium Batteries*, 2004. 24

[62] R. Clarke, B. Dougherty, S. Harrison, J. Millington, and S. Mohanta, "Us 2006/0063065 a1," *Battery with bifunctional electrolyte*, 2005. 24

[63] R. P. Kreh, R. M. Spotnitz, and J. T. Lundquist, "Mediated electrochemical synthesis of aromatic aldehydes, ketones, and quinones using ceric methanesulfonate," *The Journal of Organic Chemistry*, vol. 54, no. 7, pp. 1526–1531, 1989. 24

[64] P. Leung, C. P. De León, and F. Walsh, "An undivided zinc–cerium redox flow battery operating at room temperature (295 k)," *Electrochemistry Communications*, vol. 13, no. 8, pp. 770–773, 2011. 25

[65] F. C. Walsh, C. Ponce de Léon, L. Berlouis, G. Nikiforidis, L. F. Arenas-Martínez, D. Hodgson, and D. Hall, "The development of zn–ce hybrid redox flow batteries for energy storage and their continuing challenges," *ChemPlusChem*, vol. 80, no. 2, pp. 288–311, 2015. 25, 27

[66] P. Leung, C. P. De Leon, and F. Walsh, "The influence of operational parameters on the performance of an undivided zinc–cerium flow battery," *Electrochimica Acta*, vol. 80, pp. 7–14, 2012. 25

[67] P. Leung, C. Ponce-de León, F. Recio, P. Herrasti, and F. Walsh, "Corrosion of the zinc negative electrode of zinc–cerium hybrid redox flow batteries in methanesulfonic acid," *Journal of Applied Electrochemistry*, vol. 44, no. 9, pp. 1025–1035, 2014. 25, 26

[68] P. Leung, C. Ponce-de León, C. Low, and F. Walsh, "Zinc deposition and dissolution in methanesulfonic acid onto a carbon composite electrode as the negative electrode reactions in a hybrid redox flow battery," *Electrochimica Acta*, vol. 56, no. 18, pp. 6536–6546, 2011. 25, 128, 129

[69] P. Leung, C. Ponce-de Leon, C. Low, A. Shah, and F. Walsh, "Characterization of a zinc–cerium flow battery," *Journal of Power Sources*, vol. 196, no. 11, pp. 5174–5185, 2011. 25

[70] P. Leung, M. Mohamed, A. Shah, Q. Xu, and M. Conde-Duran, "A mixed acid based vanadium–cerium redox flow battery with a zero-gap serpentine architecture," *Journal of Power Sources*, vol. 274, pp. 651–658, 2015. 25, 26

[71] P. Leung, C. P. De León, C. Low, and F. Walsh, "Ce (iii)/ce (iv) in methanesulfonic acid as the positive half cell of a redox flow battery," *Electrochimica Acta*, vol. 56, no. 5, pp. 2145–2153, 2011. 26

[72] G. Nikiforidis and W. A. Daoud, "Effect of mixed acid media on the positive side of the hybrid zinc-cerium redox flow battery," *Electrochimica Acta*, vol. 141, pp. 255–262, 2014. 26

[73] L. F. Arenas, A. Loh, D. P. Trudgeon, X. Li, C. P. de Leon, and F. C. Walsh, "The characteristics and performance of hybrid redox flow batteries with zinc negative electrodes for energy storage," *Renewable and Sustainable Energy Reviews*, vol. 90, pp. 992–1016, 2018. 27, 32

[74] Y. Im, J. Kim, K. S. Park, T. W. Cho, J. Jeon, K.-i. Chung, K. Eguchi, and M. Kang, "Influence of small amount of mg incorporated into hexagonal zno crystal on cell performance in membrane free zinc–nickel redox battery," *Journal of Industrial and Engineering Chemistry*, 2018. 28, 29

[75] B. S. Kwak, S. W. Jo, K. S. Park, T. W. Cho, J. Jeon, K.-i. Chung, and M. Kang, "Synthesis of microcrystalline zno as an anodic material via a solvothermal method, and its electrochemical performance in ni/zn redox battery," *Journal of Industrial and Engineering Chemistry*, vol. 46, pp. 111–118, 2017. 28, 29

[76] J. Kim, Y. Im, K. S. Park, T. W. Cho, J. Jeon, K.-i. Chung, and M. Kang, "Improved cell performances in ni/zn redox batteries fabricated by zno materials with various morphologies synthesized using amine chelates," *Journal of Industrial and Engineering Chemistry*, vol. 56, pp. 463–471, 2017. 28, 29

[77] D. Coates and A. Charkey, "Nickel-zinc batteries for commercial applications," tech. rep., SAE Technical Paper, 1999. 29

[78] K. Bass, P. Mitchell, G. Wilcox, and J. Smith, "Methods for the reduction of shape change and dendritic growth in zinc-based secondary cells," *Journal of power sources*, vol. 35, no. 3, pp. 333–351, 1991. 29

[79] A.-R. El-Sayed, H. S. Mohran, and H. M. A. El-Lateef, "Effect of minor nickel alloying with zinc on the electrochemical and corrosion behavior of zinc in alkaline solution," *Journal of Power Sources*, vol. 195, no. 19, pp. 6924–6936, 2010. 29

[80] A.-R. El-Sayed, H. S. Mohran, and H. M. A. El-Lateef, "Inhibitive action of ferricyanide complex anion on both corrosion and passivation of zinc and zinc–nickel alloy in the alkaline solution," *Journal of Power Sources*, vol. 196, no. 15, pp. 6573–6582, 2011. 29

[81] R. Jain, T. Adler, F. McLarnon, and E. Cairns, "Development of long-lived high-performance zinc-calcium/nickel oxide cells," *Journal of applied electrochemistry*, vol. 22, no. 11, pp. 1039–1048, 1992. 30

[82] S. J. Banik and R. Akolkar, "Suppressing dendritic growth during alkaline zinc electrodeposition using polyethylenimine additive," *Electrochimica Acta*, vol. 179, pp. 475–481, 2015. 30

[83] R. Shivkumar, G. P. Kalaignan, and T. Vasudevan, "Effect of additives on zinc electrodes in alkaline battery systems," *Journal of power sources*, vol. 55, no. 1, pp. 53–62, 1995. 30

[84] B. Kavitha, P. Santhosh, M. Renukadevi, A. Kalpana, P. Shakkthivel, and T. Vasudevan, "Role of organic additives on zinc plating," *Surface and Coatings Technology*, vol. 201, no. 6, pp. 3438–3442, 2006. 30

[85] C. W. Lee, K. Sathiyanarayanan, S. W. Eom, H. S. Kim, and M. S. Yun, "Novel electrochemical behavior of zinc anodes in zinc/air batteries in the presence of additives," *Journal of Power Sources*, vol. 159, no. 2, pp. 1474–1477, 2006. 30

[86] C. W. Lee, K. Sathiyanarayanan, S. W. Eom, H. S. Kim, and M. S. Yun, "Effect of additives on the electrochemical behaviour of zinc anodes for zinc/air fuel cells," *Journal of power sources*, vol. 160, no. 1, pp. 161–164, 2006. 30

[87] J. L. Ortiz-Aparicio, Y. Meas, G. Trejo, R. Ortega, T. W. Chapman, and E. Chainet, "Effects of organic additives on zinc electrodeposition from alkaline electrolytes," *Journal of Applied Electrochemistry*, vol. 43, no. 3, pp. 289–300, 2013. 30

[88] D. Sylla, C. Savall, M. Gadouleau, C. Rebere, J. Creus, and P. Refait, "Electrodeposition of zn–mn alloys on steel using an alkaline pyrophosphate-based electrolytic bath," *Surface and Coatings Technology*, vol. 200, no. 7, pp. 2137–2145, 2005. 30

[89] M. Pereira, L. Barbosa, C. Souza, A. De Moraes, and I. A. Carlos, "The influence of sorbitol on zinc film deposition, zinc dissolution process and morphology of deposits obtained from alkaline bath," *Journal of applied electrochemistry*, vol. 36, no. 6, pp. 727–732, 2006. 30

[90] J. Zhu, Y. Zhou, and C. Gao, "Influence of surfactants on electrochemical behavior of zinc electrodes in alkaline solution," *Journal of Power Sources*, vol. 72, no. 2, pp. 231–235, 1998. 30

[91] N. Shaigan, W. Qu, and T. Takeda, "Morphology control of electrodeposited zinc from alkaline zincate solutions for rechargeable zinc air batteries," *Ecs Transactions*, vol. 28, no. 32, pp. 35–44, 2010. 30

[92] R. Naybour, "The effect of electrolyte flow on the morphology of zinc electrodeposited from aqueous alkaline solution containing zincate ions," *Journal of The Electrochemical Society*, vol. 116, no. 4, pp. 520–524, 1969. 31

[93] X. Li, C. Wong, and Z. Yang, "A novel flowrate control method for single flow zinc/nickel battery," in *Students on Applied Engineering (ICSAE), International Conference for*, pp. 30–35, IEEE, 2016. 31, 52, 125

[94] Y. Ito, X. Wei, D. Desai, D. Steingart, and S. Banerjee, "An indicator of zinc morphology transition in flowing alkaline electrolyte," *Journal of Power Sources*, vol. 211, pp. 119–128, 2012. 31

[95] J. F. Parker, C. N. Chervin, E. S. Nelson, D. R. Rolison, and J. W. Long, "Wiring zinc in three dimensions re-writes battery performanceâdendrite-free cycling," *Energy & Environmental Science*, vol. 7, no. 3, pp. 1117–1124, 2014. 31

[96] Z. Yan, E. Wang, L. Jiang, and G. Sun, "Superior cycling stability and high rate capability of three-dimensional zn/cu foam electrodes for zinc-based alkaline batteries," *RSC Advances*, vol. 5, no. 102, pp. 83781–83787, 2015. 31

[97] J. F. Parker, C. N. Chervin, I. R. Pala, M. Machler, M. F. Burz, J. W. Long, and D. R. Rolison, "Rechargeable nickel–3d zinc batteries: An energy-dense, safer alternative to lithium-ion," *Science*, vol. 356, no. 6336, pp. 415–418, 2017. 31, 123

[98] U. International Electrotechnical Commission, "Iec 61427-2 secondary cells and batteries for renewable energy storage â general requirements and methods of test â part 2: On-grid applications," *International Standards and Conformity Assessment for all electrical, electronic and related technologies*, 2015. 38

[99] Z. Wei, K. J. Tseng, N. Wai, T. M. Lim, and M. Skyllas-Kazacos, "Adaptive estimation of state of charge and capacity with online identified battery model for vanadium redox flow battery," *Journal of Power Sources*, vol. 332, pp. 389–398, 2016. 38, 65, 67, 72

[100] U. ABC, "Us abc electric vehicle battery test procedures manual, revision 2," *principal author: Gary Hunt, Idaho National Engineering Laboratory (INEL), US Department of Energy Idaho Field Office, DOE/ID-10479, Rev*, vol. 2, 1996. 39, 104

[101] M. Charkhgard and M. Farrokhi, "State-of-charge estimation for lithium-ion batteries using neural networks and ekf," *IEEE transactions on industrial electronics*, vol. 57, no. 12, pp. 4178–4187, 2010. 44, 45

[102] G. Dong, X. Zhang, C. Zhang, and Z. Chen, "A method for state of energy estimation of lithium-ion batteries based on neural network model," *Energy*, vol. 90, pp. 879–888, 2015. 44

[103] X. Dang, L. Yan, K. Xu, X. Wu, H. Jiang, and H. Sun, "Open-circuit voltage-based state of charge estimation of lithium-ion battery using dual neural network fusion battery model," *Electrochimica Acta*, vol. 188, pp. 356–366, 2016. 44

[104] L. Xu, J. Wang, and Q. Chen, "Kalman filtering state of charge estimation for battery management system based on a stochastic fuzzy neural network battery model," *Energy Conversion and Management*, vol. 53, no. 1, pp. 33–39, 2012. 44

[105] C. Chan, E. Lo, and S. Weixiang, "The available capacity computation model based on artificial neural network for lead–acid batteries in electric vehicles," *Journal of power sources*, vol. 87, no. 1-2, pp. 201–204, 2000. 44

[106] S.-K. Song, "State-of-charge measuring method using multilevel peukert's equation," *Journal of Power Sources*, vol. 70, no. 1, pp. 157–157, 1998. 44

[107] S.-k. Song, "State-of-charge measuring method using multilevel peukert's equation," Mar. 25 1997. US Patent 5,614,829. 44

[108] X. L. Kang Li and Z. Yang, "Teaching-learning-feedback-based optimization," in *The Eighth International Conference on Swarm Intelligence (ICSIâ2017)*, Springer, 2017. 45, 47, 49, 55

[109] K. Li, J.-X. Peng, and G. W. Irwin, "A fast nonlinear model identification method," *IEEE Transactions on Automatic Control*, vol. 50, no. 8, pp. 1211–1216, 2005. 45, 46

[110] K. Li and J.-X. Peng, "Neural input selectionâa fast model-based approach," *Neurocomputing*, vol. 70, no. 4, pp. 762–769, 2007. 46

[111] K. Li, J.-X. Peng, and E.-W. Bai, "Two-stage mixed discrete–continuous identification of radial basis function (rbf) neural models for nonlinear systems," *IEEE Transactions on Circuits and Systems I: Regular Papers*, vol. 56, no. 3, pp. 630–643, 2009. 47

[112] J. Kennedy, "Particle swarm optimization," in *Encyclopedia of machine learning*, pp. 760–766, Springer, 2011. 48

[113] Y.-X. Li, M.-C. Wong, W.-F. Ip, P.-C. Zhao, C.-K. Wong, J. Cheng, and Z.-Y. You, "Modeling of novel single flow zinc-nickel battery for energy storage system," in *Industrial Electronics and Applications (ICIEA), 2014 IEEE 9th Conference on*, pp. 1621–1626, IEEE, 2014. 52

[114] E. J. Dickinson, H. Ekström, and E. Fontes, "Comsol multiphysics®: Finite element software for electrochemical analysis. a mini-review," *Electrochemistry communications*, vol. 40, pp. 71–74, 2014. 57

[115] X. Han, M. Ouyang, L. Lu, and J. Li, "Simplification of physics-based electrochemical model for lithium ion battery on electric vehicle. part i: Diffusion simplification and single particle model," *Journal of Power Sources*, vol. 278, pp. 802–813, 2015. 58

[116] W. Gu, C. Wang, S. Li, M. Geng, and B. Liaw, "Modeling discharge and charge characteristics of nickel–metal hydride batteries," *Electrochimica Acta*, vol. 44, no. 25, pp. 4525–4541, 1999. 58

[117] D. Fan and R. E. White, "A mathematical model of a sealed nickel-cadmium battery," *Journal of the Electrochemical Society*, vol. 138, no. 1, pp. 17–25, 1991. 58

[118] V. Srinivasan, J. W. Weidner, and R. E. White, "Mathematical models of the nickel hydroxide active material," *Journal of Solid State Electrochemistry*, vol. 4, no. 7, pp. 367–382, 2000. 58

[119] P. M. Gomadam, J. W. Weidner, R. A. Dougal, and R. E. White, "Mathematical modeling of lithium-ion and nickel battery systems," *Journal of Power Sources*, vol. 110, no. 2, pp. 267–284, 2002. 58

[120] S. Yao, Y. Zhao, X. Sun, Q. Zhao, and J. Cheng, "A dynamic model for discharge research of zinc-nickel single flow battery," *Electrochimica Acta*, vol. 307, pp. 573–581, 2019. 58

[121] P. Shen, M. Ouyang, L. Lu, J. Li, and X. Feng, "The co-estimation of state of charge, state of health, and state of function for lithium-ion batteries in electric vehicles," *IEEE Transactions on Vehicular Technology*, vol. 67, no. 1, pp. 92–103, 2018. 60, 65, 104, 148

[122] X. Hu, S. Li, and H. Peng, "A comparative study of equivalent circuit models for li-ion batteries," *Journal of Power Sources*, vol. 198, pp. 359–367, 2012. 60, 65

[123] Z. Wei, S. Meng, K. J. Tseng, T. M. Lim, B. H. Soong, and M. Skyllas-Kazacos, "An adaptive model for vanadium redox flow battery and its application for online peak power estimation," *Journal of Power Sources*, vol. 344, pp. 195–207, 2017. 62, 105

[124] Z. Wei, J. Zhao, D. Ji, and K. J. Tseng, "A multi-timescale estimator for battery state of charge and capacity dual estimation based on an online identified model," *Applied Energy*, vol. 204, pp. 1264–1274, 2017. 63, 65, 72, 81, 106, 130, 131

[125] Z. Wei, C. Zou, F. Leng, B. H. Soong, and K.-J. Tseng, "Online model identification and state-of-charge estimate for lithium-ion battery with a recursive total least squares-based observer," *IEEE Transactions on Industrial Electronics*, vol. 65, no. 2, pp. 1336–1346, 2018. 64, 65, 72

[126] X. Li, K. Li, Z. Yang, and C. Wong, "A novel rbf neural model for single flow zinc nickel batteries," in *Advanced Computational Methods in Energy, Power, Electric Vehicles, and Their Integration*, pp. 386–395, Springer, 2017. 65

[127] M. Shahriari and M. Farrokhi, "Online state-of-health estimation of vrla batteries using state of charge," *IEEE Transactions on Industrial Electronics*, vol. 60, no. 1, pp. 191–202, 2013. 65

[128] C. Zhang, K. Li, J. Deng, and S. Song, "Improved realtime state-of-charge estimation of lifepo4 battery based on a novel thermoelectric model," *IEEE Transactions on Industrial Electronics*, vol. 64, no. 1, pp. 654–663, 2017. 65, 70

[129] C. Zhang, L. Y. Wang, X. Li, W. Chen, G. G. Yin, and J. Jiang, "Robust and adaptive estimation of state of charge for lithium-ion batteries," *IEEE Transactions on Industrial Electronics*, vol. 62, no. 8, pp. 4948–4957, 2015. 65

[130] T. Kim and W. Qiao, "A hybrid battery model capable of capturing dynamic circuit characteristics and nonlinear capacity effects," *IEEE Transactions on Energy Conversion*, vol. 26, no. 4, pp. 1172–1180, 2011. 65

[131] G. L. Plett, "Extended kalman filtering for battery management systems of lipb-based hev battery packs: Part 3. state and parameter estimation," *Journal of Power sources*, vol. 134, no. 2, pp. 277–292, 2004. 65, 72, 73, 108

[132] Y. Wang, H. Fang, L. Zhou, and T. Wada, "Revisiting the state-of-charge estimation for lithium-ion batteries: A methodical investigation of the extended kalman filter approach," *IEEE Control Systems Magazine*, vol. 37, no. 4, pp. 73–96, 2017. 65

[133] R. Xiong, F. Sun, Z. Chen, and H. He, "A data-driven multi-scale extended kalman filtering based parameter and state estimation approach of lithium-ion olymer battery in electric vehicles," *Applied Energy*, vol. 113, pp. 463–476, 2014. 65, 130, 131

[134] L. Zhang, K. Li, D. Du, M. Fei, and X. Li, "State-of-charge estimation of lithium batteries using compact rbf networks and aukf," in *Advanced Computational Methods in Energy, Power, Electric Vehicles, and Their Integration*, pp. 396–405, Springer, 2017. 65

[135] H. Rahimi-Eichi, F. Baronti, and M.-Y. Chow, "Online adaptive parameter identification and state-of-charge coestimation for lithium-polymer battery

cells," *IEEE Transactions on Industrial Electronics*, vol. 61, no. 4, pp. 2053–2061, 2014. 65

[136] B. Xiong, J. Zhao, Y. Su, Z. Wei, and M. Skyllas-Kazacos, "State of charge estimation of vanadium redox flow battery based on sliding mode observer and dynamic model including capacity fading factor," *IEEE Transactions on Sustainable Energy*, vol. 8, no. 4, pp. 1658–1667, 2017. 65

[137] R. Xiong, Q. Yu, L. Y. Wang, and C. Lin, "A novel method to obtain the open circuit voltage for the state of charge of lithium ion batteries in electric vehicles by using h infinity filter," *Applied Energy*, vol. 207, pp. 346–353, 2017. 65, 71, 107

[138] Y. Zhang, R. Xiong, H. He, and W. Shen, "Lithium-ion battery pack state of charge and state of energy estimation algorithms using a hardware-in-the-loop validation," *IEEE Transactions on Power Electronics*, vol. 32, no. 6, pp. 4421–4431, 2017. 65

[139] D. Zhou, K. Zhang, A. Ravey, F. Gao, and A. Miraoui, "Online estimation of lithium polymer batteries state-of-charge using particle filter-based data fusion with multimodels approach," *IEEE Transactions on Industry Applications*, vol. 52, no. 3, pp. 2582–2595, 2016. 65

[140] G. S. Misyris, T. Tengnér, A. G. Marinopoulos, D. I. Doukas, and D. P. Labridis, "Battery energy storage systems modeling for online applications," in *PowerTech, 2017 IEEE Manchester*, pp. 1–6, IEEE, 2017. 65

[141] G. Misyris, D. I. Doukas, T. A. Papadopoulos, D. P. Labridis, and V. G. Agelidis, "State-of-charge estimation for li-ion batteries: A more accurate hybrid approach," *IEEE Transactions on Energy Conversion*, 2018. 65

[142] E. Eweda and O. Macchi, "Convergence of the rls and lms adaptive filters," *IEEE Transactions on circuits and Systems*, vol. 34, no. 7, pp. 799–803, 1987. 69

[143] H. He, X. Zhang, R. Xiong, Y. Xu, and H. Guo, "Online model-based estimation of state-of-charge and open-circuit voltage of lithium-ion batteries in electric vehicles," *Energy*, vol. 39, no. 1, pp. 310–318, 2012. 71

[144] M. Morari and J. H. Lee, "Model predictive control: past, present and future," *Computers & Chemical Engineering*, vol. 23, no. 4-5, pp. 667–682, 1999. 83, 84

[145] J. H. Lee, "Model predictive control: Review of the three decades of development," *International Journal of Control, Automation and Systems*, vol. 9, no. 3, p. 415, 2011. 83

[146] J. Zhang, Y. Zhou, Y. Li, G. Hou, and F. Fang, "Generalized predictive control applied in waste heat recovery power plants," *Applied energy*, vol. 102, pp. 320–326, 2013. 83, 106

[147] M. G. Forbes, R. S. Patwardhan, H. Hamadah, and R. B. Gopaluni, "Model predictive control in industry: Challenges and opportunities," *IFAC-PapersOnLine*, vol. 48, no. 8, pp. 531–538, 2015. 83

[148] I.-S. Kim, "Nonlinear state of charge estimator for hybrid electric vehicle battery," *IEEE Transactions on Power Electronics*, vol. 23, no. 4, pp. 2027–2034, 2008. 84

[149] C. Zou, A. Klintberg, Z. Wei, B. Fridholm, T. Wik, and B. Egardt, "Power capability prediction for lithium-ion batteries using economic nonlinear model predictive control," *Journal of Power Sources*, vol. 396, pp. 580–589, 2018. 89

[150] X. Hu, D. Cao, and B. Egardt, "Condition monitoring in advanced battery management systems: moving horizon estimation using a reduced electrochemical model," *IEEE/ASME Transactions on Mechatronics*, vol. 23, no. 1, pp. 167–178, 2018. 91

[151] W. Waag, C. Fleischer, and D. U. Sauer, "Adaptive on-line prediction of the available power of lithium-ion batteries," *Journal of Power Sources*, vol. 242, pp. 548–559, 2013. 104, 105

[152] G. Liu, M. Ouyang, L. Lu, J. Li, and J. Hua, "A highly accurate predictive-adaptive method for lithium-ion battery remaining discharge energy prediction in electric vehicle applications," *Applied Energy*, vol. 149, pp. 297–314, 2015. 104, 105

[153] R. Xiong, Y. Zhang, H. He, X. Zhou, and M. G. Pecht, "A double-scale, particle-filtering, energy state prediction algorithm for lithium-ion batteries," *IEEE Transactions on Industrial Electronics*, vol. 65, no. 2, pp. 1526–1538, 2018. 104

[154] L. Pei, C. Zhu, T. Wang, R. Lu, and C. Chan, "Online peak power prediction based on a parameter and state estimator for lithium-ion batteries in electric vehicles," *Energy*, vol. 66, pp. 766–778, 2014. 104, 105

[155] X. Qiu, T. A. Nguyen, J. D. Guggenberger, M. L. Crow, and A. C. Elmore, "A field validated model of a vanadium redox flow battery for microgrids," *IEEE Transactions on Smart Grid*, vol. 5, no. 4, pp. 1592–1601, 2014. 104

[156] F. Zheng, J. Jiang, B. Sun, W. Zhang, and M. Pecht, "Temperature dependent power capability estimation of lithium-ion batteries for hybrid electric vehicles," *Energy*, vol. 113, pp. 64–75, 2016. 104

[157] G. L. Plett, "High-performance battery-pack power estimation using a dynamic cell model," *IEEE Transactions on Vehicular Technology*, vol. 53, no. 5, pp. 1586–1593, 2004. 105

[158] L. Zheng, J. Zhu, G. Wang, D. D.-C. Lu, and T. He, "Lithium-ion battery instantaneous available power prediction using surface lithium concentration of solid particles in a simplified electrochemical model," *IEEE Transactions on Power Electronics*, 2018. 105

[159] Z. Wei, J. Zhao, and B. Xiong, "Dynamic electro-thermal modeling of all-vanadium redox flow battery with forced cooling strategies," *Applied Energy*, vol. 135, pp. 1–10, 2014. 105

[160] Y. Zhang, J. Zhao, P. Wang, M. Skyllas-Kazacos, B. Xiong, and R. Badrinarayanan, "A comprehensive equivalent circuit model of all-vanadium redox flow battery for power system analysis," *Journal of Power Sources*, vol. 290, pp. 14–24, 2015. 105

[161] X. Liu, Z. Chen, C. Zhang, and J. Wu, "A novel temperature-compensated model for power li-ion batteries with dual-particle-filter state of charge estimation," *Applied Energy*, vol. 123, pp. 263–272, 2014. 106

[162] H. N. Nguyen and P. O. Gutman, "Fast constrained lqr based on mpc with linear decomposition," *IEEE Transactions on Automatic Control*, vol. 61, no. 9, pp. 2585–2590, 2016. 106

[163] Y. Cheng, Q. Lai, X. Li, X. Xi, Q. Zheng, C. Ding, and H. Zhang, "Zinc-nickel single flow batteries with improved cycling stability by eliminating zinc accumulation on the negative electrode," *Electrochimica Acta*, vol. 145, pp. 109–115, 2014. 123

[164] Y. Cheng, H. Zhang, Q. Lai, X. Li, and D. Shi, "Performance gains in single flow zinc–nickel batteries through novel cell configuration," *Electrochimica Acta*, vol. 105, pp. 618–621, 2013. 124

[165] J. Yan, J. Wang, H. Liu, Z. Bakenov, D. Gosselink, and P. Chen, "Rechargeable hybrid aqueous batteries," *Journal of Power Sources*, vol. 216, pp. 222–226, 2012. 128

[166] Y. Li and H. Dai, "Recent advances in zinc–air batteries," *Chemical Society Reviews*, vol. 43, no. 15, pp. 5257–5275, 2014. 128

[167] P. N. Ross Jr, "Zinc electrode and rechargeable zinc-air battery," June 27 1989. US Patent 4,842,963. 129

[168] K. Wang, P. Pei, Z. Ma, H. Xu, P. Li, and X. Wang, "Morphology control of zinc regeneration for zinc–air fuel cell and battery," *Journal of Power Sources*, vol. 271, pp. 65–75, 2014. 129

[169] N. Vatistas, M. Bartolozzi, and S. Arras, "The dismantling of the spent alkaline zinc manganese dioxide batteries and the recovery of the zinc from the anodic material," *Journal of Power Sources*, vol. 101, no. 2, pp. 182–187, 2001. 129

[170] C. Hu, B. D. Youn, and J. Chung, "A multiscale framework with extended kalman filter for lithium-ion battery soc and capacity estimation," *Applied Energy*, vol. 92, pp. 694–704, 2012. 131

[171] T. Kim, Y. Wang, Z. Sahinoglu, T. Wada, S. Hara, and W. Qiao, "A rayleigh quotient-based recursive total-least-squares online maximum capacity estimation for lithium-ion batteries," *IEEE Transactions on Energy Conversion*, vol. 30, no. 3, pp. 842–851, 2015. 131

[172] Y. Zou, X. Hu, H. Ma, and S. E. Li, "Combined state of charge and state of health estimation over lithium-ion battery cell cycle lifespan for electric vehicles," *Journal of Power Sources*, vol. 273, pp. 793–803, 2015. 131

[173] J. Wu, Y. Wang, X. Zhang, and Z. Chen, "A novel state of health estimation method of li-ion battery using group method of data handling," *Journal of Power Sources*, vol. 327, pp. 457–464, 2016. 131

[174] C. Hu, G. Jain, C. Schmidt, C. Strief, and M. Sullivan, "Online estimation of lithium-ion battery capacity using sparse bayesian learning," *Journal of Power Sources*, vol. 289, pp. 105–113, 2015. 131

[175] A. Eddahech, O. Briat, and J.-M. Vinassa, "Determination of lithium-ion battery state-of-health based on constant-voltage charge phase," *Journal of Power Sources*, vol. 258, pp. 218–227, 2014. 131

[176] C. Lu, L. Tao, and H. Fan, "Li-ion battery capacity estimation: A geometrical approach," *Journal of power sources*, vol. 261, pp. 141–147, 2014. 131

[177] I. Baghdadi, O. Briat, P. Gyan, and J. M. Vinassa, "State of health assessment for lithium batteries based on voltage–time relaxation measure," *Electrochimica Acta*, vol. 194, pp. 461–472, 2016. 131

[178] Z. Deng, L. Yang, Y. Cai, H. Deng, and L. Sun, "Online available capacity prediction and state of charge estimation based on advanced data-driven algorithms for lithium iron phosphate battery," *Energy*, vol. 112, pp. 469–480, 2016. 131

[179] C. Weng, Y. Cui, J. Sun, and H. Peng, "On-board state of health monitoring of lithium-ion batteries using incremental capacity analysis with support vector regression," *Journal of Power Sources*, vol. 235, pp. 36–44, 2013. 131, 133

[180] C. Weng, X. Feng, J. Sun, and H. Peng, "State-of-health monitoring of lithium-ion battery modules and packs via incremental capacity peak tracking," *Applied Energy*, vol. 180, pp. 360–368, 2016. 131

[181] M. Berecibar, M. Garmendia, I. Gandiaga, J. Crego, and I. Villarreal, "State of health estimation algorithm of lifepo4 battery packs based on differential voltage curves for battery management system application," *Energy*, vol. 103, pp. 784–796, 2016. 131, 133

[182] L. Wang, C. Pan, L. Liu, Y. Cheng, and X. Zhao, "On-board state of health estimation of lifepo4 battery pack through differential voltage analysis," *Applied energy*, vol. 168, pp. 465–472, 2016. 131, 133

[183] M. Berecibar, F. Devriendt, M. Dubarry, I. Villarreal, N. Omar, W. Verbeke, and J. Van Mierlo, "Online state of health estimation on nmc cells based on predictive analytics," *Journal of Power Sources*, vol. 320, pp. 239–250, 2016. 131

[184] M. Berecibar, I. Gandiaga, I. Villarreal, N. Omar, J. Van Mierlo, and P. Van den Bossche, "Critical review of state of health estimation methods of li-ion batteries for real applications," *Renewable and Sustainable Energy Reviews*, vol. 56, pp. 572–587, 2016. 132

[185] M. Dubarry, C. Truchot, and B. Y. Liaw, "Synthesize battery degradation modes via a diagnostic and prognostic model," *Journal of power sources*, vol. 219, pp. 204–216, 2012. 132

[186] I. Bloom, A. N. Jansen, D. P. Abraham, J. Knuth, S. A. Jones, V. S. Battaglia, and G. L. Henriksen, "Differential voltage analyses of high-power, lithium-ion cells: 1. technique and application," *Journal of Power Sources*, vol. 139, no. 1-2, pp. 295–303, 2005. 132, 133

[187] M. Dubarry and B. Y. Liaw, "Identify capacity fading mechanism in a commercial lifepo4 cell," *Journal of Power Sources*, vol. 194, no. 1, pp. 541–549, 2009. 132, 133

[188] C. Pastor-Fernández, K. Uddin, G. H. Chouchelamane, W. D. Widanage, and J. Marco, "A comparison between electrochemical impedance spectroscopy and incremental capacity-differential voltage as li-ion diagnostic techniques to identify and quantify the effects of degradation modes within battery management systems," *Journal of Power Sources*, vol. 360, pp. 301–318, 2017. 132

[189] Y. Li, M. Abdel-Monem, R. Gopalakrishnan, M. Berecibar, E. Nanini-Maury, N. Omar, P. van den Bossche, and J. Van Mierlo, "A quick on-line state of health estimation method for li-ion battery with incremental capacity curves processed by gaussian filter," *Journal of Power Sources*, vol. 373, pp. 40–53, 2018. 133

[190] M. Dubarry, B. Y. Liaw, M.-S. Chen, S.-S. Chyan, K.-C. Han, W.-T. Sie, and S.-H. Wu, "Identifying battery aging mechanisms in large format li ion cells," *Journal of Power Sources*, vol. 196, no. 7, pp. 3420–3425, 2011. 133

[191] X. Han, M. Ouyang, L. Lu, and J. Li, "Cycle life of commercial lithium-ion batteries with lithium titanium oxide anodes in electric vehicles," *Energies*, vol. 7, no. 8, pp. 4895–4909, 2014. 133

[192] Y.-l. Chou, *Probability and statistics for decision making*. Henry Holt & Co, 1972. 134

[193] T. Goh, M. Park, M. Seo, J. G. Kim, and S. W. Kim, "Capacity estimation algorithm with a second-order differential voltage curve for li-ion batteries with nmc cathodes," *Energy*, vol. 135, pp. 257–268, 2017. 134, 140

[194] S. Lever, "Life-cycle optimization and flow control in a nickel-zinc flow assisted battery," 2012. 137

[195] S. W. Smith *et al.*, "The scientist and engineer's guide to digital signal processing," 1997. 138

[196] I. Bloom, L. K. Walker, J. K. Basco, D. P. Abraham, J. P. Christophersen, and C. D. Ho, "Differential voltage analyses of high-power lithium-ion cells. 4. cells containing nmc," *Journal of Power Sources*, vol. 195, no. 3, pp. 877–882, 2010. 140

[197] X. Feng, J. Li, M. Ouyang, L. Lu, J. Li, and X. He, "Using probability density function to evaluate the state of health of lithium-ion batteries," *Journal of Power Sources*, vol. 232, pp. 209–218, 2013. 141

[198] M. Shahriari and M. Farrokhi, "Online state-of-health estimation of vrla batteries using state of charge," *IEEE Transactions on Industrial Electronics*, vol. 60, no. 1, pp. 191–202, 2012. 148

[199] K. S. Ng, C.-S. Moo, Y.-P. Chen, and Y.-C. Hsieh, "Enhanced coulomb counting method for estimating state-of-charge and state-of-health of lithium-ion batteries," *Applied energy*, vol. 86, no. 9, pp. 1506–1511, 2009. 148

[200] K.-S. Ng, Y.-F. Huang, C.-S. Moo, and Y.-C. Hsieh, "An enhanced coulomb counting method for estimating state-of-charge and state-of-health of lead-acid batteries," pp. 1–5, 2009. 148